
First-Principles Basin-Hopping for the Structure Determination of Atomic Clusters

Ralf Gehrke
Diplom-Physiker

im Fachbereich Physik
der Freien Universität Berlin eingereichte
Inaugural-Dissertation
zur Erlangung des akademischen Grades
Doctor Rerum Naturalium

Berlin
November 2008



MAX-PLANCK-GESELLSCHAFT



Diese Arbeit wurde in der Zeit von Dezember 2004 bis November 2008 unter der Aufsicht von PD Dr. Karsten Reuter in der Theorieabteilung des Fritz-Haber-Institutes der Max-Planck-Gesellschaft durchgeführt.

Erstgutachter: PD Dr. Karsten Reuter

Zweitgutachter: Prof. Dr. Eberhard K.U. Gross

Disputationstermin: 26. Januar 2009

Abstract

Research on small particles containing up to a few tens of atoms is largely driven by their novel properties that are significantly affected by quantum effects, particularly in the interplay between structural and electronic degrees of freedom. Such clusters, thus, carry the potential of major technological advances for applications exploiting their already exemplified unique optical, magnetic, and chemical properties. Atomically resolved structural information is a key prerequisite towards employing these envisioned functionalities, considering that the latter will be tailored to the atomic scale. In this respect not only the ground state isomer will be of importance, but potentially all energetically low-lying metastable isomers.

A materials modeling targeting the identification of such relevant cluster isomers involves the global and local exploration of the corresponding vast configuration space, represented by the high-dimensional potential-energy surface (PES). The exponential growth of the number of local PES minima, i.e. metastable isomers, with increasing cluster size quickly limits approaches focusing only on structural motifs provided by chemical intuition.

In this thesis the problem is addressed with a first-principles Monte Carlo approach. The essential features herein are a quantitative quantum mechanical energetics from density-functional theory, together with a basin-hopping type sampling for the global exploration of the energy surface. This approach is applied to Co_n^+Ar_m clusters, for which far-infrared vibrational spectroscopy data were provided by the group of Prof. Gerard Meijer at the Molecular Physics Department of the FHI. For the isomers obtained by the implemented first-principles sampling scheme, we calculated the infrared spectra, that are in turn compared to the experimental data. Apart from the thus gained structure information, we particularly elaborated on the role of the involved Ar probe atoms and its implication for the indirect structure determination using the vibrational fingerprints.

To suggest possible strategies for optimizing the numerically intense *ab initio* based sampling, the involved technical settings are analyzed in detail, using small silicon and copper clusters as illustrative benchmark systems. In order to assess and critically discuss the limitations and bottlenecks of the scheme, a central aspect of this part of the work was to establish a framework to quantitatively measure the sampling efficiency. The detailed insights obtained are then used to devise a robust self-adapting scheme for future applications in particular to systems involving intermediate size clusters.

“So einfach wie möglich. Aber nicht einfacher.”

Albert Einstein

Contents

| | |
|---|-----------|
| 1. Introduction | 13 |
| I. Theoretical Background | 17 |
| 2. Describing the Configurational Space of Atomic Clusters | 18 |
| 2.1. The Born-Oppenheimer Surface | 18 |
| 2.2. Fundamentals of Group Theory | 19 |
| 2.2.1. Symmetry Elements and Operations | 20 |
| 2.2.2. Symmetry Point Groups | 20 |
| 2.3. Features of the Energy Surface | 22 |
| 2.3.1. Stationary Points and Normal Modes | 22 |
| 2.3.2. Global Topology of the Energy Surface | 26 |
| 2.4. Thermodynamics | 27 |
| 2.4.1. Translational Degrees of Freedom | 28 |
| 2.4.2. Molecular Vibrations | 28 |
| 2.4.3. Molecular Rotations | 29 |
| 3. Exploring the Configurational Space | 30 |
| 3.1. Local Optimization Methods | 30 |
| 3.1.1. Steepest Descent | 30 |
| 3.1.2. Conjugate Gradient | 31 |
| 3.1.3. The Broyden-Fletcher-Goldfarb-Shanno (BFGS) Method | 32 |
| 3.2. Global Optimization Schemes | 32 |
| 3.2.1. Simulated Annealing | 33 |
| 3.2.2. Basin-Hopping | 34 |
| 3.2.3. Genetic Algorithms | 35 |
| 3.2.4. Further Algorithms | 36 |
| 3.3. Summary | 37 |
| 4. Density-Functional Theory | 38 |
| 4.1. The Electronic Wave Function | 38 |
| 4.1.1. The Electron and Pair Density | 38 |
| 4.2. Approximative Methods to solve the Many-Body Problem | 39 |
| 4.3. The Thomas-Fermi Model | 40 |
| 4.4. The Hohenberg-Kohn Theorems | 40 |

| | |
|---|-----------|
| 4.5. The Kohn-Sham Equation | 42 |
| 4.6. Present-Day Exchange-Correlation Functionals | 44 |
| 4.7. Spin-Density-Functional Theory | 45 |
| II. The Density-Functional Theory Implementation FHI-aims | 47 |
| 5. Solving the Kohn-Sham Equations with Numerical Atom-Centered Basis Sets | 48 |
| 5.1. The Eigenvalue Problem | 49 |
| 5.1.1. Achieving Self-Consistency | 50 |
| 5.2. Numerical Atom-Centered Basis Functions | 52 |
| 5.2.1. The Definition of the Basis Functions | 52 |
| 5.2.2. The Generation of Basis Functions | 53 |
| 5.3. Numerical Integration | 54 |
| 5.4. The Hartree-Potential | 56 |
| 6. Energy Derivatives in FHI-aims | 58 |
| 6.1. The Calculation of Analytical Atomic Forces | 58 |
| 6.1.1. The Individual Derivative Terms | 60 |
| 6.1.2. The Atomic Forces in the Case of LSD | 62 |
| 6.1.3. The GGA-Correction Term | 63 |
| 6.1.4. The Atomic Forces in Connection with Smearing Methods | 64 |
| 6.1.5. Grid Effects | 64 |
| 6.2. Consistency of the Forces | 65 |
| 6.3. The Second Energy Derivative | 66 |
| III. Nature of Ar Bonding to Small Co_n^+ Clusters and its Effect on the Structure Determination by Far-Infrared Absorption Spectroscopy | 69 |
| 7. The Vibrational Fingerprint of Small Co_n^+ Clusters and their Ar Complexes | 70 |
| 7.1. Introduction | 70 |
| 7.2. Far-Infrared Absorption Spectroscopy | 71 |
| 7.2.1. Experimental Setup | 71 |
| 7.2.2. Observation of Highly Coordinated $\text{Co}_n^+ \text{Ar}_m$ Complexes | 72 |
| 7.2.3. Interpretation of FIR-MPD Spectra | 73 |
| 7.3. Computational Details | 74 |
| 7.3.1. Structural Relaxation and Calculation of the IR-Spectra | 74 |
| 7.3.2. The Counterpoise Correction to the Basis Set Superposition Error | 75 |
| 7.3.3. Zero-Point Energy | 76 |
| 7.4. Selection of Structural Motifs by Spin-Extended Basin-Hopping | 77 |

| | |
|--|------------|
| 7.5. Thermodynamic Effects | 78 |
| 7.6. The Influence of the Exchange-Correlation Functional | 78 |
| 7.7. Low-lying Isomers and Vibrational Spectra of their Ar Complexes | 80 |
| 7.7.1. Co_4^+ | 80 |
| 7.7.2. Co_5^+ | 82 |
| 7.7.3. Co_6^+ | 83 |
| 7.7.4. Co_7^+ | 87 |
| 7.7.5. Co_8^+ | 88 |
| 7.8. Summary | 91 |
| 8. The Nature of the Ar-Co_n^+ Bonding | 92 |
| 8.1. Introduction | 92 |
| 8.2. Electrostatic Model of the Ar-Co_n^+ Bonding | 92 |
| 8.2.1. Multipole Decomposition via Hirshfeld Analysis | 92 |
| 8.2.2. Ar Binding Energy in the Electrostatic Model | 93 |
| 8.2.3. Electrostatic Driving Forces | 95 |
| 8.3. Summary and Conclusion | 99 |
| IV. Assessing the Efficiency of First-Principles Basin-Hopping Sampling | 101 |
| 9. Method Optimization Based upon Quantitative Efficiency Criteria | 102 |
| 9.1. Introduction | 102 |
| 9.2. Computational Details | 103 |
| 9.2.1. Density-Functional Theory | 103 |
| 9.2.2. Basin-Hopping | 104 |
| 9.2.3. Measuring Sampling Efficiency | 106 |
| 9.3. Performance Analysis For Small Cluster Sizes | 108 |
| 9.3.1. Existence of Dominant Isomers | 109 |
| 9.3.2. Approximate Hopping Matrix | 112 |
| 9.3.3. CPU Reduction by Using Optimum Sampling Parameters | 114 |
| 9.4. Adaptive Move Scheme | 120 |
| 9.5. Summary and Conclusion | 122 |
| 10. Summary and Outlook | 124 |
| V. Appendix | 126 |
| A. Basis Sets used in FHI-aims | 127 |

| | |
|---|------------|
| B. Convergence Tests for the Co_n^+Ar Complexes | 130 |
| B.1. Integration Grid | 131 |
| B.2. Basis Set Convergence | 134 |
| B.3. Cutoff Radius | 136 |
| B.4. Hartree Potential | 138 |
| B.5. Force Convergence Criterium and Finite Displacement for the Numerical Hessian and Dipole Gradient | 140 |
| C. Convergence Tests for Si and Cu clusters | 141 |
| C.1. Integration Grid | 142 |
| C.2. Basis Set Convergence | 143 |
| C.3. Cutoff Radius | 144 |
| C.4. Hartree Potential | 145 |
| C.5. Force Convergence Criterium and Finite Displacement for the Numerical Hessian | 146 |
| D. High Order Finite Difference Schemes | 147 |
| E. Computed Structures and IR Spectra of Co_n^+Ar_m Complexes | 149 |
| Publications | 178 |
| Kurzfassung | 179 |
| Curriculum vitae | 181 |
| Acknowledgements | 182 |

List of Figures

| | |
|---|-----|
| 2.1. Illustration of the symmetry elements | 20 |
| 2.2. Illustration of the most common symmetry point groups | 21 |
| 2.3. Model surface | 22 |
| 2.4. Permutation-inversions of a pentagonal bipyramid | 25 |
| 2.5. Schematical picture of a multi-funnel PES | 27 |
| 3.1. Steepest descent vs. conjugate gradient. | 32 |
| 3.2. The principle of the basin-hopping method | 35 |
| 3.3. Mating procedure | 35 |
| 6.1. Accuracy test of the analytical forces | 65 |
| 6.2. Local relaxations for Si ₇ , Si ₁₀ and Cu ₇ | 66 |
| 6.3. Convergence of the vibrational frequency w.r.t. the integration grid | 67 |
| 6.4. Convergence of the vibrational frequency w.r.t. the step width Δ | 67 |
| 7.1. Scheme of the experimental set-up used for FIR-MPD | 72 |
| 7.2. Distribution of cationic cobalt clusters and their Ar complexes | 73 |
| 7.3. The principle of spin-extended basin-hopping | 77 |
| 7.4. Free energies differences | 78 |
| 7.5. Comparison of computed vibrational spectra using PW-LDA and GGA-PBE | 79 |
| 7.6. Experimental and computed IR spectra of Co ₄ Ar _M ⁺ | 84 |
| 7.7. Experimental and computed IR spectra of Co ₅ Ar _M ⁺ | 85 |
| 7.8. Experimental and computed IR spectra of Co ₆ Ar _M ⁺ | 86 |
| 7.9. Experimental and computed IR spectra of Co ₇ Ar _M ⁺ | 89 |
| 7.10. Experimental and computed IR spectra of Co ₈ Ar _M ⁺ | 90 |
| 8.1. Electron density difference of Co ₄ ⁺ -Ar | 93 |
| 8.2. Electron density difference of Co ₄ ⁺ | 94 |
| 8.3. Electrostatic model of the Ar-Co _n ⁺ bonding | 95 |
| 8.4. Binding sites of Co ₇ ⁺ Ar | 96 |
| 8.5. Correlation between Ar binding energy and direct dipole moment | 97 |
| 8.6. Ar binding energy at Co _n ⁺ vs cluster size | 98 |
| 8.7. Attractive Hartree-type Ar-Co _n ⁺ interaction energy computed in the electrostatic model | 99 |
| 9.1. Adjusting the difference tolerance | 106 |

List of Figures

| | | |
|-------|---|-----|
| 9.2. | successful, unsuccessful and high-energy trial moves | 107 |
| 9.3. | Isomer histograms of Si ₇ , Si ₁₀ and Cu ₇ | 109 |
| 9.4. | Histogram evolution of Si ₇ | 110 |
| 9.5. | Si ₇ -isomers | 111 |
| 9.6. | Si ₁₀ -isomers | 111 |
| 9.7. | Cu ₇ -isomers | 112 |
| 9.8. | Performance analysis for Si ₇ and Cu ₇ | 116 |
| 9.9. | Diagonal elements of the hopping matrix | 117 |
| 9.10. | Performance analysis for Si ₁₀ | 119 |
| 9.11. | The convergence of $\gamma_{\text{succ.}}$ | 120 |
| 9.12. | Self-adapting move distance | 121 |
| A.1. | PW-LDA binding curves for basis set generation | 129 |
| B.1. | Co _n ⁺ Ar-complexes used for the convergence tests | 131 |
| B.2. | IR spectra vs. integration grid. | 131 |
| B.3. | IR spectra vs. basis set. | 134 |
| B.4. | IR spectra vs. cutoff radius. | 137 |
| B.5. | IR spectra vs. $l_{\text{max.}}$ | 138 |
| B.6. | IR spectra vs. force convergence criterium and finite displacement. | 140 |
| C.1. | Pentagonal bipyramid motif of Si ₇ and Cu ₇ | 141 |
| E.1. | Co ₄ ⁺ IR spectra with PBE | 150 |
| E.2. | Co ₄ ⁺ Ar IR spectra with PBE | 151 |
| E.3. | Co ₄ ⁺ Ar _m IR spectra with PBE | 152 |
| E.4. | Co ₄ ⁺ Ar IR spectra with PW-LDA | 153 |
| E.5. | Co ₅ ⁺ IR spectra with PBE | 154 |
| E.6. | Co ₅ ⁺ Ar IR spectra with PBE | 155 |
| E.7. | Co ₅ ⁺ Ar ₅ IR spectrum with PBE | 156 |
| E.8. | Co ₅ ⁺ Ar IR spectra with PW-LDA | 157 |
| E.9. | Co ₆ ⁺ IR spectra with PBE | 158 |
| E.10. | Co ₆ ⁺ Ar IR spectra with PBE | 159 |
| E.11. | Co ₆ ⁺ Ar IR spectra with PW-LDA | 160 |
| E.12. | Co ₇ ⁺ IR spectra with PBE | 161 |
| E.13. | Co ₇ ⁺ IR spectra with PBE | 162 |
| E.14. | Co ₇ ⁺ Ar IR spectra with PBE | 163 |
| E.15. | Co ₇ ⁺ Ar IR spectra with PBE | 164 |
| E.16. | Co ₇ ⁺ Ar IR spectra with PW-LDA | 165 |
| E.17. | Co ₈ ⁺ IR spectra with PBE | 166 |
| E.18. | Co ₈ ⁺ IR spectra with PBE | 167 |
| E.19. | Co ₈ ⁺ Ar IR spectra with PBE | 168 |
| E.20. | Co ₈ ⁺ Ar IR spectra with PBE | 169 |
| E.21. | Co ₈ ⁺ Ar IR spectra with PW-LDA | 170 |

List of Tables

| | |
|---|-----|
| 7.1. Corrections due to the intermolecular BSSE | 76 |
| 7.2. Corrections due to zero-point energy | 76 |
| 8.1. Binding energies in the electrostatic model | 96 |
| 9.1. The number of different versions for the dominant isomers. | 113 |
| 9.2. Performance comparison of normal and uniform move distribution | 119 |
| A.1. Radial basis functions used in FHI-aims | 127 |
| B.1. Convergence test of the integration grid for Co_4^+Ar | 132 |
| B.2. Convergence test of the integration grid for Co_6^+Ar | 132 |
| B.3. Convergence of the bond distances for Co_4^+Ar | 133 |
| B.4. Convergence of the bond distances for Co_6^+Ar | 133 |
| B.5. Convergence test of the basis sets for Co_4^+Ar | 134 |
| B.6. Convergence test of the basis sets for Co_6^+Ar | 135 |
| B.7. Convergence of the bond distances for Co_4^+Ar w.r.t. basis | 135 |
| B.8. Convergence of the bond distances for Co_6^+Ar w.r.t. basis | 135 |
| B.9. Convergence test of the cutoff radius r_{cut} for Co_4^+Ar | 136 |
| B.10. Convergence test of the cutoff radius r_{cut} for Co_6^+Ar | 136 |
| B.11. Convergence of the bond distances for Co_4^+Ar w.r.t. r_{cut} | 137 |
| B.12. Convergence of the bond distances for Co_6^+Ar w.r.t. r_{cut} | 137 |
| B.13. Convergence test of the Hartree potential for Co_4^+Ar | 138 |
| B.14. Convergence test of the Hartree potential for Co_6^+Ar | 139 |
| B.15. Convergence of the bond distances for Co_4^+Ar w.r.t. l_{max} | 139 |
| B.16. Convergence of the bond distances for Co_6^+Ar w.r.t. l_{max} | 139 |
| C.1. Convergence test of the integration grid for the four dominant Si_7 isomers | 142 |
| C.2. Convergence test of the integration grid for the three dominant Cu_7 isomers | 142 |
| C.3. Convergence test of the basis set for the four dominant Si_7 isomers | 143 |
| C.4. Convergence test of the basis set for the four dominant Cu_7 isomers . . . | 143 |
| C.5. Convergence test of r_{cut} for the four dominant Si_7 isomers | 144 |
| C.6. Convergence test of r_{cut} for the three dominant Cu_7 isomers | 144 |
| C.7. Convergence test of l_{max} for the four dominant Si_7 isomers | 145 |
| C.8. Convergence test of l_{max} for the three dominant Cu_7 isomers | 145 |
| C.9. Vibrational frequencies for Si_7 and Cu_7 w.r.t. F_{max} and Δ | 146 |
| D.1. Coefficients for the first numerical derivative | 147 |

List of Tables

| | |
|---|-----|
| D.2. Coefficients for the second numerical derivative | 148 |
|---|-----|

1. Introduction

Clusters are aggregates of atoms and thus somewhere intermediate in size between individual atoms and bulk matter. One major characteristic that separates them from the bulk is the dramatic change in the electronic structure when the system size is reduced to few atoms, thus replacing the quasi-continuous density of states by a discrete energy level spectrum. Due to the intricate relationship between structural and electronic degrees of freedom, optical, magnetic and chemical properties do therefore not vary smoothly with size and shape of the cluster but are highly governed by quantum (size) effects. The study of these effects constitutes one field of cluster physics, since they open the door to novel applications, such as small electronic devices. A second important property of clusters is the large fraction of atoms being on the surface. Due to this favourable surface to volume ratio, metal clusters are for instance ideal candidates for applications in catalysis. Atomically resolved structural information is thereby a key prerequisite towards employing these envisioned functionalities, considering that the latter will be tailored to the atomic scale.

Experimentally, structural information can for instance be obtained by photoelectron spectroscopy, which exploits the fact that different isomers exhibit different electronic structures. The measured density of states can therefore serve as a characteristic fingerprint for the underlying atomic structure. In the case of reactivity experiments, the number of adsorbed atoms on a cluster is measured, which is obviously correlated with the number of adsorption sites and therefore with the cluster shape. Another probe of cluster structure is provided by mobility experiments in which clusters are accelerated by an electric field and then traverse a chamber containing an inert gas. The travelling time is hereby affected by the collisions of the clusters with the inert gas and thus correlates with the collision cross section, being sensitive to the atomic structure. Another possibility that is particularly sensitive to the internal cluster structure is the measurement of vibrational frequencies. A corresponding technique that has recently been successfully employed to determine the structure of cationic and neutral metal clusters is far-infrared (vibrational) resonance enhanced multiple photon dissociation (FIR-MPD) spectroscopy [1, 2, 3, 4, 5]. Common to all these experimental methods is that atomic information is not directly measured, but only quantities that are coupled to the geometric configuration. At this point, theory comes into play and provides the required tool to assign the experimental data to an underlying geometry. As starting point for any such theoretical study, structural motifs are therefore required, which in the easiest approach are merely guessed, guided by chemical intuition. While for small systems, containing only few atoms such an approach might seem sufficient at first glance, it is in practice even then likely that one misses isomers. This holds in particular for systems exhibiting strong Jahn-Teller distortions, with a concomitant number of different isomers all corre-

1. Introduction

sponding to the same basic structural motif. What is thus required is a more systematic scheme which then involves the global and local exploration of the huge configurational space, represented by the potential-energy surface (PES) [6]. A central and challenging property of the PES is thereby the suspected exponential increase of the number of local minima with system size. This drastic growth has led to the famous Levinthal’s paradox according to which a protein would never reach its native state within the lifetime of the universe if it would have to go through all local PES minima completely randomly [7, 8].

Correspondingly, approaches addressing the determination of cluster structures face a twofold challenge, the first being the calculation of the PES itself. To have predictive power and in view of the intricate quantum-size effects ruling clusters in the targeted size range, a quantum-mechanical treatment of the PES is obviously required. Accurate quantum-mechanical methods become unfortunately prohibitively expensive due to their unfavourable scaling behaviour. The second order perturbation theory by Møller and Plesset (MP2) [9], for instance, scales as $O(N^5)$ with the system size, thus quickly becoming prohibitively expensive in connection with the exponentially increasing number of PES minima. As an alternative, density-functional theory scales formally as $O(N^3)$ and can be implemented to reach $O(N)$ for larger systems. It thus represents a suitable compromise between accuracy and computational demand and is the technique employed in the present work. The second major theoretical problem is the systematic and efficient exploration of the thus defined PES. A classical optimization method for this purpose is simulated annealing, in which successive trial moves, corresponding to random distortions of the cluster geometry are performed. Accepting or rejecting such moves via a Boltzmann-factor, the system is then driven towards the ground state structure. An additional key ingredient of many unbiased sampling schemes is a local structural relaxation, ensuing the trial move, which thereby reduces the PES sampling to the local minima and thus facilitates the optimization tremendously. In combination with simulated annealing, this scheme has first been proposed as Monte-Carlo minimization or basin-hopping by D. Wales and L. Scheraga [10]. A primary target for which basin-hopping is employed is to identify the global PES minimum, i.e. the most stable geometric structure in the focus of atomic clusters. However, in experiment, thermodynamic or kinetic reasons might lead to a population of metastable isomers or superpositions of it, thus making energetically higher-lying isomers subject to fundamental interest as well. By suitably adjusting the temperature controlled acceptance scheme in the simulated annealing, basin-hopping can be tuned to achieve this goal, thus identifying isomers within a thermodynamically reasonable energy range above the ground state. In the present work, a corresponding basin-hopping scheme has been coupled to the DFT implementation **FHI-aims** [11] currently developed at the FHI Theory Department, with the goal to perform a conformational sampling of cluster structures based on an accurate *ab initio* PES.

Aiming at interpreting the FIR-MPD data of Co_n^+Ar complexes measured in the group of Prof. Gerard Meijer at the Molecular Physics Department of the FHI, we first applied the developed tool to obtain candidate structures for the ensuing electronic structure studies. In an FIR-MPD experiment, the vibrational spectrum is measured by

1. Introduction

far-infrared absorption spectroscopy using argon as probe atoms. Irradiated by a free-electron laser, the Co_n^+Ar complex is heated up when the laser frequency is in resonance with a vibrational eigenmode. Multiple photons can then be absorbed, which in turn leads to the dissociation of the argon atom from the metal cluster. Recording the resulting abundance changes of the rare-gas complexes as a function of the IR frequency yields the desired spectra that can finally be compared to computed IR absorption spectra for the different isomer structures obtained in the preceding sampling. Tacitly assuming that the influence of the probe atom on the vibrational fingerprint can be neglected, this enables the structure determination of the bare cobalt clusters and provides valuable feedback on the accuracy of the energetic ordering provided by the employed approximate DFT exchange-correlation functional. Contrary to previous studies on V_n^+ ($n = 3 - 23$) [1, 2], Nb_n^+ ($n = 5 - 9$) [3, 4] and Ta_n^+ ($n = 6 - 20$) [5], however, a strong influence of the measured spectra on the number of adsorbed argon atoms has this time been observed, which motivated us to explicitly elaborate on the role of the probe atom and its implications for the structure determination. This then also involved exhaustive sampling runs, with argon ligands explicitly taken into account.

Despite the fact that due to continuing methodological improvements and vast increase of computational power *ab initio* basin-hopping runs have nowadays become possible, one still has to recognize that due to the exponential growth of the number of PES minima with system size, this method quickly reaches its limit. Unfortunately, many studies in the literature merely provide the size of the largest system studied as some kind of performance indicator of the employed sampling scheme, or at best record as benchmark the mean first encounter of the global minimum, i.e. the number of local relaxations until the ground state has been identified for the first time. What is more or less completely missing is an exact measure of efficiency that is coupled to the sampling goal used in a practical application, namely not only to find the ground state but also to identify higher-lying isomers. Motivated by the application in the first part of this work, the aim of the second part is therefore to establish a framework to quantitatively analyze the efficiency of a sampling run. Apart from identifying inefficient settings and suggesting possible optimization strategies, one has to note in this respect that already exactly pinning down the efficiency of an *ab initio* basin-hopping run is a task of its own. On the one hand one needs to define a reasonable measurable quantity which correlates with the sampling success. On the other hand, hundreds of basin-hopping runs are required to get statistically meaningful averages. This can quickly become unfeasible with straightforward DFT, whereas use of simple model-potentials is uncertain to provide answers for the practical materials-science applications. To circumvent this problem, we therefore developed the concept of a hopping matrix, which records the transition probabilities between individual isomers and thus enables the extraction of statistically meaningful quantities at tremendously reduced computational demand. Once the connectivity of the low-lying isomers is therewith represented, the hopping matrix provides the additional possibility to analyze different kind of efficiency indicators without having to run further first-principles basin-hopping runs and thus allows to further disentangle and understand the sampling process.

After introducing the different methodologies and concepts to describe and explore

1. Introduction

the configurational space of atomic clusters in Part I, the employed DFT implementation **FHI-aims** is presented in Part II. Special emphasis is hereby given on the analytical atomic forces, which are required for an efficient local structural relaxation, and the implementation of which constituted a major, preparatory part of this thesis. Part III then describes the comparison between the experimental and computed Co_n^+Ar IR-spectra based upon geometries obtained by first-principles basin-hopping. Using small silicon and copper clusters as illustrative benchmarks, Part IV finally addresses the performance of the applied basin-hopping algorithm by disentangling and critically discussing the different technical settings, and then presenting a self-adapting scheme based upon the obtained insights.

Part I.

Theoretical Background

2. Describing the Configurational Space of Atomic Clusters

2.1. The Born-Oppenheimer Surface

The starting point to get the energetics of an atomic cluster containing N_{el} electrons and N nuclei is the Schrödinger equation which in time-independent non-relativistic cases can be written as

$$\hat{H}\Psi(\{\mathbf{x}_i\}, \{\mathbf{R}_\alpha\}) = E\Psi(\{\mathbf{x}_i\}, \{\mathbf{R}_\alpha\}) , \quad (2.1)$$

where $\{\mathbf{x}_i\} \equiv \{\mathbf{x}_1, \dots, \mathbf{x}_{N_{\text{el}}}\} \equiv \{(\mathbf{r}_1, \sigma_1), \dots, (\mathbf{r}_N, \sigma_{N_{\text{el}}})\}$ is a short hand notation for all spatial and spin coordinates of the N_{el} electrons and $\{\mathbf{R}_\alpha\} \equiv \{\mathbf{R}_1, \dots, \mathbf{R}_N\}$ denotes the spatial coordinates of all nuclei. The Hamiltonian contains the following terms

$$\hat{H} = T_e + T_N + V_{Ne} + V_{ee} + V_{NN} , \quad (2.2)$$

with the individual contributions being the kinetic energy of the electrons T_e and of the nuclei T_N , the electrostatic interaction between the electrons V_{ee} , between the nuclei V_{NN} and between the electrons and nuclei V_{Ne} . Using atomic units, i.e. $\hbar = m_e = e = 4\pi\epsilon_0 = 1$, the terms have the following form:

$$T_e = \sum_{i=1}^{N_{\text{el}}} \frac{\mathbf{p}_i^2}{2} = -\frac{1}{2} \sum_{i=1}^{N_{\text{el}}} \nabla_i^2 , \quad (2.3)$$

$$T_N = \sum_{\alpha=1}^N \frac{\mathbf{p}_\alpha^2}{2M_\alpha} = -\frac{1}{2} \sum_{\alpha=1}^N \frac{1}{M_\alpha} \nabla_\alpha^2 , \quad (2.4)$$

$$V_{Ne}(\{\mathbf{r}_i\}, \{\mathbf{R}_\alpha\}) = - \sum_{i=1}^{N_{\text{el}}} \sum_{\alpha=1}^N \frac{Z_\alpha}{|\mathbf{r}_i - \mathbf{R}_\alpha|} , \quad (2.5)$$

$$V_{ee}(\{\mathbf{r}_i\}) = \sum_{i=1}^{N_{\text{el}}} \sum_{j>i}^{N_{\text{el}}} \frac{1}{|\mathbf{r}_i - \mathbf{r}_j|} , \quad (2.6)$$

$$V_{NN}(\{\mathbf{R}_\alpha\}) = \sum_{\alpha=1}^N \sum_{\beta>\alpha}^N \frac{Z_\alpha Z_\beta}{|\mathbf{R}_\alpha - \mathbf{R}_\beta|} . \quad (2.7)$$

In principle, the solution of Eq. (2.1) accurately describes the energetics of a system. However, containing $3N + 3N_{\text{el}}$ degrees of freedom, it is computationally unfeasible to

2. Describing the Configurational Space of Atomic Clusters

tackle Eq. (2.1) exactly and hence, approximations have to be applied. The first important one is the *Born-Oppenheimer Approximation* [12] which states that electronic and nuclear motions can be separated using the following ansatz for the total wavefunction:

$$\Psi(\{\mathbf{x}_i\}, \{\mathbf{R}_\alpha\}) = \Psi_e(\{\mathbf{x}_i\}, \{\mathbf{R}_\alpha\}) \Psi_N(\{\mathbf{R}_\alpha\}) , \quad (2.8)$$

with the electronic part being a solution of the electronic Hamiltonian:

$$\hat{H}_e = T_e + V_{Ne} + V_{ee} , \quad (2.9)$$

$$\hat{H}_e \Psi_e(\{\mathbf{x}_i\}, \{\mathbf{R}_\alpha\}) = E_e(\{\mathbf{R}_\alpha\}) \Psi_e(\{\mathbf{x}_i\}, \{\mathbf{R}_\alpha\}) . \quad (2.10)$$

The justification is that due to the huge ratio of the masses, electrons can instantaneously catch up with the movements of the nuclei. In the extreme case of a hydrogen atom, for instance, $M/m_e \approx 1800$. In other words, the ions are fixed from the electronic point of view or just move very slowly. Consequently, the nuclear positions appear only as parameters in the electronic wavefunction and the effect of the kinetic energy operator of the nuclei on the electronic part of the wavefunction can be neglected.

$$T_N \Psi_e(\{\mathbf{x}_i\}, \{\mathbf{R}_\alpha\}) \Psi_N(\{\mathbf{R}_\alpha\}) \approx \Psi_e(\{\mathbf{x}_i\}, \{\mathbf{R}_\alpha\}) T_N \Psi_N(\{\mathbf{R}_\alpha\}) . \quad (2.11)$$

Using this approximation, the ansatz (2.8) leads to the following equation for the nuclear part of the wave function:

$$(T_N + V_{NN}(\{\mathbf{R}_\alpha\}) + E_e(\{\mathbf{R}_\alpha\})) \Psi_N = E \Psi_N . \quad (2.12)$$

So the ions move under the influence of the effective potential

$$V_{BO}(\{\mathbf{R}_\alpha\}) \equiv V_{NN}(\{\mathbf{R}_\alpha\}) + E_e(\{\mathbf{R}_\alpha\}) , \quad (2.13)$$

which is called the *Born-Oppenheimer surface* or more generally the *potential energy surface* (PES). The total energy E_{tot} of the system is then the potential energy plus quantum mechanical corrections due to lattice vibrations.

The initial problem of solving equation (2.1) has thus been reduced to solving the electronic equation (2.10) in order to obtain $E_e(\{\mathbf{R}_\alpha\})$ which in turn defines the PES according to Eq. (2.13). Though the number of degrees of freedom has therewith been reduced from $3N_{\text{el}} + 3N$ to $3N_{\text{el}}$, a huge computational burden still remains and further approximations are required which will be discussed in chapter 4.

2.2. Fundamentals of Group Theory

Many common molecules, in particular small ones containing few atoms, possess symmetry, i.e. undergoing certain *symmetry operations*, like a rotation around a certain angle for instance, the molecule superimposes with itself. Using group theory, symmetry considerations are therefore on the one hand helpful to introduce a nomenclature for describing a molecular structure. Furthermore, features of the PES that will later on be

discussed, can be addressed more quantitatively exploiting the symmetry of the system taken into account. It is therefore of great importance to understand the fundamentals of group theory with which the symmetry properties of a molecule are described in a concise way (see e.g. [13]).

2.2.1. Symmetry Elements and Operations

The symmetry of a molecule can best be described by listing all *symmetry elements* which allow for symmetry operations. One example of a symmetry element is the *n-fold rotation axis* C_n . In such a case, the corresponding symmetry operation C_n^k is k times a rotation about an angle of $2\pi/n$ around the rotation axis which thus superimposes the molecule with itself.

Another element is the *plane of symmetry* σ , with the corresponding operation being a reflection of the molecule through this plane.

A third possible element is the *alternating axis of rotation* S_n . In that case, a rotation about an angle of $2\pi/n$ is carried

out, being followed by a reflection of the molecule through a plane perpendicular to this axis. S_n^k corresponds to k times a rotation around the axis, each being followed by a reflection. A special case of an alternating axis of rotation is $S_n^{n/2}$, n being even, which is equivalent to an *inversion* of the molecule through its center. Furthermore, if k is even, then S_n^k is simply equivalent to an ordinary rotation C_n^k . For odd n , all S_n^k with $k \leq 2n - 1$ are different operations, since then $S_n^{k>n}$ equals S_n^{k-n} followed by a reflection through the symmetry plane and thus is a new operation.

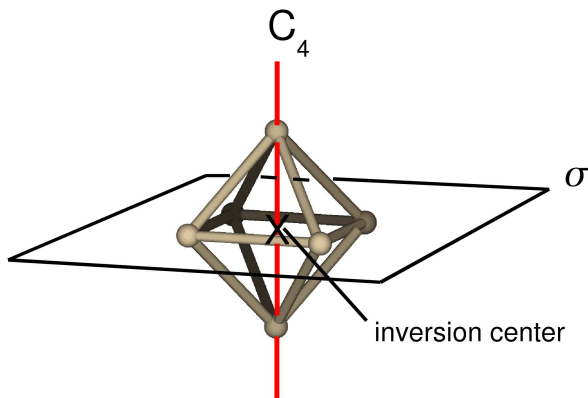


Figure 2.1.: Illustration of the symmetry elements exemplifying an octahedral structure.

2.2.2. Symmetry Point Groups

The set of all possible symmetry operations of a molecule forms a *group* which is mathematically defined by the following properties:

- The *product* of two members $A \circ B = C$ also constitutes a member of the group. In particular, the product is *associative*, i.e. $A \circ (B \circ C) = (A \circ B) \circ C$.
- A special group element is the *identity* E , which leaves any member unchanged, i.e. $E \circ A = A \circ E = A$.
- Each member A can be assigned an inverse A^{-1} so that the product $A \circ A^{-1} = A^{-1} \circ A = E$ equals the identity.

2. Describing the Configurational Space of Atomic Clusters

In the case of symmetry operations, a product of two operations corresponds to the consecutive application of these two operations, like for instance the product $C_n^1 \circ C_n^1 = C_n^2$ corresponds to twice a rotation about an angle of $2\pi/n$. The net operation C_n^2 is hence a rotation about an angle of $2 \cdot 2\pi/n$ and therefore also part of the group. The identity E is a trivial operation that does not change the molecule at all. Obviously, for each operation one can find an operation that reverts the effect of the former one, thus being the corresponding inverse element. The inverse of the rotation C_n^1 , for instance, is C_n^{n-1} .

The symmetry of the molecule is reflected by the point group of the constituent symmetry operations, with the number of different operations being an important quantity which is called the *order* of the point group.

The most common point groups describing the symmetry of molecules are:

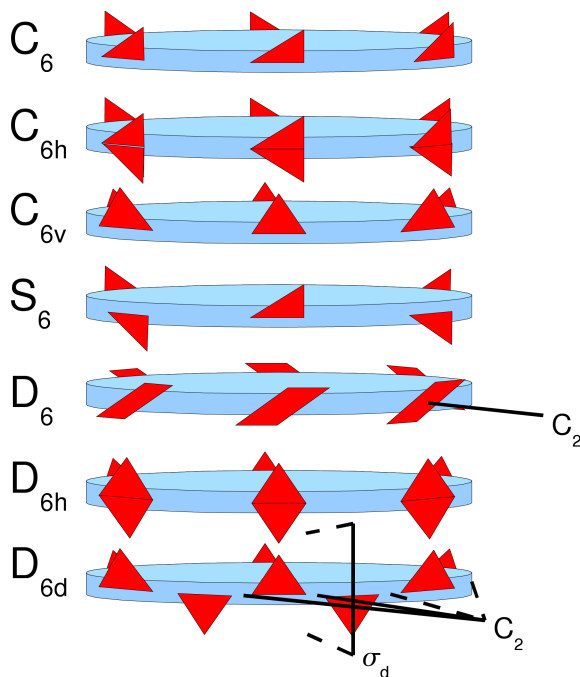


Figure 2.2.: Illustration of the most common symmetry point groups.

- $\underline{C_n}$. This simple point group is made up of an n -fold-rotation axis which thus contains the elements $\{E, C_n^1, \dots, C_n^{n-1}\} = \{E, \{C_n^k\}\}$. Correspondingly, it possesses the order n and is called a *cyclic* group.
- $\underline{C_{nh}}$. Additional to an n -fold-rotation axis, the molecule described by this cyclic group exhibits a plane of symmetry σ_h perpendicular to the axis ("horizontal"). Consequently, the alternating axis appears as well as a symmetry operation, since $\sigma_h \circ C_n^k = S_n^k$, with k being odd. For even k , S_n^k is equivalent to C_n^k since the reflections at the horizontal plane even out ($\sigma_h \circ \sigma_h = E$). The special case of C_{1h} is commonly denoted as C_s . The group therewith contains the operations $\{E, \sigma_h, \{C_n^k\}, \{S_n^k\}\}$.
- $\underline{C_{nv}}$. Additional to an n -fold-rotation axis, the molecule contains n vertical planes perpendicular to the axis. Summarized the operations are $\{E, \{\sigma_v^i\}, \{C_n^k\}\}$.
- $\underline{S_n}$. A further cyclic group is obtained by having a pure alternating axis of rotation which thus leads to the operations $\{E, \{S_n^k\}\}$. This group is only new for even n , since for n being odd, S_n is equivalent to C_{nh} .
- $\underline{D_n}$. Additional to an n -fold-rotation axis, the molecule described by the *dihedral* group features n two-fold rotation axes perpendicular to the principle symmetry

axis, which thus allows for the symmetry operations $\{E, \{C_n^k\}, \{(C_2^1)^i\}\}$, with i being an index running over the different two-fold rotation axes.

- D_{nh} . Additional to the symmetry operations of the D_n -group, the molecule possesses a plane of symmetry perpendicular to the principle axis which further introduces the alternating axis of symmetry and n vertical planes of symmetry. Hence, this dihedral group contains the operations $\{E, \sigma_h, \{\sigma_v^i\}, \{C_n^k\}, \{(C_2^1)^i\}, \{S_n^k\}\}$.
- D_{nd} . Additional to the symmetry operations of the D_n -group, the system contains n vertical planes of symmetry bisecting the n two-fold rotation axes, resulting in the set of operations $\{E, \sigma_h, \{\sigma_d^i\}, \{C_n^k\}, \{(C_2^1)^i\}, \{S_n^k\}\}$.

The remaining point groups contain multiple rotation axes of order greater than two. The *tetrahedral* group T , for instance, possesses all rotation axes of a regular tetrahedron, while the *full tetrahedral* group T_d additionally contains all mirror planes. Similarly, the *full octahedral* group O_h comprises all symmetry elements possessed by a regular cube, and the *full icosahedral* group I_h those of an icosahedron.

2.3. Features of the Energy Surface

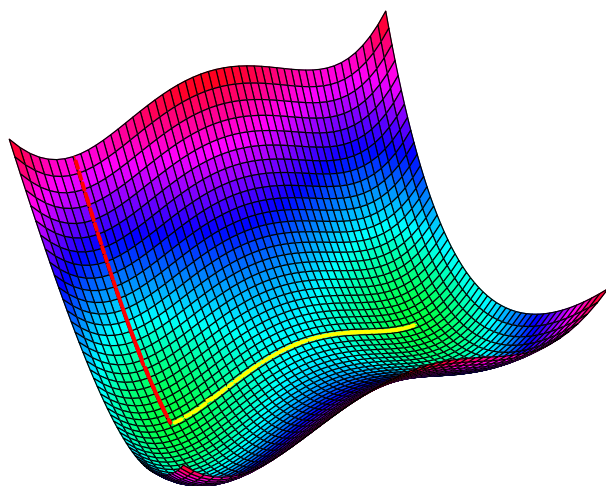


Figure 2.3: Model surface ($V = x^4 - x^2 + y^2$) exhibiting two local minima (green regions) that are connected by two steepest-descent paths crossing a transition state (yellow line). The red line exemplifies a further steepest-descent path leading to the left local minimum.

2.3.1. Stationary Points and Normal Modes

Within the Born-Oppenheimer approximation, the nuclear dynamics is typically treated semi-classically, i.e. the energy surface V_{BO} is obtained quantum-mechanically, whereas the atoms are treated as classical point masses in space. The forces are therefore obtained as total energy derivatives with respect to the atomic positions

$$\mathbf{F}_\alpha = -\frac{dV_{BO}}{d\mathbf{R}_\alpha}, \quad (2.14)$$

2. Describing the Configurational Space of Atomic Clusters

and the atomic motion is given by the solution of the classical Newton equation

$$M_\alpha \ddot{\mathbf{R}}_\alpha = -\frac{d}{d\mathbf{R}_\alpha} V_{\text{BO}}(\{\mathbf{R}_\alpha\}) . \quad (2.15)$$

Most interesting points on the PES are the *stationary points* which are configurations for which all forces vanish and the corresponding energy possesses an extremum. In particular, *local minima* exhibit a positive slope of the PES in all directions. Consequently, any small displacement of the atoms results in a restoring force that brings the atoms back to their equilibrium positions, the corresponding configuration is *stable* and called an *isomer* of the system in the context of molecules and clusters. In particular, the local minimum with the lowest total energy is the *global minimum*. In order to check the local stability of a stationary point quantitatively, a *normal mode* analysis can be performed. For that, molecular vibrations around the equilibrium position of the nuclei are considered. In the *harmonic approximation*, the PES can be expanded in a Taylor-series around $\{\mathbf{R}_{\alpha,0}\}$ and truncated after the second-order term. The first-order term is zero since the forces vanish at the equilibrium position $\{\mathbf{R}_{\alpha,0}\}$,

$$\begin{aligned} V_{\text{BO}}(\{\mathbf{R}_\alpha\}) &= V_{\text{BO}}(\{\mathbf{R}_{\alpha,0}\}) + \sum_\beta \underbrace{\frac{dV_{\text{BO}}}{d\mathbf{R}_\beta} \Big|_{\{\mathbf{R}_{\alpha,0}\}}}_{=0} \mathbf{q}_\beta + \frac{1}{2} \sum_{\beta\gamma} \underbrace{\frac{d^2 V_{\text{BO}}}{d\mathbf{R}_\beta d\mathbf{R}_\gamma} \Big|_{\{\mathbf{R}_{\alpha,0}\}}}_{\equiv H_{\beta\gamma}} \mathbf{q}_\beta \mathbf{q}_\gamma + \dots \\ &= V_{\text{BO}}(\{\mathbf{R}_{\alpha,0}\}) + \frac{1}{2} \sum_{\beta\gamma} H_{\beta\gamma} \mathbf{q}_\beta \mathbf{q}_\gamma + \dots , \end{aligned} \quad (2.16)$$

where the *displacement vector* $\mathbf{q}_\alpha = \mathbf{R}_\alpha - \mathbf{R}_{\alpha,0}$ is defined as the change of the atomic positions with respect to their equilibrium configuration. Inserting this into Eq. (2.15) yields

$$M_\alpha \ddot{\mathbf{q}}_\alpha = -\frac{1}{2} \sum_{\beta\gamma} \frac{d}{d\mathbf{R}_{\alpha,0}} (H_{\beta\gamma} \mathbf{q}_\beta \mathbf{q}_\gamma) . \quad (2.17)$$

Since $\frac{d\mathbf{q}_\beta}{d\mathbf{R}_\alpha} = \delta_{\alpha\beta}$, the equation of motion further simplifies to

$$M_\alpha \ddot{\mathbf{q}}_\alpha = -\sum_\beta H_{\alpha\beta} \mathbf{q}_\beta . \quad (2.18)$$

A solution to the above equation can be obtained by the following ansatz

$$\mathbf{q}_\alpha = \mathbf{A}_\alpha \cos(\omega t + \epsilon) , \quad (2.19)$$

with the second time derivative

$$\ddot{\mathbf{q}}_\alpha = -\omega^2 \mathbf{A}_\alpha \cos(\omega t + \epsilon) . \quad (2.20)$$

Inserting this into Eq. (2.15) gives the following eigenvalue-equation for the $3M$ amplitudes $\{\mathbf{A}_\alpha\}$.

2. Describing the Configurational Space of Atomic Clusters

$$M_{\alpha}\omega^2\mathbf{A}_{\alpha} = \sum_{\beta} H_{\alpha\beta}\mathbf{A}_{\beta} \quad (2.21)$$

Non-trivial solutions can be obtained by solving the secular equation

$$\det \left(H_{\alpha\beta} - \delta_{\alpha\beta} M_{\alpha}\omega^2 \right) \stackrel{!}{=} 0. \quad (2.22)$$

For a system containing M atoms, the Hessian $H_{\alpha\beta}$ possesses $3N$ rows and columns and the secular equation yields $3N$ solutions ω_i . Within the harmonic approximation, the atoms are therefore oscillating around their equilibrium positions with an harmonic motion having the frequency $2\pi/\omega_i$ and a constant phase ϵ_i . The normalized eigenvectors $\mathbf{Q}_{\alpha,i} = \mathbf{A}_{\alpha,i}/\sqrt{\sum_{\beta} \mathbf{A}_{\beta,i}^2}$, the *eigenmodes*, describe the relative motion of the individual atoms, where the amplitude is uniquely defined by the boundary conditions, i.e. how far the individual atoms are initially displaced. Having the same frequency and phase, all atoms reach their maximum displacements simultaneously. A vibrational mode exhibiting the above described characteristics is called a *normal mode* of the system.

It can be shown that for a non-linear molecule, only $(3N - 6)$ solutions have non-vanishing frequencies. The other six solutions correspond to the three translational and three rotational degrees of freedom of the system. In case of a linear molecule, there are $(3N - 5)$ non-vanishing solutions, since a linear system only possesses two rotational degrees of freedom.

A local minimum possesses only positive eigenvalues ω_i^2 . An imaginary frequency ω_i corresponds to a negative slope of the PES in direction of the eigenvector and thus indicates a local instability, since an infinitesimally small displacement of the atoms along the eigenvector brings the system out of the equilibrium position. The number of negative eigenvalues is often referred to as the *index* of the Hessian. An index of zero corresponds to a local minimum on the PES which hence represents a stable isomer of the system under consideration. Stationary points with indices of one or higher are called *saddle points*, in particular a saddle point with index one is a *transition state*. If two local minima are connected by any path on the PES, then according to the Murrell-Leidler theorem [14] there is a lower energy path connecting these two minima which involves a transition state. In other words, if the system undergoes a transition from one isomer to another, the path that involves the lowest energy barrier to surmount possesses a saddle point of index one at its energy maximum (see Fig. 2.3).

Steepest-Descent Path and Basin of Attraction

Loosely stated, a steepest-descent path starting from any configuration is defined by simply following the PES downhill along the forces until a stationary point is reached where the gradient vanishes. Numerically, one would therefore obtain the steepest-descent path by successively displacing the atoms by infinitesimal amounts along the force direction. One important feature is that the resulting path on the PES is uniquely defined and every point with a non-vanishing gradient in the configurational space lies exactly on one path [15]. In particular, all points whose steepest-descent paths converge to a certain

local minimum form its *basin of attraction* which thus comprises all configurations of a molecule that will relax into the corresponding isomer represented by the local minimum on the PES. Due to the uniqueness of the steepest-descent path, basins of attractions belonging to different local minima cannot interpenetrate and are a characteristic region around a local minimum.

At a transition state there are exactly two steepest-descent paths going in opposite directions along the eigenvector corresponding to the negative curvature and leading to two local minima. They constitute the minimum-energy path on the PES for a transition between these two local minima (see Fig. 2.3).

Scaling behaviour of the number of local minima with the system size

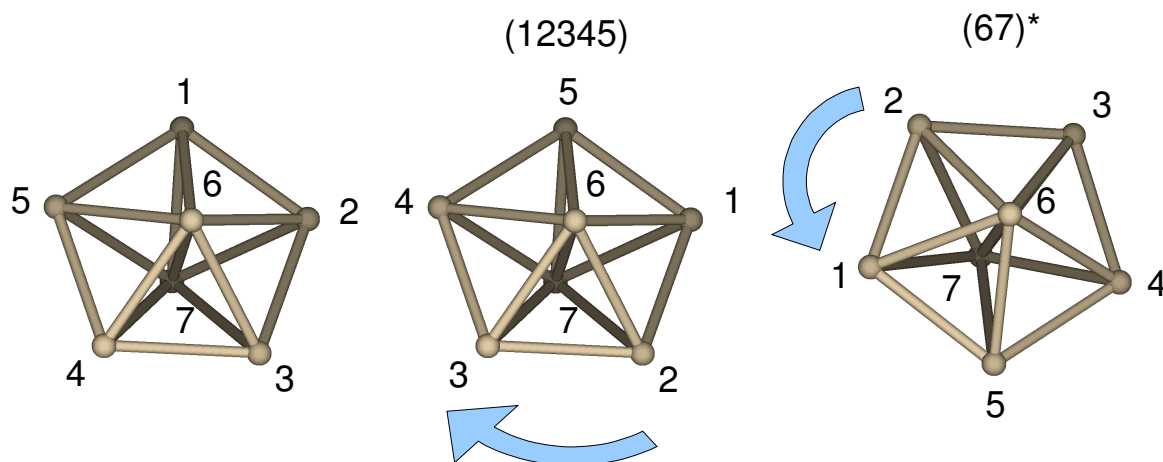


Figure 2.4.: Illustration of two permutation-inversions of a pentagonal bipyramid leading to the same local minimum. (12345) indicates a permutation that swaps atom 1 with atom 2, 2 with 3, 3 with 4, 4 with 5, 5 with 1, thus resulting in a pure rotation (indicated by the blue arrow), which in turn corresponds to the same local minimum. (67)* swaps atom 6 with 7 being followed by an inversion through the center which can also be superimposed with the unpermuted one by a pure rotation.

Regarding in particular the question how the configurational space of a system can be sampled efficiently, it is of fundamental interest to estimate how big the PES is in terms of the number of different isomers one expects to find. To address this question, one has to distinguish between two different aspects of this problem. Since the Hamiltonian of the system is invariant with respect to permutations of the nuclear coordinates of equivalent species and with respect to inversions of all the coordinates through the origin of a space-fixed coordinate system, there are many symmetry-equivalent isomers with the same geometry and energy, but corresponding to different points on the PES. Assuming the system contains N_A atoms of species A, N_B atoms of species B, N_C atoms of species C, and so forth, one would expect to have

$$2 \times N_A! \times N_B! \times N_C! \times \dots \quad (2.23)$$

symmetry-equivalent isomers, or *versions* of the structure. However, it can be shown [6, 16] that in case of a molecule with a point group of order o , there are o permutation-inversions that can be obtained from the non-permuted isomer by a pure rotation, thus not being a distinct local minimum of the isomer (see Fig. 2.4). Therefore, there are

$$N_{\text{versions}} = 2 \times N_A! \times N_B! \times N_C! \times \dots / o \quad (2.24)$$

different versions of the same isomer that cannot be superimposed by a pure rotation. In other words, every isomer possesses N_{versions} different basins of attraction on the PES. Hence, the lower the symmetry of a structure, the more symmetry-equivalent local minima it possesses on the PES.

More difficult is the question how many isomers of different energy and geometric structures exists. According to empirical observations and heuristic estimates [17, 18, 19], the number of isomers grows exponentially with increasing cluster size. The basic idea of such an estimate is to divide the system into m equivalent subsystems each containing M atoms. Assuming that the stable configurations of each subsystem can be considered independent, the number of local minima n_{min} then behaves like

$$n_{\text{min}}(mN) = n_{\text{min}}(N)^m. \quad (2.25)$$

A solution of this equation is

$$n_{\text{min}}(N) \propto \exp(\alpha N), \quad (2.26)$$

where α is a system-dependent constant.

2.3.2. Global Topology of the Energy Surface

The overall shape of the energy surface is determined by the energetic ordering of the local minima and their connectivity through transition states. One feature to describe the global topology of a PES is for instance the *monotonic sequence* introduced by Kunz and Berry [20, 21]. It is defined as a sequence of local minima connected by transition states for which the energy of the minima monotonically decreases. All monotonic sequences leading to the same local minimum therewith define a *monotonic sequence basin* or *funnel*. Another common term is *superbasin* which emphasizes the analogy to a basin of attraction on the global scale of the PES. In contrast to the latter where every point of the configurational space with a non-vanishing gradient only belongs to one basin of attraction, a local minimum can belong to several monotonic sequence basins.

Systems with only one funnel converging to the global minimum are often referred to as *single-funnel systems*. They are obviously benign systems for a global optimization since the overall topology can guide the system towards the global minimum. Contrary to that, *multi-funnel systems* contain multiple sequence basins. Once in a wrong funnel, the system then has to surmount several energy barriers to climb out of it and reach the global minimum, which makes global optimization in general more difficult [7, 8].

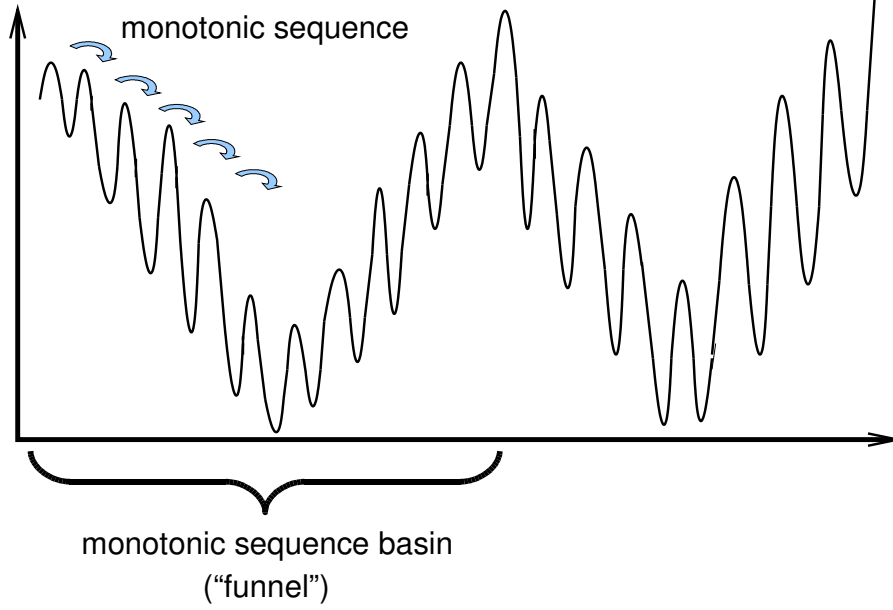


Figure 2.5.: Schematical picture of a multi-funnel potential energy surface with a depicted monotonic sequence basin.

2.4. Thermodynamics

At zero temperature, the most stable structure is the isomer with the lowest energy E_0 plus the *zero point energy* (*vide infra*) given by the vibrations. Increasing the temperature of the system, entropic effects start to play a role and the *free energy* F determines the stability of the system (see e.g.[22]).

$$F = E_0 - k_B T \ln Z , \quad (2.27)$$

where Z is the partition function of the system defined as

$$Z = \sum_i e^{-\frac{E_i}{k_B T}} , \quad (2.28)$$

with i being the index running over all possible states of the system and E_i the corresponding energy of the system. For an atomic cluster system, assuming that rotations and vibrations can be decoupled, the partition function separates into

$$Z = Z_{\text{trans}} Z_{\text{vib}} Z_{\text{rot}} , \quad (2.29)$$

where Z_{trans} , Z_{vib} and Z_{rot} are the partition functions due to the translational, vibrational and rotational degrees of freedom. The free energy then adopts the form

$$F = E + F_{\text{trans}} + F_{\text{vib}} + F_{\text{rot}} . \quad (2.30)$$

2.4.1. Translational Degrees of Freedom

The partition function Z_{trans} can be calculated in a straightforward manner and has the form [22]

$$Z_{\text{trans}} = V \left(\frac{M k_B T}{2\pi \hbar^2} \right)^{3/2}. \quad (2.31)$$

V is the volume of the box in which the cluster is placed. Since the only system-dependent parameter is the total mass M of the system, the translational degrees of freedom do not influence the energetic ordering of different isomers of the same system and can thus be neglected when addressing the energetic stability of free molecules.

2.4.2. Molecular Vibrations

The vibrational contribution to the free energy can be approximated using the vibrational frequencies obtained by the harmonic approximation. Using normal modes, the molecule can be considered as being composed of $(3N - 6)$ independent one-dimensional harmonic oscillators with the energies $E_{n,i} = \left(n + \frac{1}{2}\right) \hbar \omega_i$, where n is the principal quantum number of the vibrational state. Hence the partition function further separates into [22]

$$Z_{\text{vib}} = \sum_{i=1}^{3N-6} Z_{\text{vib},i}. \quad (2.32)$$

Each partition function can easily be evaluated analytically,

$$Z_{\text{vib},i} = \sum_{n=0}^{\infty} e^{-\left(n+\frac{1}{2}\right) \frac{\hbar \omega_i}{k_B T}} = e^{-\frac{\hbar \omega_i}{2k_B T}} \sum_{n=0}^{\infty} e^{-n \frac{\hbar \omega_i}{k_B T}} = \frac{e^{-\frac{\hbar \omega_i}{2k_B T}}}{1 - e^{-\frac{\hbar \omega_i}{k_B T}}}, \quad (2.33)$$

$$Z_{\text{vib}} = \prod_{i=1}^{3N-6} \frac{e^{-\frac{\hbar \omega_i}{2k_B T}}}{1 - e^{-\frac{\hbar \omega_i}{k_B T}}}. \quad (2.34)$$

The resulting vibrational contribution to the free energy is

$$F_{\text{vib}} = -k_B T \ln Z_{\text{vib}} = \sum_{i=1}^{3N-6} \left(\frac{\hbar \omega_i}{2} + k_B T \ln \left(1 - e^{-\frac{\hbar \omega_i}{k_B T}} \right) \right) \quad (2.35)$$

$$= E_{\text{ZPE}} + k_B T \sum_{i=1}^{3N-6} \ln \left(1 - e^{-\frac{\hbar \omega_i}{k_B T}} \right). \quad (2.36)$$

The first term corresponds to the *zero-point energy* since it contributes to the free energy already at zero temperature. It originates from the zero-point vibration of the molecules.

2.4.3. Molecular Rotations

As for the rotational contribution to the free energy, one can assume that the centrifugal forces acting upon the nuclei are negligible and do not alter the molecular structure significantly. A good approximation to the rotational partition function based upon classical mechanics is [22]

$$Z_{\text{rot}} = \frac{\sqrt{\pi}}{\sigma} \left(\frac{2k_B T}{\hbar^2} \right)^{3/2} \sqrt{I_1 I_2 I_3} , \quad (2.37)$$

where I_1, I_2, I_3 are the principle moments of inertia, e.g the eigenvalues of the moment of inertia tensor. σ is the order of the rotational subgroup of the system, so the number of pure rotational symmetry operations.

3. Exploring the Configurational Space

Determining cluster structures requires to identify the local minima of the PES, which is a high-dimensional function of the atomic coordinates. Of fundamental interest is thereby without doubt the global minimum, which constitutes the most stable isomer at zero temperature. Energetically higher-lying and therewith metastable isomers, however, might be observed in experiment due to finite temperature or kinetic effects, thus additionally being in the focus of interest.

Hence, this work faces a twofold challenge. On the one hand, the PES needs to be evaluated, thus necessitating a method that yields the total energy for a given atomic configuration. Obtaining this energy within the framework of density-functional theory is the topic of chapter 4. On the other hand, the local information of a current configuration thereby gained needs to be exploited to efficiently sample the PES and finally identify the local minima. The goal of this chapter is to condense and classify most popular corresponding schemes to explore the huge configurational space.

3.1. Local Optimization Methods

Local optimization methods are deterministic schemes that guide the system to the next local minimum of the PES from an arbitrary starting point by following the surface downhill in some way. At each iteration step, local information like the energy, forces or the Hessian of the corresponding atomic configuration are taken into account to obtain the next structure until iteratively the forces vanish and the local minimum has been identified.

3.1.1. Steepest Descent

The simplest method to implement is the steepest descent method [22] that strictly proceeds downhill to reach the local minimum. In each iteration step, the atoms are displaced according to the forces acting on them

$$\mathbf{R}_{\alpha,i+1} = \mathbf{R}_{\alpha,i} + \gamma_i \mathbf{F}_{\alpha}(\{\mathbf{R}_{\alpha,i}\}), \quad (3.1)$$

with γ_i being a technical step width parameter to adjust that does not necessarily have to be constant for the whole local optimization. If the step width is too small, many iteration steps are required and the convergence to the local minimum is rather slow. If on the other hand γ_i is too large, the system might start to oscillate around the local minimum.

3.1.2. Conjugate Gradient

The conjugate gradient scheme consists of successive line minimizations along a search direction $\mathbf{G}_{\alpha,i}$ [22, 23, 24, 25, 26]

$$\gamma_i = \arg \min_{\gamma} E(\mathbf{R}_{\alpha,i} + \gamma \mathbf{G}_{\alpha,i}(\{\mathbf{R}_{\alpha,i}\})) , \quad (3.2)$$

where $\arg \min_{\gamma} E$ denotes the argument γ which minimizes the energy E . The atomic coordinates are then correspondingly updated to

$$\mathbf{R}_{\alpha,i+1} = \mathbf{R}_{\alpha,i} + \gamma_i \mathbf{G}_{\alpha,i} . \quad (3.3)$$

Similar to the steepest descent scheme, one starts along the atomic forces as first search direction, so $\mathbf{G}_{\alpha,0} = \mathbf{F}_{\alpha}(\{\mathbf{R}_{\alpha,0}\})$. Contrary to the former scheme, however, information from previous searches are accumulated so that new line searches do not destroy the progress of previous line searches as might be the case for ill-conditioned functions (see Fig. 3.1). In these cases, the steepest descent scheme follows a criss-cross pattern since every new line step only takes local information into account. The conjugate gradient scheme instead does not strictly follow the PES downhill but along a search direction that is somewhat perpendicular ("conjugate") to the previous search directions, which is achieved by adding a fraction of the previous search direction to the atomic forces

$$\mathbf{G}_{\alpha,i} = \mathbf{F}_{\alpha,i} + \beta_i \mathbf{G}_{\alpha,i-1} . \quad (3.4)$$

There exist different flavours of the conjugate gradient scheme, differing by the definition of β_i . Some of the names associated with these schemes are Fletcher-Reeves (FR) [24, 25], Polak-Ribière (PR) [24] and Hestenes-Stiefel (HS) [26]

$$\beta_i^{\text{FR}} = \frac{\sum_{\alpha} \mathbf{F}_{\alpha,i} \cdot \mathbf{F}_{\alpha,i}}{\sum_{\alpha} \mathbf{F}_{\alpha,i-1} \cdot \mathbf{F}_{\alpha,i-1}} , \quad (3.5)$$

$$\beta_i^{\text{PR}} = \frac{\sum_{\alpha} \mathbf{F}_{\alpha,i} \cdot (\mathbf{F}_{\alpha,i} - \mathbf{F}_{\alpha,i-1})}{\sum_{\alpha} \mathbf{F}_{\alpha,i-1} \cdot \mathbf{F}_{\alpha,i-1}} , \quad (3.6)$$

$$\beta_i^{\text{HS}} = \frac{\sum_{\alpha} \mathbf{F}_{\alpha,i} \cdot (\mathbf{F}_{\alpha,i} - \mathbf{F}_{\alpha,i-1})}{\sum_{\alpha} \mathbf{G}_{\alpha,i-1} \cdot (\mathbf{F}_{\alpha,i} - \mathbf{F}_{\alpha,i-1})} . \quad (3.7)$$

The construction of the search directions \mathbf{G}_i is based upon the assumption that the PES is harmonic. If this assumption holds exactly, the conjugate gradient scheme will converge to the local minimum in $3N$ iteration steps, thus being a direct minimization scheme. In particular, all aforementioned different schemes are then equivalent. Consequently, if the system is far away from the harmonic region, the search directions become unreasonable and it is recommended to start with a few steepest descent steps to bring the system closer to the local minimum.

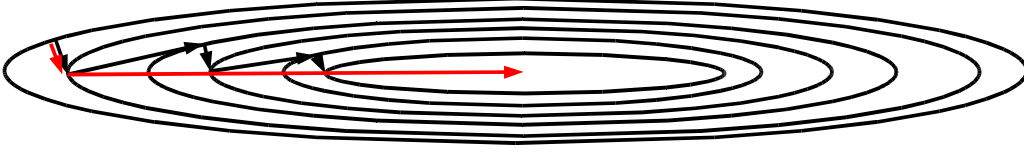


Figure 3.1.: Illustration of the steepest descent scheme (black arrows) for an ill-conditioned two-dimensional surface compared to conjugate gradient (red arrows).

3.1.3. The Broyden-Fletcher-Goldfarb-Shanno (BFGS) Method

The BFGS method is a so-called quasi-Newton scheme that takes additional information in the form of the second derivative of the PES into account [27]. Knowing the Hessian matrix $H_{\alpha\beta}$, a new search direction $\mathbf{G}_{\beta,i}$ can be obtained by solving the Newton equation

$$\sum_{\beta} H_{\alpha\beta} \mathbf{G}_{\beta,i} = \mathbf{F}_{\alpha}(\{\mathbf{R}_{\alpha,i}\}). \quad (3.8)$$

The next atomic configuration can then be obtained by performing a line minimization as in the conjugate gradient scheme (Eq. (3.2)). If the PES were perfectly harmonic and the Hessian known exactly, the local minimum would be found within one line search. In practice, however, the calculation of the Hessian matrix in each iteration step can be prohibitively expensive, so that it is instead successively approximated in each iteration step, therewith being a *quasi*-Newton scheme. Since more information of the PES is taken into account, the BFGS method can be more efficient than steepest descent or even conjugate gradient, but it works only efficiently if the system is close to the local minimum, where the harmonic approximation is justified. It is therefore typically recommended to start with a few steepest descent steps to bring the system close to the local minimum as in the case of the conjugate gradient scheme.

3.2. Global Optimization Schemes

The above described local optimization methods are deterministic schemes that approach the next local minimum from a starting point constructively, since the local information obtained for a given configuration, like the energy and forces, uniquely guides the system to the next local minimum. In order to find all isomers, particularly the global minimum, a search algorithm is required that not only scans the local environment but samples the whole PES. Since local information is not enough to locate the global minimum of the system, stochastic methods are required that provide some recipe to systematically sample the huge configurational space. The global optimization of atomic clusters is assumed to be NP-hard (non-deterministic polynomial-time hard) [28], i.e. no algorithm is known that guarantees to locate the most stable isomer within polynomial time. This difficulty is typically ascribed to the exponential growth of the number of local minima with system size. Assuming the most primitive method that simply runs through all local

3. Exploring the Configurational Space

minima, the computational burden therefore quickly becomes unfeasible which connects to the famous Levinthal's paradox according to which a protein would never reach its native state within the lifetime of universe in view of the tremendous number of different local minima [7, 8]. Correspondingly, one possible way out is that the global topology can serve as a guidance for the system to reach the global minimum. As already stated in the previous chapter, single-funnel systems are benign topologies in this sense.

One key ingredient of any sampling algorithm is the way new structures are generated. This so-called *trial move* corresponds to a jump of the system in the configurational space. A simple method for that is to randomly displace the atomic positions. After such a jump, a criterium is required which decides whether this new structure is preferred and the search should continue from there or if it should rather be discarded. Such an *acceptance criterium* is typically based upon the total energy, being a natural choice since it is the quantity to optimize. Of course, there is no need to confine to a single sequential run. Multiple search sequences can be performed and information can be exchanged to thus combine structures from different positions on the PES instead of a purely local search. The number of serial runs and the special scheme to cross them are examples of the large number of technical parameters that make up for the huge diversity of different optimization schemes of which the most archetypal ones will be described in the following.

3.2.1. Simulated Annealing

A classical optimization algorithm applied to many fields is the simulated annealing scheme that resorts to methods of statistical mechanics and is based upon the Metropolis-algorithm [29, 30]. Starting from an arbitrary configuration with a total energy E , a new structure is generated by randomly displacing the atoms, leading to a change of the total energy ΔE . If the energy has decreased, i.e. $\Delta E < 0$, the new structure is accepted and used as starting point for the next step. In the opposite case, however, the structure is not discarded unconditionally, but accepted with a probability of $P(\Delta E) = \exp(-\Delta E/k_B T)$. According to Metropolis, this acceptance criterium thus generates a canonical ensemble of atomic configurations at T . At zero temperature, only isomers that are lower in energy would be accepted which would be an intuitive choice at first glance since the system is thereby pushed towards the ground state. However, the system is then likely to get stuck in the wrong minimum. A finite temperature allows instead for controlled uphill steps thus enabling the system to get out of local minima. Starting from a high temperature, the system is then successively cooled down according to an *annealing schedule*. Coupled to the temperature are the random displacements of the individual atoms $\Delta \mathbf{R}_\alpha$ that obey a Gaussian distribution in the classical simulated annealing scheme [31]:

$$p(\Delta \mathbf{R}_\alpha) \propto \exp\left(-(\Delta \mathbf{R}_\alpha)^2/T\right) \quad (3.9)$$

With decreasing temperature, the step width is therewith reduced thus freezing the system in the ground state. The cooling rate needs to be inverse logarithmic in time to assure convergence

3. Exploring the Configurational Space

$$T \propto \frac{T_0}{\log(1+t)}. \quad (3.10)$$

Improvements can be made by adjusting the annealing scheme, as done in the *Fast Simulated Annealing* scheme, proposed by Szu *et al.* [32]. The Gaussian distribution of random displacements is replaced by a Cauchy distribution that contains longer tails additional to a Gaussian-like peak, thereby enabling the system to occasionally perform longer jumps in the configurational space. Instead of an inverse logarithmic cooling rate, the temperature can then be reduced linearly with time, converging to the ground state much faster. Both versions are special cases of the *Generalized Simulated Annealing* scheme, that introduces more technical parameters to tune the cooling rate [33]. Due to the reduction of the temperature, no canonical ensemble is generated anymore, so that unlike in the original Metropolis scheme, no thermodynamic quantities can be derived. The resulting simulated annealing scheme is a pure global optimization procedure.

3.2.2. Basin-Hopping

Loosely stated, the basin-hopping method is the simulated annealing method applied to local minima [10, 34, 35]. Additional to the trial move, a local structural relaxation is performed and the total energy of this local minimum is then assigned to the initial configuration. The PES is therewith effectively transformed into a set of interpenetrating staircases that are the basins of attractions introduced in chapter 2 (see Fig. 3.2)

$$\tilde{E}\{\mathbf{R}\} = \min E\{\mathbf{R}\}, \quad (3.11)$$

where min indicates a local structural relaxation.

This deformation is an example of the class of *hypersurface transformation* methods that aim at modifying the PES to facilitate the global optimization. In many cases, like e.g. the distance scaling method [36], the surface is smoothed out, thus decreasing the number of local minima. However, there is in general no guarantee that such a transformation does not change the global minimum, or even washes out relevant isomers. On the contrary, the basin-hopping method leaves the local minima unchanged but only removes the transition state regions, thus facilitating interbasin transitions. Hence, contrary to the original simulated annealing scheme, moves that lead the system to high points on the PES are much more likely to be accepted, since the ensuing local optimization allows the system to relax into the corresponding local minimum which is much lower in energy. This makes a complicated annealing schedule unnecessary, and in the classical BH scheme the temperature in the Boltzmann-criterium is simply kept constant [10], thereby generating a canonical ensemble of the transformed PES.

A classical trial move scheme is to randomly vary the cartesian components of all atomic coordinates

$$\Delta\mathbf{R}_{\alpha,i} = 2 \cdot \mathbf{R}_0(\text{rand} - 0.5), \quad (3.12)$$

3. Exploring the Configurational Space

with \mathbf{R}_0 being the maximum step width and rand being a random number between zero and one.

With the basin-hopping scheme, Wales *et al.* identified in 1999 all hitherto known global minima of Lennard-Jones(LJ)-clusters containing up to 110 atoms and additionally new ones. The LJ_{38} is a well-known example of a double-funnel PES [37], that contains an icosahedral funnel with a large free energy, and an fcc funnel with a comparably smaller free energy but leading to the global minimum. The unmodified surface yields only a small overlap in the canonical occupation probabilities with respect to the temperature, so that the system is likely to get trapped in the wrong funnel. Transforming the PES like in the basin-hopping scheme, however, results in a broadening of the overlap region, and enables the system to climb out of the wrong funnel [37, 38]. Hence, it is not only the alleviated interbasin transition due to the removal of the transitions state regions, but also the easier transition between different funnels because of the modified thermodynamics that make up for the success of the basin-hopping scheme.

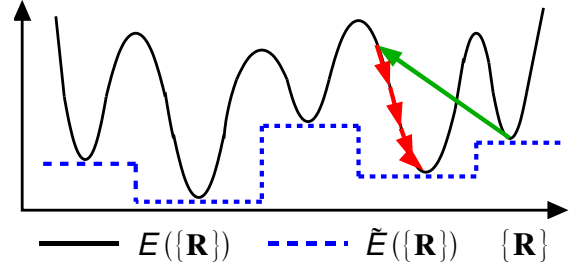


Figure 3.2.: The principle of the basin-hopping method. Depicted is a model energy surface together with its transformed landscape. The green arrow indicates a trial move performed on a local minimum, being followed by a local structural relaxation (red arrows).

3.2.3. Genetic Algorithms

The name of this class of algorithms comes from the mimicked Darwinistic principle of the survival of the fittest [39, 40]. Contrary to the basin-hopping scheme, the starting point is a *population* of randomly generated cluster structures instead of a single initial configuration. New cluster structures are hereby generated by choosing two candidate structures from the population, the *parents*, which are then *mated* to create a *child*. The mating has thereby to be appropriately designed to preserve structural properties of the parents during the mating procedure. A common choice for that is to cut the parent structures by a plane that is randomly oriented and cross the resulting halves followed by a relaxation to generate a child (see Fig. 3.3). Local structural motifs from different points on the PES are therewith combined instead of performing a pure local

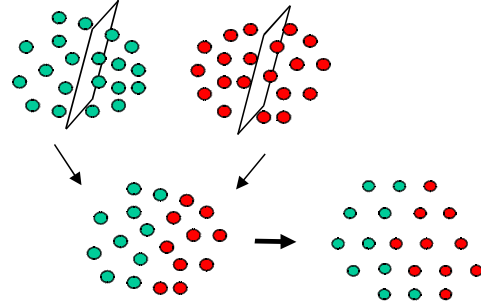


Figure 3.3.: Mating between two parent structures generating a child. After the mating, the new child is locally relaxed.

search like in the basin-hopping scheme.

A further technical aspect is the question which of the children are supposed to replace parents in the population. A simple rule of Deaven and Ho [39] is that a child has to be energetically lower than a parent structure to replace it. To keep the diversity of the population, a further constraint is that a child structure that is supposed to replace a parent structure needs additionally to be different enough from all the other members of the population. Deaven and Ho [39] therefore introduced a second energy criterium. A potentially new structure in the population needs to have an energy difference of ΔE to all other isomers in order to be considered different enough, where ΔE is another tunable parameter. With such an implementation of a genetic algorithm, Deaven and Ho independently discovered the fcc-structure for LJ_{38} in 1996 [40], and based upon a tight-binding scheme, the fullerene structure for C_{60} could be identified in 1995 [39]. It is worth pointing out that due to the involved local structural relaxation, a genetic algorithm is simply a different search algorithm applied to the same transformed PES like in the case of the basin-hopping scheme.

3.2.4. Further Algorithms

Many modifications of the above described basic types of global optimization schemes have been suggested in the literature, one of them is for instance the *minima hopping* algorithm by Stefan Goedecker [41, 42]. As indicated by the name, it can be considered as basin-hopping with a different type of move. Goedecker suggests using a molecular dynamics trajectory instead of random moves to generate new structures, thereby exploiting the *Bell-Evans-Polanyi*-principle [22, 43, 44]. This principle states that a local minimum behind a transition state is lower in energy the smaller the barrier to cross. By starting with a small kinetic energy, the MD-trajectory tends to surmount lower energy barriers and assuming the validity of the BEP-principle is therefore more likely to approach the ground state. Another key ingredient of the minima hopping method is a history feedback method which keeps track of all local minima identified during the sampling run. If the trajectory leads to an isomer that has already been found, the kinetic energy is slightly increased and higher energy barriers can be surmounted, thereby enabling the system to climb out of a wrong funnel if it has been exhaustively explored. Of course, there is no reason to constrain this kind of history feedback method to the application of MD-trajectories, it can also be combined with basin-hopping, which would simply be replacing MD-runs by random moves. Since detailed balance would then not be fulfilled, such a modified basin-hopping scheme would no longer generate a canonical ensemble, which would, however, not constitute a problem since thermodynamic quantities are not of interest in the case of global optimization. Instancing LJ_{38} , MD-steps were proven to be superior compared to random moves [41]. Averaged over a huge number of global optimization runs, roughly 34000 local minima using MD-trajectories were identified until the global minimum was found compared to 75000 in the case of random moves. However, Wales reports an average number of 2000 moves, including more efficient angular moves [10, 45] thus making basin-hopping an order of magnitude faster in this case and illustrating the intricate connection of the sampling scheme and

employed trial moves to the overall performance.

Another type of history feedback method is the concept of landscape paving [46]. The basic idea is to artificially increase the energy in regions that have already been explored. With that, moves that lead into such regions are likely to be rejected thus preventing the system from useless sampling already known regions of the PES. However, this modification, being a significant improvement at first glance, also bears some dangers. Considering the case of two-funnels that are connected by only one transition basin, the paving of this important basin prevents the system from interfunnel transitions, thus prohibiting the system to climb out of a potentially wrong funnel. Combined with basin-hopping, Zhan *et al.* suggested the *basin paving* method [47] that makes use of the histogram of already visited minima to construct an artificial increase of the PES. Using Lennard-Jones clusters, a statistically significant improvement for the global optimization could only be shown for very large systems containing around 150 atoms [47].

3.3. Summary

A concise overview of present sampling methods was given of which the basic ones are simulated annealing, basin-hopping and genetic algorithms. A few popular modifications have been presented which can be considered as derivations from basin-hopping with improvements that were proven to be advantageous for certain cases. However, the performance of the various schemes and their modifications can strongly depend upon both the actual system under consideration and upon the huge number of involved technical parameters, like e.g. the special type of move performed in the random move scheme. A critical analysis and discussion of the implemented sampling method of the present work, in particular regarding possible generic optimizations and showing clear limitations, is therefore part of this PhD project and will be presented in chapter 9.

4. Density-Functional Theory

This chapter deals with the question how to obtain the energetics of a system with a given atomic configuration as required to evaluate the PES. In this work, the method employed is density-functional theory. Before giving a short overview of other popular methods in order to properly classify DFT, some basic terminology will be introduced.

4.1. The Electronic Wave Function

The central quantity within electronic structure theory is the electronic wave function $\Psi(\mathbf{x}_1, \dots, \mathbf{x}_{N_{\text{el}}})$ which yields the probability to find an electron at position \mathbf{r}_1 with spin σ_1 , an electron at position \mathbf{r}_2 with spin σ_2 and so forth by

$$|\Psi(\mathbf{x}_1, \dots, \mathbf{x}_{N_{\text{el}}})|^2 d\mathbf{x}_1 \dots d\mathbf{x}_{N_{\text{el}}} . \quad (4.1)$$

Being fermions, electrons obey the *Pauli principle* [48, 49] which states that two electrons of like spin cannot be at the same point in space. In terms of the wavefunction, this is reflected by the antisymmetry with respect to the space- and spin-coordinates

$$\Psi(\mathbf{x}_1, \dots, \mathbf{x}_i, \dots, \mathbf{x}_j, \dots, \mathbf{x}_{N_{\text{el}}}) = -\Psi(\mathbf{x}_1, \dots, \mathbf{x}_j, \dots, \mathbf{x}_i, \dots, \mathbf{x}_{N_{\text{el}}}) , \quad (4.2)$$

which thus gives for two equal coordinates $\mathbf{x}_i = \mathbf{x}_j$

$$\Psi(\mathbf{x}_1, \dots, \mathbf{x}_i, \dots, \mathbf{x}_i, \dots, \mathbf{x}_{N_{\text{el}}}) = 0 , \quad (4.3)$$

and ensures that the probability to find two electrons of like spin at the same spatial position is zero as prescribed by the Pauli principle.

The *Variational Principle* [22, 50] states that the expectation value of any trial wave function $E[\Psi_{\text{trial}}] = \langle \hat{H} | \Psi_{\text{trial}} | \hat{H} \rangle$ is always an upper bound to the ground-state energy given by the expectation value of the ground-state wavefunction Ψ_0

$$E_0 \equiv E[\Psi_0] \leq E[\Psi_{\text{trial}}] . \quad (4.4)$$

4.1.1. The Electron and Pair Density

The electron density at the position \mathbf{r} is defined as the probability to find an electron of any spin at this point and is given by

$$\rho(\mathbf{r}) = N_{\text{el}} \sum_{\sigma_1} \rho^{\sigma_1}(\mathbf{r}) = N_{\text{el}} \sum_{\sigma_1} \int \dots \int d\mathbf{x}_2 \dots d\mathbf{x}_{N_{\text{el}}} |\Psi(\mathbf{x}_1, \dots, \mathbf{x}_{N_{\text{el}}})|^2 , \quad (4.5)$$

4. Density-Functional Theory

and is the sum of the individual *spin densities* ρ^σ which describe the probability to find an electron of a specific spin σ at the position \mathbf{r} . The prefactor N_{el} is the number of electrons in the system and ensures the right normalization

$$\int d\mathbf{r} \rho(\mathbf{r}) d\mathbf{r} = N_{\text{el}} . \quad (4.6)$$

In the same manner, the *pair density* at \mathbf{x}_1 and \mathbf{x}_2 is defined as the probability to find an electron with spin σ_1 at the point \mathbf{r}_1 and an electron with spin σ_2 at the point \mathbf{r}_2

$$\rho_2(\mathbf{x}_1, \mathbf{x}_2) = N_{\text{el}}(N_{\text{el}} - 1) \int \dots \int d\mathbf{x}_3 \dots d\mathbf{x}_{N_{\text{el}}} |\Psi(\mathbf{x}_1, \dots, \mathbf{x}_{N_{\text{el}}})|^2 , \quad (4.7)$$

where the antisymmetry of the wavefunction due to the Pauli principle correspondingly leads to an antisymmetry of the pair-density

$$\rho_2(\mathbf{x}_1, \mathbf{x}_2) = -\rho_2(\mathbf{x}_2, \mathbf{x}_1) . \quad (4.8)$$

If electrons moved completely independently, the pair density would just be the product of the spin densities $\rho_2(\mathbf{x}_1, \mathbf{x}_2) = \rho(\mathbf{x}_1)\rho(\mathbf{x}_2)$. The probability to find an electron with spin σ_1 at the point \mathbf{r}_1 is then independent of the probability distribution of the second electron. Due to the Coulomb interaction, however, the movements of both electrons are *correlated*, so in general $\rho_2(\mathbf{x}_1, \mathbf{x}_2) \neq \rho(\mathbf{x}_1)\rho(\mathbf{x}_2)$.

4.2. Approximative Methods to solve the Many-Body Problem

One fundamental approach to solve the electronic Schrödinger equation (2.10) numerically is the *Hartree-Fock* method which approximates the electronic wavefunction by a single Slater-determinant of single particle wave functions, thus ensuring the antisymmetry of the wave function to fulfil the Pauli principle. Additional to the classical Coulomb-potential V_{ee}^c , this gives rise to a quantum mechanical contribution to the potential called *exchange potential* V_X . The aforementioned Coulomb correlation, however, is not captured, and the pair density of electrons of unequal spins which are not subject to the Pauli principle just separates into the individual spin densities. The missing energy is correspondingly defined as *correlation energy* E_C and is significant to obtain accurate results though being smaller compared to the exchange and classical Hartree energy. The corresponding potential is consequently termed *correlation potential* V_C .

Among the approaches to account for the correlation energy, the most popular ones based on the electronic wave function are second or fourth order perturbation theory by Møller and Plesset (MP2 or MP4) [9], configuration interaction (CI) [51], multi-configuration self-consistent field (MCSCF) [52], coupled cluster methods (CC) [53] or Quantum Monte Carlo (QMC) [54]. Though these methods can be quite accurate, they are computationally very demanding for larger systems. MP2 for instance, nominally scales as N^5 , thus quickly becoming prohibitively expensive with increasing cluster size.

Density-functional theory (DFT) provides an alternative approach. The electronic Schrödinger equation and the corresponding wave function are replaced by a formalism based upon the much simpler electron density ρ .

4.3. The Thomas-Fermi Model

The original idea to use the electron density as the fundamental quantity goes back to 1927, when Thomas and Fermi approximated the distribution of electrons in an atom [55] and came up with their famous kinetic energy functional which is exact in the limit of a homogeneous electron gas

$$T_{\text{TF}}(\rho) = C_F \int d\mathbf{r} \rho^{5/3}(\mathbf{r}) d\mathbf{r}, \quad C_F = \frac{3}{10}(3\pi^2)^{2/3} = 2.871. \quad (4.9)$$

Additionally, the attractive electron-nucleus energy and the classical repulsive electron-electron Coulomb energy can be expressed as functions of $\rho(\mathbf{r})$.

$$V_{\text{Ne}} = Z \int d\mathbf{r} \frac{\rho(\mathbf{r})}{r}, \quad (4.10)$$

$$V_{\text{ee}}^c = \frac{1}{2} \iint d\mathbf{r}_1 d\mathbf{r}_2 \frac{\rho(\mathbf{r}_1)\rho(\mathbf{r}_2)}{|\mathbf{r}_1 - \mathbf{r}_2|}. \quad (4.11)$$

Neglecting the exchange-correlation energy, a simple formula for the total energy of an atom is derived exclusively in terms of the electron density

$$E_{\text{TF}}[\rho] = C_F \int d\mathbf{r} \rho^{5/3}(\mathbf{r}) + Z \int d\mathbf{r} \frac{\rho(\mathbf{r})}{r} + \frac{1}{2} \iint d\mathbf{r}_1 d\mathbf{r}_2 \frac{\rho(\mathbf{r}_1)\rho(\mathbf{r}_2)}{|\mathbf{r}_1 - \mathbf{r}_2|}. \quad (4.12)$$

Minimizing Eq. (4.12) with respect to the density under the normalization constraint Eq. (4.6) then yields the ground-state density ρ_0 and the corresponding ground-state energy $E[\rho_0]$. While simple, the Thomas-Fermi formula is of no practical use due to the underlying approximations of both a very crude kinetic energy functional and the complete neglect of the exchange-correlation energy.

4.4. The Hohenberg-Kohn Theorems

The Thomas-Fermi model was the first attempt to express the electronic energy in terms of the electron density only, thereby reducing the number of degrees of freedom from $3N_{\text{el}}$ to 3. Nonetheless, this approximation did not become popular due to its low accuracy. The concept of the electron density was taken up again in 1964 by Hohenberg and Kohn [56] who founded the basics of an exact theory, the *density-functional theory*. It is based upon two theorems which prove that the electron density can in principle be used alone to obtain the ground-state energy of any system.

The first theorem states that the external potential V_{ext} of a system is, within an additive constant, uniquely defined by the electron density, where the external potential is

4. Density-Functional Theory

not confined to the Coulomb-potential of the nuclei. Since V_{ext} defines the Hamiltonian, which then determines the many-body wavefunction from which all observables can be obtained, it follows that the whole physics of a system, in particular the ground-state energy, can exclusively be obtained from the electron density. For non-degenerate systems, the proof is trivial and based upon the variational principle [57]. Consider two different external potentials V_{ext} and V'_{ext} that differ by more than just an additive constant but give rise to the same ground-state electron density ρ_0 . The corresponding Hamiltonians \hat{H} and \hat{H}' then yield two different wavefunctions Ψ and Ψ' . Applying the variational principle to the unprimed Hamiltonian with Ψ' as trial wavefunction yields

$$E_0 < \langle \Psi' | \hat{H} | \Psi' \rangle = \langle \Psi' | \hat{H}' | \Psi' \rangle + \langle \Psi' | \hat{H} - \hat{H}' | \Psi' \rangle , \quad (4.13)$$

which expands to

$$E_0 < E'_0 + \langle \Psi' | T + V_{\text{ee}} + V_{\text{ext}} - T - V_{\text{ee}} - V'_{\text{ext}} | \Psi' \rangle , \quad (4.14)$$

so that the expression can be simplified to

$$E_0 < E'_0 + \int d\mathbf{r} \rho(\mathbf{r})(V_{\text{ext}} - V'_{\text{ext}}) . \quad (4.15)$$

Now the roles are exchanged, so the variational principle is applied to the primed Hamiltonian using Ψ as trial wavefunction, thus yielding

$$E'_0 < E_0 - \int d\mathbf{r} \rho(\mathbf{r})(V_{\text{ext}} - V'_{\text{ext}}) . \quad (4.16)$$

Summing Eq. (4.14) and Eq. (4.15) finally gives the following contradiction

$$E_0 + E'_0 < E'_0 + E_0 \iff 0 < 0 . \quad (4.17)$$

Hence, the basic assumption of two different external potentials giving rise to the same ground-state density was wrong. The total energy E_0 can therefore be expressed solely in terms of ρ

$$E_0[\rho] = \int d\mathbf{r} \rho(\mathbf{r}) V_{\text{Ne}} + T[\rho] + E_{\text{ee}}[\rho] \quad (4.18)$$

$$= \int d\mathbf{r} \rho(\mathbf{r}) V_{\text{Ne}} + F_{\text{HK}}[\rho] . \quad (4.19)$$

$F_{\text{HK}}[\rho]$ is called the *universal functional* of ρ since it does not depend upon the external potential. The proof can be generalized to the case of degenerate systems [57].

The second Hohenberg-Kohn theorem is a reformulation of the variational principle, now being expressed in terms of the density. It states that the energy given by any trial density $\tilde{\rho}$ is an upper bound to the ground-state energy E_0

$$E_0 = E[\rho] \leq E[\tilde{\rho}] . \quad (4.20)$$

According to the first Hohenberg-Kohn theorem, the trial density $\tilde{\rho}$ is uniquely given by the external potential \tilde{V}_{ext} , which in turn defines the corresponding Hamiltonian \hat{H}

4. Density-Functional Theory

which yields the many-body wavefunction $\tilde{\Psi}$. Applying the variational principle Eq. (4.4) then gives the desired result

$$\langle \tilde{\psi} | \hat{H} | \tilde{\psi} \rangle = \int d\mathbf{r} \tilde{\rho}(\mathbf{r}) V_{\text{ext}}(\mathbf{r}) + F_{\text{HK}}[\tilde{\rho}] = E[\tilde{\rho}] \geq E[\rho_0] . \quad (4.21)$$

Additionally, applying the variational principle to the Hohenberg-Kohn functional under the normalization constraint of the electron density and the assumption of the differentiability of E_{HK}

$$\delta \{E[\rho] - \mu [\rho(\mathbf{r})d\mathbf{r} - N_{\text{el}}]\} = 0 , \quad (4.22)$$

yields the *Euler-Lagrange equation*

$$\mu = \frac{\delta E[\rho]}{\delta \rho(\mathbf{r})} = V_{\text{ext}}(\mathbf{r}) + \frac{\delta F_{\text{HK}}[\rho]}{\delta \rho(\mathbf{r})} , \quad (4.23)$$

with μ being the chemical potential.

4.5. The Kohn-Sham Equation

In principle, DFT is an exact theory, which means that if the universal functional F_{HK} were known, minimizing the energy functional would give the exact ground-state energy. Unfortunately, F_{HK} is not known, making a direct application of the Hohenberg-Kohn theorems impossible. In 1965, Kohn and Sham approximated F_{HK} [58], thus paving the way for tackling practical problems using DFT. Their strategy was to separate everything that can be expressed exactly and only approximate the missing terms. Introducing a reference system of non-interacting electrons described by single-particle states $\psi_i(\mathbf{r})$ the kinetic energy of that reference system can then be obtained exactly as

$$T_{\text{S}} = -\frac{1}{2} \sum_i^{N_{\text{el}}} \langle \phi_i | \nabla^2 | \phi_i \rangle , \quad (4.24)$$

with ϕ_i being the *Kohn-Sham orbitals*. The non-interacting kinetic energy T_{S} is not equal to the true kinetic energy T , with $T = T_{\text{S}} + T_{\text{C}}$. Furthermore, the classical Coulomb energy $J[\rho]$ can be expressed exactly with respect to the electron density. Therefore, Kohn and Sham rewrote the universal functional as

$$F_{\text{HK}}[\rho] = T_{\text{S}}[\rho] + J[\rho] + E_{\text{XC}}[\rho] , \quad (4.25)$$

where the *exchange-correlation energy* $E_{\text{XC}}[\rho]$ contains everything that is missing: The quantum-mechanical contributions due to exchange and correlation, and the remaining part of the kinetic energy not being captured by T_{S}

$$E_{\text{XC}}[\rho] = (T[\rho] - T_{\text{S}}[\rho]) + (E_{\text{ee}}[\rho] - J[\rho]) , \quad (4.26)$$

which thus yields the *Kohn-Sham functional*

4. Density-Functional Theory

$$E^{\text{KS}}[\rho] = T_{\text{S}}[\rho] + J[\rho] + E_{\text{XC}}[\rho] + E_{\text{ext}}[\rho]. \quad (4.27)$$

Minimizing Eq. (4.27) with respect to the orbitals ϕ_i , using the expression of the electron density for a non-interacting system $\rho(\mathbf{r}) = \sum_i f_i |\phi_i(\mathbf{r})|^2$ and under the orthonormality constraint of the Kohn-Sham orbitals $\langle \phi_i | \phi_j \rangle = \delta_{ij}$, then results in the famous Kohn-Sham equation for the single-particle Kohn-Sham orbitals

$$\left[-\frac{1}{2} \nabla^2 + V_{\text{eff}}(\mathbf{r}) \right] \phi_i = \epsilon_i \phi_i, \quad (4.28)$$

with $\{\epsilon_i\}$ being the Kohn-Sham orbital energies which result as Lagrange-multipliers to ensure the orthonormality of the orbitals. V_{eff} is the effective potential, which contains the classical Coulomb potential, the exchange-correlation potential and the external potential $V_{\text{ext}}(\mathbf{r})$,

$$V_{\text{eff}}(\mathbf{r}) = \int d\mathbf{r}' \frac{\rho(\mathbf{r}')}{|\mathbf{r} - \mathbf{r}'|} + V_{\text{XC}}(\mathbf{r}) + V_{\text{ext}}(\mathbf{r}). \quad (4.29)$$

The resulting electron density $\rho(\mathbf{r}) = \sum_i f_i |\phi_i(\mathbf{r})|^2$ is by construction equal to the true electron density, where the occupation numbers $\{f_i\}$ are one for occupied states and zero otherwise. The exchange-correlation potential $V_{\text{XC}}(\mathbf{r})$ is defined as functional derivative of the exchange-correlation energy with respect to the electron density

$$V_{\text{XC}}(\mathbf{r}) \equiv \frac{\delta E_{\text{XC}}}{\delta \rho(\mathbf{r})}. \quad (4.30)$$

Being an artificial reference system, the Kohn-Sham orbitals are no real single-particle wave functions but only approximations to them. Their introduction was in particular only necessary due to the lack of knowledge of the kinetic energy functional with respect to the electron density. Attempts to keep the density-functional theory purely density-based have been made by approximating the kinetic energy functional within the so-called *orbital-free density-functional theory* (see e.g. [59]). However, common functionals that go beyond the classical Thomas-Fermi model turned out to be little successful since the kinetic energy is in the same order of magnitude as the total energy, and errors in the approximations are therewith significant. Only in simple cases, like e.g. bulk aluminum, where the electron density resembles the homogeneous electron gas, quantitative results could be obtained [60]. For systems with localized electron densities, in particular transition metals that are of interest in the present work, the crude approximation of common existing kinetic energy functionals yields unsatisfactory results [61]. Therefore, to obtain quantitative results, classical density-functional theory based upon the Kohn-Sham equation is used, which is in principle an exact theory. Hence, if the exact forms of E_{XC} and V_{XC} were known, the Kohn-Sham scheme would lead to the exact total energy E_{tot} which in turn is the correct eigenvalue of the many-body Hamiltonian. Nevertheless, the unknown functional for the exchange-correlation energy E_{XC} and its corresponding potential V_{XC} necessitates approximations to them, therewith turning DFT into an approximative method in practice. The central goal of

modern density-functional theory is therefore to find better and better approximations to these two quantities.

4.6. Present-Day Exchange-Correlation Functionals

The quality of density-functional theory results depends upon the quality of the approximation of the exchange-correlation energy. Unfortunately, there is no systematic way to successively improve the results like in wavefunction based methods. Analogous to the Thomas-Fermi model, the first attempt to find an explicit expression for E_{XC} was based on the homogeneous electron gas. The basic assumption of the *Local-Density Approximation* (LDA) is that non-local effects of the real electron gas can be neglected and the exchange-correlation energy can be expressed as a sum over space where each point contributes to the energy with a value given by the homogeneous electron gas of the same density. In other words, the exchange-correlation energy density per particle per volume $\epsilon_{\text{XC}}^{\text{LDA}}(\rho(\mathbf{r}))$ in the local-density approximation equals to the true energy density $\epsilon_{\text{XC}}(\rho(\mathbf{r}))$ of the corresponding homogeneous electron gas. The exchange-correlation energy is then given by

$$E_{\text{XC}}^{\text{LDA}}[\rho(\mathbf{r})] = \int d\mathbf{r} \rho(\mathbf{r}) \epsilon_{\text{XC}}(\rho(\mathbf{r})) , \quad (4.31)$$

and the corresponding exchange-correlation potential by

$$V_{\text{XC}}^{\text{LDA}}(\mathbf{r}) = \frac{\delta E_{\text{XC}}}{\delta \rho(\mathbf{r})} = \epsilon_{\text{XC}}(\rho(\mathbf{r})) + \rho(\mathbf{r}) \frac{\partial \epsilon_{\text{XC}}(\rho)}{\partial \rho} . \quad (4.32)$$

The exchange-correlation energy density $\epsilon_{\text{XC}}(\rho(\mathbf{r}))$ can be separated into two parts, the exchange part ϵ_{X} , resulting from the Pauli principle, and the correlation part ϵ_{C} , resulting from the Coulomb correlation

$$\epsilon_{\text{XC}}(\rho) = \epsilon_{\text{X}}(\rho) + \epsilon_{\text{C}}(\rho) , \quad (4.33)$$

where the exchange part $\epsilon_{\text{X}}(\rho)$ can be expressed analytically for the homogeneous electron gas [55, 62]

$$\epsilon_{\text{X}}(\rho(\mathbf{r})) = -\frac{3}{4} \left(\frac{3\rho(\mathbf{r})}{\pi} \right)^{\frac{1}{3}} . \quad (4.34)$$

For the correlation part $\epsilon_{\text{C}}(\rho)$, no such analytical result is known. Expressions can be obtained for the high-density [63, 64] and the low-density [65, 66] limit. The intermediate range has only been assessed numerically by highly accurate quantum Monte Carlo calculations, e.g. by Ceperley and Alder [67]. In order to use this discrete set of values, a parameterization is required, of which the most popular ones are the one by Vosko, Wilk and Nusair [68] (VWN-LDA) and the one by Perdew and Wang [69] (PW-LDA). Both schemes give usually very similar results.

Though the local-density approximation is a crude approximation to the true exchange-correlation energy, it has been widely used until the 1990's with surprisingly good results.

4. Density-Functional Theory

This can partly be related to the fact that the magnitude of the exchange-correlation energy is rather small compared to the total energy so that errors in the approximation are less significant as in the case of the kinetic energy. Drawbacks are, however, the typical overestimation of binding energies and the underestimation of bond lengths. In particular, systems with electron density distributions far away from the homogeneous electron gas, like the atomic clusters of interest in this work, often yield disappointing results.

Improvements over LDA can be achieved by taking non-local information of the density-distribution explicitly into account. A straightforward correction to the local-density approximation is a formal expansion of E_{XC} in gradients of the density suggested by Hohenberg and Kohn [56], which yields in general a functional of the form

$$E_{\text{XC}}^{\text{DGE}}[\rho(\mathbf{r})] = \int d\mathbf{r} \left[\epsilon_{\text{XC}}^{(0)}(\rho) + \epsilon_{\text{XC}}^{(1)}(\rho) \nabla \rho + \epsilon_{\text{XC}}^{(2)}(\rho) |\nabla \rho|^2 + \dots \right]. \quad (4.35)$$

However, truncating this expansion after the first order gives unsatisfying results, sometimes even being worse than LDA. Better approximations can be obtained by introducing a more generalized expansion. In this *Generalized-Gradient Approximation* (GGA), the exchange-correlation functional has the following form

$$E_{\text{XC}}^{\text{GGA}}[\rho(\mathbf{r})] = \int d\mathbf{r} f(\rho(\mathbf{r}), \nabla \rho(\mathbf{r})) d\mathbf{r} = \int \rho \epsilon_{\text{XC}}^{\text{GGA}}(\rho(\mathbf{r}), \nabla \rho(\mathbf{r})) d\mathbf{r}, \quad (4.36)$$

which typically yields better binding energies. Similar to LDA, $E_{\text{XC}}^{\text{GGA}}$ can be separated into an exchange and a correlation part. There are many different flavours of GGA-functionals that are differing in the functional form of the exchange and correlation energy which is typically constructed by fulfilling known constraints of the exchange-correlation potential V_{XC} . One popular GGA-functional was proposed by Perdew, Burke and Ernzerhof in 1996 (PBE) [70] which is almost exclusively used in the present work. This functional is based upon the PW91 functional of Perdew and Wang [71] which is an analytical fit to a numerically determined first-principles GGA, but cast into a simpler functional form by neglecting energetically irrelevant terms.

4.7. Spin-Density-Functional Theory

Many systems of interest possess an odd number of electrons. While the results obtained by the formalism described so far are quite satisfactory for closed-shell systems, extensions to open-shell systems are required, in particular for transition metals which exhibit magnetic properties. In principle, density-functional theory is an exact theory and the total energy depends exclusively upon the total electron density which also holds for open-shell systems unless there is an explicit spin-dependence in the Hamiltonian, e.g. in the case of an external magnetic field. Experience has shown, however, that approximate functionals gain more flexibility when explicitly depending upon the individual spin densities ρ^σ . In the therewith resulting *Unrestricted Kohn-Sham* method [72, 73], two sets of Kohn-Sham orbitals ϕ_i^\uparrow and ϕ_i^\downarrow are introduced, and used to represent a spin-polarized system

4. Density-Functional Theory

$$\left[-\frac{1}{2}\nabla^2 + V_{\text{eff}}^\sigma(\mathbf{r}) \right] \phi_{i\sigma} = \epsilon_{i\sigma} \phi_{i\sigma} , \quad (4.37)$$

where the spin-dependency of the effective potential V_{eff}^σ enters through the exchange-correlation potential

$$V_{\text{XC}}^\sigma(\mathbf{r}) \equiv \frac{\delta E_{\text{XC}}}{\delta \rho^\sigma(\mathbf{r})} . \quad (4.38)$$

The spin-polarized version of LDA is called local-spin-density approximation (LSDA) [72] and the corresponding exchange-correlation functional is given by

$$E_{\text{XC}}^{\text{LSD}}[\rho^\uparrow(\mathbf{r}), \rho^\downarrow(\mathbf{r})] = \int d\mathbf{r} \rho(\mathbf{r}) \epsilon_{\text{XC}}(\rho^\uparrow(\mathbf{r}), \rho^\downarrow(\mathbf{r})) . \quad (4.39)$$

Similarly, the $E_{\text{XC}}^{\text{GGA}}$ in the spin-polarized case looks in general like

$$E_{\text{XC}}^{\text{GGA}}[\rho^\uparrow, \rho^\downarrow] = \int d\mathbf{r} \rho \epsilon_{\text{XC}}(\rho^\uparrow, \rho^\downarrow, \nabla \rho^\uparrow \nabla \rho^\downarrow, \nabla \rho^\downarrow \nabla \rho^\downarrow, \nabla \rho^\uparrow \nabla \rho^\downarrow) . \quad (4.40)$$

with the special case of PBE

$$E_{\text{XC}}^{\text{PBE}}[\rho^\uparrow, \rho^\downarrow] = \int d\mathbf{r} \rho \epsilon_{\text{XC}}(\rho^\uparrow, \rho^\downarrow, |\nabla \rho|^2) . \quad (4.41)$$

Part II.

The Density-Functional Theory Implementation FHI-aims

5. Solving the Kohn-Sham Equations with Numerical Atom-Centered Basis Sets

Due to the steadily increasing importance of density-functional theory, many different implementations are nowadays available. Though the underlying theory is always the same, differences arise from the actual strategy to put DFT into a practical tool. In a dominant fraction of existing implementations the main principle is always the same in that the Kohn-Sham orbitals ϕ_i are expanded into a set of basis functions φ_j

$$\phi_i(\mathbf{r}) = \sum_j c_{ij} \varphi_j(\mathbf{r}) . \quad (5.1)$$

A priori, the choice of a certain basis set is not prescribed and thus guided by the actual problem to tackle which leads to the manifold of electronic structure codes around. Historically, there are two main classes. *Plane waves* first arose in the context of solid state physics since they are naturally cast into periodic boundary conditions applied in solid state calculations. *Localized basis functions*, on the other hand, are suitable to treat finite systems like molecules, as the tail region of the eigenstates and the surrounding vacuum requires decaying basis sets for an efficient calculation. Common choices for the latter class of basis functions are analytically defined *Gaussians* or *Slater-like* orbitals. The implementation **FHI-aims** ("ab initio molecular simulations") developed at the Theory Department of the Fritz-Haber-Institute resorts to *numerically* defined *atom-centered* orbitals of the form

$$\varphi_i(\mathbf{r}) = \frac{u_i(r)}{r} Y_{lm}(\vartheta, \phi) , \quad (5.2)$$

where $Y_{lm}(\vartheta, \phi)$ are spherical harmonics. The radial part $u_i(r)$ is numerically tabulated, thus being very flexible since any kind of desired shape can be achieved. This paves the way for generating highly efficient species-dependent basis sets, which are furthermore constructed strictly hierarchical so that the accuracy can be continuously increased from tight-binding like to the meV level. The concept of atom-centered basis functions together with a well-defined control of convergence makes **FHI-aims** a suitable tool for the aspired atomic cluster calculations. The co-development of the electronic structure code, in particular the essential atomic forces for the sampling schemes (see chapter 6), constitutes an important, preparatory part of this PhD project.

5.1. The Eigenvalue Problem

The heart of FHI-aims is to solve the Kohn-Sham equation

$$\hat{h}^{\text{KS}} |\phi_i\rangle = \epsilon_i |\phi_i\rangle , \quad (5.3)$$

with the single-particle Hamiltonian

$$\hat{h}^{\text{KS}} = -\frac{1}{2}\nabla^2 + V_{\text{eff}}([\rho], \mathbf{r}) , \quad (5.4)$$

where for simplicity the non-polarized case is considered here first. The Kohn-Sham orbitals lead to the electron density $\rho(\mathbf{r}) = \sum_i f_i |\phi_i(\mathbf{r})|^2$ which then determines the effective potential $V_{\text{eff}}[\rho]$. Equations (5.3) and (5.4) have therefore to be solved self-consistently, i.e. the exact same eigenfunctions and electron density used to construct the correct Hamiltonian must re-emerge as its output. In each iteration step towards self-consistency, the orbitals are expanded in a set of basis functions φ_j .

$$\phi_i(\mathbf{r}) = \sum_j c_{ij} \varphi_j(\mathbf{r}) . \quad (5.5)$$

Inserting this ansatz into Eq. (5.3) and multiplying the equation with φ_i finally transforms the continuous differential equation into an algebraic generalized eigenvalue problem

$$\sum_j h_{ij} c_{jl} = \epsilon_l \sum_j s_{ij} c_{jl} . \quad (5.6)$$

The Hamiltonian and overlap matrix elements h_{ij} and s_{ij} , respectively, are hereby given by

$$h_{ij} = \int d\mathbf{r} [\varphi_i(\mathbf{r}) \hat{h}^{\text{KS}} \varphi_j(\mathbf{r})] , \quad (5.7)$$

$$s_{ij} = \int d\mathbf{r} [\varphi_i(\mathbf{r}) \varphi_j(\mathbf{r})] . \quad (5.8)$$

The complex conjugate notation is not needed for finite systems and therewith omitted in this thesis.

As described in the previous chapter, the total energy of a system in DFT is given by the Kohn-Sham-Functional including the repulsive nuclei-nuclei interaction

$$E^{\text{KS}} = T_{\text{S}} + J_{\text{H}} + E_{\text{XC}} + E_{\text{ext}} + E_{\text{NN}} , \quad (5.9)$$

minimized over all possible densities according to the second Hohenberg-Kohn theorem. The discretization of the Hilbert space by the basis functions $\{\varphi_j\}$ leads to a minimization with respect to the expansion coefficients $\{c_{ij}\}$. The Kohn-Sham functional evaluated at the ground-state energy is therefore variational with respect to the $\{c_{ij}\}$, i.e.

$$\frac{\partial E_{\text{tot}}}{\partial c_{ij}} = 0 \quad (5.10)$$

The extension to the spin-polarized case is straightforward. Eq. (5.3) needs to be solved for both spin-channels, thus yielding two different sets of expansion coefficients $\{c_{i\sigma,j}\}$ for the corresponding orbitals $\{\phi_{i\sigma}\}$. Self-consistency then needs to be achieved for both spin-densities ρ^\uparrow and ρ^\downarrow due to the explicit dependency of the effective potential $V_{\text{eff}}^\sigma([\rho^\uparrow, \rho^\downarrow])$ on both quantities (see section 4.7).

Eq. (5.3) gives direct access to the Kohn-Sham eigenvalues ϵ_i . It is therefore convenient to rewrite the energy functional as

$$E^{\text{KS}} = \sum_i f_i \epsilon_i - \int d\mathbf{r} \rho(\mathbf{r}) V_{\text{XC}}(\mathbf{r}) + E_{\text{XC}}[\rho] - \frac{1}{2} \int d\mathbf{r} \rho(\mathbf{r}) V_{\text{H}}(\mathbf{r}) + E_{\text{NN}}, \quad (5.11)$$

which can trivially be extended to the spin-polarized case

$$E^{\text{KS}} = \sum_{i\sigma} f_{i\sigma} \epsilon_{i\sigma} - \sum_\sigma \int d\mathbf{r} \rho^\sigma(\mathbf{r}) V_{\text{XC}}^\sigma(\mathbf{r}) + E_{\text{XC}}[\rho^\uparrow, \rho^\downarrow] - \frac{1}{2} \int d\mathbf{r} \rho(\mathbf{r}) V_{\text{H}}(\mathbf{r}) + E_{\text{NN}}. \quad (5.12)$$

In principle, this reformulation is derived by summing up the Kohn-Sham equations, correcting the double-counting of the classical Hartree energy and replacing the exchange-correlation potential energy $\int d\mathbf{r} \rho(\mathbf{r}) V_{\text{XC}}(\mathbf{r})$ by the exchange-correlation energy E_{XC} to obtain the correct total energy.

5.1.1. Achieving Self-Consistency

Density mixing

The main problem of an electronic structure calculation is to achieve self-consistency, i.e. the correct electronic Hamiltonian h_{ij} should yield as output the same wave functions, electronic charge density and potentials that were used to construct it, which means $\rho_{\text{out}}^{(n)} = \rho_{\text{in}}^{(n)}$. To achieve self-consistency, one therefore starts with an initial trial density $\rho^{(0)}$ which in FHI-aims is constructed by superimposing the densities of the constituent atoms. Solving the Kohn-Sham equation then yields orbitals $\{\phi_i\}^{(0)}$ that lead to an output electron density $\rho_{\text{out}}^{(0)}$ which is used to construct the next input density $\rho_{\text{in}}^{(1)}$. This whole procedure is repeated until finally the output density equals the input density and thus self-consistency is achieved. The construction of the next input density is a crucial technical detail that significantly determines the performance of the calculation. The simplest scheme is to linearly mix the output density with the previous input density

$$\rho_{\text{in}}^{(n)} = \alpha \rho_{\text{out}}^{(n)} + (1 - \alpha) \rho_{\text{out}}^{(n-1)}, \quad (5.13)$$

with α being an adjustable parameter. If chosen too small, convergence is poor since the electron density approaches the self-consistent density very slowly. Choosing a too

large value might destabilize the electron density, resulting into an oscillating behaviour or even no convergence at all.

More sophisticated is the *Pulay* mixing scheme [74, 75] that is exclusively used in the present work. In that scheme, the input charge densities are stored for a number of iteration steps. The key quantity in this mixing scheme is the *charge density residual* defined as

$$R[\rho_{\text{in}}] = \rho_{\text{out}}([\rho_{\text{in}}], \mathbf{r}) - \rho_{\text{in}}(\mathbf{r}) = \Delta\rho(\mathbf{r}) , \quad (5.14)$$

which describes the change of the electron charge density at every point in space after a self-consistency iteration. If self-consistency is achieved, the norm of the residual vanishes

$$\langle R[\rho_{\text{in}}] | R[\rho_{\text{in}}] \rangle = 0 , \quad (5.15)$$

where the norm corresponds to a simple integral

$$\langle R[\rho] | R[\rho] \rangle = \int d\mathbf{r} (\Delta\rho)^2(\mathbf{r}) . \quad (5.16)$$

Hence, the density has converged to the self-consistent one at every point in space, since $\Delta\rho$ must equal zero everywhere. Achieving self-consistency therefore corresponds to minimizing the charge density residual.

A new optimal input charge density is obtained in each step as a linear combination of the input charge densities of all previous steps

$$\rho_{\text{in}}^{\text{opt}} = \sum_i \alpha_i \rho_{\text{in}}^{(i)} , \quad (5.17)$$

where the linear coefficients obviously have to fulfil the following condition to conserve the norm of the density

$$\sum_i \alpha_i = 1 . \quad (5.18)$$

The underlying assumption of the Pulay mixing scheme is the linearity of the residual so that the residual vector of the optimum charge density is given by

$$R[\rho_{\text{in}}^{\text{opt}}] = R \left[\sum_i \alpha_i \rho_{\text{in}}^{(i)} \right] = \sum_i \alpha_i R[\rho_{\text{in}}^{(i)}] . \quad (5.19)$$

Minimizing the norm of the residual

$$\langle R[\rho_{\text{in}}^{\text{opt}}] | R[\rho_{\text{in}}^{\text{opt}}] \rangle , \quad (5.20)$$

then leads to a system of equations for the coefficients α_i which finally yields the optimum input density. To prevent the electron charge density from being trapped in a subspace spanned by the previous densities, a fraction of the residual vector is added to finally obtain the new input density which is then used to construct the next Hamiltonian

$$\rho_{\text{in}}^{(n+1)} = \rho_{\text{in}}^{\text{opt}} + \gamma R[\rho_{\text{in}}^{\text{opt}}] , \quad (5.21)$$

with γ being an adjustable parameter.

For the spin-polarized case, it is crucial to combine both spin-channels to one single residual vector

$$\langle R[\rho^\uparrow, \rho^\downarrow] | R[\rho^\uparrow, \rho^\downarrow] \rangle = \sum_{\sigma} \int d\mathbf{r} (\Delta\rho^{\sigma})^2(\mathbf{r}) , \quad (5.22)$$

which is then used to determine a single set of coefficients α_i for both spin-densities ρ^\uparrow and ρ^\downarrow , thus ensuring stable convergence.

The number of stored densities and residuals is a key parameter and can significantly influence the performance. If chosen too small, too little information is taken into account and the convergence is slow. In case of too many previous densities taken into account, the individual densities might be too different, so that the assumption of linearity is not justified and the Pulay matrix becomes singular.

Occupation smearing

In systems with degenerate or quasi-degenerate eigenstates near the Fermi level, the occupation of the eigenstates might oscillate during the self-consistency iterations since the eigenstates permanently cross the Fermi level. Additional stability can then be achieved by occupying the states by a distribution $\{f_{i\sigma}\}$ which is slightly broadened about the Fermi level, thus weakening the effect of a level-crossing since the occupation then does not change discontinuously. FHI-aims supports Fermi-smearing [76], Methfessel-Paxton [77] and Gaussian [78], where the latter is exclusively used in the present work when necessary. The occupation numbers are then given by

$$f_{i\sigma} = \frac{1}{2} \left(1 - \text{erf} \left[\frac{\epsilon_{i\sigma} - \mu}{w} \right] \right) . \quad (5.23)$$

Since the PES is therewith effectively distorted, one aims at a value for the smearing width w as small as possible to not change the physics of the system significantly. Since clusters typically show Jahn-Teller distortions and therewith a HOMO-LUMO gap, w can typically be set to zero once the system is close to the local minimum. Small finite values for w in the range of tenths of eV are only chosen for the atomic configuration being far away from the local minimum.

5.2. Numerical Atom-Centered Basis Functions

5.2.1. The Definition of the Basis Functions

In FHI-aims the radial part of the basis function given by Eq. (5.2) is obtained by solving a radial Schrödinger-like equation on a logarithmic grid. A steeply increasing confinement potential is thereby used to spatially confine the basis functions to a local

region, thus allowing for an $O(N)$ -like scaling of the integrations for large systems. The shape of the potential is chosen to ensure a continuous second derivative at the onset of the potential which then increases gradually to infinity at the cutoff-radius r_{cut} . One clear advantage over analytically defined basis functions like Gaussians or Slater-like functions is the greater flexibility since any kind of potential in the Schrödinger-like equation can be chosen. In **FHI-aims** the *minimal* basis of a species is constructed by choosing the effective Kohn-Sham potential of the corresponding non-polarized, spherically symmetric free atom. This basis thus facilitates the all-electron calculation since the oscillatory behaviour of the wavefunctions in the core-region are already well described at this level. Additionally the minimal basis avoids the atomic basis set superposition error (BSSE) which can typically be observed for analytical localized basis sets: When calculating the cohesive energy of an X_N -cluster

$$E_{\text{coh}} = [E_{\text{tot}}(X_N) - NE_{\text{tot}}(X)] / N , \quad (5.24)$$

the energy contribution of a constituent atom to the total energy E_{tot} might be variationally improved by basis functions sitting on adjacent atoms, thus leading to an overestimating of E_{coh} . Using atomic states, however, the total energy is already converged at the level of the minimal basis, and neighbouring basis functions have no effect. The BSSE might still occur and should be checked in case of *intermolecular* binding energies, though.

The minimal basis set is augmented by further classes of basis functions, one of which is formed by ion-like radial functions that are in particular suitable for describing a chemical bond as demonstrated by Delley [79]. These are states obtained from calculations of positive ions, which are supposed to describe the charge transfer of a system in a chemical bond. Hydrogen-like functions are used in addition, especially as *polarisation functions* for angular momenta beyond those present in the free atom itself. These functions are derived from one-electron atoms with an arbitrary nuclear charge, that does not need to be an integer. Since radial functions originating from different potentials are not necessarily orthonormal to one another even on the same atomic site, all on-site radial functions are orthonormalized explicitly using a simple Gram-Schmidt process [80].

Contrary to Gaussians or Slater-like functions, numerically tabulated basis functions do not allow for an analytical integration, thus requiring a numerical method that is described in section (5.3).

5.2.2. The Generation of Basis Functions

The major challenge when dealing with atom-centered basis functions is the systematic convergence towards a complete basis set limit (cbs) with an as small and thus as efficient basis set as possible. Contrary to plane waves, for which the cutoff energy can be successively increased until the desired accuracy in the total energy has been achieved, there is no such simple parameter for numerical basis functions. All one can be sure of is the variational principle according to which the total energy improves when a given basis set is augmented by further basis functions. In order to produce structure-independent,

transferable basis sets, that can later on be used for production, the strategy pursued by FHI-aims is therefore to choose the best basis functions out of a huge pool of candidate radial functions. This contains ion-like functions [79, 81] of different main and angular quantum numbers and hydrogen-like functions covering a broad range of effective charges [79]. Starting from the minimal free-atom basis of size $N_{\text{min-basis}}$, the entire pool of candidate functions is sampled, adding each function to the given basis set in turn. The radial function with angular momentum l that gives the single largest improvement of a target total energy is added to the original basis set, increasing it to $(N_{\text{min-basis}} + (2l+1))$. This step is then repeated, adding again each candidate function with angular momentum \tilde{l} to the basis set of size $(N_{\text{min-basis}} + (2l+1))$ in turn and then increase it to size $(N_{\text{min-basis}} + (2l+1) + (2\tilde{l}+1))$ with the next best function. The whole procedure is performed until no further significant total energy improvements result. Regarding the optimization target for a certain chemical element, the corresponding dimer is chosen which constitutes the simplest possible chemical bond and further a rather demanding test case for atom-centered orbitals [82], since no basis function overlap from further centers can accidentally improve the total energy. The improvement resulting from adding a certain trial basis function to the basis set is then defined as

$$\Delta_{\text{basis}} = \frac{1}{N_d} \sum_i^{N_d} [\mathcal{E}_{\text{basis}}(d_i) - \mathcal{E}_{\text{cbs}}(d_i)] , \quad (5.25)$$

where $\mathcal{E}_{\text{basis}}(d_i)$ denotes the non-self-consistent total energy for the dimer at the bond distance d_i . The non-self-consistent reference energy $\mathcal{E}_{\text{cbs}}(d_i)$ for a converged basis set is obtained independently of the present procedure, by converging a very large and thus inefficient, but formally systematic basis set of confined atomic excited-state functions. The dimer distances $\{d_i\}$ are spread to sample the self-consistent LDA binding curve. Experience has shown [11] that non-selfconsistent energies are a sufficient optimization target and transferable to self-consistent calculations. Furthermore, potential instabilities of the self-consistency-cycle for pathological cases are therewith avoided.

The different basis functions resulting from the basis set generation typically arise in groups of different angular momenta, *spd* or *spdf*, and are thus organized in so-called *tiers* which contain a basis function of each angular momentum. The number of the tier thereby denotes the accuracy of the basis set. The different basis sets used in the present work are given in detail in Appendix A.

5.3. Numerical Integration

Numerical integrations are performed for several tasks. The dominant part in the computational effort constitutes the calculation of the overlap, Eq. (5.8), and Hamiltonian matrix, Eq. (5.7), which scale formally as $O(N^3)$ with the system size. In FHI-aims, the numerical integration is based upon a partitioning technique [79, 83] which decomposes a function to pieces sitting on atoms that are then integrated by an atom-centered numerical grid. The distribution among the atoms is thereby done by an atom-centered partitioning function p_α

$$\int d\mathbf{r} f(\mathbf{r}) = \sum_{\alpha} \int d\mathbf{r} p_{\alpha}(\mathbf{r}) f(\mathbf{r}) . \quad (5.26)$$

The sum of all partitioning functions equals one which is achieved by the normalization

$$p_{\alpha}(\mathbf{r}) = \frac{g_{\alpha}(\mathbf{r})}{\sum_{\beta} g_{\beta}(\mathbf{r})} . \quad (5.27)$$

g_{α} is hereby strongly peaked close to the originating atom thus integrating the function preferably on the grid sitting on the next nearest atom. In **FHI-aims** this is achieved by an approach similar to the Hirshfeld partitioning scheme [84], which is based upon the electron density of non-spinpolarized, spherical free atoms $\rho_{\alpha}^{\text{free}}$ as suggested by Delley [79]

$$g_{\alpha}(\mathbf{r}) = \frac{\rho_{\alpha}^{\text{free}}}{r^2} . \quad (5.28)$$

Every single-atom centered integrand is then integrated over N_r radial integration shells each containing N_{ang} angular integration points,

$$\int d\mathbf{r} p_{\alpha}(\mathbf{r}) f(\mathbf{r}) \approx \sum_{\mathbf{r}_{i\alpha}} \Delta \mathbf{r}_{i\alpha} p_{\alpha}(\mathbf{r}_{i\alpha}) f(\mathbf{r}_{i\alpha}) = \sum_s \sum_t \Delta \mathbf{r}_{i\alpha}(s, t) p_{\alpha}(\mathbf{r}_{i\alpha}) f(\mathbf{r}_{i\alpha}(s, t)) , \quad (5.29)$$

where the grid weights $\mathbf{r}_{i\alpha}$ can simply be obtained by the analytically given integration points. Summarized, any kind of integral in **FHI-aims** is approximated by a discrete sum of the form

$$\int d\mathbf{r} f(\mathbf{r}) \approx \sum_{\alpha} \sum_{\mathbf{r}_{i\alpha}} w_{\mathbf{r}_{i\alpha}} f(\mathbf{r}_{i\alpha}) , \quad (5.30)$$

with the integration weights $w_{\mathbf{r}_{i\alpha}}$ given by the product of the partition function and the weights of the individual atom-centered grid $w_{\mathbf{r}_{i\alpha}} = p_{\alpha}(\mathbf{r}) \Delta \mathbf{r}_{i\alpha}$.

The radial grid is defined as suggested by Baker [85]

$$r(s) = r_{\text{outer}} \frac{\log \left(1 - [s / (N_r + 1)]^2 \right)}{\log \left(1 - [N_r / (N_r + 1)]^2 \right)} , \quad (5.31)$$

which provides radial shells that are dense in the core region and then becomes successively coarser with increasing distance of the nucleus. Thus, the fast-varying localized wave function parts near the nuclei are captured, together with an efficient treatment of the smoother parts in the interstitial and far-field regions. r_{outer} gives the outermost radial shell and is chosen as 7 Å for all species and thus contains the whole basis function for cut-off radii $r_{\text{cut}} < 7 \text{ Å}$ that are used in this work. The number of radial grid points N_r further scales with the nuclear charge [85] so that heavier elements with steeper core states are integrated more accurately:

$$N_r = 16.8 (Z + 2)^{1/3} . \quad (5.32)$$

A uniform accuracy increase can be obtained by placing additional shells at integer fractions $N_{\text{r,div}}$ of the original grid, e.g. at $s = \frac{1}{2}$, $s = \frac{3}{2}$, ... , $s = 2N_{\text{r}} + \frac{1}{2}$ for $N_{\text{r,div}} = 2$.

As angular grids, the *Lebedev* grids [86, 87, 88] are chosen in a special version provided by Delley [89]. The corresponding integration points have octahedral symmetry and are constructed in such a way as to integrate angular momentum functions up to a certain order exactly [90, 91].

The number of angular grid points is not chosen fixed for all distances. Close to the nuclei with a dense radial integration grid and small surfaces of the radial shells less angular points are required compared to large distances. In **FHI-aims** the required number N_{ang} for a given radial integration shell can therefore be determined adaptively by converging the initial overlap matrix elements s_{ij} and the initial Hamiltonian matrix elements h_{ij} prior to the production run. An upper and lower bound is given by the parameter $N_{\text{ang,max}}$ and $N_{\text{ang,min}}$, respectively.

Formally, the numerical integration scales as $O(N^3)$ with the system size, since all pairs of basis functions ($\propto N^2$) must be integrated across the entire system ($\propto N$). Due to the localization of the basis functions, this scaling is reduced to $O(N)$ for large systems since the number of non-vanishing basis functions at a certain grid point becomes independent of the system size.

5.4. The Hartree-Potential

The calculation of the electrostatic potential V_{H} constitutes a further challenge. A direct integration of the Hartree potential in Eq. (4.29) would be prohibitively expensive as it requires a whole integration for each grid point. In **FHI-aims** the calculation is therefore much simplified by a multipole-decomposition method as described by Delley [79]. First, the superimposition of the non-polarized, spherical free atoms is subtracted from the electron density, leaving the much smoother difference electron density due to the chemical bond. The free electron density together with the corresponding potentials are calculated in the preparation of the production and are therewith known, thus allowing for a reconstruction of the full electrostatic potential .

$$\Delta\rho(\mathbf{r}) = \rho(\mathbf{r}) - \sum_{\alpha} \rho_{\alpha}^{\text{free}}(|\mathbf{r} - \mathbf{R}_{\alpha}|) . \quad (5.33)$$

Using the partitioning scheme presented in the previous section, the electron density is allocated to the individual atoms, followed by a multipole expansion

$$\Delta\rho_{\alpha,lm}^{\text{MP}}(r) = \int_{r=|\mathbf{r}-\mathbf{R}_{\alpha}|} d^2\Omega_{\alpha} p_{\alpha}(\mathbf{r}) \cdot \Delta\rho(\mathbf{r}) \cdot Y_{lm}(\Omega_{\alpha}) , \quad (5.34)$$

where Ω_{α} is a short-hand notation for the spherical coordinates (ϑ, φ) with respect to atom α . With the multipole components of the electron density $\Delta\rho_{\alpha,lm}^{\text{MP}}$, the corresponding components of the Hartree potential $\Delta V_{\alpha,lm}$ can then efficiently be obtained by integrating the Poisson equation on a one-dimensional, logarithmic radial grid

$$\nabla^2(\Delta V_{\alpha,lm}) = -4\pi\Delta\rho_{\alpha,lm}^{\text{MP}} . \quad (5.35)$$

5. Solving the Kohn-Sham Equations with Numerical Atom-Centered Basis Sets

The individual components are then reassembled to finally obtain the Hartree potential of the difference electron density

$$\Delta V_{\text{H}}^{\text{MP}}(\mathbf{r}) = \sum_{\alpha, lm}^{l_{\text{max}}} \Delta V_{\alpha, lm}(|\mathbf{r} - \mathbf{R}_{\alpha}|) Y_{lm}(\Omega_{\alpha}) . \quad (5.36)$$

The multipole expansion is truncated at a maximum angular momentum l_{max} , thus introducing an expansion error. According to Dunlap *et al.* [92], the first-order expansion error can be eliminated by modifying the electrostatic double-counting correction in the Kohn-Sham-functional, Eq. (5.11), like

$$-\frac{1}{2} \int d\mathbf{r} \rho V_{\text{H}}[\rho^{\text{MP}}] \longrightarrow -\frac{1}{2} \int d\mathbf{r} \rho^{\text{MP}} V_{\text{HH}}[\rho^{\text{MP}}] , \quad (5.37)$$

with

$$\rho^{\text{MP}}(\mathbf{r}) = \sum_{\alpha} \rho_{\alpha}^{\text{free}}(|\mathbf{r} - \mathbf{R}_{\alpha}|) + \sum_{\alpha, lm} \Delta \rho_{\alpha, lm}^{\text{MP}}(|\mathbf{r} - \mathbf{R}_{\alpha}|) Y_{lm}(\Omega_{\alpha}) , \quad (5.38)$$

so that quadratic total energy convergence with respect to l_{max} can be achieved.

6. Energy Derivatives in FHI-aims

The local structural relaxation is a key ingredient to the success of many global optimization schemes discussed in chapter 3, since it effectively removes the transition state regions during the exploration of the PES. Efficient structural relaxation thereby requires the knowledge of the atomic forces which are the negative first derivative of the total energy. The simplest method to obtain energy derivatives is the finite difference scheme which approximates the gradient by displacing the atomic positions like

$$\frac{dE_{\text{tot}}}{d\mathbf{R}_{\alpha,x}} \approx \frac{E_{\text{tot}}(\mathbf{R}_{\alpha,x} + \Delta\mathbf{R}_{\alpha,x}) - E_{\text{tot}}(\mathbf{R}_{\alpha,x} - \Delta\mathbf{R}_{\alpha,x})}{2\Delta\mathbf{R}_{\alpha,x}}. \quad (6.1)$$

Technical details on higher-order finite difference schemes are given in Appendix D. In principle, derivatives can thereby be evaluated up to any desired accuracy by choosing a significantly small displacement step width Δ . However, this requires the calculation of the total energy of all displaced atomic configurations for each single relaxation step, thus increasing the overall computational burden by a factor of $6N$ for the simplest finite difference scheme. Hence, analytical derivatives that can directly be obtained for a given atomic configurations are desirable, which significantly decrease the computational cost of a local structural relaxation. Accurate forces are furthermore a prerequisite for obtaining reliable vibrational spectra as used in the application described in chapter III. The implementation and critical examination of the accuracy of the analytical atomic forces in FHI-aims has therefore been a major part of the present work.

6.1. The Calculation of Analytical Atomic Forces

The forces are defined as the negative gradient of the total energy with respect to the nuclear coordinates

$$\mathbf{F}_{\alpha} = -\frac{dE_{\text{tot}}}{d\mathbf{R}_{\alpha}}. \quad (6.2)$$

The total energy in FHI-aims is the minimum of the Kohn-Sham-functional E^{KS} under the orthonormalization constraint of the Kohn-Sham orbitals

$$E_{\text{tot}} = \min_{\{c_{i\sigma,j}\}} \left(E^{\text{KS}} - \sum_{i\sigma,j\sigma'} f_{i\sigma} \epsilon_{i\sigma} \delta_{i\sigma,j\sigma'} (\langle \phi_{i\sigma} | \phi_{j\sigma'} \rangle - 1) \right) \quad (6.3)$$

$$= \min_{\{c_{i\sigma,j}\}} \left(E^{\text{KS}} - \sum_{i\sigma} f_{i\sigma} \epsilon_{i\sigma} (\langle \phi_{i\sigma} | \phi_{i\sigma} \rangle - 1) \right) = E_{\text{tot}}[\{c_{i\sigma,j}\}, \{\mathbf{R}_{\alpha}\}] , \quad (6.4)$$

6. Energy Derivatives in FHI-aims

where the sum goes over all states $\phi_{i\sigma}$ with the eigenvalue $\epsilon_{i\sigma}$. From this, it follows that

$$\mathbf{F}_\alpha = -\frac{dE_{\text{tot}}}{d\mathbf{R}_\alpha} \quad (6.5)$$

$$= -\frac{\partial E_{\text{tot}}}{\partial \mathbf{R}_\alpha} - \sum_{i\sigma,j} \underbrace{\frac{\partial E_{\text{tot}}}{\partial c_{i\sigma,j}}}_{=0} \frac{\partial c_{i\sigma,j}}{\partial \mathbf{R}_\alpha} . \quad (6.6)$$

Since at self-consistency the total energy is variational with respect to $\{c_{i\sigma,j}\}$, the corresponding term for the forces vanishes and only the partial derivative remains

$$\mathbf{F}_\alpha = -\frac{\partial E_{\text{tot}}}{\partial \mathbf{R}_\alpha} = -\frac{\partial E^{\text{KS}}}{\partial \mathbf{R}_\alpha} - \frac{\partial}{\partial \mathbf{R}_\alpha} \sum_{i\sigma} \epsilon_{i\sigma} (\langle \phi_{i\sigma} | \phi_{i\sigma} \rangle - 1) , \quad (6.7)$$

with

$$E^{\text{KS}} = T_{\text{S}} + J_{\text{H}} + E_{\text{XC}} + E_{\text{ext}} + E_{\text{NN}} , \quad (6.8)$$

with the kinetic energy

$$T_{\text{S}} = -\frac{1}{2} \sum_{i\sigma} f_{i\sigma} \langle \phi_{i\sigma} | \nabla^2 | \phi_{i\sigma} \rangle , \quad (6.9)$$

the Hartree energy

$$J_{\text{H}} = \frac{1}{2} \int \int d\mathbf{r} d\mathbf{r}' \frac{\rho(\mathbf{r})\rho(\mathbf{r}')}{|\mathbf{r} - \mathbf{r}'|} , \quad (6.10)$$

the exchange-correlation energy

$$E_{\text{XC}} = \int d\mathbf{r} \rho(\mathbf{r}) \epsilon_{\text{XC}} , \quad (6.11)$$

the electron-nuclei energy

$$E_{\text{ext}} = \int d\mathbf{r} \rho(\mathbf{r}) V_{\text{Ne}}(\mathbf{r}) , \quad (6.12)$$

with

$$V_{\text{Ne}}(\mathbf{r}) = \sum_{\beta} \frac{Z_{\beta}}{|\mathbf{r} - \mathbf{R}_{\beta}|} , \quad (6.13)$$

the nuclei-nuclei energy

$$E_{\text{NN}} = \sum_{\alpha < \beta} \frac{Z_{\alpha} Z_{\beta}}{|\mathbf{R}_{\alpha} - \mathbf{R}_{\beta}|} . \quad (6.14)$$

It is worth to point out that it is the variational property of the energy functional that fortunately allows for a direct evaluation of the analytical derivative since the total derivative therewith reduces to the partial derivative, thus making the partial derivative of the variational parameters with respect to the nuclear coordinates $\partial c_{i\sigma,j} / \partial \mathbf{R}_{\alpha}$ dispensable which would not directly be accessible.

6.1.1. The Individual Derivative Terms

The Kinetic Energy

Just taking the partial derivative in a straightforward way yields

$$-\frac{\partial T_S}{\partial \mathbf{R}_\alpha} = \frac{1}{2} \frac{\partial}{\partial \mathbf{R}_\alpha} \sum_{i\sigma} f_{i\sigma} \langle \phi_{i\sigma} | \nabla^2 | \phi_{i\sigma} \rangle \quad (6.15)$$

$$= \frac{1}{2} \sum_{i\sigma} f_{i\sigma} \left(\left\langle \frac{\partial \phi_{i\sigma}}{\partial \mathbf{R}_\alpha} \middle| \nabla^2 \middle| \phi_{i\sigma} \right\rangle + \left\langle \phi_{i\sigma} \middle| \nabla^2 \middle| \frac{\partial \phi_{i\sigma}}{\partial \mathbf{R}_\alpha} \right\rangle \right) \quad (6.16)$$

$$= -2 \sum_{i\sigma} f_{i\sigma} \left\langle \frac{\partial \phi_{i\sigma}}{\partial \mathbf{R}_\alpha} \middle| -\frac{1}{2} \nabla^2 \middle| \phi_{i\sigma} \right\rangle . \quad (6.17)$$

The nuclear gradient of the orbitals can be obtained by

$$\frac{\partial \phi_{i\sigma}}{\partial \mathbf{R}_\alpha} = \sum_{j(\alpha)} c_{i\sigma,j} \frac{\partial}{\partial \mathbf{R}_\alpha} \varphi_j(|\mathbf{r} - \mathbf{R}_\alpha|) , \quad (6.18)$$

$$= - \sum_{j(\alpha)} c_{i\sigma,j} \nabla \varphi_j(|\mathbf{r} - \mathbf{R}_\alpha|) . \quad (6.19)$$

since

$$\frac{\partial}{\partial \mathbf{R}_\alpha} \varphi_j(|\mathbf{r} - \mathbf{R}_\alpha|) = -\nabla \varphi_j(|\mathbf{r} - \mathbf{R}_\alpha|) , \quad (6.20)$$

and $j(\alpha)$ indicates a basis function sitting on atom α . The remaining basis functions do not contribute to the forces on atom α since they do not depend upon \mathbf{R}_α . So the nuclear gradients can be expressed in terms of spatial gradients of the basis functions which can then easily be evaluated numerically.

The Hartree Energy

Similar to the kinetic energy, the Hartree energy can be derived in a straightforward way

$$-\frac{\partial J_H}{\partial \mathbf{R}_\alpha} = -\frac{1}{2} \frac{\partial}{\partial \mathbf{R}_\alpha} \int \int d\mathbf{r} d\mathbf{r}' \frac{\rho(\mathbf{r})\rho(\mathbf{r}')}{|\mathbf{r} - \mathbf{r}'|} , \quad (6.21)$$

$$= - \int \int d\mathbf{r} d\mathbf{r}' \frac{\partial \rho(\mathbf{r})}{\partial \mathbf{R}_\alpha} \frac{\rho(\mathbf{r}')}{|\mathbf{r} - \mathbf{r}'|} , \quad (6.22)$$

$$= - \int d\mathbf{r} \frac{\partial \rho(\mathbf{r})}{\partial \mathbf{R}_\alpha} V_H(\mathbf{r}) . \quad (6.23)$$

Since $\rho(\mathbf{r}) = \sum_{i\sigma} f_{i\sigma} \phi_{i\sigma}(\mathbf{r}) \cdot \phi_{i\sigma}(\mathbf{r})$, the derivative of the density is given by

$$\frac{\partial \rho(\mathbf{r})}{\partial \mathbf{R}_\alpha} = 2 \sum_{i\sigma} f_{i\sigma} \frac{\partial \phi_{i\sigma}(\mathbf{r})}{\partial \mathbf{R}_\alpha} \cdot \phi_{i\sigma}(\mathbf{r}) , \quad (6.24)$$

which finally yields as derivative of the Hartree energy

$$-\frac{\partial J_H}{\partial \mathbf{R}_\alpha} = -2 \sum_{i\sigma} f_{i\sigma} \left\langle \frac{\partial \phi_{i\sigma}}{\partial \mathbf{R}_\alpha} \middle| V_H(\mathbf{r}) \middle| \phi_{i\sigma} \right\rangle, \quad (6.25)$$

which boils down to calculating the nuclear gradients of the orbitals analogous to the kinetic energy term.

The Multipole-Correction Term

The above derivation of the Hartree energy was based upon the true electronic density. In *FHI-aims*, however, the Hartree potential is based upon a multipole expansion of the density ρ^{MP} instead of the true electron density ρ . Additionally, the first-order correction of the total energy by Dunlap [92] due to the multipole expansion error yields a further correction term. So the Hartree energy term as it is precisely implemented in *FHI-aims* is given by

$$J_H = \int d\mathbf{r} \rho V_H[\rho^{\text{MP}}] - \frac{1}{2} \int d\mathbf{r} \rho^{\text{MP}} V_H[\rho^{\text{MP}}], \quad (6.26)$$

which then yields by a straightforward derivation the additional correction term

$$\mathbf{F}_{\text{MP},\alpha} = - \int d\mathbf{r} (\rho(\mathbf{r}) - \rho^{\text{MP}}(\mathbf{r})) \frac{\partial V_H[\rho^{\text{MP}}]}{\partial \mathbf{R}_\alpha}, \quad (6.27)$$

which is in agreement with the expression given by Delley [93]. As one can immediately see, the multipole-correction term vanishes, if the multipole density would be equal to the true density. The nuclear gradients of the Hartree potential are then obtained in complete analogy to the nuclear gradients of the Kohn-Sham orbitals and can be boiled down to calculating the spatial gradients. Since the multipole expansion of the Hartree potential is composed of nuclear contributions

$$V_H(\mathbf{r}) = \sum_{\beta} V_{\beta}(\mathbf{r} - \mathbf{R}_{\beta}), \quad (6.28)$$

only the components sitting on atom α contribute to its forces

$$\frac{\partial V_H}{\partial \mathbf{R}_\alpha} = \frac{\partial}{\partial \mathbf{R}_\alpha} V_{\alpha}(\mathbf{r} - \mathbf{R}_{\alpha}) = -\nabla V_{\alpha}(\mathbf{r} - \mathbf{R}_{\alpha}). \quad (6.29)$$

The Exchange-Correlation Energy

Assuming here a local-density approximation of the exchange-correlation functional yields the corresponding force term which is given in the non-polarized case by

$$-\frac{\partial E_{\text{XC}}}{\partial \mathbf{R}_\alpha} = - \int d\mathbf{r} \frac{\partial \rho(\mathbf{r})}{\partial \mathbf{R}_\alpha} \left(\epsilon_{\text{XC}}(\rho(\mathbf{r})) + \rho(\mathbf{r}) \frac{\partial \epsilon_{\text{XC}}}{\partial \rho(\mathbf{r})} \right) \quad (6.30)$$

$$= -2 \sum_i f_i \left\langle \frac{\partial \phi_i}{\partial \mathbf{R}_\alpha} \middle| V_{\text{XC}}(\mathbf{r}) \middle| \phi_i \right\rangle. \quad (6.31)$$

6. Energy Derivatives in FHI-aims

In the spin-polarized case the expression is completely analogous

$$-\frac{\partial E_{\text{XC}}}{\partial \mathbf{R}_\alpha} = -2 \sum_{i\sigma} f_{i\sigma} \left\langle \frac{\partial \phi_{i\sigma}}{\partial \mathbf{R}_\alpha} \left| V_{\text{XC}}^\sigma(\mathbf{r}) \right| \phi_{i\sigma} \right\rangle. \quad (6.32)$$

The Electron-Nuclei Energy

The electrostatic energy between the electrons and nuclei yields another force contribution

$$-\frac{\partial E_{\text{ext}}}{\partial \mathbf{R}_\alpha} = - \int d\mathbf{r} \frac{\partial \rho(\mathbf{r})}{\partial \mathbf{R}_\alpha} V_{\text{Ne}}(\mathbf{r}) - \int d\mathbf{r} \rho(\mathbf{r}) \frac{\partial V_{\text{Ne}}}{\partial \mathbf{R}_\alpha} \quad (6.33)$$

$$= -2 \sum_{i\sigma} f_{i\sigma} \left\langle \frac{\partial \phi_{i\sigma}}{\partial \mathbf{R}_\alpha} \left| V_{\text{Ne}}(\mathbf{r}) \right| \phi_{i\sigma} \right\rangle - Z_\alpha \int d\mathbf{r} \rho(\mathbf{r}) \frac{\mathbf{R}_\alpha - \mathbf{r}}{|\mathbf{R}_\alpha - \mathbf{r}|^3}. \quad (6.34)$$

The Nuclei-Nuclei Energy

The electrostatic forces between the nuclei are trivially given by

$$-\frac{\partial E_{\text{NN}}}{\partial \mathbf{R}_\alpha} = -Z_\alpha \int d\mathbf{r} \rho(\mathbf{r}) \frac{\mathbf{R}_\alpha - \mathbf{r}}{|\mathbf{R}_\alpha - \mathbf{r}|^3}. \quad (6.35)$$

The Normalization Constraint

Finally the constraint term in the Lagrange functional needs to be taken into account

$$\frac{\partial}{\partial \mathbf{R}_\alpha} \sum_{i\sigma} f_{i\sigma} \epsilon_{i\sigma} (\langle \phi_{i\sigma} | \phi_{i\sigma} \rangle - 1) = 2 \sum_{i\sigma} f_{i\sigma} \left\langle \frac{\partial \phi_{i\sigma}}{\partial \mathbf{R}_\alpha} \left| \epsilon_{i\sigma} \right| \phi_{i\sigma} \right\rangle. \quad (6.36)$$

6.1.2. The Atomic Forces in the Case of LSD

Summing up the above derivative contributions Eqs. (6.15), (6.15), (6.25), (6.27), (6.32), (6.33), (6.35) and (6.36) finally results in a total force acting on atom α

$$\mathbf{F}_\alpha = \mathbf{F}_{\text{HF},\alpha} + \mathbf{F}_{\text{Pulay},\alpha} + \mathbf{F}_{\text{MP},\alpha}. \quad (6.37)$$

These so-called *Hellman-Feynman* forces \mathbf{F}_α correspond to the classical forces by embedding each nucleus into the field of the electronic charge density and of all other nuclei [94, 95]

$$\mathbf{F}_{\text{HF},\alpha} = Z_\alpha \sum_{\beta \neq \alpha} Z_\beta \frac{\mathbf{R}_\alpha - \mathbf{R}_\beta}{|\mathbf{R}_\alpha - \mathbf{R}_\beta|^3} - Z_\alpha \int d\mathbf{r} \rho(\mathbf{r}) \frac{\mathbf{R}_\alpha - \mathbf{r}}{|\mathbf{R}_\alpha - \mathbf{r}|^3}. \quad (6.38)$$

The *Pulay* forces $\mathbf{F}_{\text{Pulay},\alpha}$ [96] result from the dependency of the basis functions on the nuclear coordinates and are given by

$$\mathbf{F}_{\text{Pulay},\alpha} = -2 \sum_{i\sigma} \left\langle \frac{\partial \phi_{i\sigma}}{\partial \mathbf{R}_\alpha} \left| \hat{h}^{\text{KS}} - \epsilon_{i\sigma} \right| \phi_{i\sigma} \right\rangle, \quad (6.39)$$

This term vanishes in case of a complete Hilbert space spanned by the basis functions, because then the approximated eigenvalues $\epsilon_{i\sigma}$ would be the exact eigenvalues of \hat{h}^{KS} and $(\hat{h}^{\text{KS}} - \epsilon_{i\sigma}) |\phi_{i\sigma}\rangle$ would therewith vanish. In practice, however, this is basically never the case and for reasonable basis set sizes, this term is mandatory. Furthermore, in case of basis sets which do not depend upon the nuclear coordinates, like e.g. plane waves, this term would vanish as well because then the nuclear gradients of the Kohn-Sham orbitals are zero.

6.1.3. The GGA-Correction Term

In the GGA-functional suggested by Perdew, Burke and Ernzerhof, the exchange-correlation functional possesses the following functional form

$$E_{\text{XC}} = \int d\mathbf{r} \rho(\mathbf{r}) \epsilon_{\text{XC}}(\rho^\uparrow, \rho^\downarrow, |\nabla \rho|^2). \quad (6.40)$$

Taking the derivative thus yields an additional term that arises due to the square of the charge density gradient

$$\frac{\partial E_{\text{XC}}}{\partial \mathbf{R}_\alpha} = \frac{\partial E_{\text{XC,LSD}}}{\partial \mathbf{R}_\alpha} + \int d\mathbf{r} \rho(\mathbf{r}) \frac{\partial \epsilon_{\text{XC}}}{\partial |\nabla \rho|^2} \frac{\partial |\nabla \rho|^2}{\partial \mathbf{R}_\alpha}, \quad (6.41)$$

so another contribution to the overall forces is given by

$$\mathbf{F}_{\text{GGA}} = - \int d\mathbf{r} \rho(\mathbf{r}) \frac{\partial \epsilon_{\text{XC}}}{\partial |\nabla \rho|^2} \frac{\partial |\nabla \rho|^2}{\partial \mathbf{R}_\alpha}. \quad (6.42)$$

The calculation of the nuclear gradient of the square of the density gradient can be further broken down to

$$\frac{\partial |\nabla \rho|^2}{\partial \mathbf{R}_\alpha} = 2 (\nabla \rho)^\text{T} \frac{\partial \nabla \rho}{\partial \mathbf{R}_\alpha}, \quad (6.43)$$

Since $\nabla \rho(\mathbf{r}) = 2 \sum_{i\sigma} \nabla \phi_{i\sigma}(\mathbf{r}) \cdot \phi_{i\sigma}(\mathbf{r})$, the calculation of the matrix $\partial \nabla \rho(\mathbf{r}) / \partial \mathbf{R}_\alpha$ yields

$$\frac{\partial \nabla \rho(\mathbf{r})}{\partial \mathbf{R}_\alpha} = 2 \sum_{i\sigma} \left(\frac{\partial \nabla \phi_{i\sigma}(\mathbf{r})}{\partial \mathbf{R}_\alpha} \cdot \phi_{i\sigma}(\mathbf{r}) + \nabla \phi_{i\sigma}(\mathbf{r}) \cdot \left(\frac{\partial \phi_{i\sigma}(\mathbf{r})}{\partial \mathbf{R}_\alpha} \right)^\text{T} \right), \quad (6.44)$$

where the second term corresponds to an outer product between two vectors thus giving a matrix. Analogous to the nuclear gradients of the orbitals that can be expressed in terms of the spatial gradients of the basis functions, the derivatives of the spatial gradient of the Kohn-Sham orbitals $\partial \nabla \phi_{i\sigma}(\mathbf{r}) / \partial \mathbf{R}_\alpha$ can be boiled down to the spatial Hessians of the basis functions $\nabla^2 \phi_j$.

6.1.4. The Atomic Forces in Connection with Smearing Methods

If an electronic smearing method is used to accelerate the convergence of the self-consistency cycle, the Lagrange functional is extended to another constraint to conserve the number of electrons

$$E_{\text{tot}} = \min_{\{c_{i\sigma,j}\}} \left(E^{\text{KS}} - \sum_{i\sigma} f_{i\sigma} \epsilon_{i\sigma} (\langle \phi_{i\sigma} | \phi_{i\sigma} \rangle - 1) - \mu \left(\sum_{i\sigma} f_{i\sigma} - N_{\text{el}} \right) \right) \quad (6.45)$$

$$= E_{\text{tot}} [\{c_{i\sigma,j}\}, \{\mathbf{R}_\alpha\}, \{f_{i\sigma}\}] , \quad (6.46)$$

with μ being the chemical potential. It can be shown that the total energy is then not a variational quantity with respect to the partial occupancies [75]. Hence, the total derivative of the total energy does not reduce to the partial derivative as in the case without electronic smearing

$$\mathbf{F}_\alpha = - \frac{dE_{\text{tot}}}{d\mathbf{R}_\alpha} \quad (6.47)$$

$$= - \frac{\partial E_{\text{tot}}}{\partial \mathbf{R}_\alpha} - \sum_{i\sigma,j} \underbrace{\frac{\partial E_{\text{tot}}}{\partial c_{i\sigma,j}}}_{=0} \frac{\partial c_{i\sigma,j}}{\partial \mathbf{R}_\alpha} - \sum_{i\sigma} \underbrace{\frac{\partial E_{\text{tot}}}{\partial f_{i\sigma}}}_{\neq 0} \frac{\partial f_{i\sigma}}{\partial \mathbf{R}_\alpha} . \quad (6.48)$$

To obtain a variational quantity, one needs to consider the electronic *free energy* F

$$F = E - \sum_{i\sigma} w S(f_{i\sigma}) , \quad (6.49)$$

with a corresponding entropy term S . Using Gaussian smearing, the entropy is e.g. given by

$$S = \frac{1}{2\sqrt{\pi}} \exp \left(- \left(\frac{\epsilon_{i\sigma} - \mu}{w} \right)^2 \right) . \quad (6.50)$$

It can be shown that the free energy is therewith variational [75]. Since the entropy correction does not depend upon the variational parameters $\{c_{i\sigma,j}\}$, the corresponding partial derivatives of the free and total energy are identical. Hence, it follows that

$$\mathbf{F}_\alpha = - \frac{\partial F}{\partial \mathbf{R}_\alpha} . \quad (6.51)$$

As a result, the atomic forces are no longer consistent with the total energy but with the free energy which therefore needs to be used for a local structural relaxation scheme.

6.1.5. Grid Effects

The integrals to calculate the total energy and therewith the atomic forces are not calculated exactly, but approximated by a discrete sum according to Eq. (5.30)

$$I = \int d\mathbf{r} f(\mathbf{r}, \{\mathbf{R}_\alpha\}) \quad (6.52)$$

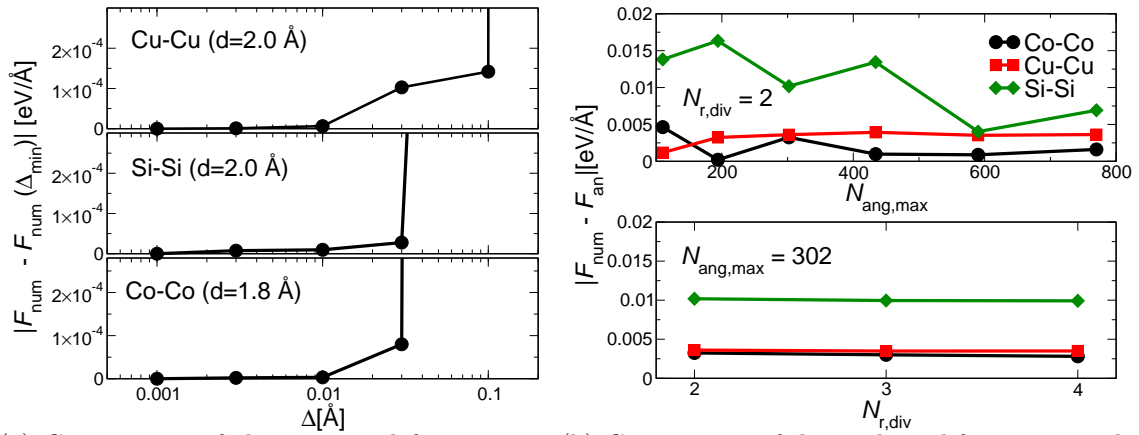
$$\approx \sum_\alpha \sum_{\mathbf{r}_{i\alpha}} w_{\mathbf{r}_{i\alpha}}(\mathbf{R}_\alpha) f(\mathbf{r}_{i\alpha}, \{\mathbf{R}_\alpha\}) . \quad (6.53)$$

Since the integration weights depend upon the atomic coordinates, they need to be taken into account explicitly for an exact derivative of the numerically evaluated total energy

$$\frac{\partial I}{\partial \mathbf{R}_\alpha} = \sum_\alpha \sum_{\mathbf{r}_{i\alpha}} w_{\mathbf{r}_{i\alpha}} \frac{\partial f}{\partial \mathbf{R}_\alpha} + \sum_\alpha \sum_{\mathbf{r}_{i\alpha}} \frac{\partial w_{\mathbf{r}_{i\alpha}}}{\partial \mathbf{R}_\alpha} f . \quad (6.54)$$

Hence, each integration term in the forces yields an additional correction term to capture the grid derivatives. This term can in principle be evaluated as the integration weights are given by a simple analytical formula. The actual calculation represents, however, a computational burden. Fortunately, grid effects are known to be negligible for grid densities used in practice [85] and turn out to play no role for the cases of the present work as well (see section 6.2).

6.2. Consistency of the Forces



(a) Convergence of the numerical forces w.r.t. the step width Δ instancing Cu_2 , Si_2 and Co_2 integration grid instancing Cu_2 , Si_2 and Co_2 for non-equilibrium bond-distances. Depicted are the differences in the numerical forces with respect to the smallest displacement applied $\Delta_{\text{min}} = 10^{-2}$ Å. The upper panel presents the convergence w.r.t. $N_{\text{ang,max}}$ with fixed $N_{\text{r,div}}$. In the lower panel, $N_{\text{ang,max}}$ is kept fixed to check the convergence w.r.t. the $N_{\text{r,div}}$.

Figure 6.1.: Accuracy test of the analytical forces.

We illustrate the accuracy of the analytical atomic forces implemented in FHI-aims by a comparison with numerical forces obtained by the finite difference scheme for some

non-equilibrium dimers as test cases. Since the numerical forces can in principle be evaluated up to any desired accuracy by choosing a sufficiently small step width, it serves as a reliable reference value for the analytical forces. Caution is advised when converging the numerical force with respect to Δ , though. Since the integration is done on a discrete grid, a too small displacement might result in noise, thus yielding an unreasonable numerical force. Fig. 6.1(a) presents the convergence test for Δ for some non-equilibrium dimers of the species treated in the present work using a converged tier2 basis set. The numerical forces are hereby obtained by a finite difference scheme of sixth order (see Appendix D). The results clearly show that for all test cases, the numerical force is converged within $O(10^{-5})$ eV/Å at a step width of $\Delta = 0.01$ Å, thus providing a sufficiently accurate reference value. With the optimized step width, the convergence of the analytical force with respect to the integration grid is then investigated. The results are presented in Fig. 6.1(b). For Cu_2 and Co_2 , the accuracy is within $O(10^{-3})$ eV/Å and seems to be independent of the chosen integration grid. Hence in these cases, grid effects seem to play no role. In the case of Si_2 , the agreement between analytical and numerical force is slightly worse and seems to be improved by augmenting the grid, indicating small grid effects. However, the difference is at most 10^{-2} eV/Å for even the smallest integration grid and therewith negligible. Since a typical force convergence criterium for a local relaxation scheme is 10^{-2} eV/Å, such an accuracy is sufficient. Figure 6.2 illustrates this at a local relaxation of the ground-state isomers of Si_7 , Si_{10} and Cu_7 . In all three cases, the change of the atomic configuration was only in the order of 10^{-3} Å at that force convergence level and therewith sufficiently converged.

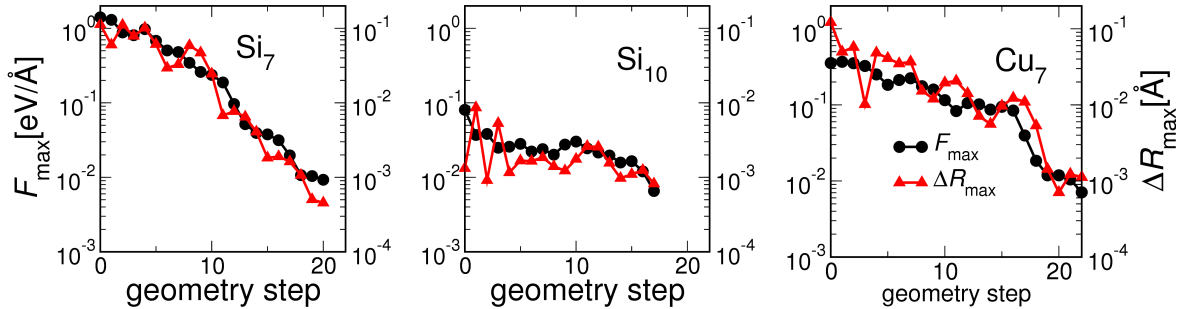


Figure 6.2.: Local relaxations for the ground-state isomers of Si_7 , Si_{10} and Cu_7 with BFGS and PBE-DFT. Plotted are the maximum force component F_{max} and maximum displacement ΔR_{max} of the atomic geometry vs. the geometry step.

6.3. The Second Energy Derivative

The vibrational analysis, in particular the calculation of the IR-spectra in chapter III, necessitates the knowledge of the Hessian matrix, i.e. the second energy derivative with respect to the atomic positions. The Hessian matrix of the total energy can be obtained by taking the total derivative of the forces. Contrary to the total energy, the

atomic forces are not a variational quantity, though. Hence the total derivative does not reduce to the partial derivative, thus making a direct evaluation of the analytical Hessian impossible

$$\frac{dE_{\text{tot}}}{d\mathbf{R}_\alpha d\mathbf{R}_\beta} = -\frac{d\mathbf{F}_\alpha}{d\mathbf{R}_\beta} \quad (6.55)$$

$$= -\frac{\partial \mathbf{F}_\alpha}{\partial \mathbf{R}_\beta} - \sum_{i\sigma,j} \underbrace{\frac{\partial \mathbf{F}_\alpha}{\partial c_{i\sigma,j}}}_{\neq 0} \frac{\partial c_{i\sigma,j}}{\partial \mathbf{R}_\beta}. \quad (6.56)$$

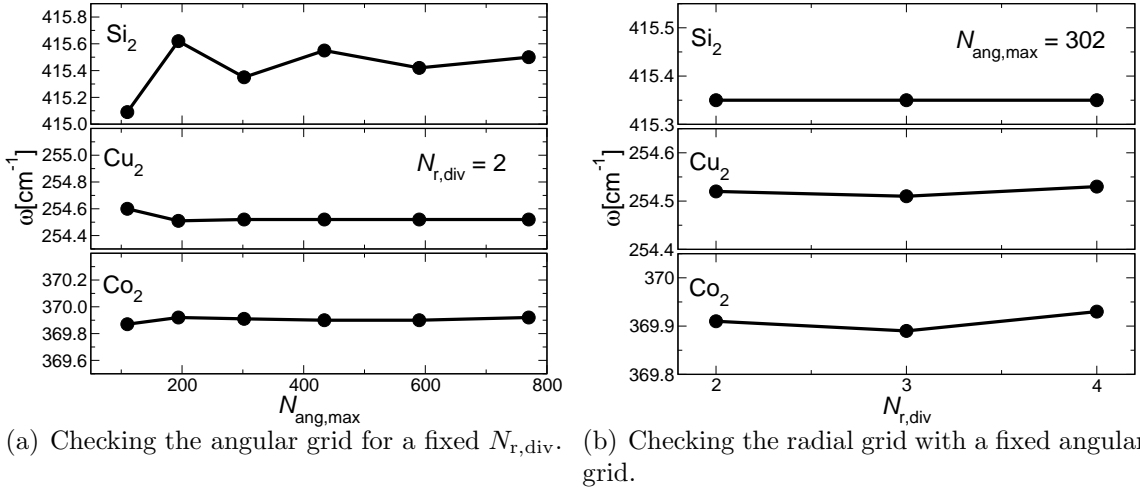


Figure 6.3.: Convergence of the vibrational frequency w.r.t. to the integration grid instancing Cu₂, Si₂ and Co₂.

In the present work the Hessian is therefore obtained by taking numerical derivatives of the analytical forces. Since the vibrational analysis is only a post-processing step done at the local minimum, the additional computational burden due to the displacements remains small for the cluster sizes considered in the present work. Fig. 6.4 shows the vibrational frequencies for some dimers at their equilibrium bond distance with respect to different finite displacements Δ using a converged basis set tier2. Like in the case of numerical forces, the frequencies can clearly be converged

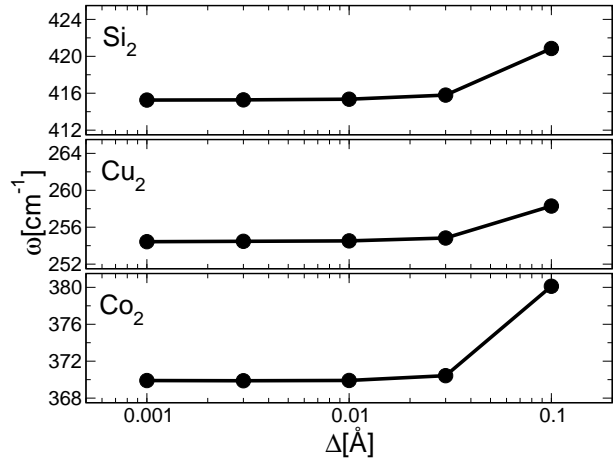


Figure 6.4.: Convergence of the vibrational frequency w.r.t. the step width Δ instancing Cu₂, Si₂ and Co₂.

6. Energy Derivatives in *FHI-aims*

with respect to Δ in all cases and grid effects play no role. With a displacement of $\Delta = 0.01 \text{ \AA}$, the convergence with respect to the integration grid was explicitly checked and summarized in Fig. 6.3. In all cases, even for the silicon dimer with a considerably higher inaccuracy in the atomic forces, the vibrational frequencies are converged below 1 cm^{-1} and are therefore more than accurate enough for the requirements of the ensuing applications. It is worth to point out that the high accuracy of the atomic forces and the vibrational frequencies shown above of course only indicates a high consistency between the calculated derivatives and the underlying energy surface. If the latter describes the system poorly, the forces and vibrational frequencies are equally unphysical.

Part III.

Nature of Ar Bonding to Small Co_n^+ Clusters and its Effect on the Structure Determination by Far-Infrared Absorption Spectroscopy

7. The Vibrational Fingerprint of Small Co_n^+ Clusters and their Ar Complexes

7.1. Introduction

The determination of atomic cluster structures constitutes a nice example of a mutual support between experiment and theory. In case of a pure computational treatment of the problem, there is never a guarantee to find the global minimum or all relevant higher-lying isomers, regardless how sophisticated the sampling scheme is designed. Furthermore, for the cluster size range of interest, where highly accurate quantum chemical methods become prohibitively expensive, there is no systematic way to converge the quality of the energetics. As a consequence, a poor description of the underlying PES might yield wrong isomers. Experimentally, it is impossible to directly measure the atomic structure but only quantities that are correlated with the underlying configuration. Theory is therefore required to interpret the measured data by simulating the experiment based upon putative cluster structures. If the computed and measured data match, the candidate structure can be considered as confirmed.

Experimentally, obtaining information on the atomic arrangement of such small clusters in the gas phase remains a challenge. Investigations of the reactivity of metal clusters with small molecules, in particular their saturation behaviour, have been used to draw conclusions about the clusters atomic arrangements [97]. Photoelectron spectroscopy provides direct information on the electronic structure of clusters which can be related to their geometries [98]. Information on the shape of cluster ions can be obtained from ion mobility measurements [99, 100, 101] and, recently, electron diffraction of trapped charged clusters has shown to be promising for revealing their structure [102, 103, 104]. Another possibility that is particularly sensitive to the internal cluster structure is the measurement of vibrational frequencies. A corresponding technique that has recently been successfully employed to determine the structure of cationic and neutral metal clusters containing between three and 20 atoms is far-infrared (vibrational) resonance enhanced multiple photon dissociation (FIR-MPD) spectroscopy [1, 2, 3, 4, 5]. The essential idea of this technique is to irradiate rare-gas complexes of the targeted clusters with infrared (IR) light in the range of the structure-specific vibrational fundamentals. When the IR light is resonant with a vibrational mode in the cluster complex, the complex can absorb several photons and subsequently evaporate off one or more rare-gas atoms. Recording the resulting abundance changes of the rare-gas complexes

as a function of the IR frequency yields the desired spectra that can then be compared to computed IR absorption spectra for different isomer structures obtained e.g. using density-functional theory (DFT). As long as different isomers exhibit distinct vibrational fingerprint patterns this then enables a unique determination of the atomic structure.

Performing the measurements on the rare-gas metal complexes, a fundamental assumption behind this approach is that the rare-gas atoms do not significantly influence the vibrational spectrum and merely act as a probe for detecting the resonant absorption of IR photons by the metal cluster [105]. A negligible influence of the employed rare-gas atoms was indeed inferred from only insignificant differences in the IR spectra of previously studied cationic V_n^+ ($n = 3 - 23$) [1, 2], Nb_n^+ ($n = 5 - 9$) [3, 4] and Ta_n^+ ($n = 6 - 20$) [5] complexes that contained one or more Ar atoms. Restricted test calculations comparing the IR spectra of bare and Ar-complexed V_3^+ and V_4^+ clusters led to the same conclusion [1, 2], so that the ensuing theoretical modeling for the mentioned systems focused exclusively on the IR spectra of the bare metal clusters.

The situation is markedly different for small cationic Co clusters. Here, the measured FIR-MPD spectra show an intriguing dependence on the number of adsorbed Ar atoms, which is strongest for clusters containing less than six cobalt atoms. The motivation for this work is therefore to investigate on the nature of the Ar-Co_n^+ bond and its implications for the vibrational spectra instancing the series Co_4^+ to Co_8^+ . Among the sampling algorithms presented in chapter 3, basin-hopping was chosen in a spin-extended version to sample both the configurational and spin space on an equal footing. Additionally, the Ar probe atom was explicitly taken into account, thus identifying the Ar-binding sites in a completely unbiased way. In this chapter, the comparisons of the computed IR spectra with the measured data are presented, which allow in some cases for a unique assignment of the experimental cluster structure. The calculations reveal furthermore a characteristic increase of the Ar binding energy for the smaller clusters, rationalizing the observed increased influence of the Ar probe atoms on the IR spectra.

In the next chapter, the binding energy trend is further analysed and traced back to the predominant contribution to the Ar-Co_n^+ bond arising from the polarization of the rare-gas atom in the electrostatic field of the cationic cluster. This motivates a simple electrostatic model, that not only reproduces the binding energy trend, but also explains why the interaction of Ar is much stronger than in the previously studied systems, where little influence of the probe atoms on the vibrational spectra had been observed.

7.2. Far-Infrared Absorption Spectroscopy

7.2.1. Experimental Setup

The experiments were carried out in the group of Prof. Gerard Meijer at the Molecular Physics Department of the FHI. They employed a molecular-beam setup [2, 4, 105] that is coupled to a beam line of the Free Electron Laser for Infrared eXperiments (FELIX) at the FOM-Institute for Plasma Physics in Nieuwegein, The Netherlands [106]. Metal clusters were produced by pulsed laser ablation of a cobalt rod using the 2nd harmonic

output of a Nd:YAG laser and by subsequent condensation of the plasma in a mixture of Ar in He. Neutral, anionic, and cationic clusters were produced in this process and passed through a temperature controllable copper channel. Only cationic clusters were investigated in this study. Two different experimental conditions had been used. With a mixture of 0.1 % Ar in He at liquid-nitrogen-temperature, clusters containing six or more cobalt atoms bound one and to a much lesser degree two argon atoms. At the same conditions small clusters up to Co_5^+ formed complexes with up to five argon ligands. At a higher temperature of 340 K and using a mixture of 0.3 % Ar in He no attachment to bigger cobalt clusters was observed, whereas Co_4^+ and Co_5^+ added one and two rare-gas atoms which is in line with similar observations by Minemoto *et al.* [107].

The molecular beam expanded into vacuum and passed through a skimmer and an aperture before entering the extraction region of a reflectron time-of-flight mass spectrometer. A counter-propagating pulsed far-IR laser beam delivered by FELIX was overlapped with the aperture to ensure that all species in the beam that were detected in the mass spectrometer had been exposed to the IR radiation. The laser pulse consisted of a 1 GHz train of ps-duration micropulses. The duration of such a macropulse is several μs while its energy ranged typically between 15 and 30 mJ, depending on the wavelength. When the IR radiation is resonant with an IR-allowed transition of the cluster complex, sequential absorption of single photons can take place [108]. The resulting heating of the cluster may induce evaporation of the argon atoms, which leads to depletion of the complexes in the beam. IR depletion spectra were constructed by recording the ion intensities of the metal argon complexes as a function of the FELIX frequency; from these, the far-infrared absorption spectra were obtained as described in ref. [105]. As the detection is mass selective, the simultaneous measurement of far-IR spectra for different cluster sizes is possible.

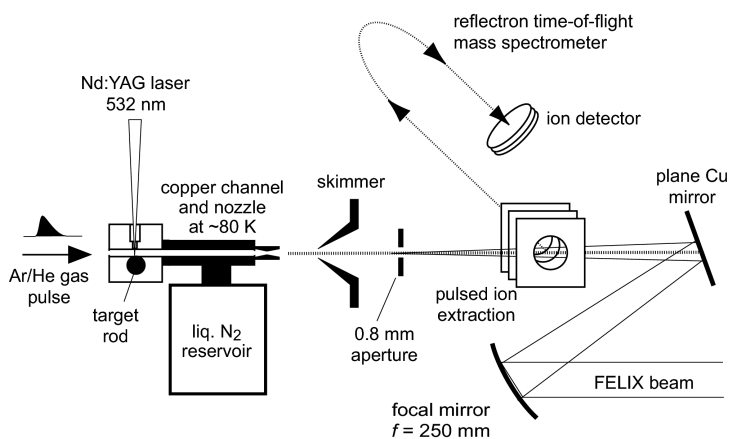


Figure 7.1.: Scheme of the experimental set-up used for IR multiple photon dissociation of metal cluster-rare gas complexes.

7.2.2. Observation of Highly Coordinated Co_n^+Ar_m Complexes

For both employed complex formation conditions (77 K/0.1% Ar vs. 340 K/0.3% Ar) the recorded mass spectra of the cationic cobalt-argon complexes reveal profound differences in the binding of the rare-gas ligands to clusters containing more or less than six atoms. As shown in Fig. 7.2, at the low-temperature conditions, in which the bigger clusters

bind only one or at maximum two Ar atoms, Co_4^+ and Co_5^+ readily attach up to five ligands. The affinity of these small clusters to the rare-gas atoms is so pronounced that they still form complexes with one or two Ar atoms even at a temperature as high as 340 K. This change of the interaction with the probe atoms with cluster size is also reflected in the obtained FIR-MPD spectra, which were measured in the range 75-350 cm^{-1} with no IR absorption bands detected at higher wavenumbers. The spectra show an intriguing dependence on the number of adsorbed Ar atoms, which is strongest for the smallest clusters and is essentially lost for clusters of more than seven atoms.

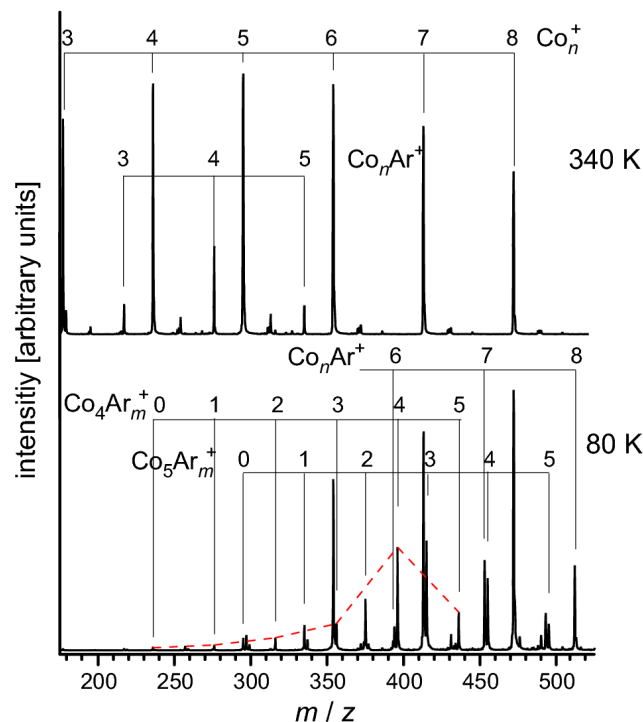


Figure 7.2: Distribution of cationic cobalt clusters and their Ar complexes obtained at source temperatures of 340 K (top) and 80 K (below). At the higher temperature rare gas complexes are only observed up to Co_5^+ , whereas at low temperature also larger clusters attach Ar and the small clusters bind multiple Ar atoms. The dashed red line in the lower plot connects the maxima of the Co_4Ar_m^+ peaks.

7.2.3. Interpretation of FIR-MPD Spectra

Compared to linear absorption spectra, FIR-MPD spectra are known to be subject to distortions, such as an incomplete fragmentation of complexes containing more rare-gas atoms and (cross)anharmonicities in the multiple photon excitation process [105]. For the prior effect one has to keep in mind that there is no mass selection before the fragmentation of a certain complex. The spectrum of a given complex thus contains both a contribution from the depletion due to evaporation of the argon ligand as well as an increase in intensity due to incomplete fragmentation of complexes containing more argon ligands. This can lead to missing bands especially at the low-frequency end of spectra and is avoided by considering only the spectra of a certain cluster size with the maximum number of argon ligands. The effect of (cross)anharmonicities is instead rather to change the width and positions of existing lines. Corresponding effects have been observed in preceding work on cationic V_n^+ ($n = 3 - 23$) [1, 2], Nb_n^+ ($n = 5 - 9$)

[3, 4] and Ta_n^+ ($n = 6 - 20$) [5] complexes. However, the influence of the rare-gas atoms was typically small, with only minor shifts of the frequencies of the absorption bands of the order of a few cm^{-1} and with the relative intensities of the observed bands barely affected. This situation is markedly different in the case of the small cationic Co clusters, where the spectra from different Ar containing complexes exhibit much more pronounced frequency shifts and rather strong changes in the relative intensities, cf. Figs. 7.6 and 7.7 below.

7.3. Computational Details

The DFT calculations are carried out using the all-electron full-potential code **FHI-aims** [11], described in part II, and the generalized gradient approximation (GGA-PBE) [70] to describe electronic exchange and correlation (xc). For comparison, some calculations are also performed using the local density approximation (PW-LDA) [69]. All calculations reported here are done with the “tier2” basis set which contains 67 and 45 basis functions for Co and Ar, respectively and are further detailed in Appendix A. As integration grids, we used $N_{\text{r,div}} = 2$, corresponding to 158 and 140 radial shells for Co and Ar, respectively. The angular grid is found to be converged for $N_{\text{ang,max}} = 302$ with a fixed $N_{\text{ang,min}} = 110$. The cut-off radius was conservatively chosen with $r_{\text{cut}} = 5 \text{ \AA}$ for both species, as well as the maximum angular momentum in the multipole decomposition l_{max} with a value of 6. Convergence tests focused on the D_{2d} ground state ($S=7/2$) and the higher-lying D_{2h} isomer ($S=9/2$) of Co_4^+Ar as well as the D_{3d} ground state ($S=15/2$) and higher-lying C_{2v} isomer ($S=13/2$) of Co_6^+Ar (*vide infra*), and are given in detail in the Appendix B. Using the hierarchically constructed larger basis sets provided in **FHI-aims**, as well as denser integration grids, we recomputed the relaxed geometric structure and vibrational spectra of the isomers, as well as their energetic difference

$$\Delta E = E_{\text{tot}}(\text{isomer1}) - E_{\text{tot}}(\text{isomer2}) , \quad (7.1)$$

and the Ar binding energy

$$E_{\text{b}} = E_{\text{tot}}(\text{Co}_n^+\text{Ar}) - E_{\text{tot}}(\text{Co}_n^+) - E_{\text{tot}}(\text{Ar}) , \quad (7.2)$$

and found these quantities to be converged within 0.01 \AA , 2 cm^{-1} and 10 meV , respectively, which is fully sufficient for the arguments and conclusions put forward below. Furthermore, no electronic smearing method as described in section 5.1.1 was required to achieve self-consistency. All calculated results are therefore based upon an undistorted energy surface.

7.3.1. Structural Relaxation and Calculation of the IR-Spectra

Local structural optimization is done using the Broyden-Fletcher-Goldfarb-Shanno method described in section 3.1.3 [27], relaxing all cartesian force components to smaller than 10^{-2} eV/\AA . After relaxation, the Hessian matrix is determined numerically by finite

7. The Vibrational Fingerprint of Small Co_n^+ Clusters and their Ar Complexes

displacements of all atomic positions by $\Delta = 10^{-3} \text{ \AA}$, and then diagonalized to get the vibrational modes. The corresponding infrared intensities are obtained by taking the derivative of the dipole moments along these modes [109]

$$I_i^{\text{IR}} = \frac{N_{\text{AV}}\pi}{3c} \left| \frac{d\mu}{d\mathbf{Q}_i} \right|^2, \quad (7.3)$$

where the derivatives along the eigenmodes can easily be obtained by the derivatives with respect to cartesian coordinates, the latter being calculated along the numerical calculation of the Hessian by finite displacements.

$$\frac{d\mu}{d\mathbf{Q}_i} = \sum_{\alpha} \frac{d\mu}{d\mathbf{R}_{\alpha}} \cdot \mathbf{Q}_{\alpha,i} \quad (7.4)$$

The influence of the force convergence criterium as well as the finite displacement Δ on the calculated quantities has been carefully tested. Details on the test calculations focusing on Co_4^+Ar and Co_6^+Ar are given in the Appendix B. In order to facilitate the visual comparison to the experiment, the resulting IR spectra are finally folded with a Gaussian line shape function of half-width 1 cm^{-1} .

7.3.2. The Counterpoise Correction to the Basis Set Superposition Error

As already mentioned in section 5.2, the numerical atom-centered basis sets prevent an atomic BSSE by construction, since the total energy of the free atom is already converged at the minimum basis set level and can therefore not be variationally improved by further basis functions originating from neighbouring atoms. In the case of the Ar binding energies, calculated according to Eq. (7.2), however, the reference energy is not exclusively constituted by free atoms, but partially by the total energy of the bare Co_n^+ cluster. Hence, it is *a priori* not clear, whether the neighbouring Ar basis functions improve the total energy of the bare cluster or not. To investigate on that, the counterpoise correction of quantum chemistry [110, 111] was applied to the four test isomers of Co_4^+Ar and Co_6^+Ar as

$$\Delta^{\text{CP}} = E_{\text{fragment}}^{\text{CP}}(\text{Co}_n^+) - E_{\text{fragment}}(\text{Co}_n^+). \quad (7.5)$$

To compensate for a potential BSSE, the total energies of the Co_n^+ fragments are hereby calculated using both the bare Co basis sets ($E_{\text{fragment}}(\text{Co}_n^+)$), and as additional *ghost* basis functions the Ar basis functions originating from an empty site at the position of the Ar atom in the Co_nAr^+ complex $E_{\text{fragment}}^{\text{CP}}(\text{Co}_n^+)$. In this context, “fragment” means that the Co_n^+ structure is cut out from the Ar complex without further relaxing it. The difference Δ^{CP} is then a measure for the variational improvement of the total energy due to the Ar basis functions which is responsible for the overestimation of the binding energy. Hence, the corrected binding energy is obtained by

$$E_b \longrightarrow E_b - \Delta^{\text{CP}}. \quad (7.6)$$

7. The Vibrational Fingerprint of Small Co_n^+ Clusters and their Ar Complexes

The results based upon the tier2 basis set for Co and Ar are summarized in Table 7.1. Clearly, the BSSE is below 10 meV and thus negligible at this basis set level. This conclusion is in line with ref. [11] and the counterpoise correction was therefore neglected in this work.

| | Δ^{CP} [eV] | |
|--------------------------|---------------------------|-------|
| Co_4^+Ar | D _{2d} | 0.005 |
| | D _{2h} | 0.005 |
| Co_6^+Ar | D _{3d} | 0.004 |
| | C _{2v} | 0.006 |

Table 7.1.: Corrections to the Ar binding energy due to the intermolecular BSSE.

7.3.3. Zero-Point Energy

Even at zero temperature, the total energy is increased by the zero-point energy resulting from the vibrational motion according to Eq. (2.36). In the calculation of the Ar binding energy, however, most of the zero point energy is expected to cancel in the difference $E_{\text{tot}}(\text{Co}_n^+\text{Ar}) - E_{\text{tot}}(\text{Co}_n^+)$, since the influence of the Ar on the vibrational spectra is rather small. The resulting differences in the zero point energies due to changes in the vibrational spectra are presented in Table 7.2 for the above introduced test systems. As already mentioned in the introduction, the influence of Ar on the vibrational spectrum increases with decreasing cluster size. Nevertheless, even the smallest isomer Co_4^+ only exhibits a correction to the binding energy of 12 meV. Therefore, zero-point corrections to the binding energies are negligible and are not considered in this work.

| | ΔE_{ZPE} [eV] | |
|--------------------------|------------------------------|-------|
| Co_4^+Ar | D _{2d} | 0.012 |
| | D _{2h} | 0.011 |
| Co_6^+Ar | D _{3d} | 0.007 |
| | C _{2v} | 0.008 |

Table 7.2.: Corrections to the Ar binding energy due to zero-point energy.

7.4. Selection of Structural Motifs by Spin-Extended Basin-Hopping

In order to identify energetically low-lying isomers all structures for the bare clusters were tested that had been discussed previously in the literature. For increasing cluster sizes this approach is likely to miss relevant geometries. This holds in particular for Co, where one has to expect several, differently Jahn-Teller distorted versions of the same structural motif. In addition, extended basin-hopping [35] runs have therefore been run to achieve a better sampling of configurational space as described in section 3.2.2.

As specific implementation so-called single-particle trial moves were chosen, in which a randomly picked atom is displaced in a random direction by a distance of 3.00 \AA (corresponding to 1.5 times the GGA-PBE computed Co dimer bond length). In order to prevent an entropy-driven dissociation of the cluster during the BH run, trial moves as well as local relaxations were discarded that generate loosely connected or partly dissociated structures characterized by an atom having a nearest-neighbour distance larger than twice the dimer bond length. Similarly discarded were moves that place atoms at distances of less than 0.5 \AA from each other.

In view of the specific electronic configuration of Co, the spin degree of freedom was furthermore included into the sampling procedure, i.e. after the trial atomic displacement the electronic self-consistency cycle was initiated with a random magnetic moment. For specific isomers this search was supplemented by fixed-spin moment calculations enforcing spin-states that had not been found in the BH runs. However, in almost all cases these states turned out not to be local minima of the spin hypersurface, suggesting that the chosen spin sampling in the BH runs yields the relevant spin minima. Equivalent BH runs were performed for the Co_n^+Ar_m complexes, randomly displacing both Ar and Co atoms. The most favourable structures determined by this completely unbiased treatment of the Ar probe atoms were always Co clusters with Ar adsorbed at a top site, with Ar-Co bond lengths that range for the most stable adsorption site from 2.45 \AA for the Co_4^+ ground state to 2.63 \AA for the most stable isomer of Co_8^+ .

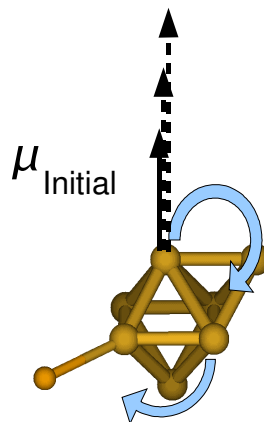


Figure 7.3.: The principle of the spin-extended basin-hopping method. Additional to a random displacement of the atomic positions, the initial spin moments sitting on each atom are randomly varied to allow the system to adopt different spin states.

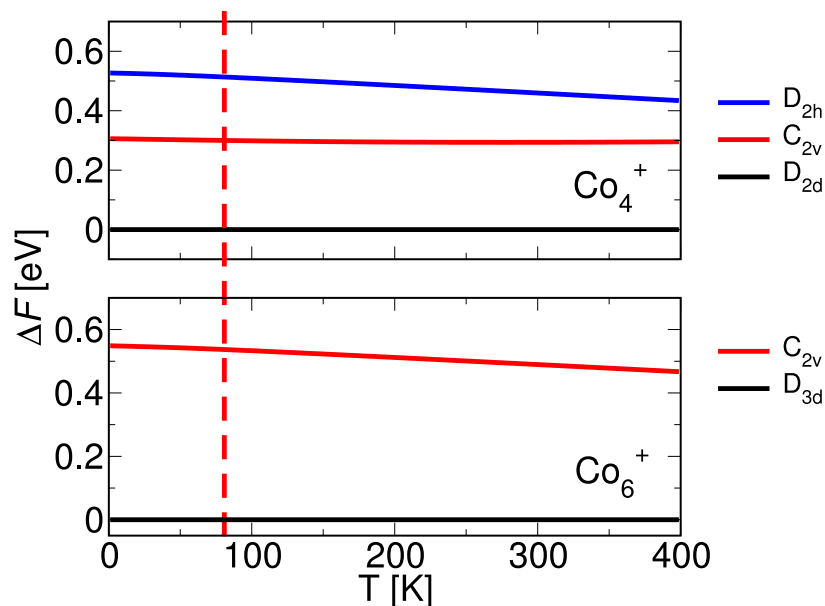


Figure 7.4.: Differences in the free energies of low-lying Co_4^+ and Co_6^+ isomers. The red dashed line depicts the temperature at which the presented IR spectra have been measured.

7.5. Thermodynamic Effects

Since the experiments were performed at finite temperatures, it can *a priori* not be ruled out that thermodynamic effects might change the energetic order of the isomers. Particularly, the vibrational frequencies and principal moments of inertia, determining both the vibrational and rotational contribution to the free energy, are sensitive to the atomic structure. The free energies according to Eq. (2.30) have therefore been calculated for the three Co_4^+ and two Co_6^+ isomers, discussed below, over a wide temperature range including the cryogenic temperature of $T=77$ K at which the measurements have been performed. As one can clearly see, the free energy differences do not change at all. We conclude that thermodynamic effects are insignificant for the present study and will no further be discussed.

7.6. The Influence of the Exchange-Correlation Functional

In general, there is little reason to expect that DFT with present-day local and semi-local xc functionals yields an accurate description of the intricate electronic structure of such small Co clusters. The difficulty of electronic structure calculations to properly account for the delicate balance between exchange and correlation, between magnetism and chemical bonding, and between populating *d* and *s* orbitals in these systems is al-

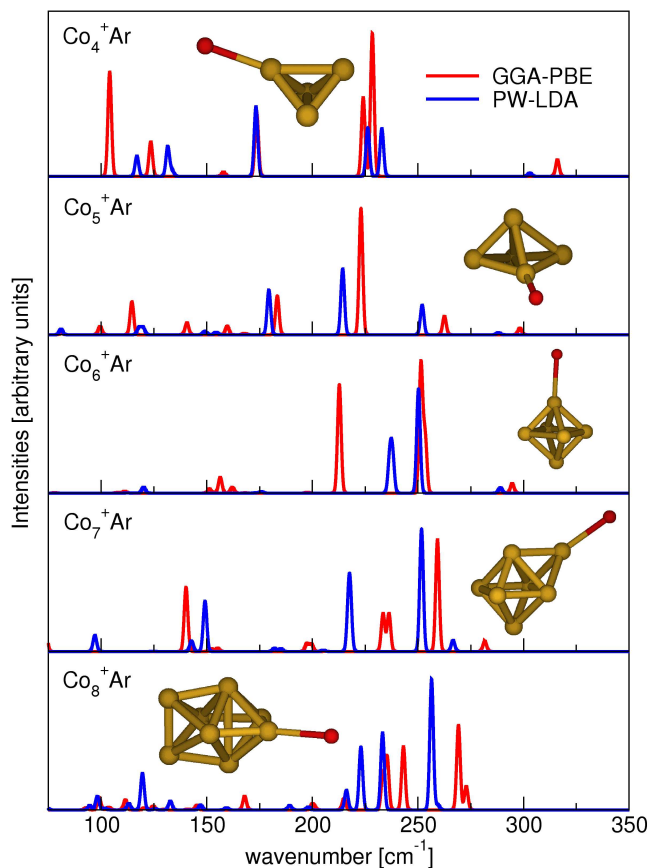


Figure 7.5.: Comparison of computed vibrational spectra of the identified most stable isomers of Co_4^+Ar to Co_8^+Ar and using the PW-LDA (blue line) or GGA-PBE (red line) functional. Applied is a common scaling factor, matching the main peak of the experimental Co_6^+Ar spectrum. See text and Figs. 7.6-7.10 below for a description of the different isomers.

ready well exemplified by the still controversial predictions of the true ground state of the neutral Co dimer (see e.g. ref. [112] and refs. therein). With respect to vibrational frequencies a common procedure to correct for some (systematic) errors due to an approximate xc treatment is to apply a general scaling factor to the calculated frequencies to bring the computed spectra in better agreement with the measured ones. The limitations of this approach for the cationic Co clusters is, however, well apparent from Fig. 7.5, which compiles the computed and scaled vibrational spectra of the identified most stable isomers of Co_n^+Ar complexes in the targeted size range (*vide infra*), and compares them to the corresponding spectra obtained using the PW-LDA functional. In light of the particularly controversial situation for the dimer, we did not follow the usual practice to determine the scaling factor from the comparison of the computed and experimental dimer vibrational frequency, but used the main peak of the simple fingerprint spectrum of Co_6^+Ar , cf. Fig. 7.8 below, instead. However, regardless of which reference is actually used, the validity of such a common scaling approach would have shown up in basically

identical spectra for all cluster sizes after scaling the PW-LDA and GGA-PBE data, which is obviously not the case.

In this situation, it makes little sense to strive for a quantitative agreement of the absolute frequencies when comparing the experimental to the theoretical spectra. Additionally considering the mentioned differences between linear IR absorption and FIR-MPD spectra, the best one can hope for is if at all a match between (relative) spacings between different peaks in the spectrum, or more modestly to identify some characteristic fingerprint pattern that is unique to a specific isomer and which would then allow for a structural assignment. It is within this perspective that we augment the detailed presentation of the low-lying isomers of Co_4^+ to Co_8^+ identified in the BH runs with a comparison of the computed and measured vibrational spectra of the corresponding Ar complexes. Despite the discussed limitations, we apply thereby a global scaling to the theoretical spectra simply to enable a better visual comparison. Using the main peak of the experimental Co_6^+Ar spectrum as reference, this yields a global scaling factor of 0.881 for GGA-PBE and 0.749 for PW-LDA, respectively.

7.7. Low-lying Isomers and Vibrational Spectra of their Ar Complexes

In the following, an overview of the putative ground-state structures and higher-lying isomers for the series Co_4^+Ar_m to Co_8^+Ar_m is given. For the sake of a concise overview, only a selection of the metastable structures is presented. Vibrational spectra have thereby been preferentially chosen that exhibit similar qualitative fingerprints, thus being candidate structures apart from the ground-state isomer, as well as completely different fingerprints, exemplifying identified isomers that can safely be ruled out. Shown are the spectra of the bare Co_n^+ -clusters together with their Co_n^+Ar -complexes, where the most stable binding site for the Ar is depicted. For the smaller cluster structures, where the experiment yielded complexes with several Ar atoms bound to the Co_n^+ cluster, the computational counterparts are additionally presented and discussed. An exhaustive overview of all calculated structures, including all different structural motifs, spin states, Jahn-Teller distortions, and binding sites for the Ar probe atoms, can be found in the Appendix E.

7.7.1. Co_4^+

The calculations for Co_4^+ reveal as most stable isomer structure a distorted tetrahedron with D_{2d} symmetry and a magnetic moment of $7\mu_B$. This still quite symmetric geometry has two (opposite) bonds of 2.50 \AA length, while the remaining four bonds are 2.17 \AA . The next lowest structure determined is already 0.32 eV higher in energy, has a magnetic moment of $9\mu_B$ and corresponds to an even further distorted tetrahedron, in which one bond is elongated to 2.90 \AA to yield a kind of butterfly geometry. Even further up in energy (0.53 eV) is the lowest-energy planar structure, with $9\mu_B$, a D_{2h} symmetry and bond lengths of 2.22 \AA and 2.38 \AA . The thus obtained energetic order is consistent with

the interpretation of photodissociation spectroscopy data favouring a three-dimensional structure for the cationic Co tetramer [107]. A corresponding preference for a pyramidal ground state was also obtained in earlier DFT calculations for neutral Co_4 clusters, albeit with a much smaller energetic difference to the lowest lying planar isomer [113, 114]. Theory predicts hence similar geometries for the neutral and cationic Co_4 ground state, which is in line with a corresponding interpretation derived from measured bond energy data [115].

From this quite consistent picture of the structural motif of the Co_4^+ ground state it is somewhat unexpected to achieve only a rather poor comparison of the computed vibrational spectra of its Ar complexes with the corresponding FIR-MPD measurements. Turning first to the experimental data shown in Fig. 7.6, pronounced differences are observed for the spectra derived from Co_4^+Ar , Co_4^+Ar_2 and Co_4^+Ar_5 . This concerns frequency shifts and changes in the relative intensities of a group of presumably three modes in the range $160\text{--}210\text{ cm}^{-1}$, as well as the appearance of a strong mode at 110 cm^{-1} and tentatively a small mode at 120 cm^{-1} only in the spectrum from the complex with five Ar atoms. As already mentioned, such apparent missing peaks at the low-frequency end of the spectrum from complexes having only one or two Ar atoms are not uncommon in FIR-MPD, and are generally ascribed to an incomplete fragmentation of complexes containing more rare-gas atoms [105]. The frequency shifts particularly of the central peak observed for the group at higher wavenumbers are, however, much stronger than those in preceding work on cationic clusters from group 5 of the Periodic Table [1, 2, 3, 4, 5]. The spectrum of the Co_4^+Ar_5 complex, however, cannot be affected by an incomplete fragmentation of complexes containing even more Ar ligands. From the relative abundances of Co_4^+Ar_4 and Co_4^+Ar_5 in the mass spectrum shown in Fig. 7.6 the latter complex is presumably best described as Co_4^+Ar_4 with an additional rather loosely bound Ar atom. Correspondingly, the spectrum derived from Co_4^+Ar_5 should give a most faithful representation of the vibrational frequencies of a Co_4^+Ar_4 complex.

The computed IR absorption spectra of the most stable D_{2d} isomer complexed with one or two Ar atoms reproduce the strong low-frequency mode observed in experiment quite well, cf. Fig. 7.6. Comparing to the also shown computed spectrum of the bare cluster it is furthermore clear that this agreement is only achieved because of the explicit consideration of the rare-gas atom(s) in the calculations. Only the unexpectedly strong binding of the Ar atom of 0.3 eV breaks the symmetry of the bare cluster and leads to the appearance of IR-active modes in the low-frequency range at all. This unusual strength of the Ar- Co_4^+ interaction prevails for up to four ligands, each time filling one of the top sites at the four corners of the pyramid. Presumably due to the lacking dispersive interactions in the semi-local xc functional, it was, however, not possible to reliably bind a fifth Ar atom to the cluster at the GGA-PBE level, which unfortunately prevents a direct comparison to the measured spectrum from the Co_4^+Ar_5 complex. Further complications in the experiment-theory comparison arise when turning to the higher-frequency group of bands in the experimental data. In contrast to the more or less evenly spaced three main peaks in this group, theory predicts a large spacing between one lower-energy peak and a higher-energy doublet. While the frequencies of the latter correspond quite well to the lower and higher frequency main peak of the experimental

group, either the central and dominant experimental peak is completely missing or the splitting of the doublet is significantly underestimated in the theoretical spectrum.

The calculated spectra of the second and third lowest-energy isomer also shown in Fig. 7.6 can neither achieve a better agreement with the experimental data, so that a significant population of a higher-energy isomer is not readily invoked as reason for the discrepancy. Two possible reasons for the discomforting disagreement between measured and computed data could be either an insufficient description provided by the employed GGA-PBE functional or strong (cross)anharmonicities in the experimental data, which could both particularly affect the splitting of the higher-energy doublet in the D_{2d} spectrum. The latter is very sensitive to the distortions of the pyramidal ground-state structure caused by Jahn-Teller effects [113] and the Ar bonding, both of which might not be sufficiently treated at the level of a semi-local xc functional. Simultaneously, one has to keep in mind, however, that the unusually strong Ar bonding in the complex that will be further discussed in the next chapter severely enhances the multiple photon excitation aspect of FIR-MPD, and makes the comparison to computed linear IR absorption spectra possibly less justified.

7.7.2. Co_5^+

For Co_5^+ we determine as most stable isomers three slightly differently distorted versions of a trigonal bipyramid that are all within a 0.06 eV energy range and possess all a magnetic moment of $10\mu_B$. The energetically highest of the three has still C_{2v} symmetry, while the other two are further Jahn-Teller distorted to C_1 symmetry by tilts of the apex Co atom away from the symmetry axis of the slightly folded rhombohedral base. In all three structures there are sets of shorter Co bonds of around $\sim 2.2 - 2.3 \text{ \AA}$ and more elongated bonds to the apex atom of the order of 2.5 \AA . A more symmetric C_{4v} tetragonal pyramid with $12\mu_B$ is found at 0.15 eV above the ground state, followed by the lowest-lying planar structure already at 0.81 eV. This strong preference for a distorted three-dimensional structure in a high-spin state is again similar to corresponding findings for the neutral pentamer [113, 114], further confirming that neutral and cationic Co clusters exhibit similar geometries [115]. The comparison of the computed IR absorption spectra to the FIR-MPD data is this time slightly more favourable. Figure 7.7 shows the corresponding data for one of the degenerate distorted tetragonal pyramids (the spectra of the other two differ only insignificantly), as well as for the more symmetric tetragonal pyramid and the planar structure. The measured spectra from Co_5^+Ar and Co_5^+Ar_5 complexes show comparable differences as in the case of the tetramer complexes: A peak at the low-frequency end of the spectrum is only observed for the complex containing more Ar atoms and a group of bands in the range $175\text{-}230 \text{ cm}^{-1}$ exhibits pronounced frequency shifts and intensity changes. From the overall shape one would expect at least three components behind this group and this indeed is what is found in this frequency range in the computed spectrum for the lowest-energy distorted pyramids. However, even though only containing two main peaks in this frequency range, the overall spectrum of the symmetric tetragonal pyramid isomer does also fit the experimental data rather well, so that we cannot safely discriminate between these two (in any case rather similar)

structures. What is instead quite clear from Fig. 7.7 is that the planar structure can not be reconciled with the measurements.

Due to the already severely distorted geometry of the bare ground state the influence of the rare-gas atom on the computed spectrum is less dramatic than in the case of the Co tetramer. Rather than leading to the appearance of a series of additional IR-active bands, its effect is more to shift existing peaks and change their intensities. With an again rather strong computed binding energy of around 0.3 eV this concerns primarily those modes that involve displacements in the direction of the Ar adsorbate. A particularly pronounced example of such a change in intensity is the computed mode at 260 cm^{-1} for the spectra from the Co_5^+Ar and Co_5^+Ar_5 complexes, in nice analogy to the variations observed in the corresponding experimental spectra.

7.7.3. Co_6^+

The two most stable determined isomers of Co_6^+ correspond to slightly distorted tetragonal bipyramids, with the lowest-energy structure exhibiting a magnetic moment of $15\mu_B$ and another one 0.10 eV higher with $13\mu_B$. Both structures possess D_{3d} symmetry and bond lengths around 2.3 Å. The third lowest-energy geometry is a capped trigonal bipyramid also with $13\mu_B$, but with 0.56 eV above the ground state this is already significantly higher in energy. With the DFT calculations for Co_6 by Datta *et al.* [114] also arriving at a tetragonal bipyramid ground state, the similarity between the structural motif of cationic and neutral clusters thus continues also for the hexamer.

The clear energetic preference for the tetragonal bipyramid motif is supported by the comparison of computed and experimental vibrational spectra. The FIR-MPD data is shown in Fig. 7.8 and exhibits this time only little differences between the measurements of Co_6^+Ar and Co_6^+Ar_2 complexes. In both cases the spectrum is simple and consists only of two peaks around 250 cm^{-1} . This pattern is fully reproduced in the calculated spectra for the two tetragonal bipyramids and certainly inconsistent with the computed spectrum for the capped trigonal bipyramid. In the case of the cationic hexamer theory therefore achieves an unambiguous assignment of the structural motif. Furthermore, the computed spectra for the identified ground-state structure either bare or with one or two Ar atoms shown in Fig. 7.8 are virtually identical. This is distinctly different to the findings for the smaller Co_n^+ clusters, and goes hand in hand with a significant reduction of the Ar bond strength, computed as 0.12 eV for the $15\mu_B$ ground-state tetragonal bipyramid.

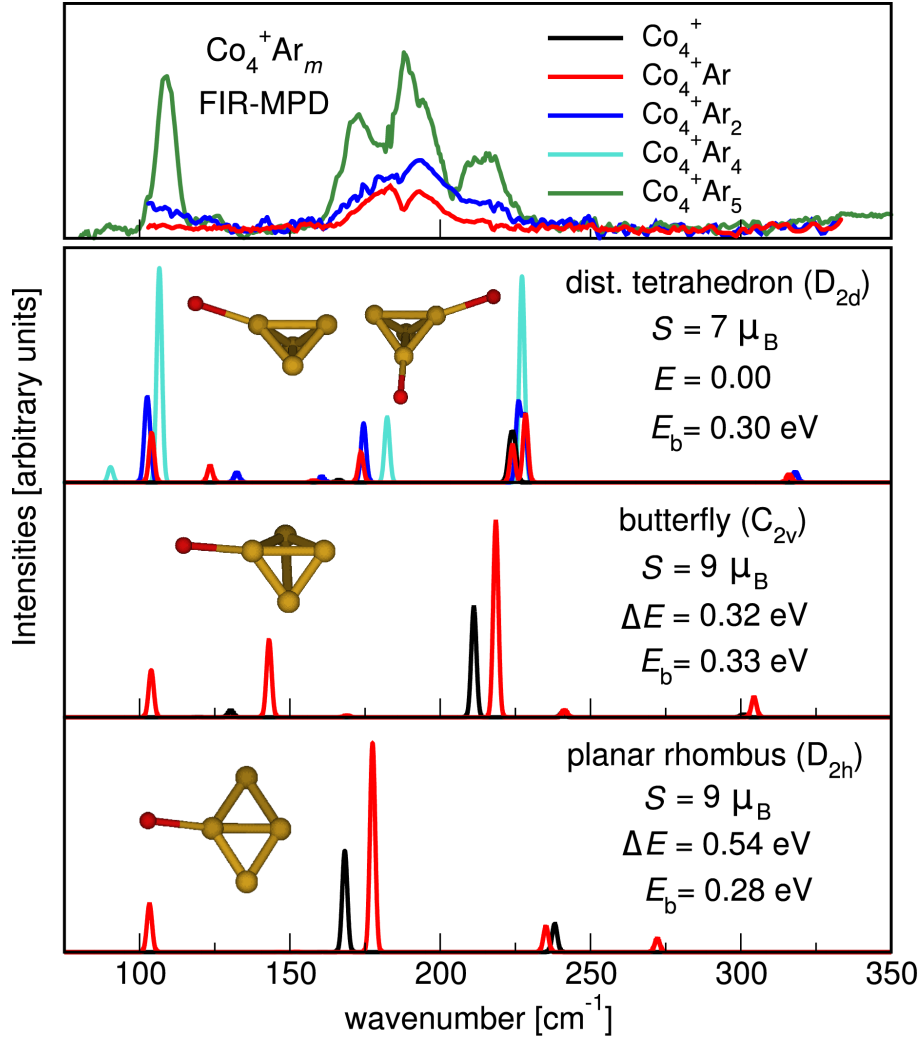


Figure 7.6.: Comparison of experimental FIR-MPD spectra (upper panel) with the computed IR absorption spectra of Ar complexes of the identified three energetically lowest isomers of Co_4^+ : The most stable distorted tetrahedron (second panel from top), a butterfly-type tetrahedron (third panel from top), and a planar rhombus (bottom panel), see text. Each of the theoretical panels additionally displays a schematic representation of the cluster geometry also indicating the position of the adsorbed Ar atom in the $\text{Co}_4^+ \text{Ar}$ complex, the point group symmetry, the total energy difference ΔE of the bare cluster with respect to the most stable isomer, and the Ar binding energy E_b in the $\text{Co}_4^+ \text{Ar}$ complex. For the lowest-energy isomer, we additionally show a representation of the cluster geometry indicating the position of both adsorbed Ar atoms in the $\text{Co}_4^+ \text{Ar}_2$ complex. In the $\text{Co}_4^+ \text{Ar}_4$ complex each of the four Co atoms is directly coordinated to one Ar atom.

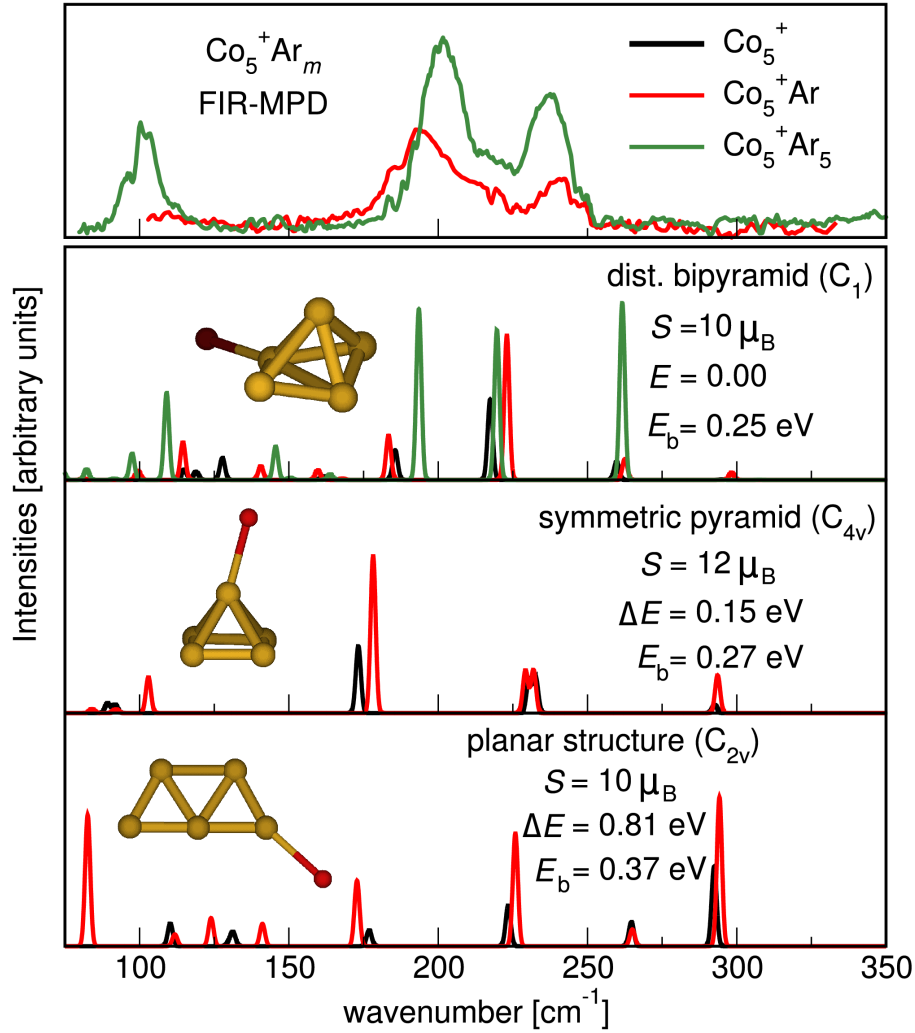


Figure 7.7.: Comparison of experimental FIR-MPD spectra (upper panel) with the computed IR absorption spectra of Ar complexes of identified energetically lowest isomers of Co_5^+ : One of the three almost degenerate distorted tetragonal pyramids (second panel from top), a more symmetric C_{4v} pyramid (third panel from top), and a planar structure (bottom panel), see text. Each of the theoretical panels additionally displays a schematic representation of the cluster geometry also indicating the position of the adsorbed Ar atom in the Co_5^+ -Ar complex, the point group symmetry, the total energy difference ΔE of the bare cluster with respect to the most stable isomer, and the Ar binding energy E_b in the Co_5^+ Ar complex.

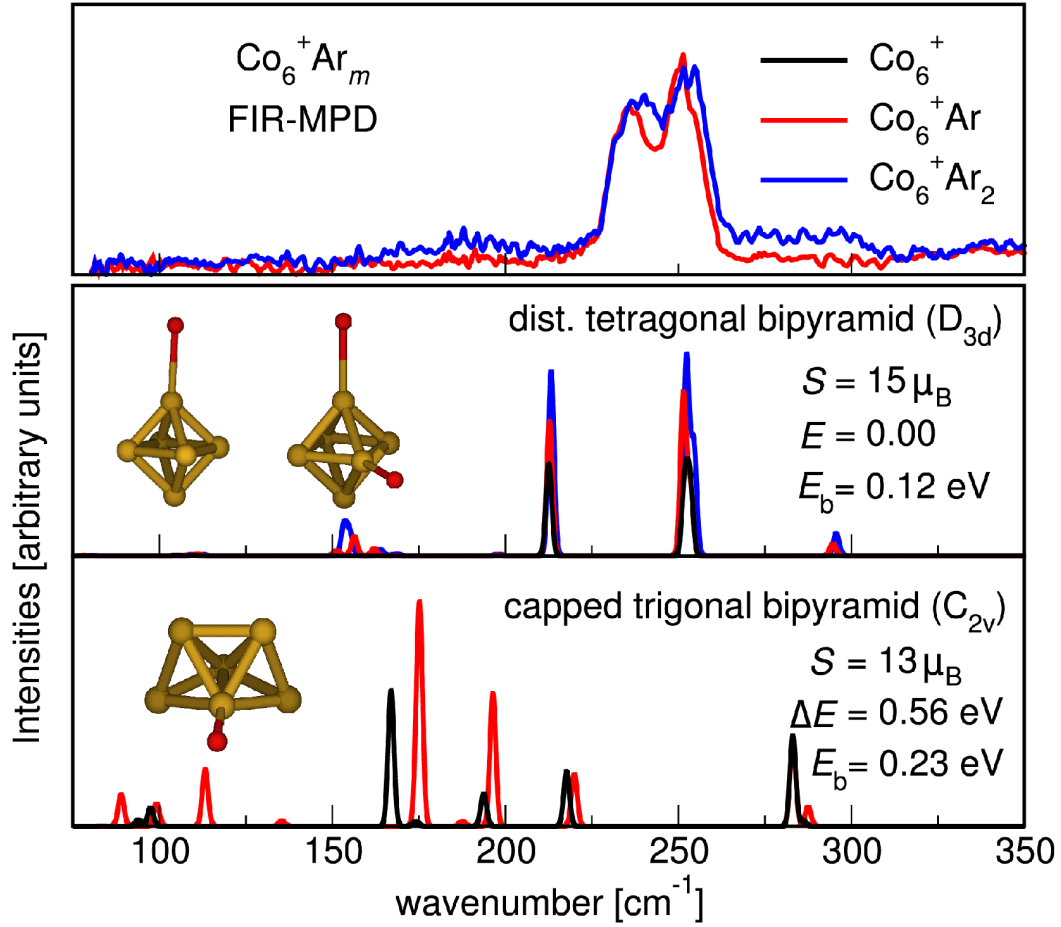


Figure 7.8.: Comparison of experimental FIR-MPD spectra (upper panel) with the computed IR absorption spectra of Ar complexes of identified energetically lowest isomers of Co_6^+ : The tetragonal bipyramid with $15\mu_B$ (second panel from top) and the capped trigonal bipyramid (third panel from top). The spectrum for a second tetragonal bipyramid with $13\mu_B$ is very similar to the one of the $15\mu_B$ pyramid and omitted for brevity, see text. Each of the theoretical panels additionally displays a schematic representation of the cluster geometry also indicating the position of the adsorbed Ar atom in the $\text{Co}_6^+ \text{Ar}$ complex, the point group symmetry, the total energy difference ΔE of the bare cluster with respect to the most stable isomer, and the Ar binding energy E_b in the $\text{Co}_6^+ \text{Ar}$ complex.

7.7.4. Co_7^+

In the case of Co_7^+ , a capped tetragonal bipyramid with C_{3v} symmetry and magnetic moment of $16\mu_B$ is identified as most stable structure. Again, the same structural motif for the cationic ground state is therefore found as in the preceding work for the neutral clusters [114]. The bond length in the triangle far side from the apex atom is 2.31 \AA and is thus close to the computed bond length of 2.36 \AA of the uncapped Co_6^+ ground-state structure, whereas the triangle near side of the apex atom has elongated bonds of 2.43 \AA . The resulting average bond length of 2.34 \AA for the entire cluster is thus slightly extended compared to the corresponding neutral isomer reported by Datta *et al.* [114] with an average bond length of 2.29 \AA . Energetically only insignificantly higher than the capped tetragonal bipyramid are two spin-variants of a distorted pentagonal bipyramid with C_{2v} symmetry, namely one with $14\mu_B$ only 0.06 eV higher and one with $16\mu_B$ only 0.08 eV higher. The structural variety is further complemented by the energetically next lowest isomer, which corresponds to a capped trigonal prism also in a $16\mu_B$ high-spin state and 0.15 eV higher than the ground state. Still energetically quite close this is then followed by another, slightly differently distorted $16\mu_B$ C_{3v} tetragonal bipyramid (0.18 eV) and a low-symmetry $16\mu_B$ structure at 0.29 eV .

With this close energetic spacing it is particularly interesting to compare to the vibrational spectra from the FIR-MPD experiments and see if the obtained fingerprint pattern does maybe conform with one of the slightly higher-energy isomers. The corresponding measurements are shown in Fig. 7.9, exhibiting slightly larger differences between the data from the complexes with different number of Ar atoms than in the case of Co_6^+ , yet still significantly less than in the case of the smaller clusters Co_4^+ and Co_5^+ . The computed IR absorption spectrum for the ground-state tetragonal bipyramid agrees overall rather well with the experiments, reproducing all three higher-frequency bands. The observed influence of the Ar atom in the comparison to the bare cluster spectrum is also in line with the experimental trend, i.e. it is somewhat larger than in the case of Co_6^+ , but less than in the case of Co_4^+ and Co_5^+ . Deferring the detailed discussion to the next chapter, particular emphasis is placed on the clear correlation with the now again slightly larger computed Ar binding energy of 0.18 eV .

A major concern in the comparison to the experimental data is the computed strong Ar-induced mode at the lower frequency end of the spectrum. For this, one cannot resort to the argument of apparent missing peaks in the spectra of complexes with one or two Ar atoms, as there are no complexes with more Ar atoms stabilized under the employed beam conditions, cf. Fig. 7.2. Comparing the theoretical spectra of the bare and Ar-complexed C_{3v} ground-state isomer it is, however, clear that the intensity of this particular mode depends sensitively on the interaction with the Ar ligand. The second most stable adsorption site at this isomer is atop one of the basal Co atoms that are on the opposite side from the capping atom, and its binding energy is only 60 meV lower. In the corresponding spectrum (see Appendix E) the mode does hardly show up. Most likely, the discrepancies between experimental and theoretical data with respect to this mode can be attributed to subtle shortcomings of the employed xc functional in describing the cluster-ligand interaction. Returning to the question of a unique structural

assignment, one would probably still conclude that the spectrum of the ground-state capped tetragonal bipyramid agrees overall best with the experimental data. Nevertheless, one also has to recognize that the fingerprint pattern of the different low-energy isomers is not sufficiently distinct to rule out small percentages of these isomers in the experimental beam as well.

7.7.5. Co_8^+

The most stable isomer found for Co_8^+ is a double-capped distorted tetragonal bipyramid with $17\mu_{\text{B}}$, which thus – like already the Co_7^+ ground state – also contains the very stable tetragonal bipyramid as a structural sub-unit and again coincides with the structural motif determined as most stable for the corresponding neutral cluster [114]. The geometry has nearly D_{2d} symmetry, with only bond distance differences of the order of $\sim 0.01 \text{ \AA}$ reducing it to the C_s point group. The next lowest isomer found is only marginally higher in energy (0.09 eV) and corresponds to a slightly distorted double-capped trigonal prism with a magnetic moment of $17\mu_{\text{B}}$. This is followed by another double-capped tetragonal bipyramid of the same magnetic moment (0.21 eV), and then several differently distorted and energetically virtually degenerate capped pentagonal bipyramid structures at around 0.47 eV.

For this largest studied cluster the comparison of the computed and measured vibrational data is unfortunately again rather inconclusive with respect to a potential structural assignment. The experimental spectra are shown in Fig. 7.10 and exhibit primarily two main peaks with some suggested shoulders at the high-frequency end. There are only marginal differences between the measurements from the Co_8^+Ar and Co_8^+Ar_2 complexes, which is characteristic for all further FIR-MPD spectra recorded for larger clusters up to 18 Co atoms (not shown). This minor influence of the adsorbed rare-gas atom is similarly found in all computed spectra for the three most stable Co_8^+ isomers, concomitant with a moderate Ar binding energy of around 0.15 eV. In all cases the data obtained is furthermore more or less similarly consistent with the measured fingerprint pattern, with maybe a slightly better agreement for the ground-state isomer. Put more modestly there is at least no compelling evidence that it is not the latter structure that is predominantly observed, and thus there is neither a reason to question the energetic order determined at the GGA-PBE level nor to invoke the kinetic stabilization of a significant fraction of higher-energy isomers in the experiments. Part of the reason for the disappointing inconclusiveness are the rather strong Jahn-Teller deformations found for the high-spin isomers, which make it partly a matter of semantics to distinguish between e.g. a double-capped distorted trigonal prism or a double-capped distorted tetragonal bipyramid. Without clearly distinct symmetries the various geometries exhibit only quantitative differences in the IR spectra, which in turn severely limits a technique like FIR-MPD which relies on an indirect structure determination through characteristic fingerprint patterns.

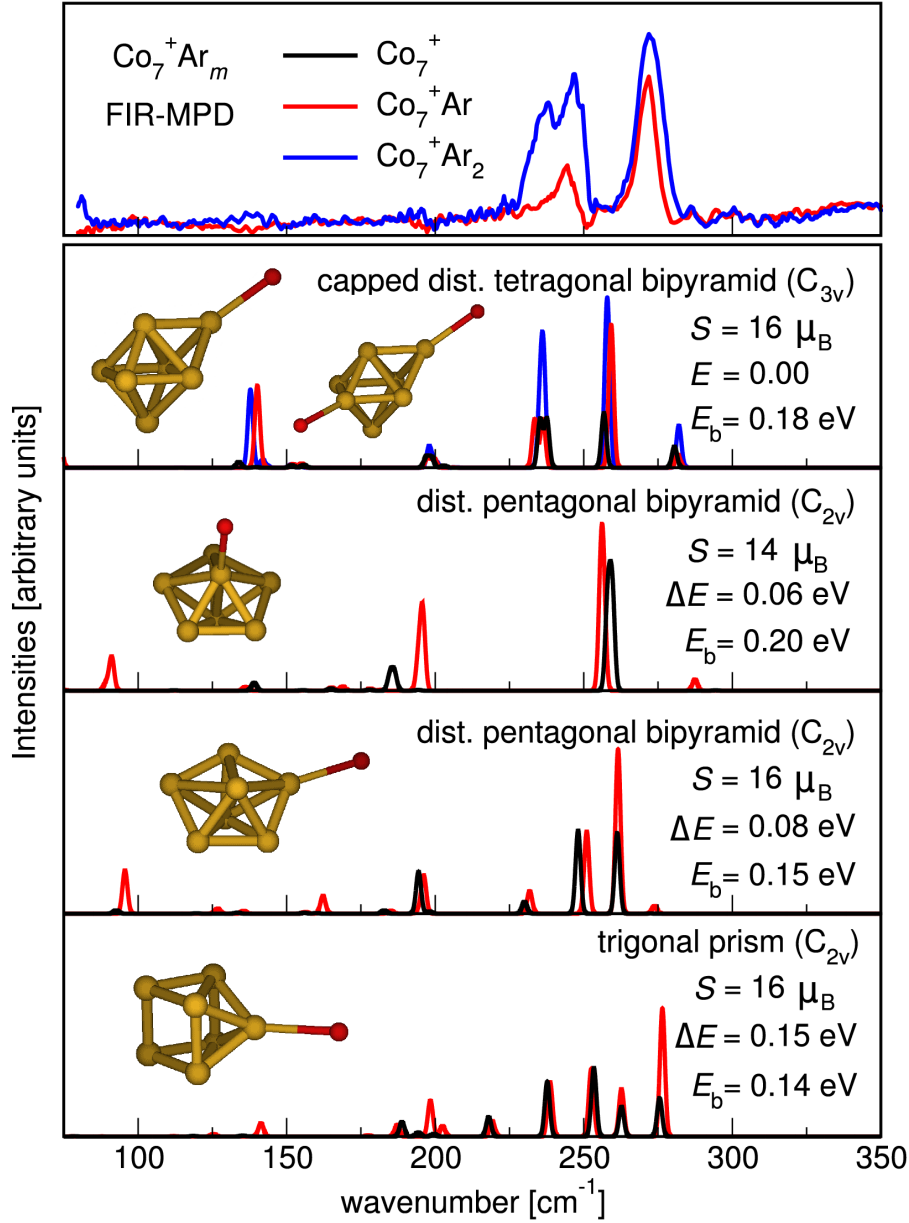


Figure 7.9.: Comparison of experimental FIR-MPD spectra (upper panel) with the computed IR absorption spectra of Ar complexes of identified energetically lowest isomers of Co_7^+ : The capped tetragonal bipyramid with $16\mu_B$ (second panel from top), two spin-variants of a pentagonal bipyramid (third and fourth panel from top), as well as a capped trigonal prism (bottom panel), see text. Each of the theoretical panels additionally displays a schematic representation of the cluster geometry also indicating the position of the adsorbed Ar atom in the Co_7^+Ar complex, the point group symmetry, the total energy difference ΔE of the bare cluster with respect to the most stable isomer, and the Ar binding energy E_b in the Co_7^+Ar complex.

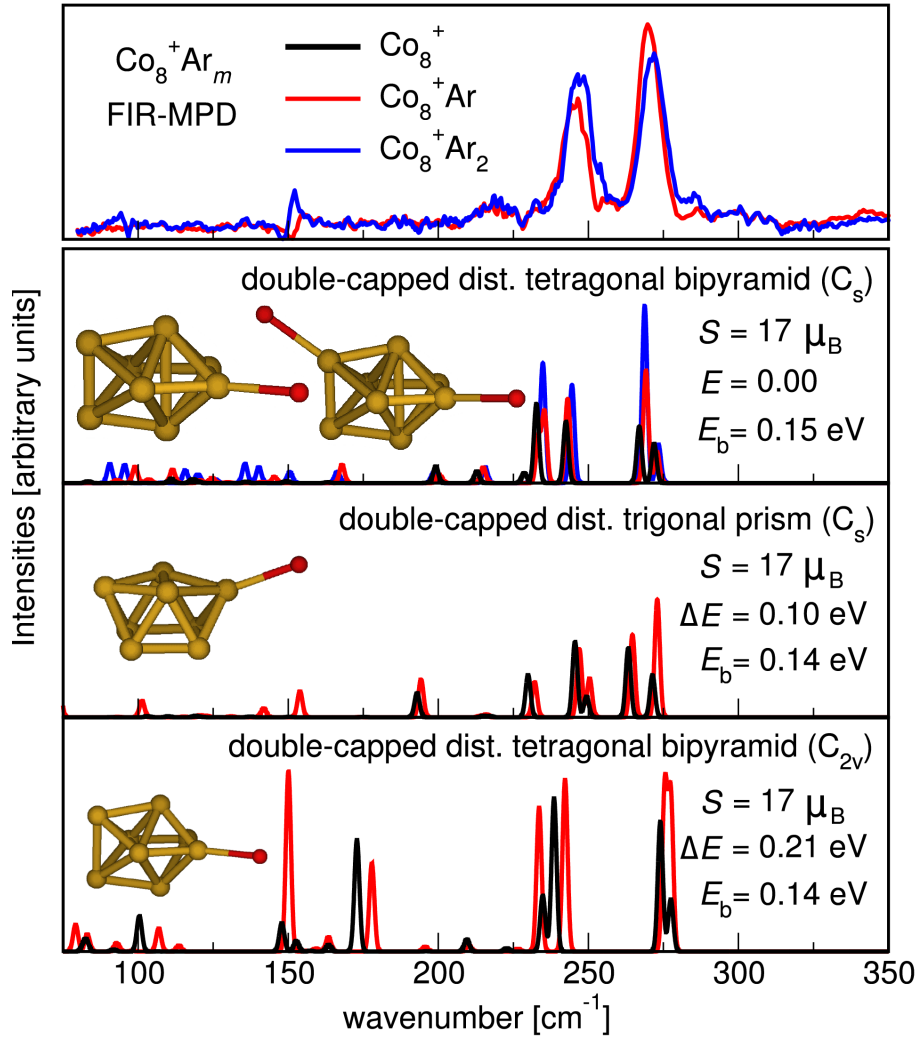


Figure 7.10.: Comparison of experimental FIR-MPD spectra (upper panel) with the computed IR absorption spectra of Ar complexes of identified energetically lowest isomers of Co_8^+ : The double-capped distorted tetragonal bipyramid with $17\mu_B$ (second panel from top), the double-capped trigonal prism (third panel from top), as well as another double-capped tetragonal bipyramid (bottom panel), see text. Each of the theoretical panels additionally displays a schematic representation of the cluster geometry also indicating the position of the adsorbed Ar atom in the Co_8^+Ar complex, the point group symmetry, the total energy difference ΔE of the bare cluster with respect to the most stable isomer, and the Ar binding energy E_b in the Co_8^+Ar complex.

7.8. Summary

Summarizing this chapter, density-functional theory has been used to study energetically low-lying isomers of cationic Co clusters containing from four to eight atoms. Supplementing the search for structural motifs with first-principles basin-hopping sampling the identified ground-state structures agree for each cluster size with the geometry determined in preceding DFT studies for the corresponding neutrals. All structures are in high-spin states and exhibit sizable Jahn-Teller distortions. The specific motivation has been a detailed comparison of the vibrational properties of the clusters with experimental far-infrared multiple photon dissociation data. While this comparison allows only in few cases for a unique structural assignment and leaves some open questions and doubts in particular for Co_4^+ , there is at least no compelling evidence that would question the energetic order of the isomers obtained at the GGA-PBE level or reciprocally indicate a kinetic stabilization of a significant fraction of higher-energy isomers in the experiments.

Reproduced quite well by the calculations is the general trend of the influence of the rare-gas probe atoms used in the measurements, with Ar-induced changes of the IR spectra becoming smaller for larger clusters. This correlates nicely with an overall reduction of the calculated Ar- Co_n^+ bond strength from 0.3 eV for the lowest lying isomers of Co_4^+ to around 0.1 eV for the largest studied clusters. This clear correlation therefore motivates a deeper analysis of the nature of the Ar- Co_n^+ bond, presented in the next chapter, with the expectation of understanding the behaviour in the previously reported studies on cationic vanadium, niobium and tantalum clusters [1, 2, 3, 4, 5].

For the investigated Co_n^+ vibrational spectra, complexation with Ar leads in general to the appearance of new IR-active modes, hand in hand with frequency shifts and splittings of existing peaks and often an increase in the absorption intensity. These effects can be primarily traced back to Ar-induced symmetry breakings in the geometric structure of the cluster. The latter become obviously stronger with increasing Ar binding energy, but can never be excluded. For a cluster geometry on the verge of a Jahn-Teller distortion even the tiniest disturbance by a rare-gas ligand may induce symmetry breakings that can then substantially affect the spectrum. In this respect, the present work casts some doubts on the hitherto employed practice of comparing experimental data to computed IR spectra of bare clusters. The influence of the probe atom can not be judged from a comparison of experimental spectra from different complexes, as the latter reveal only the differences between adsorption of one or more rare-gas atoms, and not with respect to the bare cluster. A computed negligible effect of Ar on the spectrum of one cluster isomer does neither justify to dismiss the ligand in the calculations, since this tells nothing about the liability toward symmetry breaking of other isomers of the same or other cluster sizes. In this situation, explicit consideration of the rare-gas atoms in the modelling is always advisable at little additional computational cost.

The appearance of Jahn-Teller distortions and therefore qualitatively similar vibrational fingerprints clearly limits FIR-MPD in connection with DFT as a method for structure determination. Since a unique assignment of a computed spectrum is impossible in these cases, it is recommended to additionally resort to further spectroscopic data, in the hope of gaining a more reliable picture of the cluster structure under consideration.

8. The Nature of the Ar-Co_n^+ Bonding

8.1. Introduction

While the comparison of computed and measured vibrational spectra in particular of the smallest studied Co clusters leaves a number of open questions and doubts with respect to the detailed interpretation of the FIR-MPD data, the general trend of the influence of the rare-gas atoms with cluster size is reproduced quite well by the calculations presented in the previous chapter. In general, the Ar-induced changes of the IR spectra become smaller for larger clusters, correlating nicely with an overall reduction of the Ar-Co_n^+ bond strength from an “unusually” high value of 0.3 eV for the lowest lying isomers of Co_4^+ to the more “intuitive” value of around 0.1 eV for the largest studied clusters. Particularly for the smallest clusters, the complexation with Ar leads to the appearance of new IR-active modes in the spectra, hand in hand with frequency shifts and splittings of existing peaks and often an increase in the absorption intensity. These effects can be primarily traced back to Ar-induced symmetry breakings in the geometric structure of the cluster, together with an enhanced polarization of the cluster electron density. Both effects depend obviously on the strength of the Ar-Co_n^+ interaction, rationalizing the correlation with the computed Ar binding energy. The explanation for the observation of a much more pronounced dependence of the FIR-MPD spectra on the number of Ar atoms compared to the preceding work on the cationic group 5 clusters [1, 2, 3, 4, 5] is therefore coupled to the understanding of the larger Ar binding energy at the smaller Co clusters compared to the e.g. ~ 0.1 eV computed also with GGA-PBE for the previously studied V_n^+ clusters [1, 2]. Hence, the motivation for this part of the work is to analyze the origin of the Ar-Co_n^+ binding in order to deduce an explanation of the different behaviour of the Ar probe atom in the previous studies.

8.2. Electrostatic Model of the Ar-Co_n^+ Bonding

8.2.1. Multipole Decomposition via Hirshfeld Analysis

As an important key to understand the particularities of the Ar-Co_n^+ binding energy, Fig. 8.1 shows a plot of the electron density redistribution when adsorbing an Ar atom at the ground-state isomer of Co_4^+ . Observable is a strong polarization of the Ar atom, which is equivalently obtained in a corresponding analysis of Ar adsorption at all larger cluster sizes studied. This suggests as the predominant contribution to the Ar-Co_n^+ bond a mere polarization of the rare-gas atom in the electrostatic field of the cationic cluster. Figure 8.2 provides further insights into the charge density distribution of the bare Co_4^+ cluster

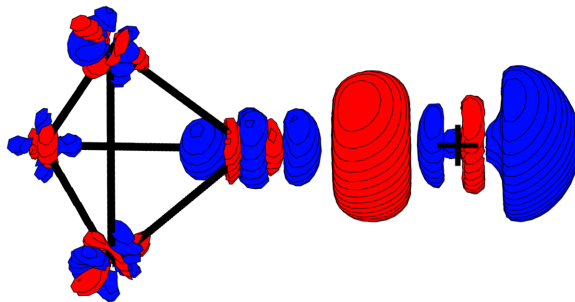


Figure 8.1.: Electron density difference induced by the adsorption of Ar at the ground-state isomer of Co_4^+ , see text. For the optimized geometry of the Co_4^+Ar complex, the plot shows the isosurface corresponding to 0.015 \AA^{-3} electron accumulation (red) and depletion (blue) upon Ar addition, obtained by subtracting from the full self-consistent electron density of the Co_4^+Ar complex the self-consistent electron densities of the bare Co_4^+ cluster and an isolated Ar atom at the corresponding atomic positions. For better visualization, the drawn skeleton of black “bonds” at the left of the figure represents the cluster geometry, while the black cross marks the position of the Ar atom.

and clearly indicates that the positive charge seems to be smeared out over the surface thus leading to local dipoles pointing outward of the atomic cluster. Further support for this view on the nature of the Ar- Co_n^+ interaction comes from a multipole decomposition of the charge density of the determined ground-state isomers of the bare Co_n^+ clusters. Via Hirshfeld analysis [84] the point charge and dipole moment on each atom in the bare Co_n^+ cluster is computed, yet at the relaxed geometry of the corresponding Co_n^+Ar complex. The qualitatively expected results of having radially outward pointing local dipoles is herewith confirmed and depicted in Fig. 8.3, instancing both spin states of the ground-state structure of Co_6^+ .

8.2.2. Ar Binding Energy in the Electrostatic Model

In a second step the Hartree-type interaction energy of an Ar atom is then computed, which is placed at the position in the $\text{Co}_n^+\text{-Ar}$ complex into the frozen electrostatic field generated by the computed point charges and dipole moments of the bare cluster. The correspondingly obtained binding energies, which are henceforth termed $E_b(q + \text{all } p)$, are finally compared to the fully self-consistently computed Ar binding energies at the different cluster sizes in the upper panel of Fig. 8.6. The rather good agreement suggests that the polarization of the Ar atom describes indeed the predominant character of the bond, with larger multipole moments and the back-reaction of the Co charge density on the polarized Ar atom contained in the true self-consistent calculation forming only a small correction. These findings hold similarly for all of the studied cluster sizes, and even carry over to less stable Ar adsorption sites and other low-energy isomers than the ground state (see Table 8.1), for all of which we obtain a similarly good agreement of the Ar

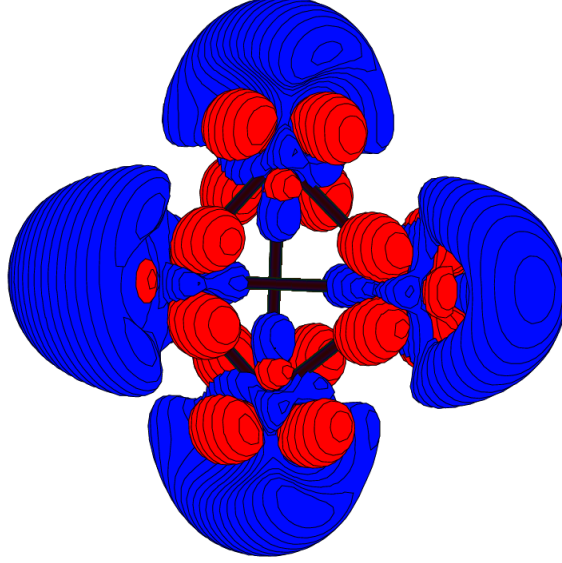


Figure 8.2.: Electron density difference between the ground-state isomer of Co_4^+ and the corresponding neutral isomer to illustrate the distribution of the positive charge. The plot shows the isosurface corresponding to 0.02 \AA^{-3} electron accumulation (red) and depletion (blue) obtained by subtracting from the full self-consistent electron density of the Co_4^+ the self-consistent electron densities of the neutral Co_4^+ cluster at exactly the same geometry. For better visualization, the drawn skeleton of black “bonds” represents the cluster geometry.

binding energy computed in the electrostatic model with the true self-consistent value. In order to better understand the tendency of the Ar binding energy, the individual energy contributions have further been disentangled. The binding energy that arises in the electrostatic model when the local monopoles are exclusively considered is termed as $E_b(q)$. Additionally considering the dipole to which the Ar atom is directly correlated (therefore denoted as the direct dipole p_d) yields a binding energy that is termed $E_b(q + p_d)$. The contribution due to the direct dipole can then be defined as

$$E_b(p_d) \equiv E_b(q + p_d) - E_b(q) . \quad (8.1)$$

Correspondingly, the contribution arising from the other dipoles can conveniently be defined as

$$E_b(p_{\text{other}}) \equiv E_b(q + \text{all } p) - E_b(q + p_d) . \quad (8.2)$$

Figure 8.6 clearly shows that taking the local monopoles exclusively into account yields only a low binding energy below 100 meV in the electrostatic model. Most of the binding energy instead results from the direct dipole field which is further offset by the other dipoles, obviously being unfavourably oriented. Both dipole contributions show

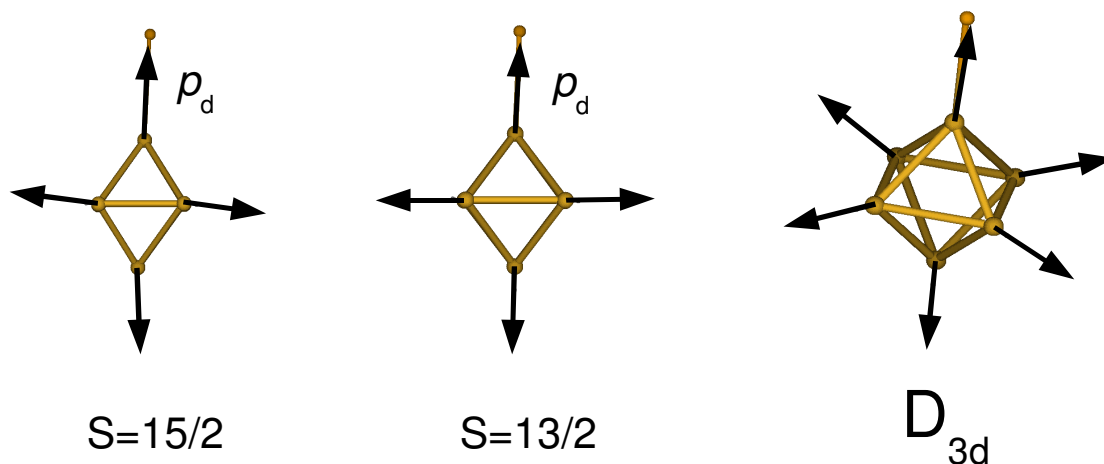


Figure 8.3.: Electrostatic model of the Ar-Co_n⁺ bonding instancing both spin states of the D_{3d} structure of Co₆⁺Ar. The local dipole moments obtained by a Hirshfeld analysis are pointing outwards. The two different spin states exhibit slightly different orientations of the dipoles. The dipole to which the Ar atom is directly coordinated is depicted as p_d .

the overall tendency to get smaller with increasing cluster size, with the variation of the binding energy predominantly resulting from the attractive direct dipole field. Figure 8.5 furthermore reveals the striking correlation between p_d and the resulting binding energy, once more underlining the picture of the direct dipole field playing the dominant role in the electrostatic interaction of the Ar probe atom with the Co cluster. With that picture in mind, the behaviour of the binding energy is easy to understand. The local dipole moments are obviously correlated with the cluster structure which discontinuously varies, thus giving rise to some kind of zig-zag trend, being typical for properties in the context of cluster physics as already mentioned in the introduction of the thesis. Superimposed is the general tendency towards a lower binding energy, which can be rationalized by the picture of the positive charge being smeared over an increasing cluster surface. The larger the cluster surface on which the single positive charge is distributed, the smaller the local charge density, thus giving rise to smaller local dipole moments. The clear correlation between the direct dipole and the overall binding energy again carries over to less stable adsorption sites and different spin states, as computed in Table 8.1.

8.2.3. Electrostatic Driving Forces

On the basis of the established electrostatic picture a rather consistent explanation for the observed trend of the Ar binding energy with Co cluster size can be achieved, as well as for the stronger interaction compared to the previously studied cationic clusters from group 5 of the Periodic Table. Taking the ground-state isomer of Co₄⁺ and Co₈⁺ as well as both spin states of the Co₆⁺ ground-state structure as examples for stronger and weaker Ar bonding, respectively, the upper panel of Fig. 8.7 shows the variation of the interaction energy in the electrostatic model when changing the Ar-Co_n⁺ bond length by

8. The Nature of the Ar- Co_n^+ Bonding

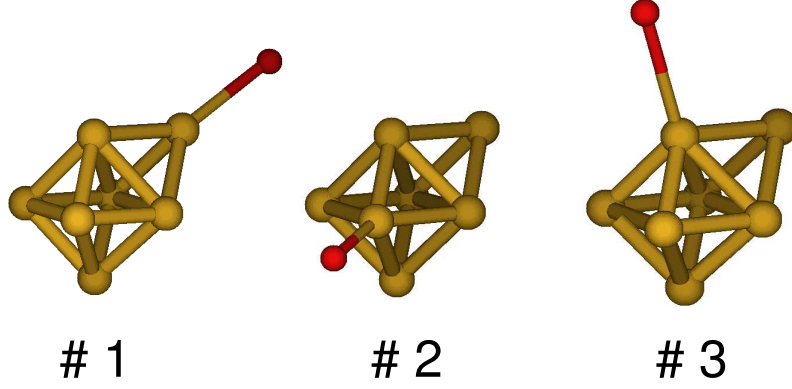


Figure 8.4.: The three symmetry-inequivalent on-top binding sites of Co_7^+Ar .

| | | $p_d[\text{e}\hat{\text{A}}]$ | $E_b(\text{PBE})$ | $E_b(q + \text{all } p)$ | $E_b(q)$ | $E_b(p_d)$ | $E_b(p_{\text{other}})$ |
|--------------------------|----------|-------------------------------|-------------------|--------------------------|----------|------------|-------------------------|
| Co_6^+Ar | $S=15/2$ | 0.46 | 0.12 | 0.10 | 0.04 | 0.13 | -0.07 |
| | $S=13/2$ | 0.56 | 0.30 | 0.27 | 0.07 | 0.37 | -0.17 |
| Co_7^+Ar | # 1 | 0.50 | 0.18 | 0.20 | 0.05 | 0.20 | -0.05 |
| | # 2 | 0.46 | 0.13 | 0.11 | 0.04 | 0.14 | -0.07 |
| | # 3 | 0.39 | 0.07 | 0.05 | 0.03 | 0.07 | -0.05 |

Table 8.1.: Binding energies in the electrostatic model for different spin states and Ar binding sites. The different binding sites of Co_7^+Ar , labeled as # 1, # 2, and # 3, are illustrated in Fig. 8.4

moving the Ar atom radially away from the cluster. Immediately apparent is the smaller attraction in the case of Co_8^+ and the $15\mu_B$ state of Co_6^+ which can be rationalized with the weaker direct dipole moment compared to Co_4^+ and Co_6^+ being in the $13\mu_B$ state. The lower panels shows the contributions to the interaction energy due to the attractive field constituted by the monopoles and the direct dipole on the one hand (left lower panel) and the repulsive field due to the unfavourably oriented other dipoles (right lower panel) on the other hand. Perfectly in line with the observations of the previous section, the differences in the attraction predominantly arise from the differences in the direct dipole part, with the other dipoles only playing a minor role. Neglecting electronic self-consistency effects, the equilibrium Ar- Co_n^+ bond length is determined by the interplay of this attractive electrostatic contribution and a strongly repulsive short-range component arising from Pauli repulsion. Since the latter is primarily due to the inner shell electrons of the directly coordinated Co atom, one can assume this component to be rather similar for the four test cases to a first approximation. With the stronger electrostatic attraction this then leads to a shorter Ar- Co_4^+ and Ar- $\text{Co}_6^+(13\mu_B)$ bond length compared to Ar- Co_8^+ and Ar- $\text{Co}_6^+(15\mu_B)$, and in turn to a stronger Ar binding energy. In the same spirit one can also attribute the comparably stronger interaction of Ar with Co_n^+ than with the previously studied V_n^+ , Nb_n^+ and Ta_n^+ clusters to this interplay of electrostatic attraction and Pauli repulsion. The distance at which the latter sets in depends of course

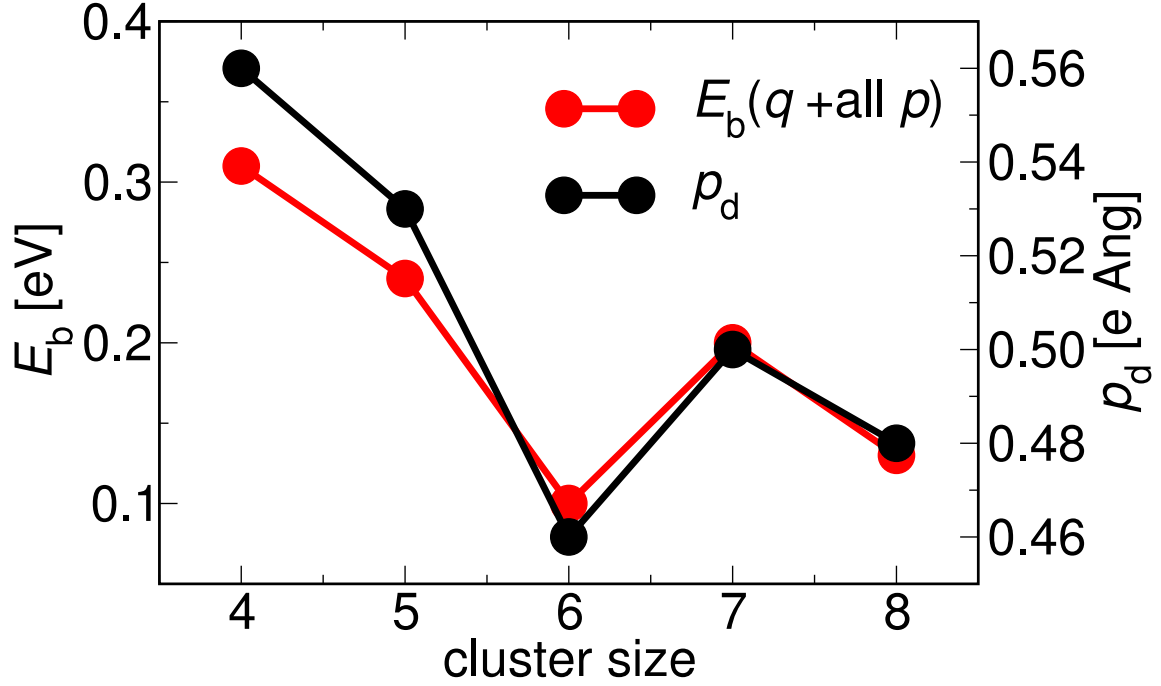


Figure 8.5.: Correlation between Ar binding energy and direct dipole moment p_d .

on the size of the atomic radius, which is smaller for Co than for any of the group 5 elements. With the steep Pauli repulsion setting in at already larger distances, one can in general expect longer equilibrium Ar-metal cluster bond lengths and therewith smaller Ar binding energies for the group 5 elements. As suggested by Fig. 8.7, the differences in the electrostatic driving forces is also smaller at such increased interaction distances, so that one would furthermore conclude on a smaller variation of the Ar binding energy with cluster size as in the case of Co.

Simplistically equating the Ar bond strength with the influence of the rare-gas atom on the measured FIR-MPD spectra as discussed above, the electrostatic picture can thus fully account for the general trends observed in the corresponding experiments on these materials. Tacitly assuming a similar character of the rare-gas–metal cluster bond, one would even predict that equally pronounced effects of the probe atoms as in the case of Co will be obtained whenever studying cationic clusters formed of other elements with small atomic radii or for more polarizable heavier rare-gas atoms.

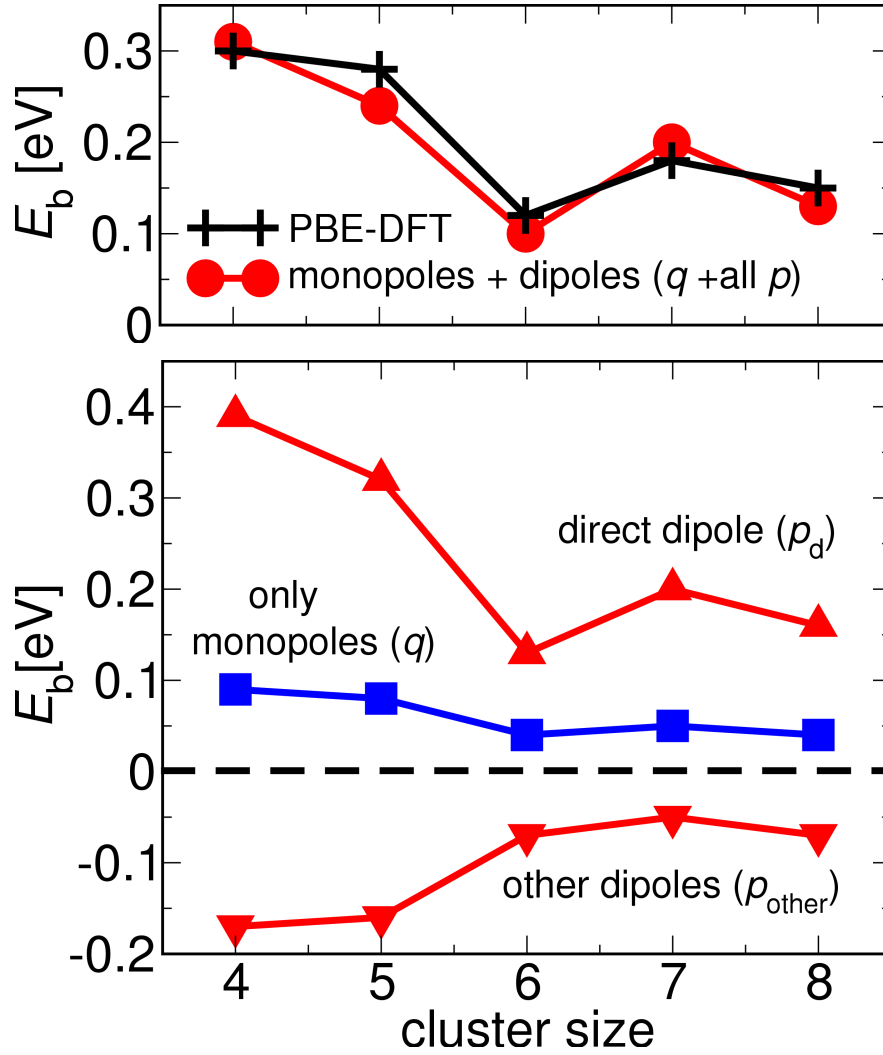


Figure 8.6.: Ar binding energy at the most stable adsorption site offered by the determined ground-state isomers of Co_4^+ to Co_8^+ . In the upper panel, values obtained from the real self-consistent calculation (black crosses) are compared to the Hartree-type interaction energy obtained when placing Ar into the frozen electrostatic field formed by the point charges and dipole moments of the bare cluster (red circles), see text. The lower panel shows the separation of this interaction energy into contributions due to the monipoles (blue squares), the direct dipole (upper triangles) and the other dipoles (lower triangles).

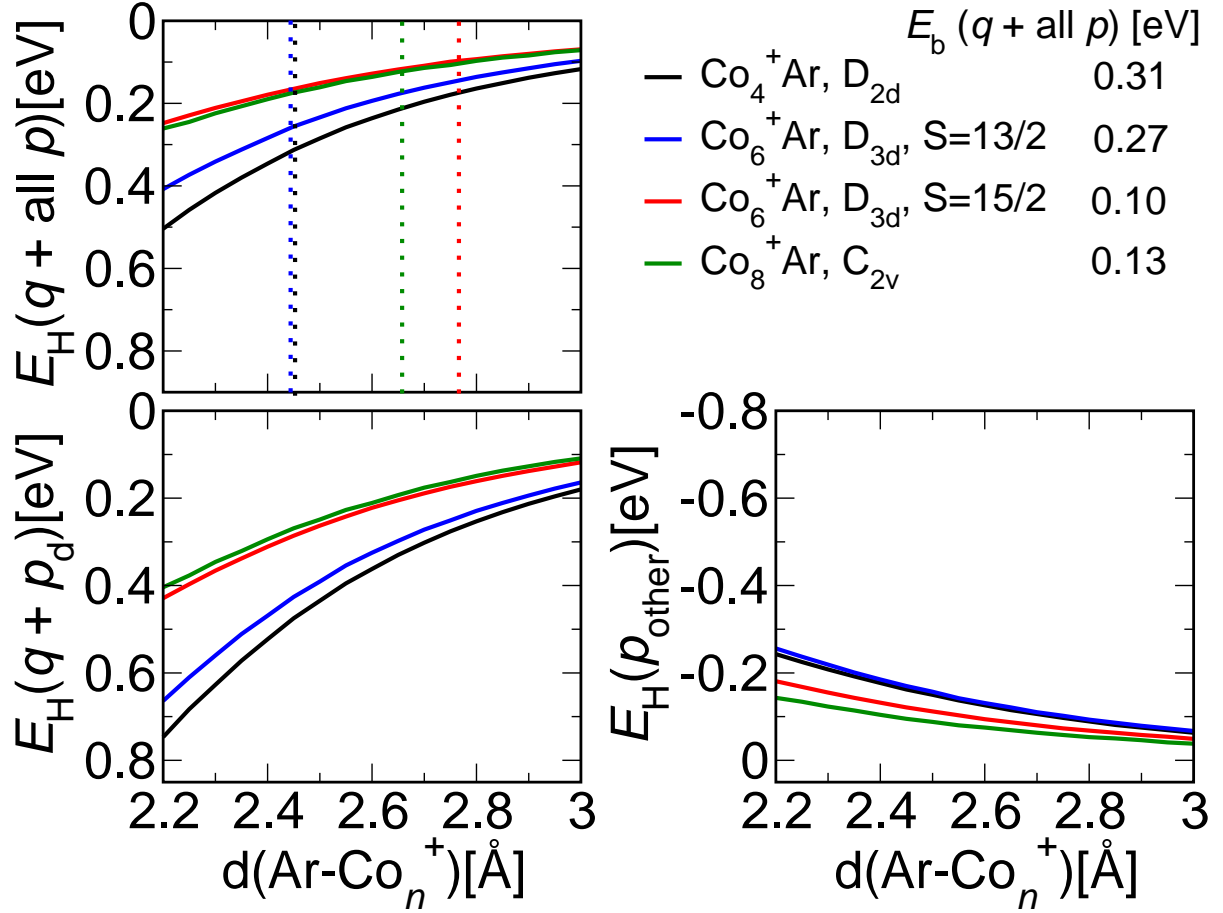


Figure 8.7.: Attractive Hartree-type Ar-Co_n⁺ interaction energy computed in the electrostatic model, see text. Shown is the variation with bond length when moving the Ar atom radially outwards in the four complexes Co₄⁺Ar (D_{2d}, black line), Co₈⁺Ar (C_{2v}, green line), Co₆⁺Ar (D_{3d}, S=15/2, red line) and Co₆⁺Ar (D_{3d}, S=13/2, blue line). The four dotted vertical lines indicate the corresponding computed equilibrium bond lengths.

8.3. Summary and Conclusion

In this chapter, an electrostatic model was established that can capture most of the Ar-Co_n⁺ binding energy, in particular it can fully account for the variation of the binding energy with the cluster size. For this, the Ar atom is self-consistently calculated in the multipole field set up by the local monopoles and dipoles in the bare Co_n⁺ cluster obtained via Hirshfeld analysis. Disentangling the individual energy contributions reveals that the binding energy predominantly results from the dipole moment to which the Ar atom is directly coordinated, being offset by the unfavourably oriented dipole fields originating from the other Co atoms. Supported is this picture by the striking correlation between the full binding energy in the electrostatic model with the direct dipole strength, the latter being highly sensitive to the cluster structure. Superimposed to the thus resulting

8. *The Nature of the Ar-Co_n⁺ Bonding*

zig-zag behaviour is the general trend towards lower binding energies with increasing cluster sizes since the larger surface area on which the positive charge is distributed yields smaller local dipoles. In the real cluster, the bond distance results from the interplay between the attractive Hartree energy and the Pauli repulsion, where the latter acts locally between the Ar atom and the Co atom to which the former is directly coordinated, thus being more or less constant for all isomers under consideration. The variation in the bond distances and the corresponding binding energies can therefore be traced back to the variation in the electrostatic driving forces resulting from the variation of the direct dipole strength. The interatomic distance at which the Pauli repulsion sets in is clearly controlled by the atomic radii of the constituent atoms. Hence, the larger binding energy for Ar-Co_n⁺ can be attributed to the smaller radius of Co compared to V, Nb and Ta in the previous studies. As for the binding site, the preference for on-top sites becomes trivial to understand since this maximizes the polarization of the charge density in the radially outwards pointing direct dipole and in turn the resulting binding energy. As further conclusion, a stronger influence on the IR spectra is to be expected for heavier, more polarizable probe atoms.

Part IV.

Assessing the Efficiency of First-Principles Basin-Hopping Sampling

9. Method Optimization Based upon Quantitative Efficiency Criteria

9.1. Introduction

In the previous study with systems containing only few atoms (Co_4^+Ar to Co_8^+Ar), the sampling efficiency is not critical, reasonable settings for sampling parameters provided. In the context of the applied basin-hopping scheme, this means large enough move distances, enabling the system to find new isomers. The average move distance for displacing single randomly chosen atoms has therefore been empirically set to 1.5 times the corresponding dimer bond length for the whole sampling run, which worked satisfactorily. With increasing cluster size, however, the exponential growth of the number of different isomers clearly requires a more careful analysis of the involved technical parameters. Taking the well studied Lennard-Jones clusters as an example, the number of different isomers grows from 64 to 1505, when going from ten to only thirteen atoms [6]. To reveal inefficient settings, such an analysis necessitates a proper definition of efficiency, with which runs under different settings can quantitatively be compared. Such a quantity must obviously be coupled to the desired sampling goal. A common scheme is to investigate the mean first encounter, i.e. one counts the number of moves, or local structural relaxations, respectively, until the global minimum has been identified for the first time (see chapter 3). If it were exclusively the ground state being of interest, such a quantity would clearly be correlated with the overall computational time, thus being an appropriate efficiency indicator. However, as the previous study on Co_n^+Ar_m has illustrated, also energetically higher-lying isomers are to be identified and discussed. Hence, the move number should be somehow coupled to the relevant isomers, where one has to consider the actual problem to decide which isomers are relevant. Moreover, rather than revealing inefficient settings only *a posteriori*, this optimization would best be carried out by monitoring on-the-fly analyzable performance indicators that allow to adapt an ongoing run. Unfortunately, there are few to none general prescriptions of how to set technical move parameters that do not require detailed system-specific insight. With respect to on-the-fly performance indicators there exists at best the empirical rule-of-thumb to aim at an overall acceptance of new trial structures of roughly one half [45, 116]. However, this rule emerges from the empirical observation that a factor one half ensures an efficient sampling of canonic ensemble averages and must not necessarily carry over to the intended goal of searching for the energetically lowest lying isomers with the least possible number of energy and force evaluations. A second complication arises from the stochastic nature of the BH algorithm. Any analysis mea-

asuring the efficiency of technical BH settings or the reliability of suggested on-the-fly performance indicators therefore necessarily needs to involve an averaging over a sufficiently large number of different BH runs starting from different initial structures and using different random number seeds. This would not be too much of a problem when using numerically undemanding model potentials, but then it would be unclear whether the obtained findings are meaningful for proper quantum-mechanical PESs. A straightforward evaluation based on first-principles energetics, on the other hand, is hitherto computationally prohibitive even when only considering smaller clusters up to say 10 atoms. In this situation, the aim of the present study is to establish a corresponding framework for a systematic performance analysis of first-principles BH sampling runs. An important ingredient herein is the use of a hopping matrix type concept that significantly brings down the computational cost for the manifold of first-principles BH runs required in the averaging procedure and thus allows to arrive at statistically reliable performance values. Using DFT, this scheme is illustrated for Si clusters as a system with more directional, covalent type of bonding and for Cu clusters as representative of a metallic system. With the obtained insights, a simple adaptive scheme based upon on-the-fly efficiency indicators is finally suggested and illustrated.

9.2. Computational Details

9.2.1. Density-Functional Theory

The underlying PES is again obtained by DFT in the generalized-gradient approximation (GGA-PBE) [70] in order to transfer the gained insights to practical applications that require a quantum-mechanical treatment of the energetics. In order to suppress a potential complication in the performance analysis due to the spin degrees of freedom all calculations were consistently carried out in a non-polarized way. All calculations reported here were conducted with the so-called “minimal+*spd*” basis set (see Appendix A). For each considered system we recomputed all stable cluster isomers within an energy range up to 1 eV above the ground state, namely those listed in Figs. 9.5-9.7 below, also with hierarchically constructed larger basis sets available in FHI-aims. These calculations clearly show that the relative energies between these isomers are converged to within 10 meV at the “minimal+*spd*” basis set level, which is fully sufficient for the arguments and conclusions put forward below since it is the sampling efficiency that is in the focus of interest, not tightly converged physical quantities. To be on the safe side, several further basin-hopping runs with larger basis sets have been run, but no isomers other than those already revealed at the “minimal+*spd*” level have been obtained. This suggests that not only the local minima, but also the other parts of the PES are sufficiently described with the employed “minimal+*spd*” basis, in order to pursue the aspired efficiency study. The integration grids are found to be converged at $N_{\text{ang,max}} = 302$ with $N_{\text{r,div}} = 2$. The cut-off radius is slightly reduced to 4 Å which is again fully sufficient for the energy differences and thus saves computational time for the sampling. As l_{max} a conservative value of 6 was chosen. Furthermore, a slight Gaussian smearing of width 0.1

eV was employed to ensure scf-convergence for the distorted structures resulting from the trial move. Details of the convergence tests can be found in Appendix C.

Local structural optimization is done using the Broyden-Fletcher-Goldfarb-Shanno (BFGS) method [27], relaxing all force components to smaller than 10^{-2} eV/Å. In order to check whether the thus identified different isomers are true local minima and not saddle points, they were subjected after the BH run to a vibrational analysis based upon a Hessian matrix obtained by finite differences of the analytical atomic forces when displacing all atoms by 10^{-3} Å.

9.2.2. Basin-Hopping

In this section, the intricate technical details of the basin-hopping scheme that influence the efficiency of the sampling, are further analyzed. The key ingredients are the way new structures are generated, the trial move scheme, and the acceptance criterium, which decides, whether a new structure is accepted or not. While in the previously presented study on Co_n^+Ar_m -complexes these parameters have been adjusted intuitively, they are now subject to a critical discussion.

Sampling Parameter

As a representative and widely used move class this work focuses on single-particle and collective moves, in which either a single randomly chosen atom or all atoms in the cluster are randomly displaced, respectively. The corresponding displacement vector of atom α is suitably expressed in spherical coordinates as

$$\Delta\mathbf{R}_\alpha = r\vec{e}_r(\theta, \phi) \quad , \quad (9.1)$$

where $\vec{e}_r(\theta, \phi)$ is a unit vector in the displacement direction defined by the angles θ and ϕ with respect to an arbitrary, but fixed axis. In order to obtain an unbiased sampling, $\theta \in [0, \pi]$ and $\phi \in [0, 2\pi]$ must obviously be obtained as uniformly distributed random numbers. On the contrary, the move distance r is *a priori* not specified, but will sensitively determine the jumps in configuration space and therewith the algorithmic performance. It provides therefore a nice example of a technical parameter that one would like to optimize for a first-principles sampling run, yet without introducing bias or system-specific insight. As any one specifically chosen value for r (suitably measured in units of the dimer bond length a) could potentially already be too restrictive and therewith lead to a biased result, it appears advantageous to use a distribution of r values around a specified average value r_0 . As two natural distributions, both a normal distribution (width $0.07\sqrt{r_0}$) around r_0 and a uniform distribution (width r_0) around r_0 are therefore investigated.

Apart from the move class the second important ingredient that needs to be specified in a BH run is the acceptance criterion according to which a generated trial structure is accepted and replaces the current cluster structure as starting point for the following trial move. In order to introduce a downhill driving force towards the energetically low-lying (and ultimately ground-state) isomers it is clear that a more stable trial structure should

always be unconditionally accepted. In its classical form, the BH scheme also accepts less stable trial structures according to a Metropolis rule, $\exp(-\Delta E/k_{\text{B}}T_{\text{eff}})$, where k_{B} is the Boltzmann constant and introducing another unspecified technical parameter which crucially affects the algorithmic performance, the effective temperature T_{eff} . The original motivation behind this Metropolis rule is that the finite possibility to climb uphill enables the algorithm to effectively surmount high-energy barrier regions on multiple-funnel type transformed PESs $\tilde{E}(\{\mathbf{R}_{\alpha}\})$. However, as long as the employed move class enables efficient jumps between all parts of configuration space, this acceptance criterion is only of subordinate importance. As it will become clear below this is still the case for the small cluster sizes studied here, and therefore in this work simply all generated cluster structures within a predefined energy range of interest are accepted. This allows to separate the analysis of the performance variation with the move distance from the specifically employed acceptance criterion.

In order to prevent an entropy-driven dissociation of the cluster during the BH run, trial moves as well as local relaxations are discarded that generate loosely connected or partly dissociated structures characterized by an atom having a nearest-neighbour distance larger than twice the dimer bond length. Similarly discarded were moves that place atoms at distances of less than 0.5 Å from each other.

Structure Distinction

For a performance analysis, it is of particular importance that the algorithm achieves to uniquely distinguish structures. In case of a simple analytical model potential, the total energy can be converged up to any desired accuracy, so that two isomers can be distinguished from each other exclusively by their different energetics. Using *ab initio* methods, however, the energy is noisy, thus prohibiting the structure distinction exclusively based upon the energy to uniquely distinguish different isomers from each other, in particular when Jahn-Teller distortions show up that are close in energy or in case of accidental degeneracies in energy space. Hence, the difference norm of all interatomic distances in the cluster is used as additional tool for the comparison of isomer structures. Two isomers a and b are hereby considered to be equivalent if

$$\frac{\sum_i (d_{a,\{i\}} - d_{b,\{i\}})^2}{\sum_i (d_{a,\{i\}}^2 + d_{b,\{i\}}^2)} < \Delta, \quad (9.2)$$

where $d_{a,\{i\}}$ and $d_{b,\{i\}}$ are the sorted interatomic distances of the two isomers to compare. The denominator serves as normalization which yields a dimensionless quantity that is furthermore species- and cluster-size independent. Δ can be tuned such that all isomers are unambiguously distinguished and was taken as 10^{-4} as is illustrated in Fig. 9.1. Shown are the number of different isomers that are considered to be different with respect to the tolerance Δ . Additionally, the maximum energy interval ΔE associated with an isomer is given, which is the range of the total energies of all structures that are found to be identical according to the difference norm. A large value in the range of eV hereby indicates that different isomers could obviously be not distinguished. Hence, a small

value of ΔE is a necessary criterium for a sufficiently small tolerance value Δ . In case of a too large threshold, isomers are considered to be identical, though being different, and the number of different structures that are identified is too small and the energy range is way above the typical noise of DFT calculations in the meV range. Taking an extremely large value of 10^{-1} , for instance, structures cannot be distinguished at all and thus there is only one isomer yielded by the structure distinction scheme. Reducing Δ consequently increases the number of isomers until it saturates at 10^{-4} when all different structures can uniquely be distinguished from each other. This perfectly coincides with a drop of the maximum energy range down to few meV, indicating that only energy noise due to the finite self-consistency criterium and force convergence criterium of the DFT calculations is left. Decreasing the threshold further leads again to a slight increase of the number of isomers. This can be rationalized by a second effect. In this case, the noise in the bond distances is too large and two structures are considered to be different, though corresponding to the same isomer. This picture is supported by the fact that the new structures that pop up must be energetically close to the already identified structures at a larger tolerance value since the maximum energy range ΔE is already at the order of meV. As Fig. 9.1 clearly shows, 10^{-4} is a reasonable value for all three cases. Hence, Eq. (9.2) indeed leads to a size- and species-independent norm for the structural difference between two isomers.

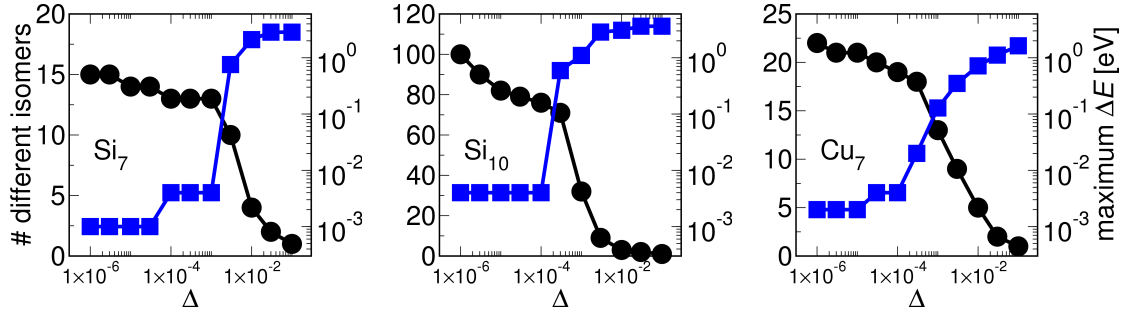


Figure 9.1.: Adjusting the difference tolerance Δ according to Eq. (9.2). Shown are the three cases Si_7 , Si_{10} and Cu_7 discussed in this work. The sets of isomers result from sampling runs, using single-particle moves and a normal distribution of the move distance around 1.5 times the corresponding dimer bond length.

9.2.3. Measuring Sampling Efficiency

The intended performance analysis requires a well-defined measure for the success of a sampling run. A common choice for this in the literature is the number of moves until the global minimum has been found for the first time. Here, we adapt this criterion to the stated goal of identifying not only the global minimum, but also all relevant energetically lowest-lying isomers. Correspondingly, the considered indicator of sampling efficiency which we aim to optimize is the number of moves N until all relevant isomers have been found at least once, where, of course, one needs to define what a relevant isomer

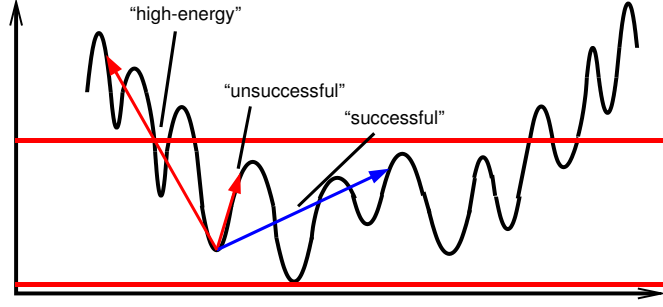


Figure 9.2.: Schematic illustration of successful, unsuccessful and high-energy trial moves in the BH scheme. The horizontal red lines indicate an energy window as acceptance criterium according to which moves within the target window are accepted.

is. While certainly a useful measure for the performance of the employed BH moves, it should still be stressed that due to the slightly varying number of geometry steps for the local relaxation of each trial structure, N is only roughly proportional to the total computational cost of the first-principles basin-hopping run.

Due to the stochastic nature of the BH method, both with respect to the generation of the initial starting structure and the generation of trial structures, N is only a statistically meaningful quantity after averaging over sufficiently many runs. Even for the small cluster sizes considered here, this implies having to run hundreds of different first-principles BH runs to obtain an N_{av} that is converged to within ± 1 , and this for each BH setting (e.g. move distance) one wants to analyze. Since this straightforward approach would quickly lead to an unfeasible computational cost, we instead resort to the concept of a “hopping matrix” h_{ij} , which summarizes the transition probabilities between all isomers under the chosen BH settings. Specifically, the matrix element h_{ij} is then the probability to jump from the local minimum i to the local minimum j . If all local minima are explicitly accounted for, one obviously has the condition

$$\sum_j h_{ij} = 1 \quad . \quad (9.3)$$

Assuming that the matrix h_{ij} is completely known, a sufficiently large number of sampling runs starting in random isomers can be quickly simulated entirely on the basis of these transition probabilities without the need for further first-principles calculations. Notwithstanding, with an exponentially growing number of isomers with cluster size this approach merely shifts the computationally unfeasible number of direct BH runs to the equally unfeasible computation of an exploding number of hopping matrix elements, i.e. converged transition probabilities. Yet, below we will show that an approximate, but for our purposes sufficient determination of N_{av} is possible by restricting the explicit calculations to a limited number of hopping matrix elements.

Even then, N_{av} is only a quantity that reflects the efficiency of the sampling run *a posteriori*. As potential on-the-fly indicators of the sort as discussed in the introduction, we therefore disentangle the different possible outcomes of a trial move. First of all, the

system might relax back into the structure from which the trial move has been performed so that in terms of isomer information nothing has been gained. Correspondingly, we denote such a move as unsuccessful (see Fig. 9.2) and define at the n th trial move during the run the fraction of hitherto unsuccessful moves $\gamma_{\text{unsucc.}}$ as

$$\gamma_{\text{unsucc.}} = \frac{n_{\text{unsucc.}}}{n} , \quad (9.4)$$

where $n_{\text{unsucc.}} < n$ is the number of unsuccessful moves up to that point. Even if the trial move leads to a different local minimum, the move might still be rejected due to the acceptance criterion, if the new minimum is higher up in energy. The fraction of moves rejected on this basis is defined as

$$\gamma_{\text{high}E} = \frac{n_{\text{high}E}}{n} , \quad (9.5)$$

where $n_{\text{high}E} < n$ is the corresponding number of rejected moves up to that point. Only the remaining fraction

$$\gamma_{\text{succ.}} = 1 - \gamma_{\text{unsucc.}} - \gamma_{\text{high}E} \quad (9.6)$$

are successful moves at least in the sense that they bring the algorithm to a new minimum out of which the next trial move is performed, albeit not necessarily leading to a minimum that had hitherto not yet been sampled. Just as in the case of N_{av} , it only makes sense to analyze the fractions $\gamma_{\text{unsucc.,av}}$, $\gamma_{\text{high}E,\text{av}}$ and $\gamma_{\text{succ.,av}}$ once averaged over sufficiently many different BH runs, and for the small cluster sizes we will also evaluate only the fractions for the entire run until all relevant isomers are found. Yet, it is obvious from the construction that one can also evaluate these fractions on-the-fly at any trial move and furthermore possibly also only considering the outcomes of a certain number of the most recently performed trial moves, and we will further discuss this possibility in section 9.4.

9.3. Performance Analysis For Small Cluster Sizes

Our performance analysis concentrates on small clusters formed of Si and small clusters formed of Cu atoms. Both systems have already been subject to extensive theoretical studies and are therefore natural choices for the intended benchmarking. Extensive works on small silicon clusters have been done with Hartree-Fock methods and beyond [117, 118]. Further calculations based upon DFT are e.g. [119, 120]. A database of small silicon isomers based upon the PBE functional and an exhaustive sampling based upon minima hopping can be found in the PhD-thesis by Hellmann [121]. Recent works on small copper clusters based upon *ab initio* methods are e.g. [122, 123, 124, 125, 126]. The choice of these two materials is further motivated by their different chemistry, which can be characterized as more covalent and directional in the case of Si, and more metallic in the case of Cu. The direct comparison of the results obtained for Si₇ and Cu₇ will therefore reflect a possible material-specificity of the findings, while an additional

comparison of the results obtained for Si_7 and Si_{10} aims at assessing the variation with cluster size in the range where due to the limited dimensionality of the configuration space the BH acceptance criterion does not yet play a role (*vide infra*).

9.3.1. Existence of Dominant Isomers

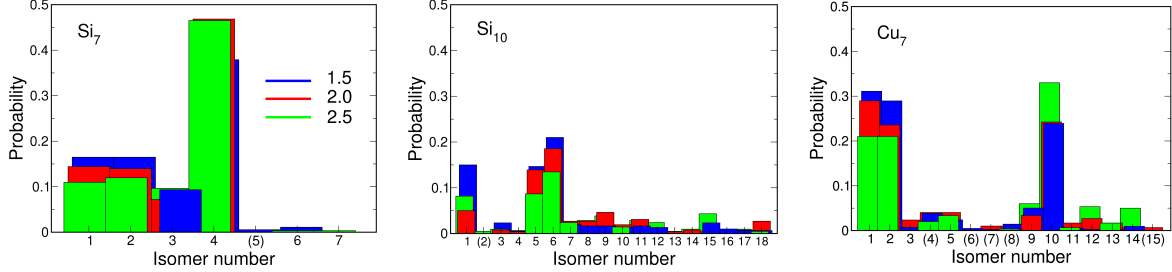


Figure 9.3.: Histograms of the probability with which trial moves end up in the lowest-energy isomers of Si_7 , Si_{10} and Cu_7 . The identified isomers are numbered with decreasing stability, with isomer #1 corresponding to the ground state and those isomers shown with bracketed numbers in fact revealed as unstable by an *a posteriori* vibrational analysis (see text). The histograms comprise all isomers found in an energy range up to 2 eV above the ground-state isomer, as obtained from long BH hopping runs using single-particle moves and normally distributed move distances around the average values $r_0 = 1.5 a$, $2.0 a$ and $2.5 a$ (with a the computed dimer bond length). The geometric structures behind the truly stable isomers in an energy range up to 1 eV above the identified ground state are summarized in Figs. 9.5-9.7.

As a prelude to the actual performance analysis we present in Fig. 9.3 the histograms of the number of times with which low-energy isomers were identified in long BH runs for the three systems addressed, i.e. Si_7 , Si_{10} , and Cu_7 . Each run consisted of several hundred moves and was carried out until the shape of the histogram, i.e. the normalized probability with which the different low-energy isomers are identified, was fully converged. In all cases the evolution towards convergence was rather uniform as demonstrated by Fig. 9.4 for Si_7 , which presents the histogram entries binned over consecutive sampling periods containing 50 moves each. Apparently, the ratios of the histogram entries for each sampling period are roughly the same. In view of the overall rather limited system dimensionality and concomitant small number of low-energy isomers, this is most naturally interpreted in terms of the initially made assumption that the employed move types enable jumps between any parts of the PES, thereby suggesting that for these systems the algorithm efficiency is dominated by the actual moves and not the acceptance criterion.

Even though Fig. 9.3 comprises the data obtained using single-particle moves with three quite different move distances it is interesting to observe that some isomers are always sampled much more often than others. For Si_7 for example, more than one third of

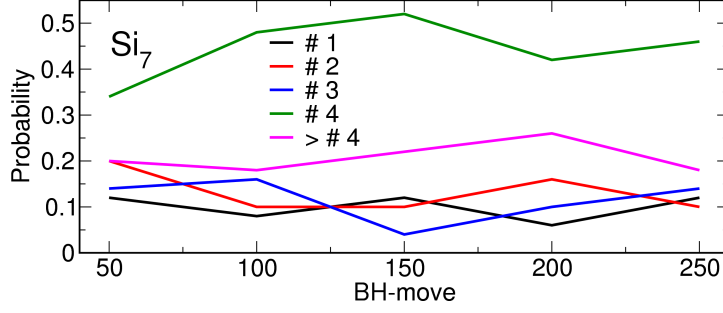


Figure 9.4.: Normalized histogram entries for the lowest-energy isomers of Si_7 as in Fig. 9.3. Shown is the evolution when binning the histogram entries over consecutive sampling periods containing 50 moves each using single-particle moves and normally distributed move distances around the average values $r_o = 2.5$. Entries for all isomers higher in energy than isomer #4 are bundled into one entry labeled $> \#4$.

all executed moves in the BH runs ended up in the isomer structure labeled #4, regardless of the actual move distance employed. In the case of collective moves, the corresponding histograms look qualitatively the same so that the existence of such “preferred” isomers, which we will henceforth term dominant isomers, is even independent of the specific move class employed. In this respect, one should mention that some of the isomers listed in Fig. 9.3 turned out to be unstable in the concluding vibrational analysis and are correspondingly not further considered below. Distinguishing and discarding these structures which correspond either to flat or saddle-point PES regions directly in the BH run is unfortunately impossible as it would imply a prohibitive computational cost when performing a vibrational analysis directly after each trial move. As apparent from Fig. 9.3 the total number of times in which the BH runs end up in such unstable structures is at least not too large, so that the actual computational time wasted is small. The one notable exception is isomer #4 of Cu_7 , which exhibits small imaginary eigenmodes, but is sampled about as frequently as the truly stable isomer #5. Since the algorithm thus spends some appreciable time in this basin, we retained isomer #4 in the ensuing performance analysis despite its instability.

One immediate rationalization for the existence of dominant isomers is simply that their corresponding basins of attraction on the PES is huge and thus hit by the trial moves many times. Inspection of the geometric structures of the lowest-energy isomers as summarized in Figs. 9.5 - 9.7 for the three systems points, however, at a second potential reason. Many of the dominant isomers correspond to rather low-symmetry structures, e.g. isomer #4 for Si_7 , isomer #6 for Si_{10} or isomer #10 for Cu_7 . More clearly stated, Si_7 can e.g. be regarded as composed of a Si_6 subunit with one capped facet. In the case of its low-symmetric isomer #4 this capping can be done in four different ways whereas in the case of the high-symmetry C_{3v} -structure #2 there are only two possibilities. Quantitatively, this can be expressed in terms of the number of versions of an isomer that correspond to the multiplicity of the basins of attractions leading to this isomer, which is given by Eq. (2.24). Table 9.1 summarizes the number of versions

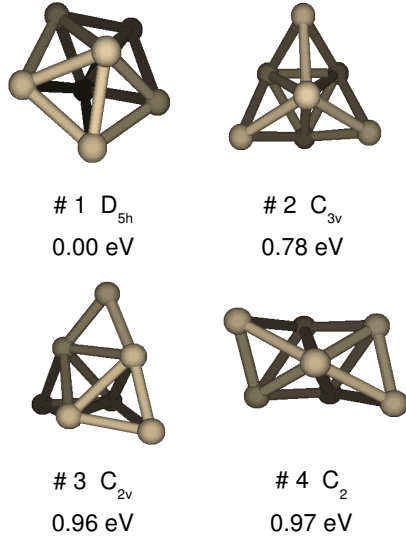


Figure 9.5: Identified stable Si_7 -isomers in the energy range up to 1 eV above the ground state. The isomer numbering follows the one of Fig. 9.3 and reflects the decreasing cluster stability as indicated by the stated energies relative to the ground-state isomer #1.

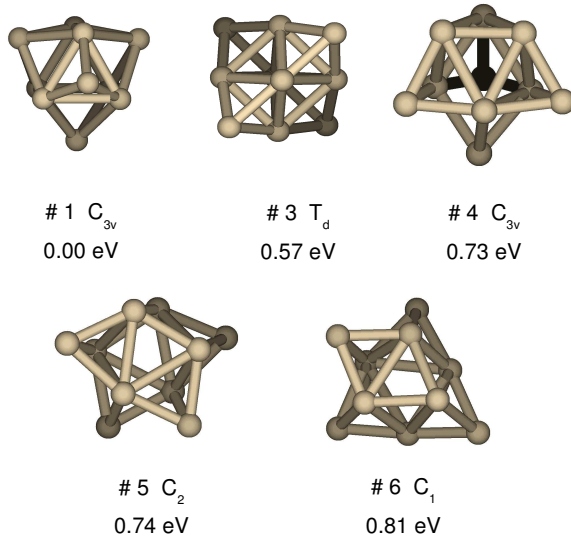


Figure 9.6: Identified stable Si_{10} -isomers in the energy range up to 1 eV above the ground state. The isomer numbering follows the one of Fig. 9.3 and reflects the decreasing cluster stability as indicated by the stated energies relative to the ground-state isomer #1.

for the dominant isomers. In the case of Si_7 and Cu_7 , for instance, the dominant isomers with low-symmetry have ten times more local minima on the PES than the symmetric ground-state structures and are therefore identified in the sampling much more often. Hence, the histogram can be regarded as a convolution of the size of the basin with the number of versions.

This relation to the underlying PES shape also motivates why certain isomers are dominant irrespective of the employed move class. Any general purpose move class that is intended to achieve unbiased jumps on the PES will be similarly affected by a varying size or multiplicity of the different basins of attraction. This is an important point as an at first glance appealing approach to improve the efficiency of BH sampling would be to reduce the number of times that the algorithm gets stuck in always the same dominant isomers and instead aim to increase jumps into the rare minima. Within the understanding of the relation to the PES shape it seems unlikely that this can be realized without either resorting to moves that are specifically tailored to the system at hand or

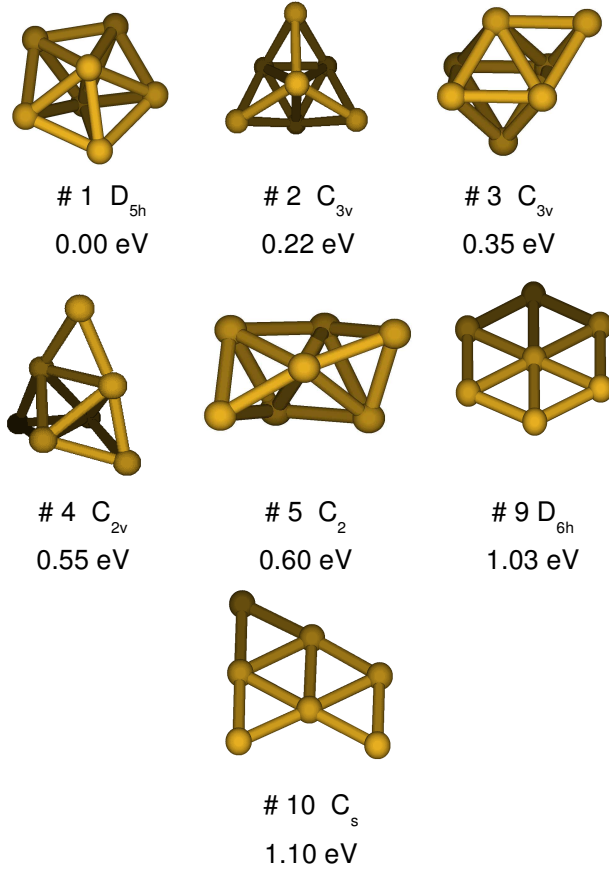


Figure 9.7: Identified stable Cu_7 -isomers in the energy range up to 1.1 eV above the ground state. The isomer numbering follows the one of Fig. 9.3 and reflects the decreasing cluster stability as indicated by the stated energies relative to the ground-state isomer #1. Note that isomer #4 exhibits small imaginary eigenmodes but is nevertheless retained in the performance analysis, see text.

use other local PES information. From the perspective of an unbiased sampling ansatz with purely stochastic moves it correspondingly seems inevitable that the algorithm will (at least for the limited isomer number of the small cluster sizes studied here) often revisit the same dominant isomers. The overall performance is then obviously dictated by the way the algorithm can deal with these dominant isomers, e.g. how efficiently it can hop out of them.

9.3.2. Approximate Hopping Matrix

On the basis of the histograms presented in Fig. 9.3 we can now specify which of the energetically lowest-lying isomers are the target of the sampling runs. In the general case, this would be dictated by the physics of the problem at hand, e.g. prescribing that the sampling should yield the ground-state isomer, as well as all isomers in a certain energy range above it. However in view of the discussion above, it is clear that the overall sampling performance is governed by the dominant isomers, since the algorithm spends most of its time jumping out of these few minima. For the intended performance analysis we therefore choose as the sampling target the identification of all dominant isomers. As indicator of the sampling efficiency we correspondingly focus on the number

| | | point group | N_{versions} |
|------------------|------|------------------------|-----------------------|
| Si_7 | # 1 | $\text{D}_{5\text{h}}$ | 504 |
| | # 2 | $\text{C}_{3\text{v}}$ | 1680 |
| | # 3 | $\text{C}_{2\text{v}}$ | 2520 |
| | # 4 | C_2 | 5040 |
| Cu_7 | # 1 | $\text{D}_{5\text{h}}$ | 504 |
| | # 9 | $\text{D}_{6\text{h}}$ | 420 |
| | # 10 | C_s | 5040 |
| Si_{10} | # 1 | $\text{C}_{3\text{v}}$ | 1209600 |
| | # 5 | C_2 | 3628800 |
| | # 6 | C_1 | 7257600 |

Table 9.1.: The number of different versions for the dominant isomers.

of moves N until all dominant isomers are found at least once. In the case of Si_7 and Si_{10} all dominant isomers are included in an energy range up to 1 eV above the ground state as apparent from Figs. 9.3, 9.5 and 9.7. In the case of Cu_7 , this energy range is slightly extended to 1.1 eV above the ground state to also include the dominant isomer #10, cf. Figs. 9.3 and 9.7.

With a thus defined sampling target the natural BH acceptance criterion is to unconditionally accept trial moves that lead into any isomer in the corresponding energy window, and to unconditionally reject any trial move that leads into an isomer that is higher in energy. It would only be necessary to change the latter to some, e.g. Boltzmann weighted, conditional acceptance rule, if a multiple-funnel type PES would necessitate passages via such higher energy isomers. However, as discussed above this is not the case for the systems studied here. In terms of a hopping matrix corresponding energy-window BH runs require only the knowledge of a limited number of hopping matrix elements. Definitely required are the transition probabilities between any of the targeted low-energy isomers. Since trial moves into higher energy isomers are rejected, it suffices to know the overall probability to jump from each one of the low-energy isomers into any of the higher energy ones, without the need to further resolve the latter. For the example of Si_7 the targeted energy window comprises 4 different isomers, and energy-window BH runs can therefore be simulated on the basis of 20 hopping matrix elements: 16 transition probabilities between any of the 4 different low-energy isomers, as well as one hopping matrix element per low-energy isomer that describes the sub-summed transition probability to jump out of the isomer into any of the higher energy ones.

For a specified BH setting (i.e. fixed move type and fixed technical move parameters) we obtain the required hopping matrix elements by simply performing a fixed number of trial moves out of each of the low-energy isomers, recording the probabilities with which the moves led into each of the other low-energy isomers or any of the higher-energy ones. After 100 moves these probabilities are converged to within ± 0.1 at a confidence interval

at the level of 95%, which we found to be sufficient for the conclusions put forward below. With the thus determined hopping matrix, a large number of energy-window BH runs from different starting isomers and with different random number sequences can be quickly simulated without the need for further first-principles calculations. This allows to arrive at a properly averaged number N_{av} of moves required to determine all low-energy isomers at least once, albeit with the disadvantage that the transition probabilities are only known within the confidence interval of ± 0.1 . To account for the latter, we therefore randomly varied the individual hopping matrix elements within this uncertainty range and under the constraint of Eq. (9.3). Determining the N_{av} for several hundreds of correspondingly created hopping matrices, we finally quote below the average value together with error bars given by the standard deviation.

This remaining uncertainty incurred from the approximate hopping matrix procedure does not affect any of the trend conclusions made below, yet on the other hand leads to a substantial reduction in the computational effort: In order to determine a well converged N_{av} for the systems studied here, required is typically an averaging over several hundreds BH runs starting from different initial isomers and with different random number sequences. As apparent below N_{av} for e.g. Cu_7 is of the order of 50, so that a straightforward determination of N_{av} by averaging over individual first-principles BH runs would require of the order of 5000 or more trial moves, with a corresponding number of first-principles energy and force evaluations. For the described hopping matrix based approach, however, only 100 moves out of each of the six low-energy isomers need to be done on the basis of first-principles calculations, while the ensuing hopping matrix based simulations are computationally undemanding. This reduces the overall computational cost by about an order of magnitude.

9.3.3. CPU Reduction by Using Optimum Sampling Parameters

For the ensuing move analysis, we first focus on a normal distribution which one would intuitively consider to be better, since it centers on a potential optimum value for the move distance. Further below, we then elaborate more on the random number distribution, taking additionally the uniform distribution into account.

Si₇ and Cu₇

In Fig. 9.8 we plotted the average move number along with the different fractions of moves introduced in section 9.2.3. It is apparent that for all cases a too small value of r_0 leads to a large move number N_{av} which goes down with increasing move distance until an optimum value for r_0 is reached. This rather obvious behaviour is reflected in the fraction of unsuccessful moves $\gamma_{\text{unsucc.}}$ which approaches one for too small move distances and goes down with increasing values for r_0 . Intriguingly, $\gamma_{\text{unsucc.}}$ never reaches zero but seems to asymptotically approach a finite value. To understand this behaviour we take a closer look at the diagonal elements of the hopping matrix h_{ii} , which describe the probability of the system to relax back in the previous structure after a trial move.

Obviously, $\gamma_{\text{unsucc.}}$ is just the average of $\{h_{ii}\}$ weighted by the corresponding histogram entries H_i :

$$\gamma_{\text{unsucc.}} = \frac{1}{N} \sum_{i=1}^N H_i h_{ii} \quad (9.7)$$

Consequently, if all diagonal elements vanished, $\gamma_{\text{unsucc.}}$ would reach zero. The upper panel of Fig. 9.9 presents the diagonal elements of all dominant isomers of Si_7 and Cu_7 with respect to the move distance for single-particle moves. For the case of Si_7 , the diagonal elements of the rather symmetric isomers # 1 - # 3 vanish with large enough distances as one would expect since the trial move then brings the system out of the current basin of attraction. For the unsymmetric Si_7 isomer with pointgroup C_2 , however, the hopping matrix element seems to stay constant. The same tendency can be observed for the case of Cu_7 , yet less pronounced. Clearly, the diagonal element of the unsymmetric C_s isomer does not further decrease when increasing the move distance beyond $2.0 a$ while the corresponding matrix elements of the more symmetric isomers seem to decrease monotonically. This is a further consequence of the comparably large number of versions of the low-symmetry structures of Si_7 and Cu_7 the system can relax into. In other words, by choosing a sufficiently large move distance, the system can be prevented from relaxing back into the previous structure but not from jumping between symmetry-equivalent basins of attraction. Consequently, $\gamma_{\text{unsucc.}}$ saturates at some point and N_{av} does not decrease any further. A similar behaviour can be observed for collective moves shown in the lower panel of Fig. 9.9.

In almost all cases, the move number starts to grow again, albeit insignificantly for practical purposes. A rational for this behaviour can be obtained by having a closer look at the fraction of rejected moves γ_{highE} which monotonically increases with the move distance r_0 . In other words, the larger r_0 , the more often the system jumps out of the energy region of interest. The remaining fraction of accepted moves $\gamma_{\text{succ.}}$ is finally the kind of moves that yield new isomers within the energy window of interest, so that intuitively it should be correlated with the overall move number N_{av} . This is indeed true for all four cases, in which $\gamma_{\text{succ.}}$ reaches a maximum at the optimum move distance that minimizes N_{av} .

For Si_7 , using single-particle moves, the optimum value for r_0 lies somewhere between $r_0 = 1.5 a$ and $2.5 a$ with only minor differences in the move number. Using collective moves, the best choice of r_0 is $0.75 a$. It is clear that displacing all atoms at once, the absolute value of r_0 can be smaller compared to single-particle moves, since the more atoms are involved the less each of them needs to be disturbed to change the configuration significantly. In the case of Cu_7 , the optimum move distance seems to be slightly extended to $2.0 a$ and $1.0 a$ using single-particle and collective moves, respectively. Comparing the move numbers N_{av} at the optimum value of r_0 for both move schemes, we note that there is basically no performance difference.

We further note that the fraction of accepted moves $\gamma_{\text{succ.}}$ is different for Si_7 and Cu_7 at their maximum. In the first case, roughly half of all the moves need to be accepted to optimize the efficiency, while for the latter case, the optimum fraction is

significantly higher (roughly 70 %). Hence, this example illustrates that aiming at a certain and system-independent absolute value for the acceptance ratio for all different kinds of systems is clearly not the best strategy to obtain an optimized sampling. For instance, in the case of Cu_7 using collective-moves, the move number and thus the overall efficiency is more than twice as large for an acceptance fraction of roughly a half ($N_{\text{av}} > 20$) compared to the optimum value of roughly 70 % ($N \approx 10$).

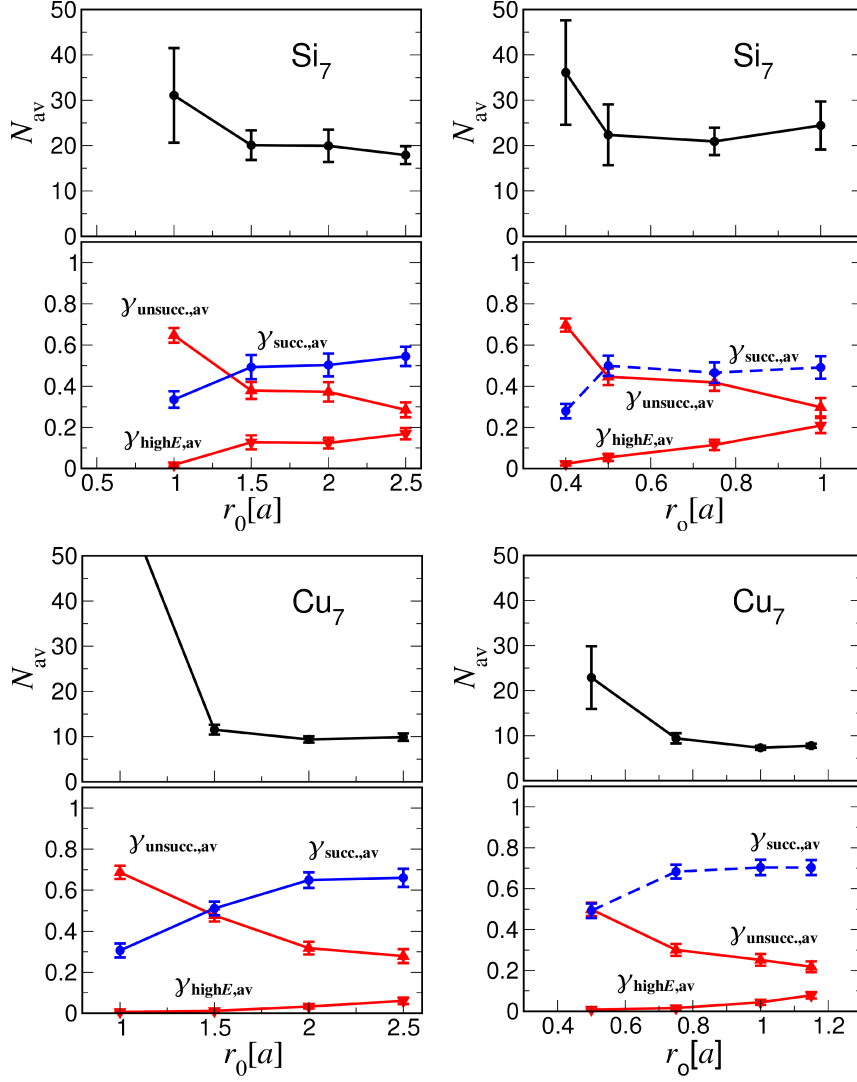


Figure 9.8.: Performance analysis for Si_7 and Cu_7 for both single-particle (left) and collective (right) moves. Given are the move number N_{av} including error-bar (upper panels) along with the different fraction of moves including error-bar (lower panels) γ_{unsucc} . (red curves with triangles pointing up), γ_{highE} (red curves with triangles pointing down) and γ_{succ} . (blue curve with circles).

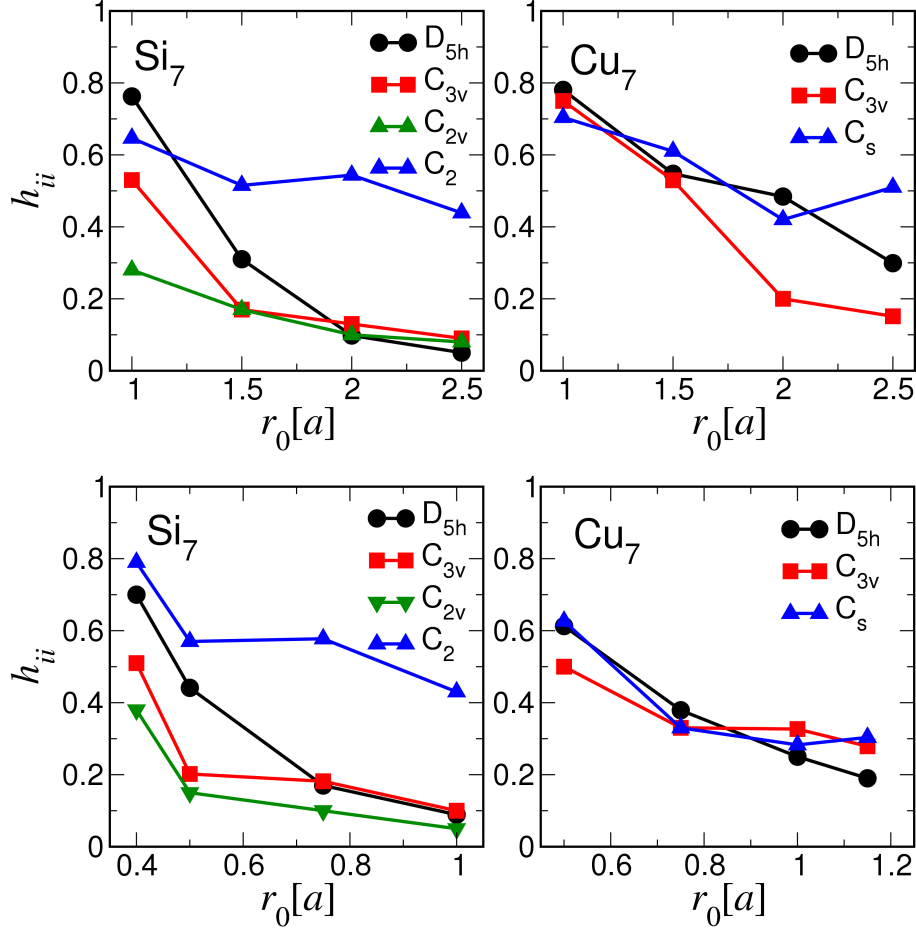


Figure 9.9.: Diagonal elements of the hopping matrix of the dominant isomers of Si₇ (# 1 (D_{5h}), # 2 (C_{3v}), # 3 (C_{2v}) and # 4 (C_2)) and Cu₇ (# 1 (D_{5h}), # 2 (C_{3v}), # 10 (C_s)) using single-particle (left) and collective (right) moves.

Si₁₀

Figure 9.10 presents the same analysis as above for Si₁₀ using collective moves. There are two striking features that can be assigned to the exponential growth of the number of different isomers. Since there are obviously more isomers above the energy window of interest, the probability to jump in the high-energy region is much higher than in the case of the smaller system Si₇. This is reflected in much higher values for $\gamma_{\text{high}E}$. At the maximum move distance of 1.0 a , roughly 20 % of the moves have led out of the energy window in the case of Si₇. With the same move parameter setting, four times as many moves jumped into the high-energy region in case of the larger system Si₁₀. The second effect is the stronger dependence of the unsuccessful moves $\gamma_{\text{unsucc.}}$ on the move distance. Due to the higher number of local minima, the effect of the multiplicity of individual isomers that saturates the fraction of unsuccessful moves becomes less significant, thus making $\gamma_{\text{unsucc.}}$ approach zero more closely. Consequently, the two competing effects of

having a too small or a too large move distance, reflected in the two different fractions of disadvantageous moves $\gamma_{\text{unsucc.}}$ and $\gamma_{\text{high}E}$, become much stronger, thus yielding a clear optimum of $\gamma_{\text{succ.}}$, which again nicely correlates with the move number N , the latter having a clear minimum in the range around 0.5 to 0.6 a . It is in particular the intuitively chosen acceptance criterium that gives rise to this clear correlation, thus making $\gamma_{\text{succ.}}$ a potential candidate for an on-the-fly indicator of efficiency. Since moves are unconditionally accepted if they lie within the energy window of interest, $\gamma_{\text{succ.}}$ corresponds exactly to the fraction of moves that explore the regions of the PES of interest.

As to the overall sampling efficiency, we further note that except for extremely unreasonable move distances, the basin-hopping scheme using unbiased collective moves is quite robust with respect to the exact value of the move distance. Around the range of 0.5 and 0.6 a , the move number varies less than a factor of two, which is in practice an insignificant uncertainty.

normal vs. uniform distribution

We now turn our attention to the random number distribution for the move distances. Intuitively, one would expect that focusing on an appropriate value r_0 as was done above is more efficient than using a uniform distribution around r_0 . The rational is simple. A uniform distribution contains both a large fraction of moves with quite small distances and a fraction of moves with rather large displacements as well. While the former is inefficient since the system tends to relax back into the previous structure, the latter can decrease the efficiency since the system jumps to high in energy as was shown above. To investigate on this we explicitly compared the efficiency of both distributions. The results are summarized in Table 9.2 and clearly prove that in the case of single-particle moves using the optimum value of r_0 , the normal distribution is more efficient than the uniform one. In the case of Si_7 with 1.5 a for instance, an average move number of 30.8 is obtained with the uniform distribution compared to 20.1 using a normal distribution. The same holds for Cu_7 with r_0 equals 1.5 or 2.0 a , where the uniform distribution yields an average move number about twice as large as in the case of the normal distribution. In the case of collective-moves, however, both uniform and normal distribution perform roughly the same for Si_7 and Cu_7 . The rational is here simply that in the case of collective moves, each atom has an individual move distance determined by a random number around r_0 . Consequently, even if some atoms are disturbed too much or too little, there are always certain atoms which are displaced with an appropriate move distance. In the case of Si_{10} , however, the uniform distribution seems to get less efficient compared to the normal distribution (e.g. 15.1 compared to 9.8 moves in the case of the optimum move distance 1.5 a). Again, this can be rationalized with the effect that a huge fraction of the moves lead to high-energy regions since the uniform distribution contains a larger ratio of move distances that are larger than the average value r_0 . Summarized, the uniform distribution can only be disadvantageous for the systems under consideration and is thus no longer considered.

| | move settings | normal | uniform |
|------------------|---------------|--------|---------|
| Si_7 | single | 1.0 a | 31.1 |
| | | 1.5 a | 34.6 |
| | collective | 0.5 a | 20.1 |
| | | 0.75 a | 30.8 |
| Cu_7 | single | 0.5 a | 22.4 |
| | | 0.75 a | 20.3 |
| | collective | 1.5 a | 11.5 |
| | | 2.0 a | 20.3 |
| Si_{10} | collective | 0.5 a | 22.9 |
| | | 0.75 a | 24.7 |
| | collective | 9.4 | 8.0 |
| | | 15.1 | 29.1 |

Table 9.2.: Performance comparison of normal-distributed and uniformly distributed random numbers for the move distance.

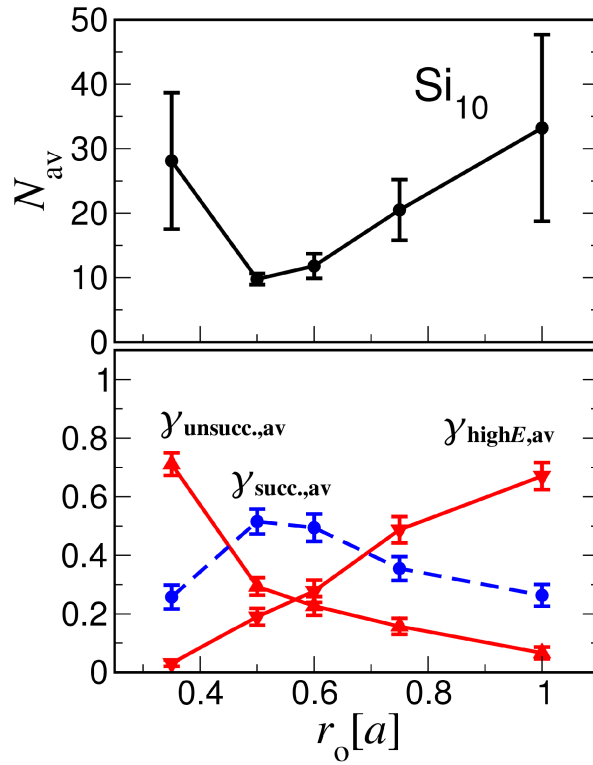


Figure 9.10.: Performance analysis for Si_{10} using collective moves.

9.4. Adaptive Move Scheme

On the basis of the above obtained insights, a simple adaptive scheme is now presented, which guides an unknown system towards reasonable move settings based upon optimizing $\gamma_{\text{succ.}}$. This efficiency indicator is therefore averaged over the last 50 moves, thus being converged up to ± 0.1 at a confidence interval at the level of 90 % (see as an example Fig. 9.11). As move scheme, collective moves are applied with a normal distribution around an average value r_0 . Our suggested self-adapting scheme then updates the average move distance according to simple rules. Starting with some initial value r_0 and a step width Δr , the change in the fraction of successful moves $\Delta\gamma_{\text{succ.}}$ between two averaging periods with r_0 and $r_0 + \Delta r$ is then monitored. Since $\gamma_{\text{succ.}}$ contains noise, the sign of $\Delta\gamma_{\text{succ.}}$ cannot directly be used as an indicator whether an updated move distance has improved the efficiency or not. Hence, a tolerance value of γ_{tol} needs to be defined which was set according to the convergence rate discussed above to 0.1. After two averaging periods, three cases then need to be distinguished. If $\gamma_{\text{succ.}}$ has increased more than the prescribed tolerance value

$$\Delta\gamma_{\text{succ.}} > \gamma_{\text{tol}} , \quad (9.8)$$

the change in the step width Δr has obviously improved the efficiency significantly.

Consequently, the adjustment Δr points into the direction of the maximum of $\gamma_{\text{succ.}}$ and the sign is therefore kept for the next move distance adaption. Additionally, the magnitude is slightly increased to accelerate the approach to the optimum value of r_0 , so $\Delta r \rightarrow \beta_1 \Delta r$, with $\beta_1 = 1.2$.

In the opposite case, if $\gamma_{\text{succ.}}$ has decreased more than the prescribed tolerance value

$$\Delta\gamma_{\text{succ.}} < -\gamma_{\text{tol}} , \quad (9.9)$$

the efficiency has significantly degraded and the sign of the adjustment Δr is therefore changed.

To enable the system to pin down the optimum value of the move distance, the magnitude is decreased in this case, so $\Delta r \rightarrow -\beta_2 \Delta r$, with $\beta_2 = 0.3$.

If $\Delta\gamma_{\text{succ.}}$ has not changed within the tolerance range,

$$-\gamma_{\text{tol}} < \Delta\gamma_{\text{succ.}} < \gamma_{\text{tol}} , \quad (9.10)$$

the current move distance r_0 is obviously close to the optimum range. However, in case of small “gradients” of $\gamma_{\text{succ.}}$, the system thus might get stuck in regions away from the maximum. Hence, the adjustment Δr is not set to zero, but instead only decreased in magnitude, so $\Delta r \rightarrow +\beta_2 \Delta r$.

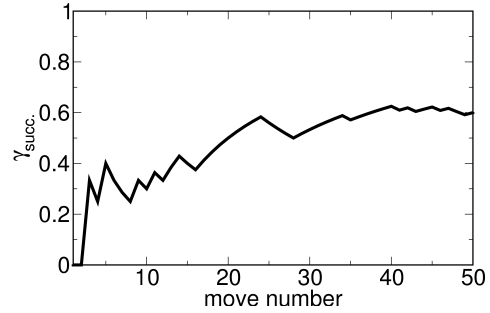


Figure 9.11.: The convergence of γ_{succ} with respect to the move number.

9. Method Optimization Based upon Quantitative Efficiency Criteria

Further fast adjustments according to $\gamma_{\text{unsucc.}}$ and $\gamma_{\text{high}E}$ additionally lead to a quick and coarse adjustment of the move distance by directly exploiting the obtained insights from the move analysis in the previous section. If the system got stuck in at least 9 out of 10 moves, it is clear that the current move distance must be way too small without further averaging $\gamma_{\text{succ.}}$. So if

$$\gamma_{\text{unsucc.}} \geq 0.9 , \quad (9.11)$$

the move distance r_0 is immediately increased by a certain amount Δr , which was typically chosen as equal to the initial adjustment. If on the other hand, more than half of the previous 10 moves lead to the high-energy region, so

$$\gamma_{\text{high}E} \geq 0.5 , \quad (9.12)$$

the move distance is likely to be too large and thus decreased by Δr , again (arbitrarily) set to the initial adjustment.

This simple scheme is illustrated for Si_{10} , using collective moves, for which the optimum parameter range for r_0 is known.

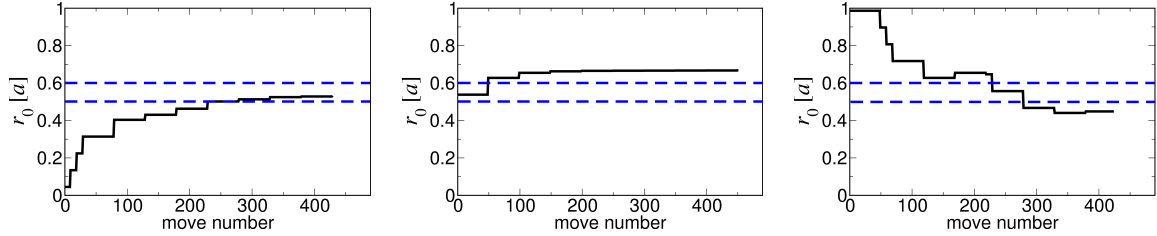


Figure 9.12.: Self-adapting move distance during a Si_{10} sampling run with window acceptance criterium and collective moves. Exemplified are three runs starting with a way too small move distance (left panel), a move distance that lies already in the optimum range (middle panel) and a way too large move distance (right panel). $\gamma_{\text{succ.}}$ is averaged over 50 moves with additional fast adjustments according to $\gamma_{\text{unsucc.}}$ and $\gamma_{\text{high}E}$. The blue dotted lines indicate the optimum range according to the performance analysis in section 9.3.3. The initial step adjustment Δr is set to 0.2 \AA or $0.09 a$, respectively.

Fig. 9.12 instances three cases, starting with a way too small move distance, a way too large one and with a setting that lies already within the reasonable range. Indicated are the two values 0.5 and $0.6 a$ that are optimum values according to sec. 9.3.3. As these three examples clearly show, the self-adapting scheme succeeds in guiding the system towards a reasonable move distance within $O(100)$ moves. Compared to this computational demand, even one data point in the move analysis for Si_{10} required 2000 trial moves, 100 moves for each of the 20 hopping matrix elements. Hence, our suggested self-adapting scheme provides an efficient scheme which exploits the on-the-fly efficiency indicators, thus preventing the system from inefficient sampling due to unreasonable move settings. As to the converged move distances in the three example runs, we note

that the optimum range where $\gamma_{\text{succ.}}$ is maximized, obviously lies somewhere between 0.45 and 0.7, thus not exhibiting a sharp peak but rather a broad plateau where the overall sampling efficiency is quite unaffected by the exact value of the move distance, which is in line with the insights obtained in section 9.3.3.

9.5. Summary and Conclusion

In this part of the work, the efficiency of an *ab initio* based basin-hopping run was quantitatively analyzed to reveal inefficient settings, thus suggesting potential ways to optimize the technical settings, in particular discussing consequences and possible strategies for larger cluster runs. To pin down the efficiency of a sampling run under a certain set of parameters, the common scheme in literature to measure the mean first encounter was extended to the number of moves until all relevant isomers within a pre-defined energy range have been identified at least once. This defined measure of efficiency is therewith coupled to the sampling goal of not only finding the ground state but also higher-lying isomers. To make the analysis computationally tractable, the concept of a so-called hopping matrix has been developed, thereby circumventing the necessity to perform hundreds of *ab initio* basin-hopping runs in order to get a statistically meaningful move number with respect to the stochastic noise and the dependence upon the starting geometry. Further on-the-fly measurable quantities have additionally been suggested that monitor the efficiency during a sampling run instead of just identifying an inefficient setting *a posteriori*, thus being candidates for possible self-adapting schemes. In order to elaborate on the question which isomers are relevant, long basin-hopping runs for Si_7 , Si_{10} and Cu_7 under different move settings, using both single-particle and collective moves, have been performed, revealing dominant isomers as an intrinsic feature of the PES. This property can be traced back to either a huge size of the corresponding basin of attraction or to the huge multiplicity of different versions corresponding to the same isomer. Since the system spends most of the time jumping between the dominant isomers, they obviously govern the overall performance and have thus been chosen as sampling goal. The performance analysis of the trial move is thereby separated from the acceptance criterium by using a window acceptance scheme, according to which isomers that lie within the energy window containing the dominant isomers are unconditionally accepted. Supported is this strategy by the fact, that for these cluster sizes, the simple stochastic trial move schemes enable efficient jumps between all parts of the configuration space. Using both single-particle and collective moves, the performance analysis yields a clear correlation between the move number N_{av} and the on-the-fly indicator $\gamma_{\text{succ.}}$, which is defined as the fraction of moves that lead to new isomers that lie within the energy window of interest. Comparing single-particle and collective moves, there is basically no difference between the move numbers at the corresponding optimum move distances. Further analysis of the random number distribution for the move distance only revealed a slight disadvantage of the uniform distribution compared to the normal distribution. Hence, the sampling in connection with simple stochastic moves turns out to be quite robust with respect to the analyzed parameters. Significantly inefficient

settings result mainly from way too small move distances, so that the system relaxes essentially always back to the previous minimum, or way too large distances, which tend to bring the system into high-energy PES regions, thus being out of the energy range of interest. In particular the last tendency becomes stronger with increasing cluster size, since the number of isomers exponentially grows and with that the configurational space in the high-energy region. Such inefficient settings can be avoided by a simple self-adapting scheme that is based upon the optimization of the indicator $\gamma_{\text{succ.}}$, which has been presented and illustrated for Si_{10} . Apart from unknown systems, for which this scheme is able to quickly identify the reasonable range of move distances, the system is expected to locally adjust the move distance in case of significant differences in the topologies in multi-funnel-systems. To gain further significant improvements in the sampling efficiency, more sophisticated trial moves would have to be designed that are able to explore the properties of the PES, like in the spirit of the MD-trajectories exploiting the BEP-principle. However, this always bears the danger of biasing the sampling. A completely different strategy would therefore be not to put emphasis on the sampling of the PES, but on the evaluation of the PES itself using sophisticated analytical potentials that are able to capture at least the same structural motifs as an *ab initio* energy surface.

10. Summary and Outlook

The motivation of the present work was to develop and analyze a DFT based basin-hopping algorithm for the structure determination of atomic clusters. This methodological approach has been applied for the interpretation of FIR-MPD data of small Co_n^+Ar_m ($n=4-8$) clusters, measured in the group of Prof. Gerard Meijer at the Molecular Physics Department of the FHI. The dataset of isomers generated from the unbiased sampling of configurational space included several cases of differently Jahn-Teller distorted versions of the same basic structural motif, which consequently would likely have been missed using the commonly employed scheme to simply try out “usual suspect” structures derived from chemical intuition. Specific conclusions concerning this part of the work, in particular on the nature of the Co-Ar binding, were already presented at the end of the corresponding chapter, which is why this final chapter is restricted to an outlook of only the methodological aspects.

The structure determination based on the comparison of vibrational spectra relies on the fundamental assumption that different isomers do exhibit distinguishable fingerprints. In the present work, however, many isomers, in particular the differently Jahn-Teller distorted ones, exhibited rather similar fingerprints with only minor quantitative differences, which in turn severely limited the approach to exclusively use FIR-MPD data to indirectly determine the atomic structure. Only in few cases the structure could be unambiguously determined, while in many cases some isomers could at best be ruled out or, put more modestly, turned out to be energetically rather unlikely. Taking additional experimental data into account, like for instance photoelectron spectroscopy, can therefore significantly facilitate the structural assignment by analyzing different independent fingerprints.

The involved exploration of the PES requires to combine two aspects. In order to obtain reliable energetics, a quantum-mechanical description of the PES is essential, which is nowadays typically achieved by density-functional theory. While single local optimizations of clusters at the size of few atoms constitute simple tasks with present day computational facilities, a basin-hopping run already at this system size may contain a few hundred optimizations, dictating already a high efficiency of both the calculation of the underlying PES and the sampling parameter. Using small silicon and copper clusters, we therefore demonstrated how the efficiency of an *ab initio* basin-hopping run can be critically assessed. For the system sizes studied, the crucial aspect is the trial move scheme, i.e. the way a new trial structure is generated from the previous one. The comparison of the efficiency for different move settings herein necessitates a quantity that pins down the computational demand of a certain run. For this, we extended the common scheme in the literature to count the number of moves until the ground state has been identified for the first time, to the mean first encounter of defined low-energy

isomers, since it is not only the ground-state structure that is of fundamental interest. The first step of the performance analysis hereby identified dominant (or frequently visited) isomers as an intrinsic feature of the PES. For the size range investigated, they consequently govern the overall computational demand of the sampling and are therefore the relevant isomers for the performance analysis. To lower the computational cost and additionally obtain detailed analysis data we circumvented the straightforward calculation of the manifold of sampling runs by introducing the concept of a hopping matrix. By recording the transition probabilities between the individual isomers within the energy range of interest, statistically meaningful quantities can then be extracted without the need for further first-principles calculations and the converged hopping matrix elements provide the connectivity of the low-lying isomers. This led to the observation of clear correlations between the number of required moves with on-the-fly efficiency indicators, that could then be used to develop a simple self-adapting scheme.

The move analysis focused on single-particle and collective moves. At the small cluster sizes studied no clear dominance of one move class over the other could be identified. Furthermore, each individual class turned out to be quite robust with respect to the average step width with which atoms are randomly displaced. The governing factors leading to this optimum move distance are the inability to escape from the basin of attraction of the present configuration at too short distances and the increased probability to end up in high-energy isomers at too large distances. The suggested self-adapting scheme exploits these insights and its performance has been demonstrated for Si_{10} , for which the self-adapting scheme guides and keeps the system within reasonable move settings.

In this respect, one has to note that simple stochastic move schemes provide only little flexibility to significantly improve the sampling efficiency. While this motivates the design of more sophisticated trial moves at first glance, such an approach always bears the danger to introduce bias or loose the general-purpose character. Nevertheless, when assessing such more specialized move types (also in view of the much more demanding size range beyond ten atoms) the evaluation should be based on a performance analysis protocol as presented in this work. In any case, orders of magnitude in the efficiency are much more likely to be gained not by optimizing the exploration, but instead the calculation of the PES itself. Simple empirical potentials can thereby not guarantee that the same structural motifs are captured, not to speak of their energetic order, thus making them unsuitable for a fast coarse screening of the configurational space. More promising are approaches that are based upon a parameterization of the *ab initio* PES, and therefore allow for a systematic convergence of the accuracy. In a collaboration with Dr. Jörg Behler from the Ruhr-Universität Bochum, we currently pursue this direction based on a neural network approach, which has recently been successfully applied to bulk silicon and achieved *ab initio* accuracy [127]. With an equally accurate parameterization for finite systems, this approach would then be an ideal candidate to enable sampling runs for significantly larger cluster sizes that are presently unfeasible with straightforward DFT energetics.

Part V.

Appendix

A. Basis Sets used in FHI-aims

| | Si | Cu | Co | Ar |
|---------|--------------------------------------|---------------------------------------|--------------------------------------|-----------------------|
| minimal | [Ne]+3s ² 3p ² | [Ar]+3d ¹⁰ 4s ¹ | [Ar]+3d ⁷ 4s ¹ | [Ar] |
| tier1 | H(3d, 4.2) | Cu ²⁺ (4p) | H(3p, 5.8) | Ar ²⁺ (3d) |
| | H(2p, 1.4) | H(4f, 7.2) | H(4f, 8.2) | Ar ²⁺ (4p) |
| | H(4f, 6.2) | H(3s, 2.6) | H(3d, 5.4) | H(4f, 7.4) |
| | Si ²⁺ (3s)* | H(3d, 4.9) | H(5g, 12.0) | H(3s, 4.5) |
| | | H(5g, 10.4) | Co ²⁺ (4s)* | |
| tier2 | H(3d, 9.0)* | H(4p, 5.8) | Co ²⁺ (4p)* | H(4d, 7.8) |
| | H(5g, 9.6) | H(6h, 14.8) | H(6h, 16.4) | H(5g, 10.4) |
| | H(4p, 4.0) | H(5s, 10.4) | H(4d, 5.6) | Ar ²⁺ (3p) |
| | H(1s, 0.65) | H(3d, 2.9) | H(4f, 17.2) | H(1s, 15.2)* |
| | H(4f, 8.2) | H(4f, 15.2) | H(1s, 0.75) | |
| tier3 | Si ²⁺ (3d) | H(3d, 3.6) | H(4d, 7.8) | H(4d, 5.8)* |
| | H(3s, 2.6) | H(3s, 2.5) | H(2p, 5.8) | H(5f, 9.2) |
| | H(3d, 3.4) | H(3p, 2.3) | H(4f, 8.0) | H(4s, 11.2) |
| | H(3p, 3.0) | H(5f, 8.4) | H(5g, 11.6) | H(5p, 10.8) |
| | H(4p, 6.4) | H(6g, 12.4) | H(4s, 4.3) | |
| | H(5g, 10.8) | | | |
| | ... | ... | ... | ... |

Table A.1.: Radial basis functions used in FHI-aims as they were selected during the basis optimization for the elements studied in this work Si, Cu, Co and Ar. "H(nl, z)" denotes a hydrogen-like basis function for the bare Coulomb potential z/r , including its radial and angular momentum quantum numbers n and l . $X^{2+}(nl)$ denotes a n, l radial function of a doubly positive free ion of species X. The radial functions marked with an asterisk have artificially been swapped to retain the otherwise consistent order into successive angular momentum shells ("tiers", see section 5). The minimal basis set simply contains the atomic functions according to the ground-state electronic configuration of the corresponding species.

The radial basis functions (each with $(2l+1)$ angular momentum functions) employed

in the present work together with their explanation are summarized in Table A.1. Apart from two exceptions, where in each case two basis functions have been artificially swapped, all angular momenta appeared naturally during the basis set generation procedure in the first tier. In the third tier, where improvements in the total energy lie only in the meV range, the order of the angular momenta is more or less arbitrary. The additional "minimal+*spd*" basis set, employed in chapter 9, is simply the tier1 set without the expensive *f* and *g* radial functions, which correspond to 7 and 9 basis functions, respectively. The bond distances $\{d_i\}$ used in the basis set generation according to Eq. 5.25 are spread to sample the self-consistent PW-LDA binding curve of the non-polarized dimer and are illustrated in Fig. A.1. We note that PW-LDA is unphysical for the Ar dimer since the latter is bound by pure van-der-Waals forces. In the basis set construction, however, it can still be used to simulate some kind of bonding to which the basis set is then optimized. Of course, in practical applications, extra care has to be taken whether a used tier is really converged.

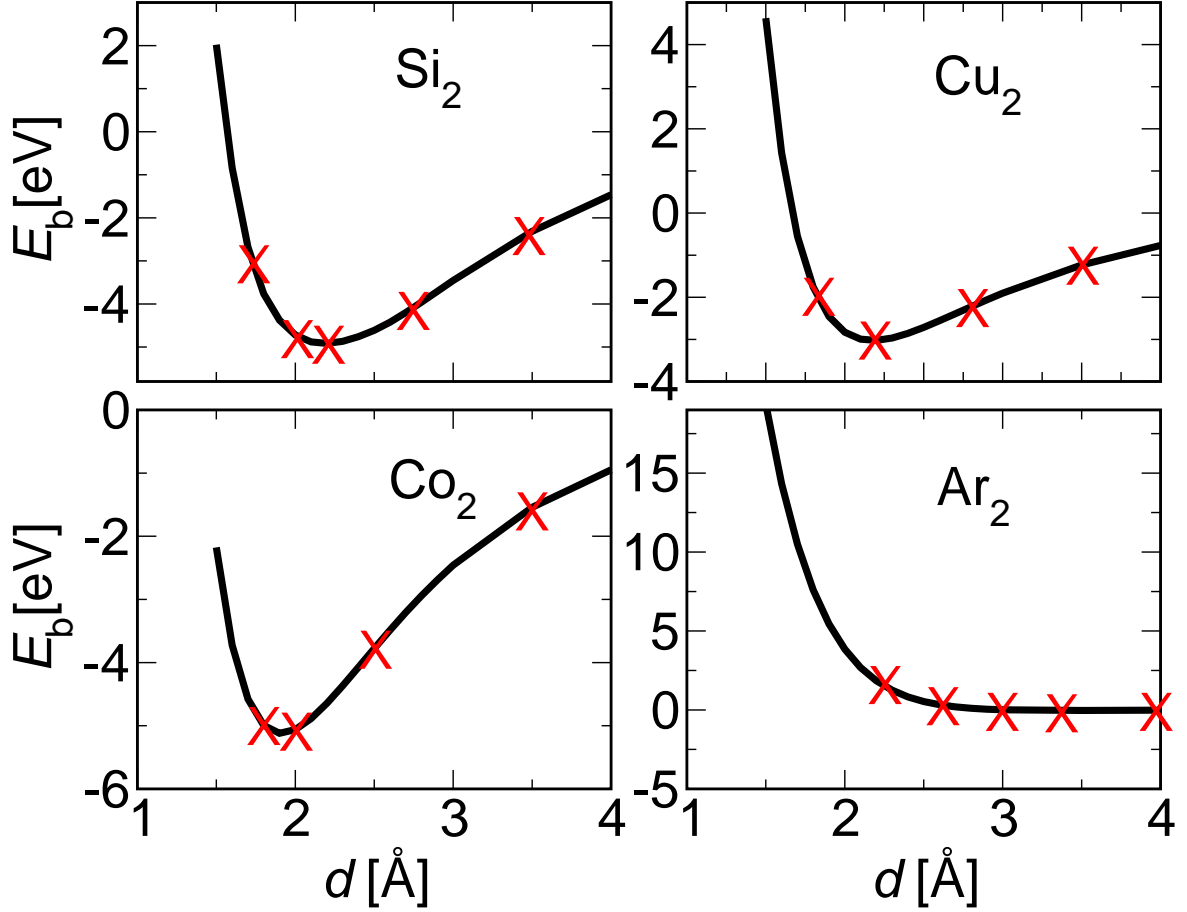


Figure A.1.: PW-LDA binding curves for basis set generation using a converged tier3 basis set to illustrate the chosen bond distances (marked by red crosses). $d_i[\text{\AA}] = \{1.75, 2.0, 2.25, 2.75, 3.5\}$ for Si, $d_i[\text{\AA}] = \{1.8, 2.2, 2.8, 3.5\}$ for Cu, $d_i[\text{\AA}] = \{1.8, 2.0, 2.5, 3.5\}$ for Co, $d_i[\text{\AA}] = \{2.25, 2.625, 3.0, 3.375, 4.0\}$ for Ar. All technical parameters are converged ($N_{\text{ang,max}}=302$, $N_{\text{r,div}}=2$, $l_{\text{max}}=6$, $r_{\text{cut}}=5$ Å, cf. Appendix B and C).

B. Convergence Tests for the Co_n^+Ar Complexes

The technical parameters to converge together with their default values in brackets are:

1. The integration grid which is determined by $N_{\text{r,div}}$ (2) and $N_{\text{ang,max}}$ (302). Cf. section 5.3.
2. The basis set (tier2). Cf. section 5.2.
3. The cutoff radius r_{cut} (5 Å). Cf. section 5.2.
4. The maximum angular momentum in the multipole decomposition of the Hartree potential l_{max} (6). Cf. section 5.4.
5. The force convergence criterium F_{max} (10^{-2} eV/Å). Cf. section 6.2.
6. The step width Δ (10^{-3} Å) for the finite displacement to calculate the Hessian and dipole derivatives. Cf. section 6.3.

For the ensuing convergence tests, each parameter is in turn individually varied whereas for the other parameters the default value is used and kept fixed. As will be shown below, these default settings are converged and have therefore been used in the production runs. All tests are done using the PBE functional. For the convergence tests, it is crucial to choose proper target quantities with respect to which the settings have to be converged, which in turn depends upon the actual problem to tackle. The starting point for the study of IR spectra of Co_n^+Ar complexes are isomers that are obtained from first-principles basin-hopping, both the bare Co clusters as well as the Co_n^+Ar complexes. Consequently, the corresponding energy differences ΔE between different isomers of the bare clusters and the complexes with Ar, respectively, need to be converged as well as the bond distances. Since we are interested in IR spectra, the frequencies ω together with the IR activities are additional target quantities. We therefore explicitly checked the convergence of the frequencies and the overall IR spectrum. Furthermore, the Ar binding energy was in the focus of interest, which is thus explicitly checked as well. The convergence tests focus on the the ground-state isomers of Co_4^+Ar and Co_6^+Ar , as well as a higher-lying isomer of each (see Fig. B.1). The bond distances, Ar binding energies, vibrational frequencies and IR spectra are considered for the ground-state isomers of the Co_n^+Ar complexes, whereas the energy differences are considered between the ground states and higher-lying isomers of the bare Co_n^+ clusters and additionally the Co_n^+Ar complexes. For the first four parameters, that are species-dependent, first the Co setting

has been converged with the Ar setting kept fixed. In a second step, the corresponding Ar setting has been varied with a fixed Co setting.

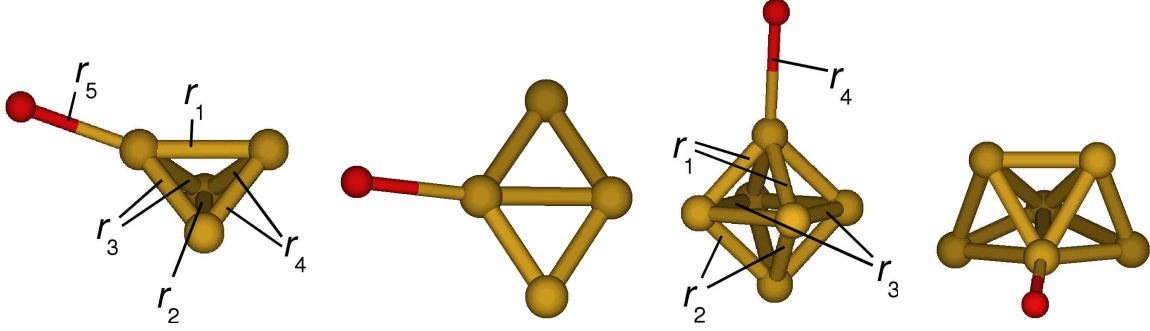


Figure B.1.: Co_n^+Ar -complexes used for the convergence tests. From left to right: ground-state isomer D_{2d} of Co_4^+Ar ($S=7/2$), higher-lying D_{2h} isomer ($S=9/2$), ground-state isomer D_{3d} of Co_6^+Ar ($S=15/2$), higher-lying C_{2v} isomer ($S=13/2$). Some bonds of the ground-state isomers are labelled that are used for the convergence tests.

B.1. Integration Grid

The angular part of the integration grid $N_{\text{ang,max}}$ is varied over several different Lebedev-grids, that are 194, 302, 434, 590 and 770. Using 302 the radial part which is determined by $N_{\text{r,div}}$ is augmented from 2 to 4. The convergence tests are summarized in Tables B.1, B.2, B.3, B.4 as well as in Fig. B.2.

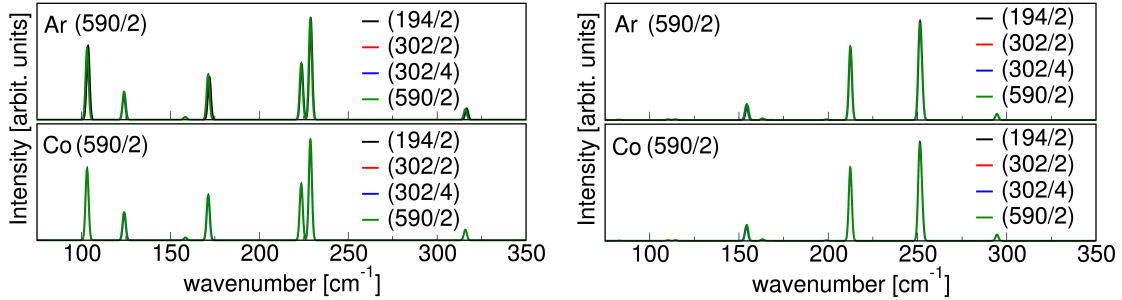


Figure B.2.: IR spectrum of the ground state of Co_4^+Ar (left panels) and Co_6^+Ar (right panels) vs. integration grid ($N_{\text{ang,max}}/N_{\text{r,div}}$). In the upper panels, the Ar integration grid is kept fixed, while the Co grid is varied. In the lower panels, vice versa.

As one can see, the integration grid is completely uncritical and convergence seems to be reached already for the smallest setting (194/2). For the production runs, we chose (302/2). We note that due to the adaptive grid scheme, this does not mean that the overall computational time is enhanced by a factor of 1.5, since $N_{\text{ang,max}}$ actually denotes only the maximum amount of angular integration points per radial shell that is possible.

B. Convergence Tests for the $\text{Co}_n^+ \text{Ar}$ Complexes

| Co-/Ar-grid | $\Delta E_{\text{CoN+Ar}}$ | $\Delta E_{\text{CoN+}}$ | E_b | ω_{lowest} | $\omega_{\text{main,1}}$ | $\omega_{\text{main,2}}$ | ω_{largest} |
|-------------------|----------------------------|--------------------------|-------|--------------------------|--------------------------|--------------------------|---------------------------|
| (194/2) / (590/2) | 0.562 | 0.537 | 0.303 | 27 | 224 | 229 | 317 |
| (302/2) / (590/2) | 0.562 | 0.536 | 0.303 | 30 | 224 | 229 | 316 |
| (434/2) / (590/2) | 0.562 | 0.536 | 0.303 | 30 | 224 | 229 | 316 |
| (590/2) / (590/2) | 0.562 | 0.537 | 0.303 | 29 | 224 | 229 | 316 |
| (770/2) / (590/2) | 0.562 | 0.537 | 0.303 | 30 | 224 | 229 | 316 |
| (302/4) / (590/2) | 0.562 | 0.536 | 0.303 | 30 | 224 | 229 | 316 |
| (590/2) / (194/2) | 0.562 | - | 0.303 | 30 | 224 | 229 | 316 |
| (590/2) / (302/2) | 0.562 | - | 0.303 | 30 | 224 | 229 | 316 |
| (590/2) / (434/2) | 0.562 | - | 0.303 | 30 | 224 | 229 | 316 |
| (590/2) / (590/2) | 0.562 | - | 0.303 | 29 | 224 | 229 | 316 |
| (590/2) / (770/2) | 0.562 | - | 0.303 | 30 | 224 | 229 | 316 |
| (590/2) / (302/4) | 0.562 | - | 0.302 | 30 | 224 | 229 | 316 |

Table B.1.: Convergence of the energy difference $\Delta E_{\text{CoN+Ar}}$ [eV] between the D_{2d} - and D_{2h} isomers of $\text{Co}_4^+ \text{Ar}$ as well as between the corresponding bare clusters $\Delta E_{\text{CoN+}}$ [eV], the Ar binding energy of the ground-state isomer D_{2d} of $\text{Co}_4^+ \text{Ar}$ and the lowest, largest and two main vibrational frequencies ω [cm^{-1}] of the D_{2d} isomer of $\text{Co}_4^+ \text{Ar}$ with respect to the integration grid ($N_{\text{ang,max}}/N_{\text{r,div}}$).

| Co-/Ar-grid | $\Delta E_{\text{CoN+Ar}}$ | $\Delta E_{\text{CoN+}}$ | E_b | ω_{lowest} | $\omega_{\text{main,1}}$ | $\omega_{\text{main,2}}$ | ω_{largest} |
|-------------------|----------------------------|--------------------------|-------|--------------------------|--------------------------|--------------------------|---------------------------|
| (194/2) / (590/2) | 0.445 | 0.561 | 0.116 | 17 | 213 | 251 | 295 |
| (302/2) / (590/2) | 0.442 | 0.559 | 0.116 | 15 | 212 | 251 | 295 |
| (434/2) / (590/2) | 0.441 | 0.558 | 0.115 | 17 | 213 | 251 | 295 |
| (590/2) / (590/2) | 0.442 | 0.559 | 0.117 | 17 | 212 | 251 | 295 |
| (770/2) / (590/2) | 0.441 | 0.559 | 0.115 | 18 | 213 | 251 | 295 |
| (302/4) / (590/2) | 0.442 | 0.559 | 0.116 | 15 | 212 | 251 | 295 |
| (590/2) / (194/2) | 0.442 | - | 0.116 | 19 | 212 | 251 | 295 |
| (590/2) / (302/2) | 0.442 | - | 0.116 | 19 | 212 | 251 | 295 |
| (590/2) / (434/2) | 0.442 | - | 0.116 | 17 | 212 | 251 | 295 |
| (590/2) / (590/2) | 0.442 | - | 0.117 | 17 | 212 | 251 | 295 |
| (590/2) / (770/2) | 0.442 | - | 0.116 | 19 | 212 | 251 | 295 |
| (590/2) / (302/4) | 0.442 | - | 0.116 | 19 | 212 | 251 | 295 |

Table B.2.: Convergence of the energy difference $\Delta E_{\text{CoN+Ar}}$ [eV] between D_{3d} - and C_{2v} isomers of $\text{Co}_6^+ \text{Ar}$ as well as between the corresponding bare clusters $\Delta E_{\text{CoN+}}$ [eV], the Ar binding energy of the ground-state isomer D_{3d} of $\text{Co}_6^+ \text{Ar}$ and the lowest, largest and two main vibrational frequencies ω [cm^{-1}] of the D_{3d} isomer of $\text{Co}_6^+ \text{Ar}$ with respect to the integration grid ($N_{\text{ang,max}}/N_{\text{r,div}}$).

B. Convergence Tests for the $\text{Co}_n^+ \text{Ar}$ Complexes

| Co-/Ar-grid | r_1 | r_2 | r_3 | r_4 | r_5 |
|-------------------|-------|-------|-------|-------|-------|
| (194/2) / (590/2) | 2.51 | 2.49 | 2.18 | 2.16 | 2.45 |
| (302/2) / (590/2) | 2.51 | 2.49 | 2.18 | 2.16 | 2.45 |
| (434/2) / (590/2) | 2.51 | 2.49 | 2.18 | 2.16 | 2.45 |
| (590/2) / (590/2) | 2.51 | 2.49 | 2.18 | 2.16 | 2.45 |
| (770/2) / (590/2) | 2.51 | 2.49 | 2.18 | 2.16 | 2.45 |
| (302/4) / (590/2) | 2.51 | 2.49 | 2.18 | 2.16 | 2.45 |
| (590/2) / (194/2) | 2.51 | 2.49 | 2.18 | 2.16 | 2.45 |
| (590/2) / (302/2) | 2.51 | 2.49 | 2.18 | 2.16 | 2.45 |
| (590/2) / (434/2) | 2.51 | 2.49 | 2.18 | 2.16 | 2.45 |
| (590/2) / (590/2) | 2.51 | 2.49 | 2.18 | 2.16 | 2.45 |
| (590/2) / (770/2) | 2.51 | 2.49 | 2.18 | 2.16 | 2.45 |
| (590/2) / (302/4) | 2.51 | 2.49 | 2.18 | 2.16 | 2.45 |

Table B.3.: Convergence of the bond distances [\AA] with respect to the integration grid ($N_{\text{ang,max}}/N_{\text{r,div}}$) for the ground-state isomer D_{2d} of $\text{Co}_4^+ \text{Ar}$.

| Co-/Ar-grid | r_1 | r_2 | r_3 | r_4 |
|-------------------|-------|-------|-------|-------|
| (194/2) / (590/2) | 2.37 | 2.27 | 2.26 | 2.76 |
| (302/2) / (590/2) | 2.37 | 2.27 | 2.26 | 2.76 |
| (434/2) / (590/2) | 2.37 | 2.27 | 2.26 | 2.76 |
| (590/2) / (590/2) | 2.37 | 2.27 | 2.26 | 2.74 |
| (770/2) / (590/2) | 2.37 | 2.27 | 2.26 | 2.76 |
| (302/4) / (590/2) | 2.37 | 2.27 | 2.26 | 2.76 |
| (590/2) / (194/2) | 2.37 | 2.27 | 2.26 | 2.76 |
| (590/2) / (302/2) | 2.37 | 2.27 | 2.26 | 2.76 |
| (590/2) / (434/2) | 2.37 | 2.27 | 2.26 | 2.76 |
| (590/2) / (590/2) | 2.37 | 2.27 | 2.26 | 2.74 |
| (590/2) / (770/2) | 2.37 | 2.27 | 2.26 | 2.76 |
| (590/2) / (302/4) | 2.37 | 2.27 | 2.26 | 2.76 |

Table B.4.: Convergence of the bond distances [\AA] with respect to the integration grid ($N_{\text{ang,max}}/N_{\text{r,div}}$) for the ground-state isomer D_{3d} of $\text{Co}_6^+ \text{Ar}$.

B.2. Basis Set Convergence

The basis set composition is given in Appendix A. The convergence tests are summarized in Tables B.5, B.6, B.7, B.8 and Fig. B.3.

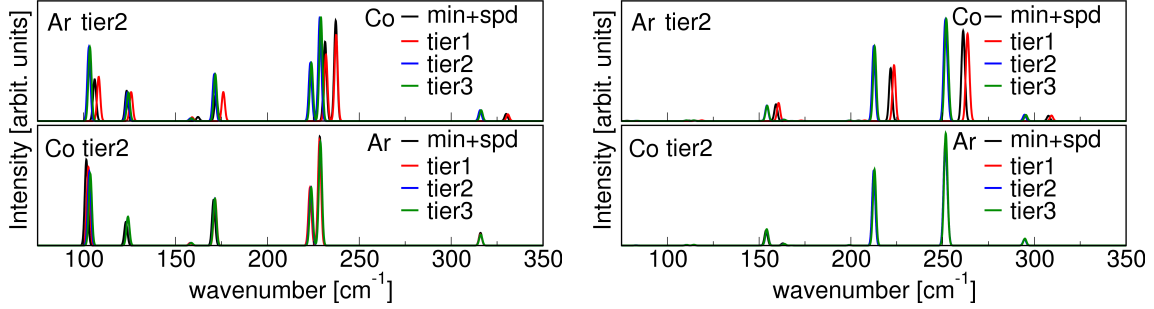


Figure B.3.: IR spectrum of the ground state of Co_4^+Ar (left panels) and Co_6^+Ar (right panels) vs. the basis set. In the upper panels, the Ar basis is kept fixed, while the Co basis is varied. In the lower panels, vice versa.

| Co-/Ar-basis | $\Delta E_{\text{CoN+Ar}}$ | $\Delta E_{\text{CoN+}}$ | E_b | ω_{lowest} | $\omega_{\text{main,1}}$ | $\omega_{\text{main,2}}$ | ω_{largest} |
|---------------|----------------------------|--------------------------|-------|--------------------------|--------------------------|--------------------------|---------------------------|
| min+spd/tier2 | 0.182 | 0.133 | 0.345 | 29 | 231 | 237 | 330 |
| tier1/tier2 | 0.259 | 0.211 | 0.346 | 29 | 232 | 237 | 331 |
| tier2/tier2 | 0.562 | 0.536 | 0.303 | 30 | 224 | 229 | 316 |
| tier3/tier2 | 0.569 | 0.543 | 0.295 | 31 | 224 | 229 | 316 |
| tier2/min+spd | 0.560 | - | 0.285 | 27 | 224 | 229 | 316 |
| tier2/tier1 | 0.562 | - | 0.295 | 30 | 223 | 228 | 316 |
| tier2/tier2 | 0.562 | - | 0.303 | 30 | 224 | 229 | 316 |
| tier2/tier3 | 0.562 | - | 0.306 | 30 | 224 | 229 | 316 |

Table B.5.: Convergence of the energy difference $\Delta E_{\text{CoN+Ar}}$ [eV] between the D_{2d} - and D_{2h} isomers of Co_4^+Ar as well as between the corresponding bare clusters $\Delta E_{\text{CoN+}}$ [eV], the Ar binding energy of the ground-state isomer D_{2d} of Co_4^+Ar and the lowest, largest and two main vibrational frequencies ω [cm^{-1}] of the D_{2d} isomer of Co_4^+Ar with respect to the basis sets.

In order to get quantitative results, a tier2 basis set for Co is obviously required, while for Ar the smaller tier1 basis set would be sufficient. Energy differences are then converged within 10 meV. The vibrational modes are accurate within 1 cm^{-1} and all bond distances are converged to 0.01 \AA . In most of the studied cases, there are only few Ar atoms, typically even only one, compared to several Co atoms in the cluster. Consequently, the Ar basis contributes only a minor fraction to the overall computational time and is thus not critical. Therefore, we consistently chose a tier2 basis for both species. Since the bond distances are decently converged already at the level of the minimal+spd basis, this reduced basis set has been used for the basin-hopping sampling prior to the electronic structure study. However, one cannot trust the energetics at this level. We therefore postrelaxed all structural motifs identified during the sampling using the tier2 basis set, regardless of their energy differences.

B. Convergence Tests for the $\text{Co}_n^+ \text{Ar}$ Complexes

| Co-/Ar-basis | $\Delta E_{\text{CoN+Ar}}$ | ΔE_{Co} | E_b | ω_{lowest} | $\omega_{\text{main,1}}$ | $\omega_{\text{main,2}}$ | ω_{largest} |
|------------------------|----------------------------|------------------------|-------|--------------------------|--------------------------|--------------------------|---------------------------|
| min+ <i>spd</i> /tier2 | 0.556 | 0.701 | 0.127 | 16 | 222 | 261 | 308 |
| tier1/tier2 | 0.586 | 0.736 | 0.128 | 17 | 224 | 263 | 309 |
| tier2/tier2 | 0.442 | 0.559 | 0.116 | 15 | 212 | 251 | 295 |
| tier3/tier2 | 0.441 | 0.555 | 0.110 | 14 | 213 | 251 | 295 |
| tier2/min+ <i>spd</i> | 0.447 | - | 0.106 | 13 | 213 | 251 | 295 |
| tier2/tier1 | 0.443 | - | 0.110 | 14 | 212 | 251 | 295 |
| tier2/tier2 | 0.442 | - | 0.116 | 15 | 212 | 251 | 295 |
| tier2/tier3 | 0.441 | - | 0.118 | 15 | 213 | 251 | 295 |

Table B.6.: Convergence of the energy difference $\Delta E_{\text{CoN+Ar}}$ [eV] between the D_{3d} and C_{2v} isomers of $\text{Co}_6^+ \text{Ar}$ as well as between the corresponding bare clusters $\Delta E_{\text{CoN+}}$ [eV], the Ar binding energy of the ground-state isomer D_{3d} of $\text{Co}_6^+ \text{Ar}$ and the lowest, largest and two main vibrational frequencies ω [cm^{-1}] of the D_{3d} isomer of $\text{Co}_6^+ \text{Ar}$ with respect to the basis sets.

| Co-/Ar-basis | r_1 | r_2 | r_3 | r_4 | r_5 |
|------------------------|-------|-------|-------|-------|-------|
| min+ <i>spd</i> /tier2 | 2.52 | 2.50 | 2.18 | 2.16 | 2.42 |
| tier1/tier2 | 2.50 | 2.49 | 2.16 | 2.14 | 2.42 |
| tier2/tier2 | 2.51 | 2.49 | 2.18 | 2.16 | 2.45 |
| tier3/tier2 | 2.51 | 2.49 | 2.18 | 2.17 | 2.45 |
| tier2/min+ <i>spd</i> | 2.51 | 2.49 | 2.18 | 2.16 | 2.47 |
| tier2/tier1 | 2.51 | 2.49 | 2.18 | 2.16 | 2.45 |
| tier2/tier2 | 2.51 | 2.49 | 2.18 | 2.17 | 2.45 |
| tier2/tier3 | 2.51 | 2.49 | 2.18 | 2.17 | 2.45 |

Table B.7.: Convergence of the bond distances [\AA] with respect to the basis sets for the ground-state isomer D_{2d} of $\text{Co}_4^+ \text{Ar}$.

| Co-/Ar-basis | r_1 | r_2 | r_3 | r_4 |
|------------------------|-------|-------|-------|-------|
| min+ <i>spd</i> /tier2 | 2.37 | 2.27 | 2.26 | 2.76 |
| tier1/tier2 | 2.35 | 2.25 | 2.24 | 2.74 |
| tier2/tier2 | 2.37 | 2.27 | 2.26 | 2.76 |
| tier3/tier2 | 2.37 | 2.27 | 2.26 | 2.76 |
| tier2/min+ <i>spd</i> | 2.37 | 2.27 | 2.26 | 2.76 |
| tier2/tier1 | 2.37 | 2.27 | 2.26 | 2.76 |
| tier2/tier2 | 2.37 | 2.27 | 2.26 | 2.76 |
| tier2/tier3 | 2.37 | 2.27 | 2.26 | 2.74 |

Table B.8.: Convergence of the bond distances [\AA] with respect to the basis sets for the ground-state isomer D_{3d} of $\text{Co}_6^+ \text{Ar}$.

B.3. Cutoff Radius

The cutoff radius r_{cut} is varied over the range of 3 to 6 Å. The results are summarized in Tables B.9, B.10, B.11, B.12 and Fig. B.4.

| $\text{Co-}/\text{Ar-}r_{\text{cut}}$ | $\Delta E_{\text{CoN+Ar}}$ | $\Delta E_{\text{CoN+}}$ | E_{b} | ω_{lowest} | $\omega_{\text{main,1}}$ | $\omega_{\text{main,2}}$ | ω_{largest} |
|---------------------------------------|----------------------------|--------------------------|----------------|--------------------------|--------------------------|--------------------------|---------------------------|
| 3 / 5 | 0.567 | 0.542 | 0.298 | 31 | 224 | 229 | 316 |
| 4 / 5 | 0.562 | 0.536 | 0.302 | 30 | 224 | 229 | 316 |
| 5 / 5 | 0.562 | 0.536 | 0.303 | 30 | 224 | 229 | 316 |
| 6 / 5 | 0.562 | 0.536 | 0.303 | 30 | 224 | 229 | 316 |
| 5 / 3 | 0.562 | - | 0.299 | 30 | 224 | 229 | 316 |
| 5 / 4 | 0.562 | - | 0.303 | 30 | 224 | 229 | 316 |
| 5 / 5 | 0.562 | - | 0.303 | 30 | 224 | 229 | 316 |
| 5 / 6 | 0.562 | - | 0.303 | 30 | 224 | 229 | 316 |

Table B.9.: Convergence of the energy difference $\Delta E_{\text{CoN+Ar}}$ [eV] between the $\text{D}_{2\text{d}}$ and $\text{D}_{2\text{h}}$ isomers of Co_4^+Ar as well as between the corresponding bare clusters $\Delta E_{\text{CoN+}}$ [eV], the Ar binding energy of the ground-state isomer $\text{D}_{2\text{d}}$ of Co_4^+Ar and the lowest, largest and two main vibrational frequencies ω [cm^{-1}] of the $\text{D}_{2\text{d}}$ isomer of Co_4^+Ar with respect to the cutoff radius r_{cut} [Å].

| $\text{Co-}/\text{Ar-}r_{\text{cut}}$ | $\Delta E_{\text{CoN+Ar}}$ | $\Delta E_{\text{CoN+}}$ | E_{b} | ω_{lowest} | $\omega_{\text{main,1}}$ | $\omega_{\text{main,2}}$ | ω_{largest} |
|---------------------------------------|----------------------------|--------------------------|----------------|--------------------------|--------------------------|--------------------------|---------------------------|
| 3 / 5 | 0.439 | 0.558 | 0.112 | 14 | 213 | 252 | 296 |
| 4 / 5 | 0.442 | 0.559 | 0.115 | 15 | 212 | 251 | 295 |
| 5 / 5 | 0.442 | 0.559 | 0.116 | 15 | 212 | 251 | 295 |
| 6 / 5 | 0.442 | 0.559 | 0.116 | 15 | 212 | 251 | 295 |
| 5 / 3 | 0.442 | - | 0.112 | 15 | 212 | 251 | 295 |
| 5 / 4 | 0.442 | - | 0.115 | 15 | 212 | 251 | 295 |
| 5 / 5 | 0.442 | - | 0.116 | 15 | 212 | 251 | 295 |
| 5 / 6 | 0.442 | - | 0.116 | 15 | 212 | 251 | 295 |

Table B.10.: Convergence of the energy difference $\Delta E_{\text{CoN+Ar}}$ [eV] between the $\text{D}_{3\text{d}}$ and $\text{C}_{2\text{v}}$ isomers of Co_6^+Ar as well as between the corresponding bare clusters ΔE_{Co} [eV], the Ar binding energy of the ground-state isomer $\text{D}_{3\text{d}}$ of Co_6^+Ar and the lowest, largest and two main vibrational frequencies ω [cm^{-1}] of the $\text{D}_{3\text{d}}$ isomer of Co_6^+Ar with respect to the cutoff radius r_{cut} [Å].

All results are tightly converged up to 2 meV, 1 cm^{-1} and 0.01 Å already at $r_{\text{cut}} = 4$ Å and decently converged up to 10 meV, 2 cm^{-1} and 0.01 Å with $r_{\text{cut}} = 3$ Å. Therefore, our conservatively chosen value of 5 Å provides tight convergence of all quantities at the tier2 basis set level.

B. Convergence Tests for the $\text{Co}_n^+ \text{Ar}$ Complexes

| Co-/Ar- r_{cut} | r_1 | r_2 | r_3 | r_4 | r_5 |
|--------------------------|-------|-------|-------|-------|-------|
| 3 / 5 | 2.51 | 2.49 | 2.18 | 2.16 | 2.45 |
| 4 / 5 | 2.51 | 2.49 | 2.18 | 2.16 | 2.45 |
| 5 / 5 | 2.51 | 2.49 | 2.18 | 2.16 | 2.45 |
| 6 / 5 | 2.51 | 2.49 | 2.18 | 2.16 | 2.45 |
| 5 / 3 | 2.51 | 2.49 | 2.18 | 2.16 | 2.45 |
| 5 / 4 | 2.51 | 2.49 | 2.18 | 2.16 | 2.45 |
| 5 / 5 | 2.51 | 2.49 | 2.18 | 2.16 | 2.45 |
| 5 / 6 | 2.51 | 2.49 | 2.18 | 2.16 | 2.45 |

Table B.11.: Convergence of the bond distances [\AA] with respect to the cutoff radius r_{cut} [\AA] for the ground-state isomer D_{2d} of $\text{Co}_4^+ \text{Ar}$.

| Co-/Ar- r_{cut} | r_1 | r_2 | r_3 | r_4 |
|--------------------------|-------|-------|-------|-------|
| 3 / 5 | 2.37 | 2.27 | 2.26 | 2.76 |
| 4 / 5 | 2.37 | 2.27 | 2.26 | 2.76 |
| 5 / 5 | 2.37 | 2.27 | 2.26 | 2.76 |
| 6 / 5 | 2.37 | 2.27 | 2.26 | 2.76 |
| 5 / 3 | 2.37 | 2.27 | 2.26 | 2.76 |
| 5 / 4 | 2.37 | 2.27 | 2.26 | 2.76 |
| 5 / 5 | 2.37 | 2.27 | 2.26 | 2.76 |
| 5 / 6 | 2.37 | 2.27 | 2.26 | 2.76 |

Table B.12.: Convergence of the bond distances [\AA] with respect to the cutoff radius r_{cut} [\AA] for the ground-state isomer D_{3d} of $\text{Co}_6^+ \text{Ar}$.

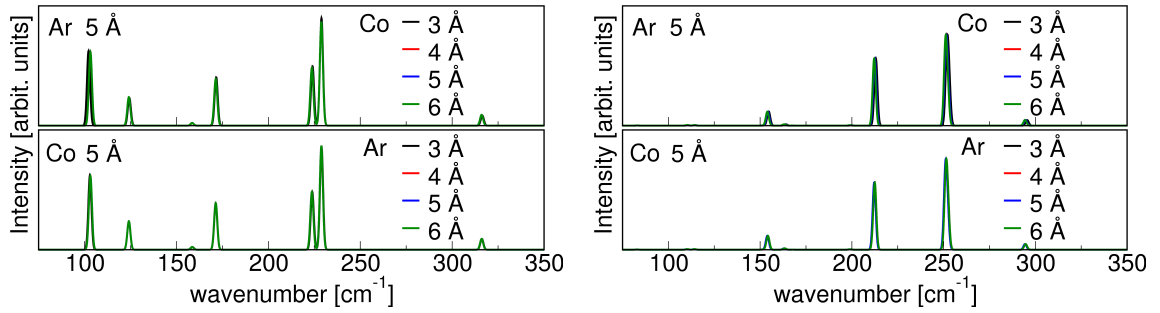


Figure B.4.: IR spectrum of the ground state of $\text{Co}_4^+ \text{Ar}$ (left panels) and $\text{Co}_6^+ \text{Ar}$ (right panels) vs. cutoff radius r_{cut} . In the upper panels, the Ar cutoff radius is kept fixed, while the Co cutoff radius is varied. In the lower panels, vice versa.

B.4. Hartree Potential

For the maximum angular momentum l_{max} in the multipole decomposition scheme, we tried a value of 3, 4, 6 and 8. The results are summarized in Tables B.13, B.14, B.15, B.16 and Fig. B.4.

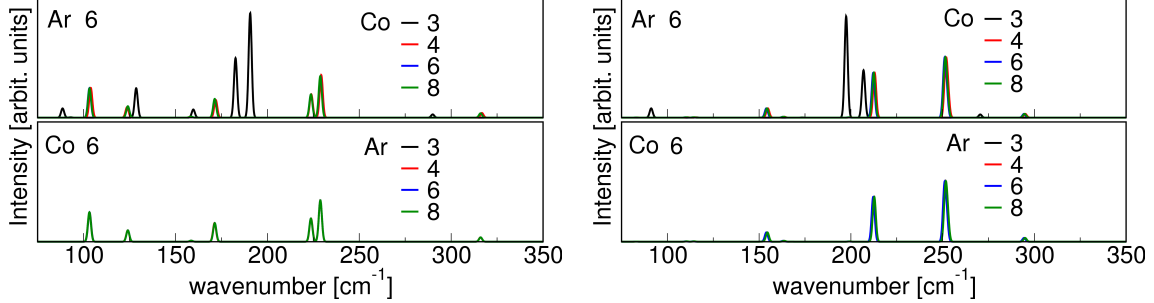


Figure B.5.: IR spectrum of the ground state of Co_4^+Ar (left panels) and Co_6^+Ar (right panels) vs. l_{max} . In the upper panels, the Ar l_{max} is kept fixed, while the Co l_{max} is varied. In the lower panels, vice versa.

| Co-/Ar- l_{max} | $\Delta E_{\text{CoN+Ar}}$ | $\Delta E_{\text{CoN+}}$ | E_b | ω_{lowest} | $\omega_{\text{main},1}$ | $\omega_{\text{main},2}$ | ω_{largest} |
|--------------------------|----------------------------|--------------------------|-------|--------------------------|--------------------------|--------------------------|---------------------------|
| 3 / 6 | 0.219 | 0.191 | 0.298 | 27 | 183 | 191 | 290 |
| 4 / 6 | 0.561 | 0.536 | 0.303 | 26 | 224 | 229 | 317 |
| 6 / 6 | 0.562 | 0.536 | 0.303 | 30 | 224 | 229 | 316 |
| 8 / 6 | 0.562 | 0.536 | 0.303 | 30 | 224 | 229 | 316 |
| 6 / 3 | 0.562 | - | 0.303 | 30 | 224 | 229 | 316 |
| 6 / 4 | 0.562 | - | 0.303 | 30 | 224 | 229 | 316 |
| 6 / 6 | 0.562 | - | 0.303 | 30 | 224 | 229 | 316 |
| 6 / 8 | 0.562 | - | 0.303 | 30 | 224 | 229 | 316 |

Table B.13.: Convergence of the energy difference $\Delta E_{\text{CoN+Ar}}$ [eV] between the D_{2d} and D_{2h} isomers of Co_4^+Ar as well as between the corresponding bare clusters $\Delta E_{\text{CoN+}}$ [eV], the Ar binding energy of the ground-state isomer D_{2d} of Co_4^+Ar and the lowest, largest and two main vibrational frequencies ω [cm^{-1}] of the D_{2d} isomer of Co_4^+Ar with respect to l_{max} .

A value of 3 for l_{max} is obviously too small, the energy differences are tenths of eV off. Bond distances are not converged within several hundredths of Å. Furthermore, the IR spectra do change a lot with increasing l_{max} . The C_{2v} isomer of Co_6^+ could not even be converged with $l_{\text{max}} = 3$. With a value of 4, however, tight convergence can be achieved. For Ar, l_{max} is not critical, since the density sitting on the single Ar atom contributes only little to the complete density. However, the contribution to the computational time is, like in the case of the basis set, not critical. We therefore chose for both species a conservative value of 6, for which tight convergence also for Co_4+Ar is achieved, where little noise was still observed for $l_{\text{max}} = 4$.

B. Convergence Tests for the Co_n^+Ar Complexes

| Co-/Ar- l_{max} | $\Delta E_{\text{CoN+Ar}}$ | ΔE_{Co} | E_{b} | ω_{lowest} | $\omega_{\text{main,1}}$ | $\omega_{\text{main,2}}$ | ω_{largest} |
|--------------------------|----------------------------|------------------------|----------------|--------------------------|--------------------------|--------------------------|---------------------------|
| 3 / 6 | N./A. | N./A. | 0.096 | 3 | 197 | 207 | 271 |
| 4 / 6 | 0.442 | 0.559 | 0.116 | 15 | 213 | 251 | 295 |
| 6 / 6 | 0.442 | 0.559 | 0.116 | 15 | 212 | 251 | 295 |
| 8 / 6 | 0.442 | 0.559 | 0.116 | 15 | 212 | 251 | 295 |
| 6 / 3 | 0.442 | - | 0.116 | 15 | 212 | 251 | 295 |
| 6 / 4 | 0.442 | - | 0.116 | 15 | 212 | 251 | 295 |
| 6 / 6 | 0.442 | - | 0.116 | 15 | 212 | 251 | 295 |
| 6 / 8 | 0.442 | - | 0.116 | 15 | 212 | 251 | 295 |

Table B.14.: Convergence of the energy difference $\Delta E_{\text{CoN+Ar}}$ [eV] between the $\text{D}_{3\text{d}}$ and $\text{C}_{2\text{v}}$ isomers of Co_6^+Ar as well as between the corresponding bare clusters $\Delta E_{\text{CoN+}}$ [eV], the Ar binding energy of the ground-state isomer $\text{D}_{3\text{d}}$ of Co_6^+Ar and the lowest, largest and two main vibrational frequencies ω [cm^{-1}] of the $\text{D}_{3\text{d}}$ isomer of Co_6^+Ar with respect to l_{max} .

| Co-/Ar- l_{max} | r_1 | r_2 | r_3 | r_4 | r_5 |
|--------------------------|-------|-------|-------|-------|-------|
| 3 / 6 | 2.51 | 2.49 | 2.21 | 2.20 | 2.44 |
| 4 / 6 | 2.51 | 2.49 | 2.18 | 2.16 | 2.45 |
| 6 / 6 | 2.51 | 2.49 | 2.18 | 2.16 | 2.45 |
| 8 / 6 | 2.51 | 2.49 | 2.18 | 2.17 | 2.45 |
| 6 / 3 | 2.51 | 2.49 | 2.18 | 2.16 | 2.45 |
| 6 / 4 | 2.51 | 2.49 | 2.18 | 2.16 | 2.45 |
| 6 / 6 | 2.51 | 2.49 | 2.18 | 2.16 | 2.45 |
| 6 / 8 | 2.51 | 2.49 | 2.18 | 2.16 | 2.45 |

Table B.15.: Convergence of the bond distances [\AA] with respect to l_{max} for the ground-state isomer $\text{D}_{2\text{d}}$ of Co_4^+Ar .

| Co-/Ar- l_{max} | r_1 | r_2 | r_3 | r_4 |
|--------------------------|-------|-------|-------|-------|
| 3 / 6 | 2.42 | 2.41 | 2.30 | 2.84 |
| 4 / 6 | 2.37 | 2.27 | 2.26 | 2.76 |
| 6 / 6 | 2.37 | 2.27 | 2.26 | 2.76 |
| 8 / 6 | 2.37 | 2.27 | 2.26 | 2.76 |
| 6 / 3 | 2.37 | 2.27 | 2.26 | 2.76 |
| 6 / 4 | 2.37 | 2.27 | 2.26 | 2.76 |
| 6 / 6 | 2.37 | 2.27 | 2.26 | 2.76 |
| 6 / 8 | 2.37 | 2.27 | 2.26 | 2.76 |

Table B.16.: Convergence of the bond distances [\AA] with respect to l_{max} for the ground-state isomer $\text{D}_{3\text{d}}$ of Co_6^+Ar .

B.5. Force Convergence Criterium and Finite Displacement for the Numerical Hessian and Dipole Gradient

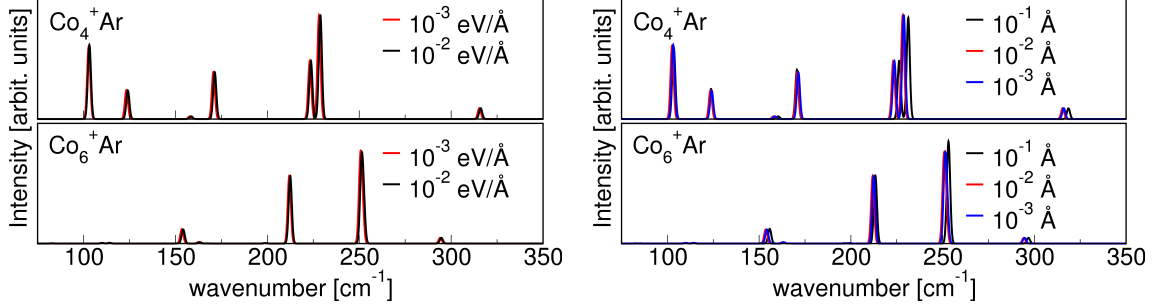


Figure B.6.: IR spectrum of the ground state of Co_4^+Ar and Co_6^+Ar vs. force convergence criterium F_{max} (left panels) and finite displacement Δ (right panels).

Though the bond distances, as was illustrated in section 6.2, are typically converged within 10^{-3} Å using a force convergence criterium for the local relaxation scheme of 10^{-2} eV/Å, it is *a priori* not clear, whether such a value is enough to converge the vibrational frequencies and IR spectra, for which it is essential to be in a local minimum. We therefore further relaxed the ground-state isomers of Co_4^+Ar and Co_6^+Ar further to a tighter force convergence criterium of 10^{-3} eV/Å and recomputed the IR spectra, which are presented in the left panel of Fig. B.6. As one can see, the IR spectra do not change at all. The step width Δ for the finite difference scheme to calculate the Hessian and dipole gradient numerically turns out to be uncritical (see the right panel of Fig. B.6). Our chosen value of 10^{-3} Å is small enough, ensuring a converged IR spectrum without showing grid noise due to the discrete integration grid.

C. Convergence Tests for Si and Cu clusters

The technical parameters to converge together with their default values in brackets are:

1. The integration grid which is determined by $N_{\text{r,div}}$ (2) and $N_{\text{ang,max}}$ (302). Cf. section 5.3.
2. The basis set (minimal+*spd*). Cf. section 5.2.
3. The cutoff radius r_{cut} (4 Å). Cf. section 5.2.
4. The maximum angular momentum in the multipole decomposition of the Hartree potential l_{max} (6). Cf. section 5.4.
5. The force convergence criterium F_{max} (10^{-2} eV/Å). Cf. section 6.2.
6. The step width Δ (10^{-3} Å) for the finite displacement to calculate the Hessian. Cf. section 6.3.

For the ensuing convergence tests, each parameter is in turn individually varied whereas for the other parameters the default value is used and kept fixed. As will be shown below, these default settings are sufficiently converged for the purpose of the intended study and have therefore been used in the production runs. All tests are done using the PBE functional with a Gaussian smearing of 0.1 eV width consistent to the production runs (see section 9.2). For the convergence tests, it is crucial to choose proper target quantities with respect to which the settings have to be converged, which in turn depends upon the actual problem to tackle. The focus of the study here lies in the sampling performance. Tightly converged physical quantities are therefore not crucial. Important are instead the right energetic order of the isomers and the correct structural motifs. We therefore check the energy differences with respect to the atomization energy

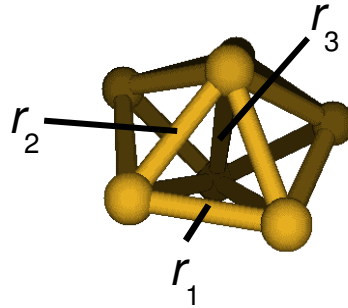


Figure C.1.: Pentagonal bipyramid motif of Si_7 and Cu_7 together with labelled bonds used for the convergence tests.

$$E_{\text{at}} = E_{\text{tot}}(X_N) - NE_{\text{tot}}(X) . \quad (\text{C.1})$$

of the ground state ($X=\text{Si}, \text{Cu}$) as well as the bond distances. The vibrational frequencies are important for the vibrational stability analysis. The convergence tests focus on the dominant isomers of Si_7 and Cu_7 (cf. section 9.3.1) concerning the energy difference. Bond distances, as well as the smallest and largest vibrational frequency are only given for the D_{5h} ground-state isomer.

C.1. Integration Grid

The angular part of the integration grid $N_{\text{ang,max}}$ is varied over several different Lebedev-grids, that are 194, 302, 434, 590 and 770. Using 302 the radial part which is determined by $N_{\text{r,div}}$ is augmented from 2 to 4. The convergence tests are summarized in Tables C.1 and C.2.

| grid | E_{at} | $\Delta E(\#2)$ | $\Delta E(\#3)$ | $\Delta E(\#4)$ | r_1 | r_2 | r_3 | ω_{smallest} | ω_{largest} |
|---------|-----------------|-----------------|-----------------|-----------------|-------|-------|-------|----------------------------|---------------------------|
| (194/2) | -31.362 | 0.780 | 0.957 | 0.968 | 2.51 | 2.49 | 2.55 | 170 | 435 |
| (302/2) | -31.361 | 0.782 | 0.956 | 0.965 | 2.51 | 2.49 | 2.55 | 171 | 435 |
| (434/2) | -31.362 | 0.782 | 0.959 | 0.966 | 2.51 | 2.49 | 2.55 | 171 | 435 |
| (590/2) | -31.363 | 0.782 | 0.958 | 0.967 | 2.51 | 2.49 | 2.55 | 170 | 435 |
| (770/2) | -31.363 | 0.782 | 0.958 | 0.967 | 2.51 | 2.49 | 2.55 | 170 | 435 |
| (302/4) | -31.361 | 0.782 | 0.956 | 0.965 | 2.51 | 2.49 | 2.55 | 171 | 435 |

Table C.1.: Convergence of the atomization energy E_{at} [eV] and energy differences w.r.t. the ground state ΔE [eV] for the four dominant isomers of Si_7 as well as the bond distances, smallest and largest vibrational frequency [cm^{-1}] of the ground state w.r.t. the integration grid ($N_{\text{ang,max}}/N_{\text{r,div}}$).

| grid | E_{at} | $\Delta E(\#2)$ | $\Delta E(\#10)$ | r_1 | r_2 | r_3 | ω_{smallest} | ω_{largest} |
|---------|-----------------|-----------------|------------------|-------|-------|-------|----------------------------|---------------------------|
| (194/2) | -14.701 | 0.225 | 1.105 | 2.46 | 2.46 | 2.60 | 70 | 240 |
| (302/2) | -14.700 | 0.223 | 1.103 | 2.46 | 2.46 | 2.60 | 70 | 240 |
| (434/2) | -14.699 | 0.222 | 1.103 | 2.46 | 2.46 | 2.60 | 70 | 240 |
| (590/2) | -14.699 | 0.222 | 1.103 | 2.46 | 2.46 | 2.60 | 70 | 240 |
| (770/2) | -14.699 | 0.222 | 1.103 | 2.46 | 2.46 | 2.60 | 70 | 240 |
| (302/4) | -14.700 | 0.223 | 1.103 | 2.46 | 2.46 | 2.60 | 70 | 240 |

Table C.2.: Convergence of the atomization energy E_{at} [eV] and energy differences w.r.t. the ground state ΔE [eV] for the three dominant isomers of Cu_7 as well as the bond distances, smallest and largest vibrational frequency [cm^{-1}] of the ground state w.r.t. the integration grid ($N_{\text{ang,max}}/N_{\text{r,div}}$).

The integration grids are not critical at all and all quantities are tightly converged using the default value of (302/2).

C.2. Basis Set Convergence

The basis set composition is given in Appendix A. The convergence tests are summarized in Tables C.3 and C.4.

| basis | E_{at} | $\Delta E(\#2)$ | $\Delta E(\#3)$ | $\Delta E(\#4)$ | r_1 | r_2 | r_3 | ω_{smallest} | ω_{largest} |
|-----------------|-----------------|-----------------|-----------------|-----------------|-------|-------|-------|----------------------------|---------------------------|
| min | -23.715 | 0.446 | N./A. | 0.618 | 2.78 | 2.79 | 2.95 | 114 | 346 |
| min+ <i>spd</i> | -31.361 | 0.782 | 0.956 | 0.965 | 2.51 | 2.49 | 2.55 | 171 | 435 |
| tier1 | -31.669 | 0.798 | 0.985 | 0.990 | 2.50 | 2.48 | 2.54 | 172 | 438 |
| tier2 | -31.788 | 0.784 | 0.977 | 0.986 | 2.50 | 2.47 | 2.52 | 172 | 437 |
| tier3 | -31.817 | 0.782 | 0.973 | 0.984 | 2.50 | 2.47 | 2.52 | 172 | 437 |

Table C.3.: Convergence of the atomization energy E_{at} [eV] and energy differences w.r.t. the ground state ΔE [eV] for the four dominant isomers of Si₇ as well as the bond distances, smallest and largest vibrational frequency [cm⁻¹] of the ground state w.r.t. the basis set.

| basis | E_{at} | $\Delta E(\#2)$ | $\Delta E(\#10)$ | r_1 | r_2 | r_3 | ω_{smallest} | ω_{largest} |
|-----------------|-----------------|-----------------|------------------|-------|-------|-------|----------------------------|---------------------------|
| min | -9.507 | 0.007 | 0.325 | 2.61 | 2.76 | 3.28 | 60 | 171 |
| min+ <i>spd</i> | -14.700 | 0.223 | 1.103 | 2.46 | 2.46 | 2.60 | 70 | 240 |
| tier1 | -14.906 | 0.226 | 1.097 | 2.45 | 2.45 | 2.57 | 71 | 240 |
| tier2 | -14.991 | 0.228 | 1.110 | 2.45 | 2.45 | 2.57 | 71 | 241 |
| tier3 | -15.030 | 0.231 | 1.118 | 2.45 | 2.45 | 2.57 | 71 | 241 |

Table C.4.: Convergence of the atomization energy E_{at} [eV] and energy differences w.r.t. the ground state ΔE [eV] for the three dominant isomers of Cu₇ as well as the bond distances, smallest and largest vibrational frequency [cm⁻¹] of the ground state w.r.t. the basis set.

Though tight convergence up to a few meV in the energy differences and 0.01 Å in the bond distances can only be achieved using a tier2 basis, the energetic order is already correct using a minimal+*spd* basis. Bond distances are converged within a few hundreds Å, so that the structural motifs are established. We therefore chose the reduced minimal+*spd* basis for the sampling performance analysis.

C.3. Cutoff Radius

The cutoff radius r_{cut} is varied over the range of 3 to 6 Å. The results are summarized in Tables C.5 and C.6.

| r_{cut} | E_{at} | $\Delta E(\#2)$ | $\Delta E(\#3)$ | $\Delta E(\#4)$ | r_1 | r_2 | r_3 | ω_{smallest} | ω_{largest} |
|------------------|-----------------|-----------------|-----------------|-----------------|-------|-------|-------|----------------------------|---------------------------|
| 3 | -31.198 | 0.786 | 0.953 | 0.966 | 2.51 | 2.49 | 2.55 | 170 | 434 |
| 4 | -31.361 | 0.782 | 0.956 | 0.965 | 2.51 | 2.49 | 2.55 | 171 | 435 |
| 5 | -31.368 | 0.782 | 0.956 | 0.964 | 2.51 | 2.49 | 2.55 | 170 | 435 |
| 6 | -31.368 | 0.782 | 0.956 | 0.964 | 2.51 | 2.49 | 2.55 | 170 | 435 |

Table C.5.: Convergence of the atomization energy E_{at} [eV] and energy differences w.r.t. the ground state ΔE [eV] for the four dominant isomers of Si₇ as well as the bond distances, smallest and largest vibrational frequency [cm⁻¹] of the ground state w.r.t. r_{cut} [Å].

| r_{cut} | E_{at} | $\Delta E(\#2)$ | $\Delta E(\#10)$ | r_1 | r_2 | r_3 | ω_{smallest} | ω_{largest} |
|------------------|-----------------|-----------------|------------------|-------|-------|-------|----------------------------|---------------------------|
| 3 | -14.510 | 0.222 | 1.081 | 2.46 | 2.46 | 2.60 | 70 | 240 |
| 4 | -14.700 | 0.223 | 1.103 | 2.46 | 2.46 | 2.60 | 70 | 240 |
| 5 | -14.723 | 0.224 | 1.107 | 2.46 | 2.46 | 2.60 | 70 | 239 |
| 6 | -14.725 | 0.224 | 1.108 | 2.46 | 2.46 | 2.60 | 70 | 239 |

Table C.6.: Convergence of the atomization energy E_{at} [eV] and energy differences w.r.t. the ground state ΔE [eV] for the three dominant isomers of Cu₇ as well as the bond distances, smallest and largest vibrational frequency [cm⁻¹] of the ground state w.r.t. r_{cut} [Å].

The bond distances do not vary at all over the range of the considered cutoff radii. Furthermore, the energy differences are converged within 10 meV and the vibrational frequencies within 2 cm⁻¹ at $r_{\text{cut}} = 4$ Å so that we chose this value for the production runs.

C.4. Hartree Potential

For the maximum angular momentum l_{\max} in the multipole decomposition scheme, we tried a value of 3, 4, 6 and 8. The results are summarized in Tables C.7 and C.8.

| l_{\max} | E_{at} | $\Delta E(\#2)$ | $\Delta E(\#3)$ | $\Delta E(\#4)$ | r_1 | r_2 | r_3 | ω_{smallest} | ω_{largest} |
|------------|-----------------|-----------------|-----------------|-----------------|-------|-------|-------|----------------------------|---------------------------|
| 3 | -31.369 | 0.779 | 0.954 | 0.961 | 2.51 | 2.49 | 2.55 | 170 | 435 |
| 4 | -31.365 | 0.781 | 0.956 | 0.964 | 2.51 | 2.49 | 2.55 | 170 | 435 |
| 6 | -31.361 | 0.782 | 0.956 | 0.965 | 2.51 | 2.49 | 2.55 | 171 | 435 |
| 8 | -31.361 | 0.782 | 0.956 | 0.965 | 2.51 | 2.49 | 2.55 | 170 | 435 |

Table C.7.: Convergence of the atomization energy E_{at} [eV] and energy differences w.r.t. the ground state ΔE [eV] for the four dominant isomers of Si₇ as well as the bond distances, smallest and largest vibrational frequency [cm⁻¹] of the ground state w.r.t. l_{\max} .

| l_{\max} | E_{at} | $\Delta E(\#2)$ | $\Delta E(\#10)$ | r_1 | r_2 | r_3 | ω_{smallest} | ω_{largest} |
|------------|-----------------|-----------------|------------------|-------|-------|-------|----------------------------|---------------------------|
| 3 | -14.713 | 0.223 | 1.104 | 2.46 | 2.46 | 2.60 | 70 | 240 |
| 4 | -14.704 | 0.223 | 1.104 | 2.46 | 2.46 | 2.60 | 70 | 240 |
| 6 | -14.700 | 0.223 | 1.103 | 2.46 | 2.46 | 2.60 | 70 | 240 |
| 8 | -14.700 | 0.223 | 1.103 | 2.46 | 2.46 | 2.60 | 70 | 240 |

Table C.8.: Convergence of the atomization energy E_{at} [eV] and energy differences w.r.t. the ground state ΔE [eV] for the three dominant isomers of Cu₇ as well as the bond distances, smallest and largest vibrational frequency [cm⁻¹] of the ground state w.r.t. l_{\max} .

Again, the results do not critically depend upon l_{\max} and with the default value of 6, all results are converged within 1 meV, 0.01 Å and 1 cm⁻¹ at the minimal+*spd* basis set level.

C.5. Force Convergence Criterium and Finite Displacement for the Numerical Hessian

| | | Si ₇ | | Cu ₇ | |
|-------------------------|-----------|----------------------------|---------------------------|----------------------------|---------------------------|
| | | ω_{smallest} | ω_{largest} | ω_{smallest} | ω_{largest} |
| F_{max} [eV/Å] | 10^{-2} | 170 | 435 | 70 | 240 |
| | 10^{-3} | 170 | 435 | 70 | 240 |
| Δ [Å] | 10^{-1} | 170 | 437 | 70 | 241 |
| | 10^{-2} | 170 | 435 | 70 | 240 |
| | 10^{-3} | 170 | 435 | 70 | 240 |

Table C.9.: Vibrational frequencies for the ground-state isomers of Si₇ and Cu₇ w.r.t. the force convergence criterium F_{max} and the finite displacement Δ .

Though the bond distances, as was illustrated in section 6.2, are typically converged within 10^{-3} Å using a force convergence criterium for the local relaxation scheme of 10^{-2} eV/Å, it is *a priori* not clear, whether such a value is enough to converge the vibrational frequencies, for which it is essential to be in a local minimum. We therefore further relaxed the ground-state isomers of Si₇ and Cu₇ further to a tighter force convergence criterium of 10^{-3} eV/Å and recomputed the vibrational spectra, of which the smallest and largest frequencies are presented in Table C.9. As one can see, the frequencies do not change at all. The step width Δ for the finite difference scheme to calculate the Hessian turns out to be uncritical. Our chosen value of 10^{-3} Å is small enough, ensuring a converged vibrational spectrum without showing grid noise due to the discrete integration grid.

D. High Order Finite Difference Schemes

Numerical derivatives are required for the calculation of the Hessian, which is composed of the first derivatives of the atomic forces. Furthermore, numerical forces are used as reference values for the accuracy tests of analytical forces. Accurate high-order schemes up to any desired order can herein be obtained by a Taylor-expansion.

$$\frac{\partial}{\partial x} f = \frac{1}{\tilde{C}h} \sum_{n=-N}^N C_n f(x_i + nh, y_j, z_k) + O(h^{2N}) . \quad (\text{D.1})$$

The coefficients are anti-symmetric with respect to the central node $f(x_i, y_j, z_k)$, i.e. $C_{-n} = -C_n$ and are given in Table D.1.

| N | \tilde{C} | C_3 | C_2 | C_1 | C_0 |
|-----|-------------|-------|-------|-------|-------|
| 1 | 2 | | | 1 | 0 |
| 2 | 12 | | -1 | 8 | 0 |
| 3 | 60 | 1 | -9 | 45 | 0 |

Table D.1.: Coefficients for the first numerical derivative

D. High Order Finite Difference Schemes

| N | \tilde{C} | C_6 | C_5 | C_4 | C_3 | C_2 | C_1 | C_0 |
|-----|-------------|-------|-------|-------|-------|---------|---------|----------|
| 1 | 1 | | | | | | 1 | -2 |
| 2 | 12 | | | | | -1 | 16 | -30 |
| 3 | 180 | | | | 2 | -27 | 270 | -490 |
| 4 | 5040 | | | -9 | 128 | -1008 | 8064 | -14350 |
| 5 | 25200 | | 8 | -125 | 1000 | -6000 | 42000 | -73766 |
| 6 | 831600 | -50 | 864 | -7425 | 44000 | -222750 | 1425600 | -2480478 |

Table D.2.: Coefficients for the second numerical derivative

Correspondingly, the second derivative can be discretized

$$\frac{\partial^2}{\partial x^2} \phi = \frac{1}{\tilde{C} h^2} \sum_{n=-N}^N C_n \phi(x_i + nh, y_j, z_k) + O(h^{2N+2}) . \quad (\text{D.2})$$

Here, the coefficients (Table D.2) are symmetric, i.e. $C_{-n} = C_n$.

E. Computed Structures and IR Spectra of Co_n^+Ar_m Complexes

In the following, all calculated Co_n^+Ar_m complexes for both PBE and PW-LDA are listed. Shown are the IR spectra together with the underlying geometry. For each structure, the spin state and the energy difference with respect to the ground-state isomer is given. All bond distances are given in units of Å. For each cluster size, the bare Co_n^+ clusters are presented first, being followed by Co_n^+Ar_m complexes, which are overlapped with the IR spectra of the corresponding bare clusters to emphasize the influence of the Ar probe atom on the vibrational fingerprint. For the larger Co_n^+Ar_m -complexes ($n=6-8$), only the Co-Ar bond distances are shown for the sake of overview, since the Co-Co distances are in these cases only slightly distorted in the order of few hundreds of Å with respect to the bare cluster. For a few larger clusters, the bond distances are not explicitly given in the plot, but the atoms are labelled instead and the corresponding distances are given on the last page of this Appendix. Furthermore, the energy differences shown for the Co_n^+Ar_m complexes are referred to the corresponding ground-state isomer of the Co_n^+ cluster structure. Complemented are the data by the binding energy of the Ar atom and the symmetry point group, the latter being defined within a threshold of 0.01 Å. We note that in the case of the Co_n^+Ar_m complexes, the symmetry point group is given for the corresponding bare cluster structure, since the Ar atom always breaks the symmetry which reduces the exact point group almost always to C_1 and thus makes the concept of the point group useless in the context of nomenclature if implying the Ar atom explicitly.

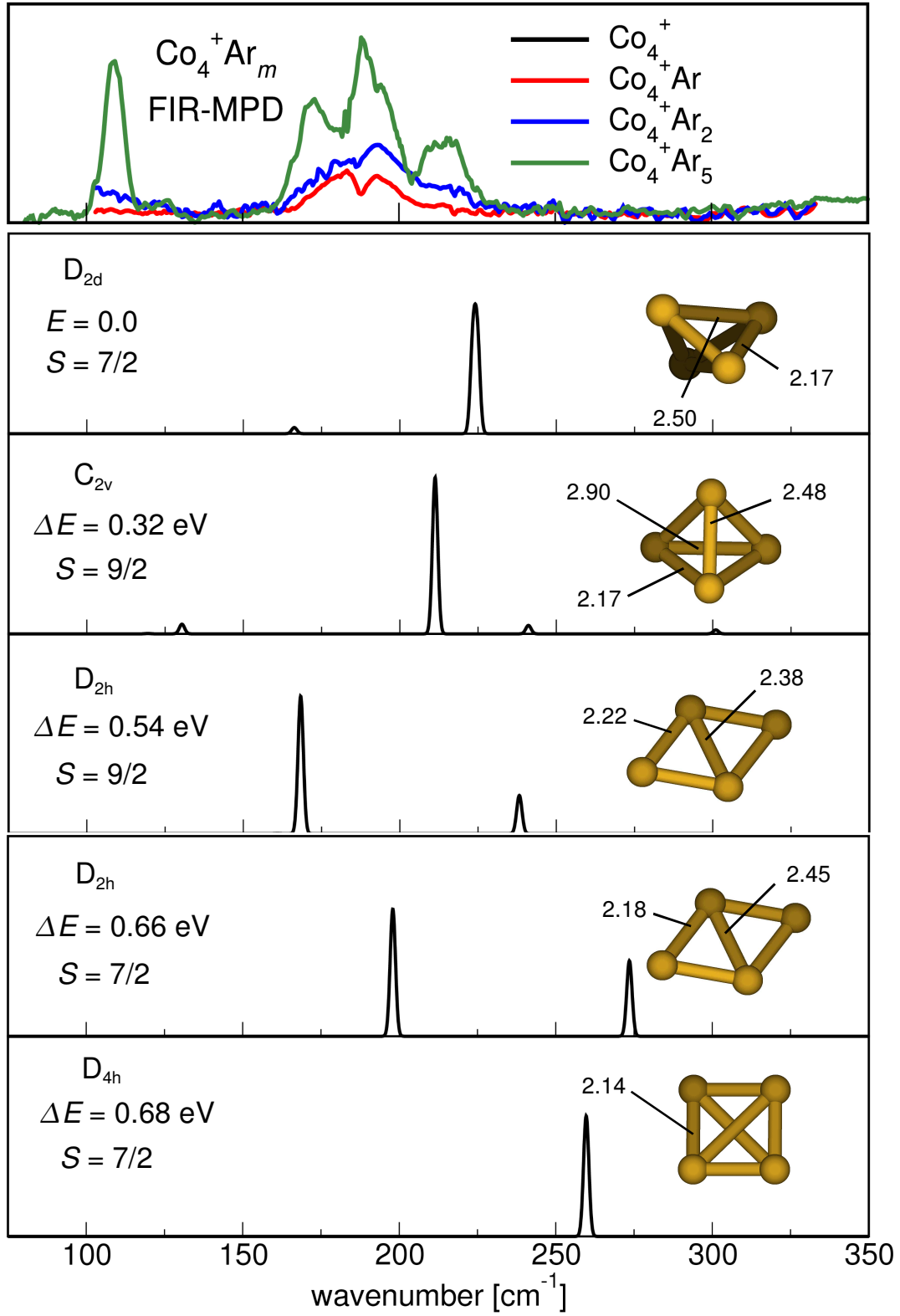


Figure E.1.: Co_4^+ IR spectra with PBE

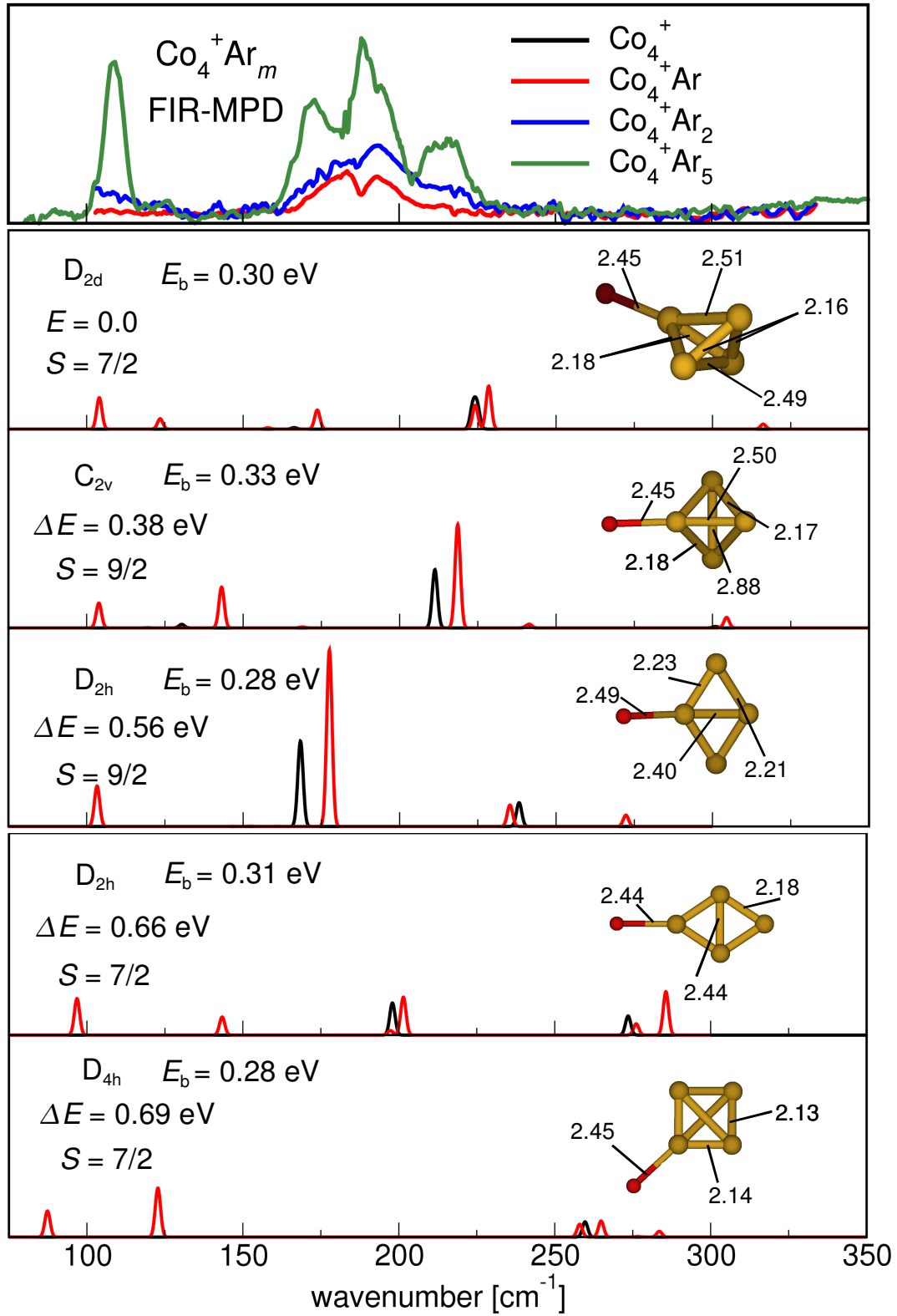


Figure E.2.: $\text{Co}_4^+ \text{Ar}$ IR spectra with PBE

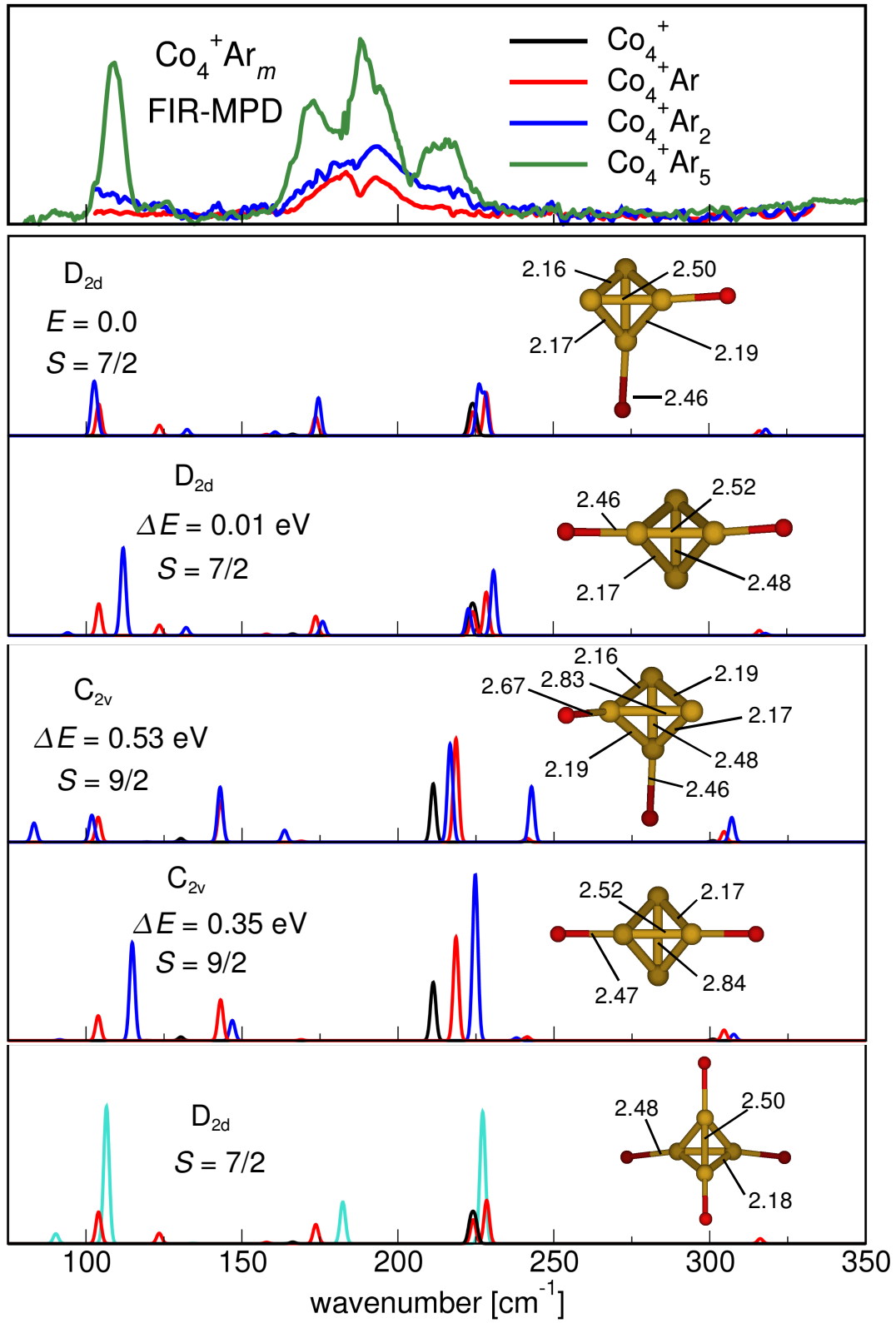


Figure E.3.: $\text{Co}_4^+ \text{Ar}_m$ IR spectra with PBE

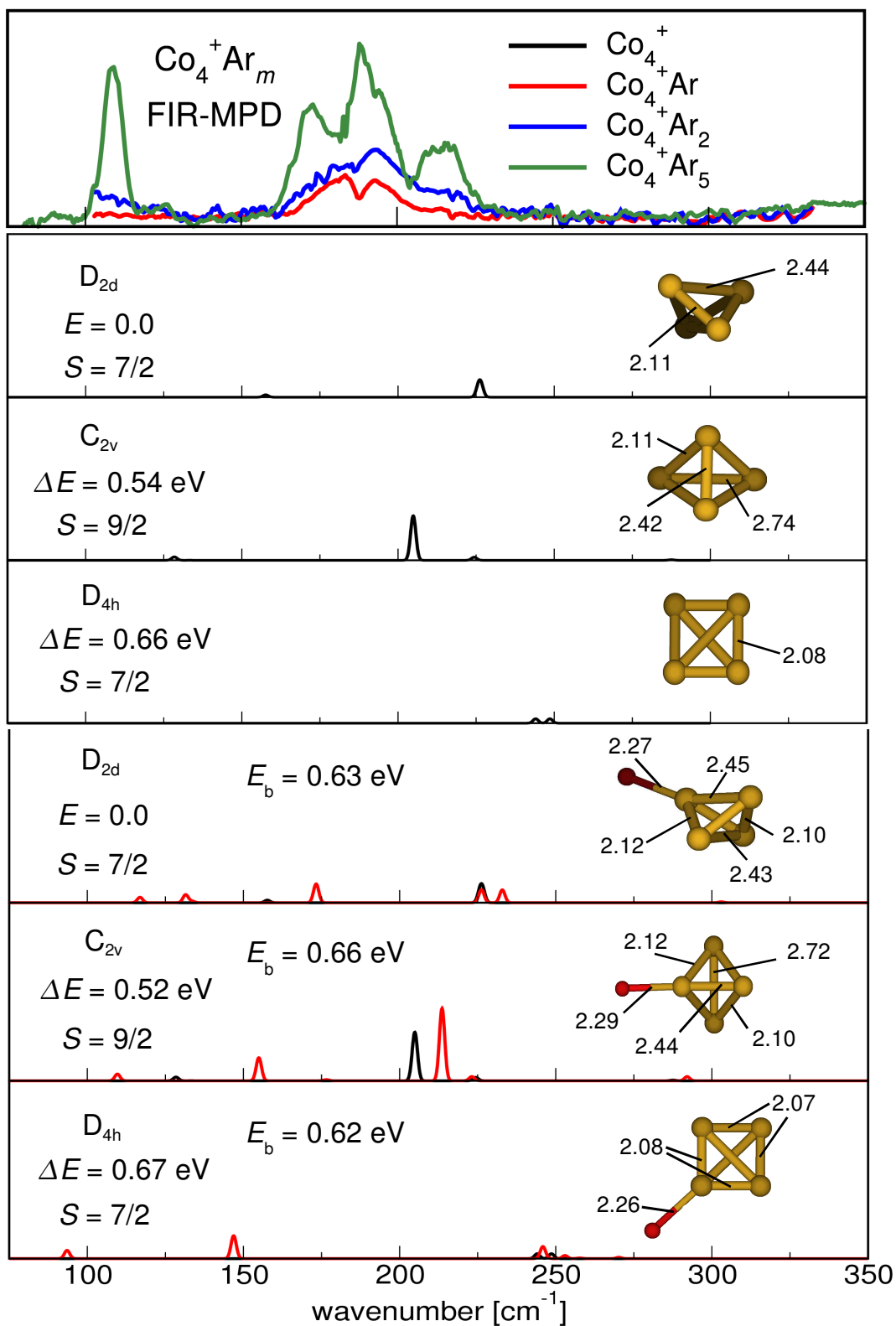


Figure E.4.: $\text{Co}_4^+ \text{Ar}$ IR spectra with PW-LDA

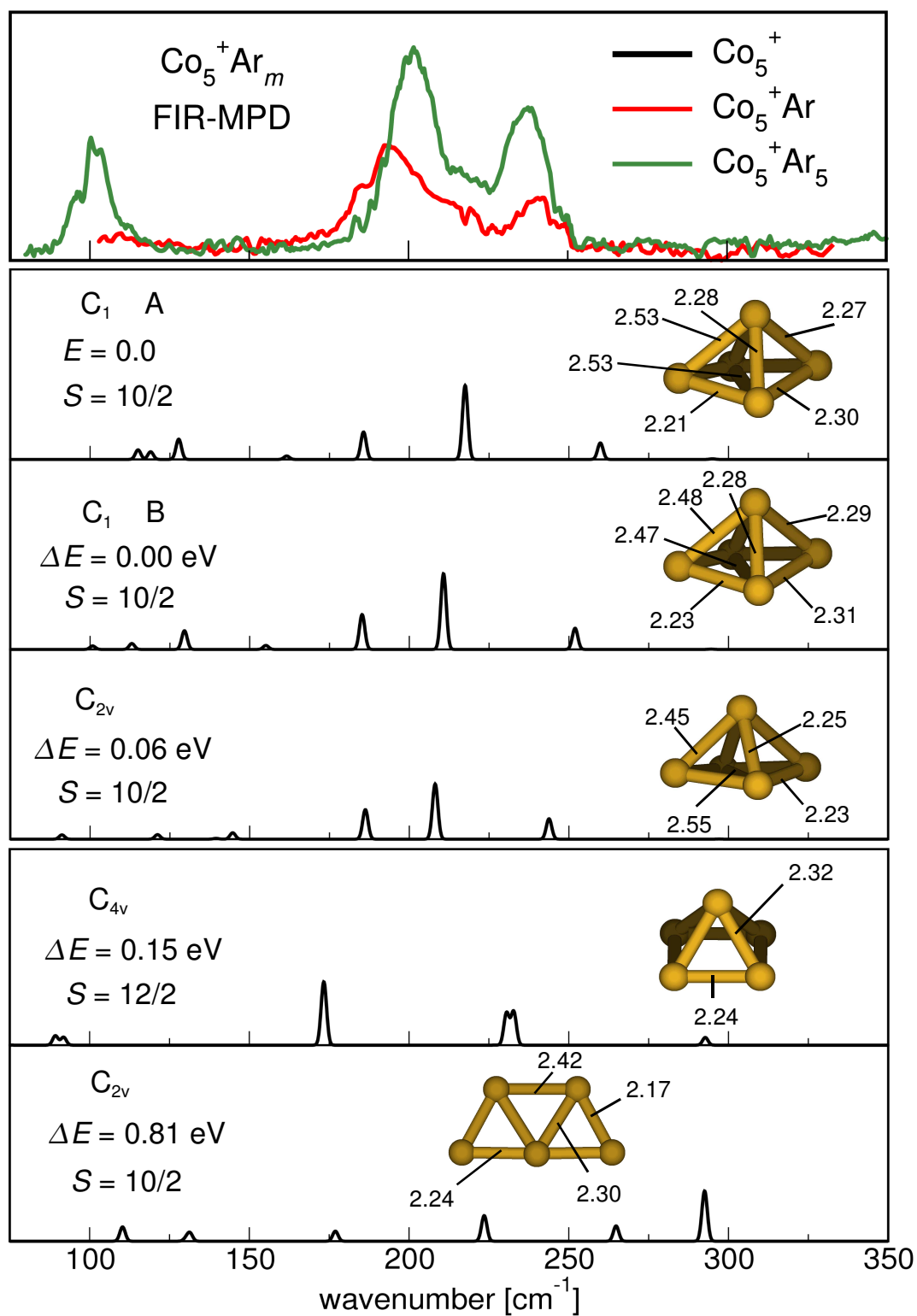


Figure E.5.: Co_5^+ IR spectra with PBE

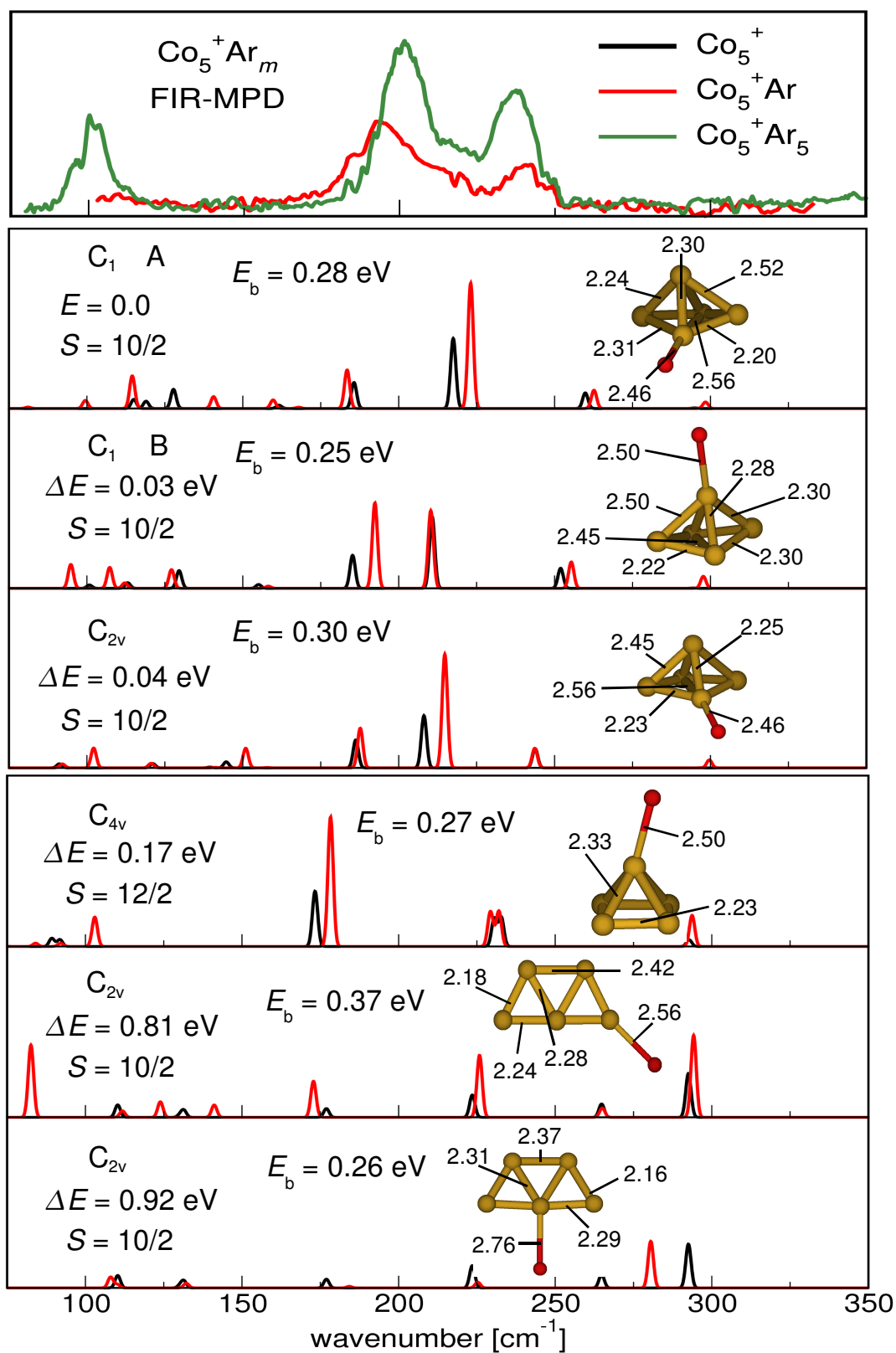


Figure E.6.: Co_5^+Ar IR spectra with PBE

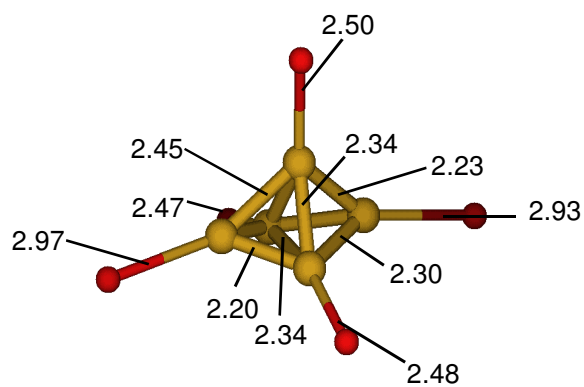
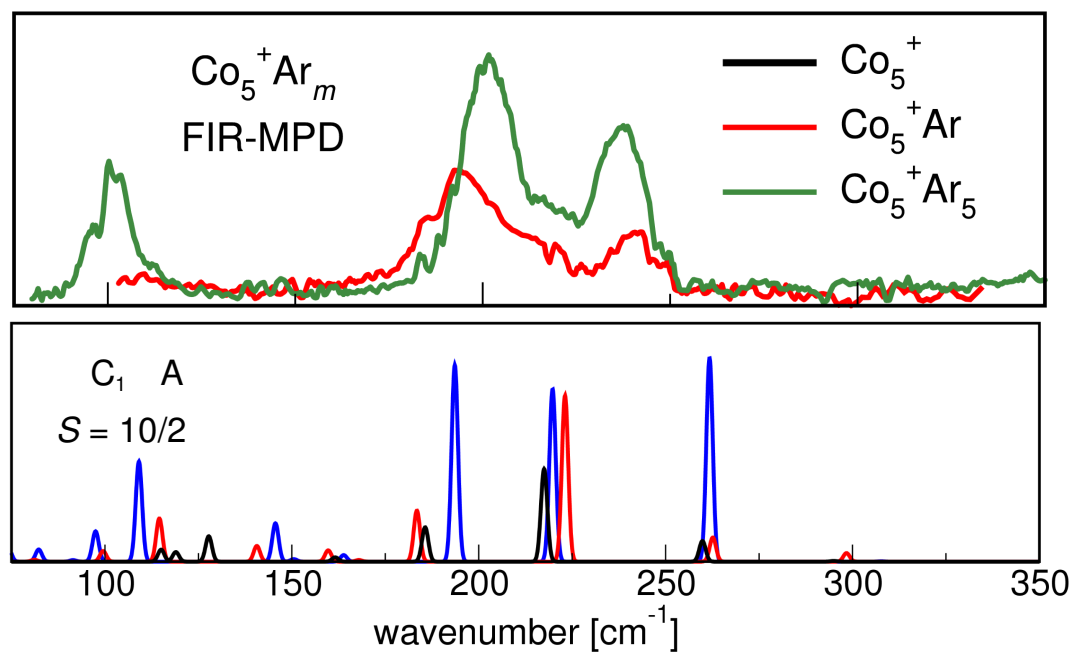


Figure E.7.: Co_5^+Ar_5 IR spectrum with PBE

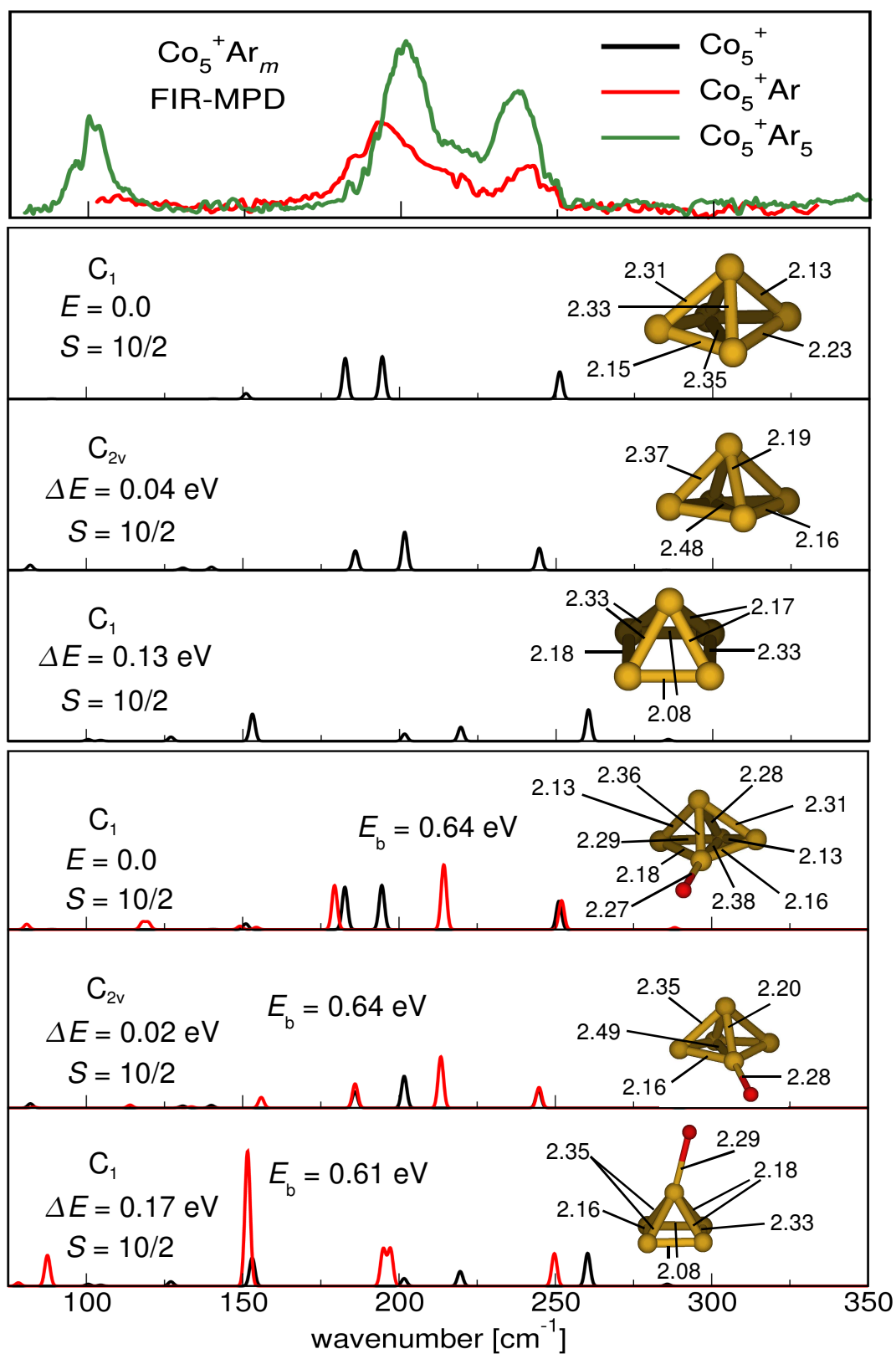


Figure E.8.: Co_5^+Ar IR spectra with PW-LDA

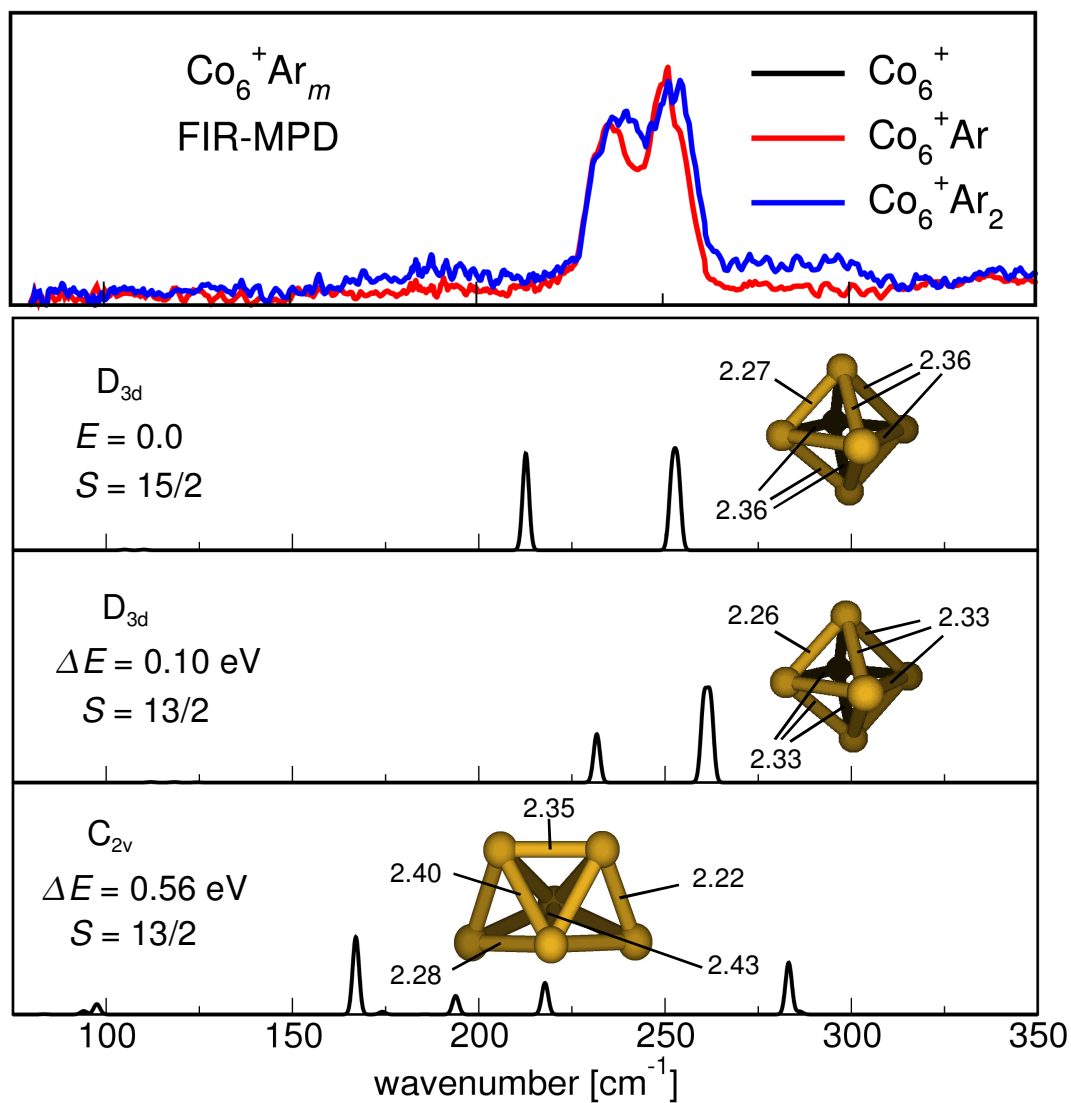


Figure E.9.: Co_6^+ IR spectra with PBE

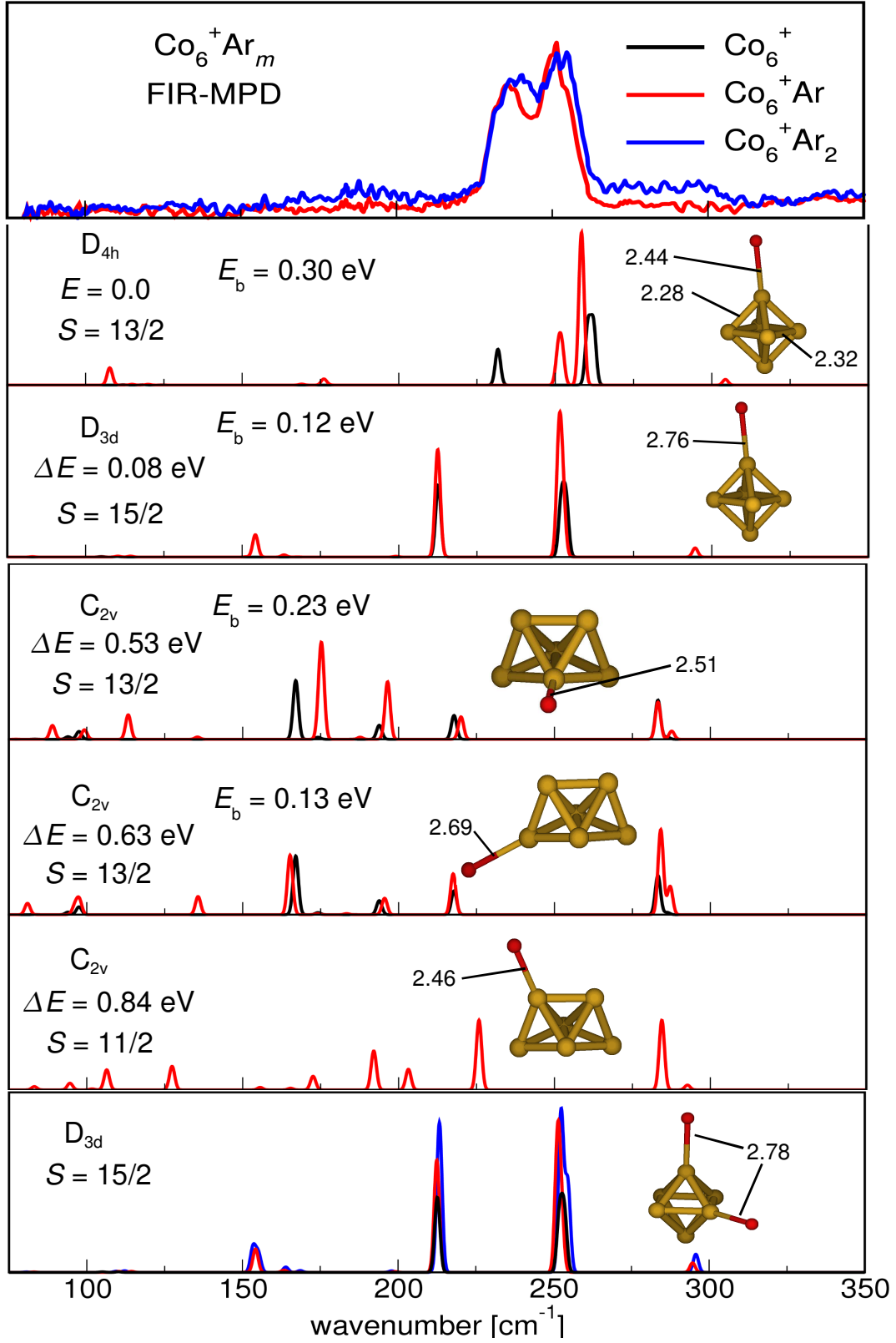


Figure E.10.: Co_6^+Ar IR spectra with PBE. We note that the $S=13/2$ ground-state isomer traverses a slight structural rearrangement when an Ar atom is bound and possesses D_{4h} symmetry contrary to the corresponding bare cluster with D_{3d} symmetry.

E. Computed Structures and IR Spectra of $\text{Co}_n^+ \text{Ar}_m$ Complexes

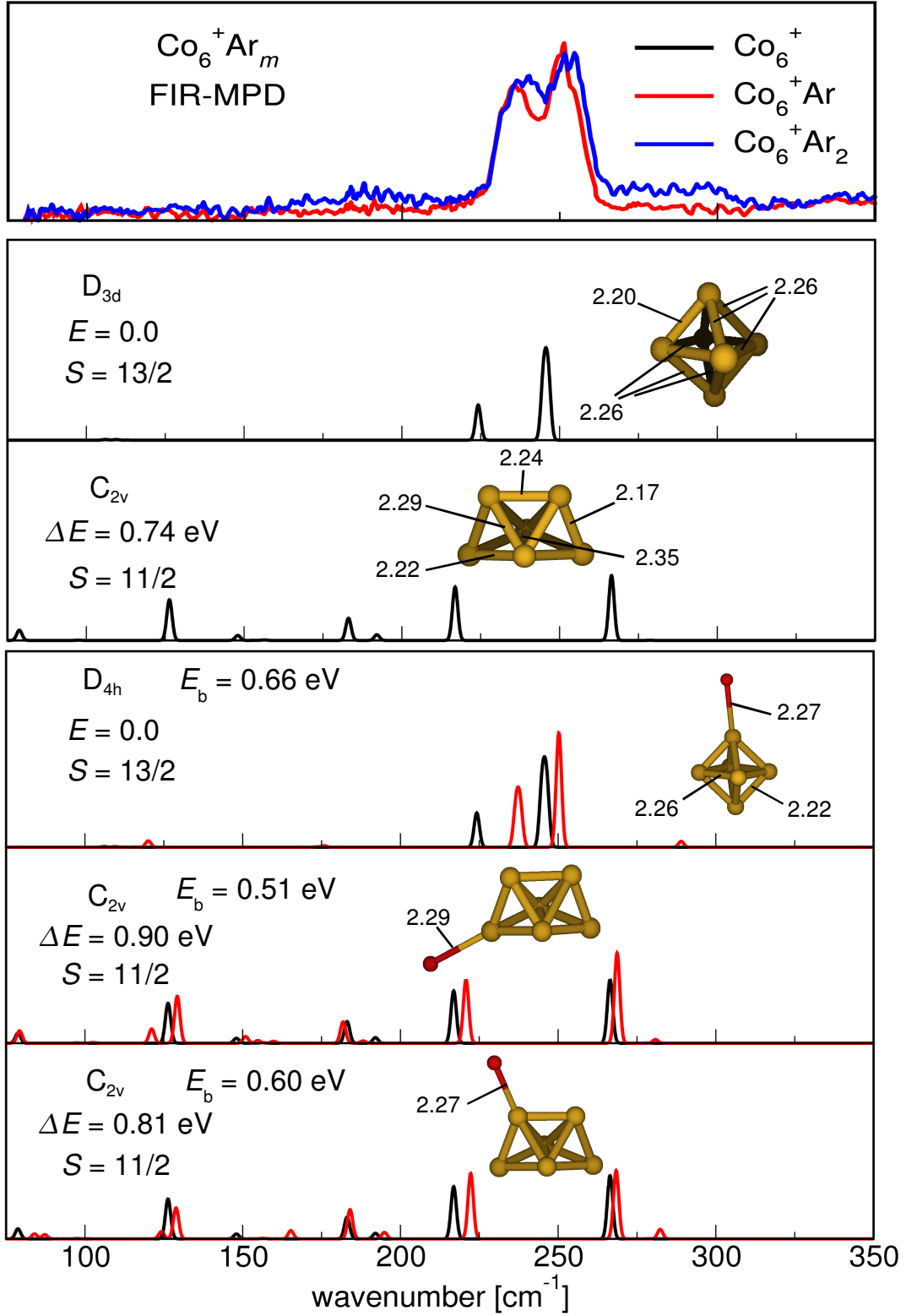


Figure E.11.: $\text{Co}_6^+ \text{Ar}$ IR spectra with PW-LDA. We note that the $S=13/2$ ground-state isomer traverses a slight structural rearrangement when an Ar atom is bound and possesses D_{4h} symmetry contrary to the corresponding bare cluster with D_{3d} symmetry.

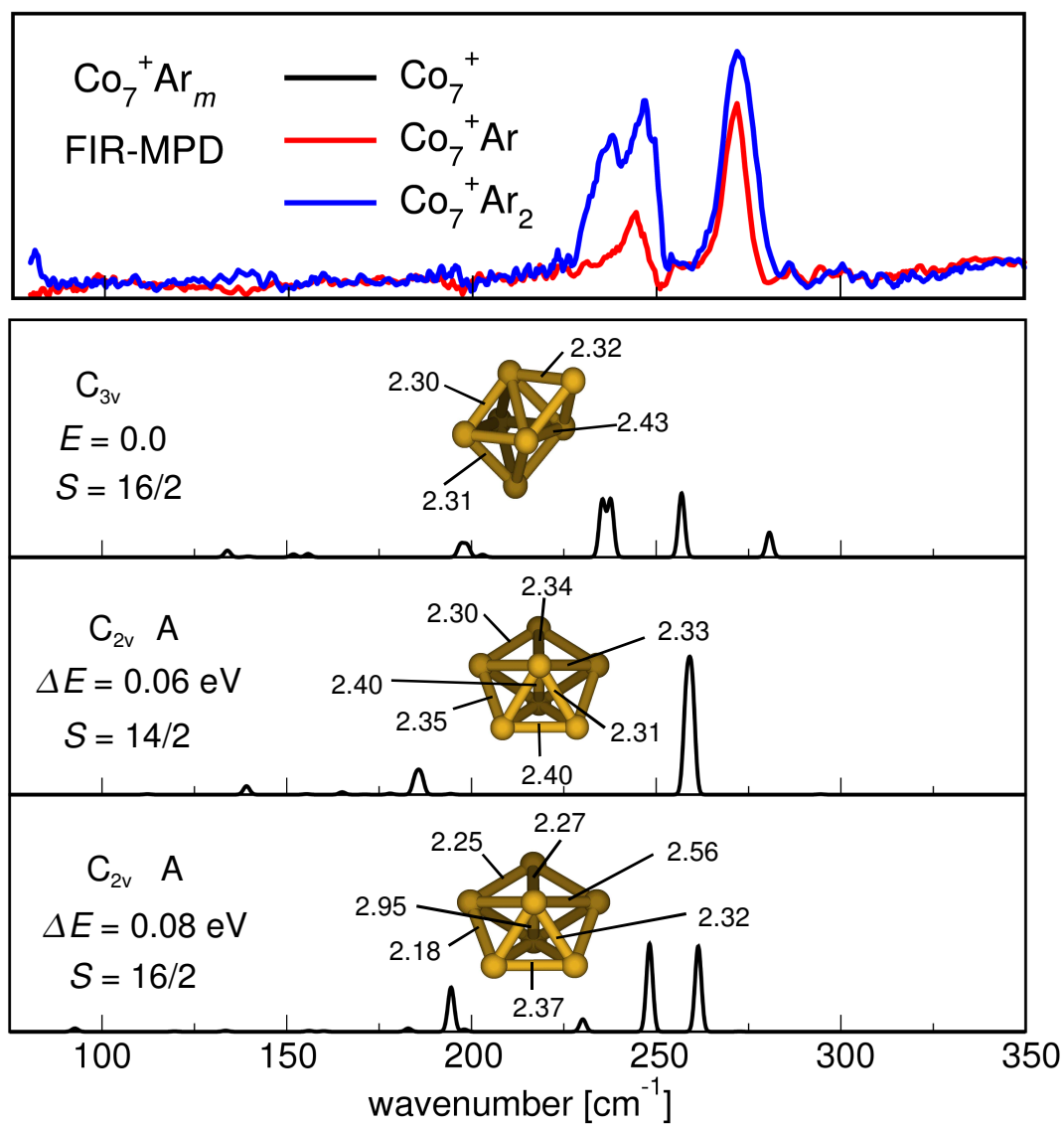


Figure E.12.: Co_7^+ IR spectra with PBE

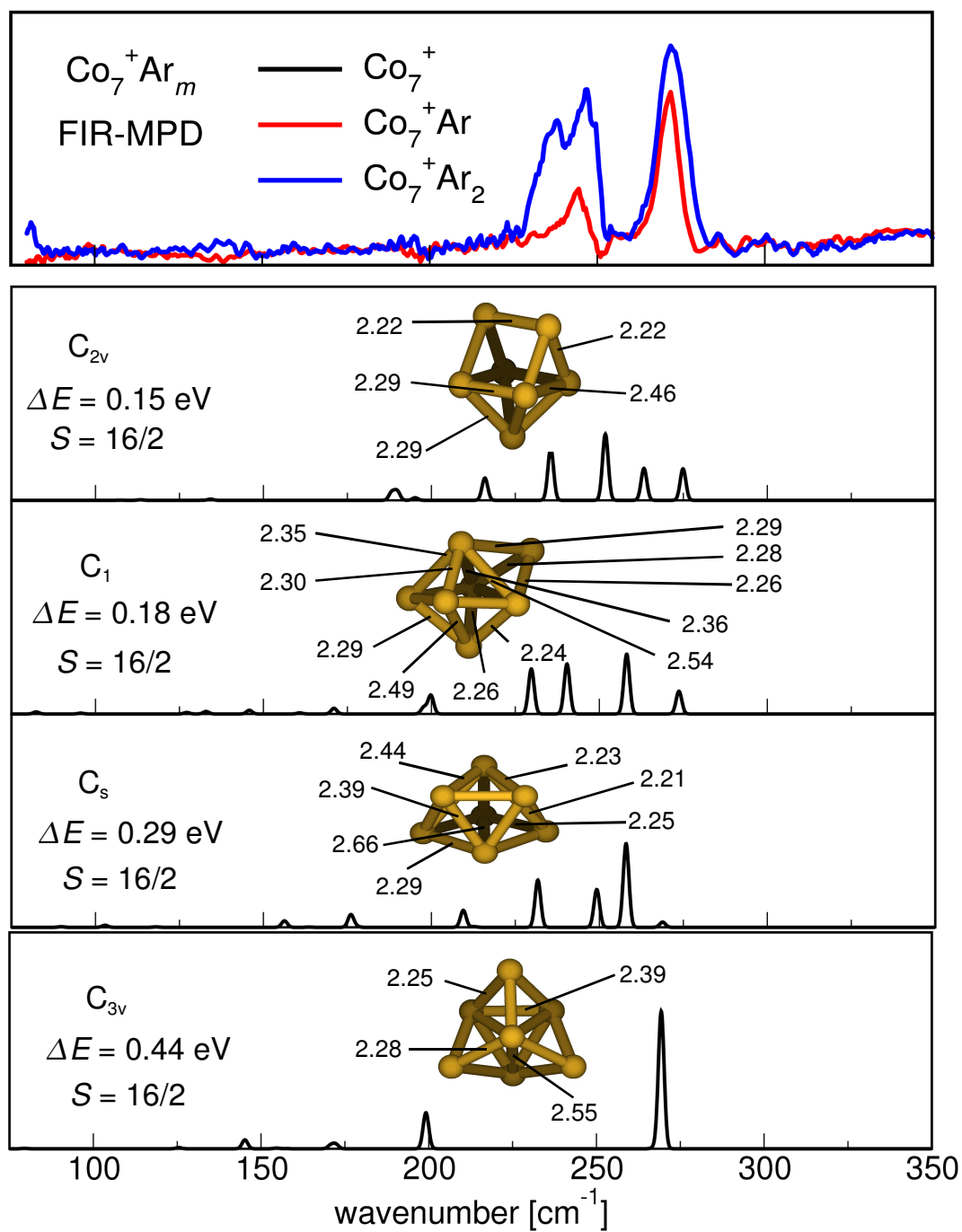


Figure E.13.: Co_7^+ IR spectra with PBE

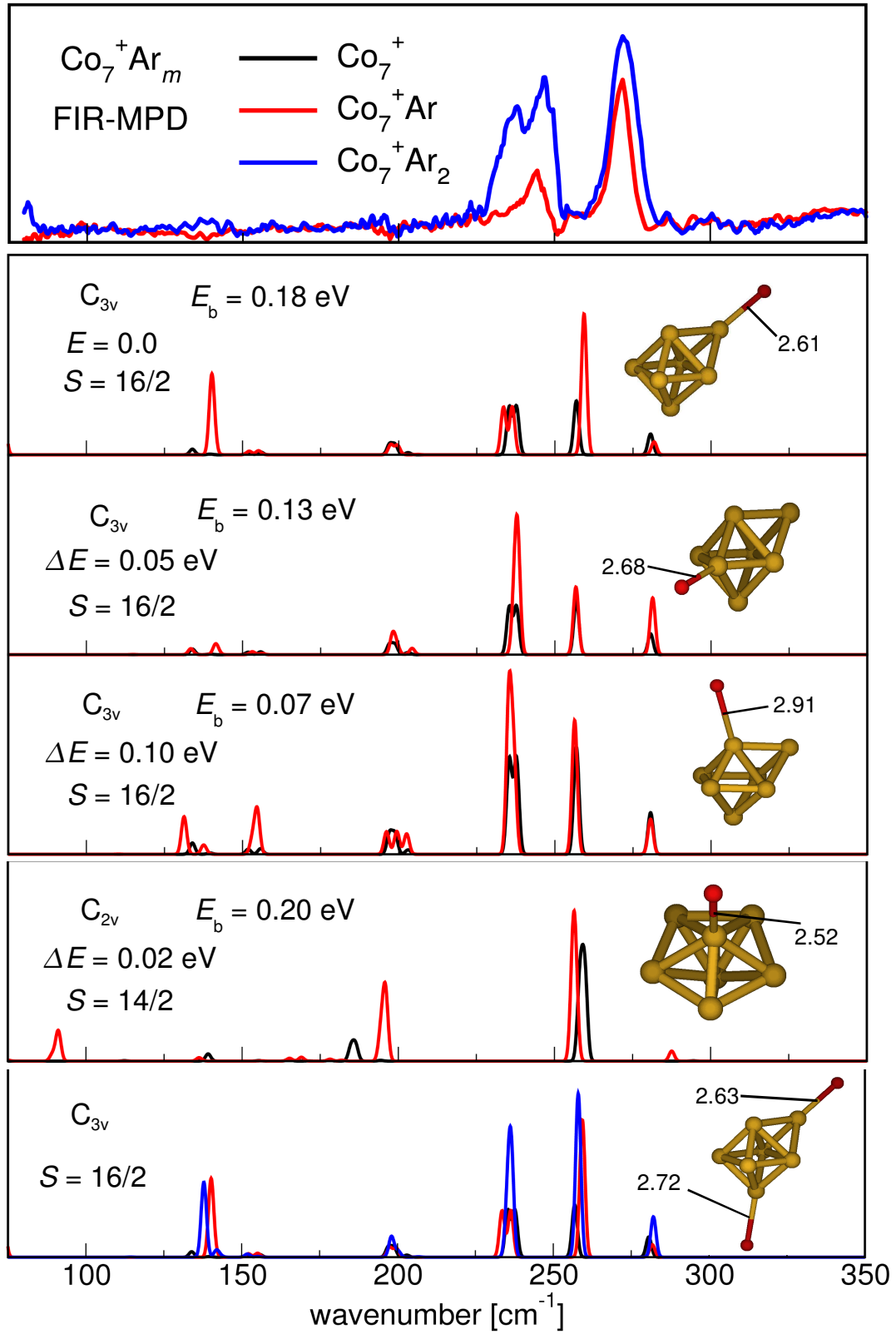


Figure E.14.: $\text{Co}_7^+ \text{Ar}$ IR spectra with PBE

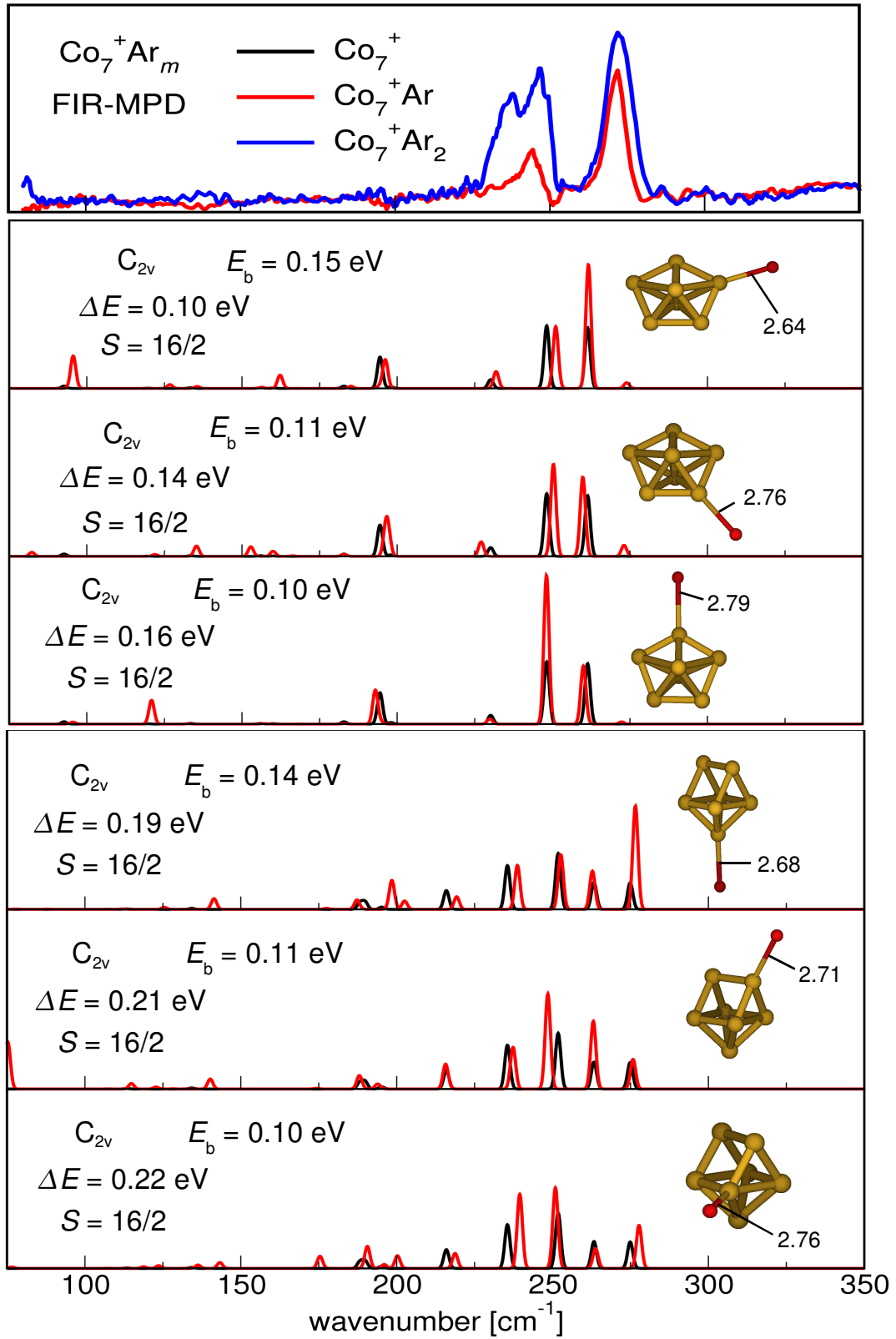


Figure E.15.: $\text{Co}_7^+ \text{Ar}$ IR spectra with PBE

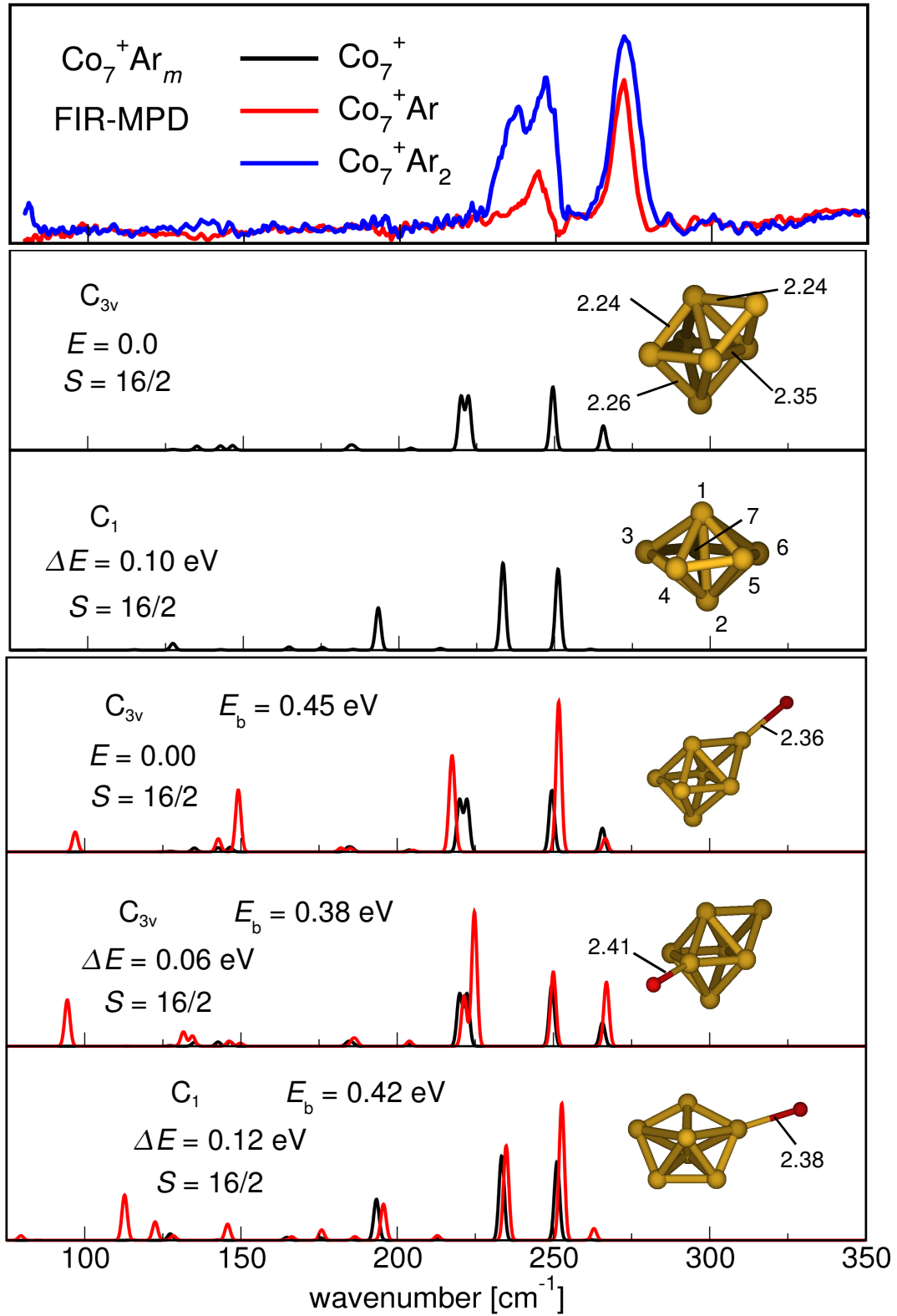


Figure E.16.: Co_7^+Ar IR spectra with PW-LDA

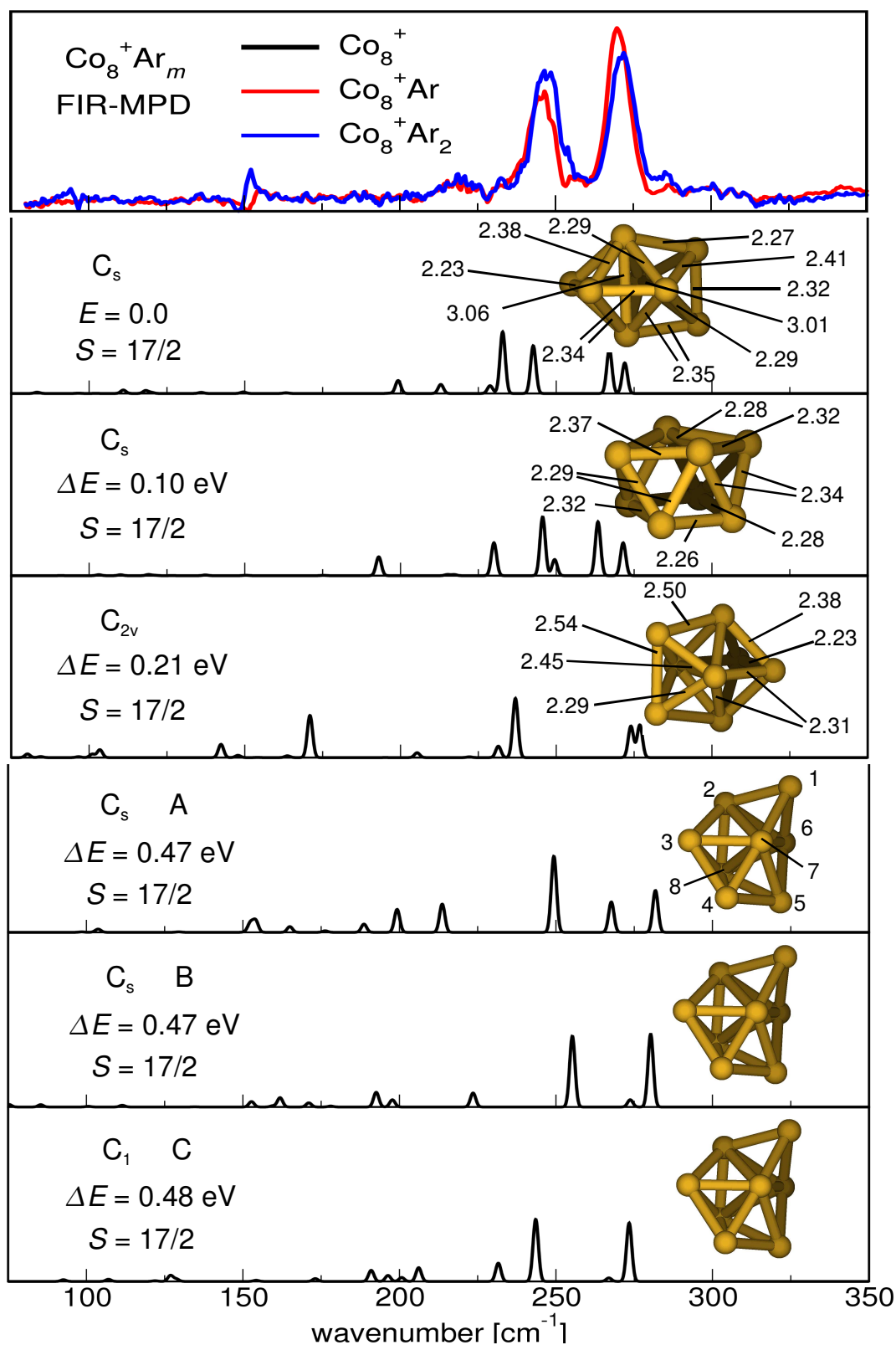


Figure E.17.: Co_8^+ IR spectra with PBE. We note that contrary to the C_s A and B isomers, the C_1 C isomer does not have a mirror plane, since the apex atom which caps the distorted pentagonal bipyramid, is slightly tilted, thus reducing it to the C_1 point group.

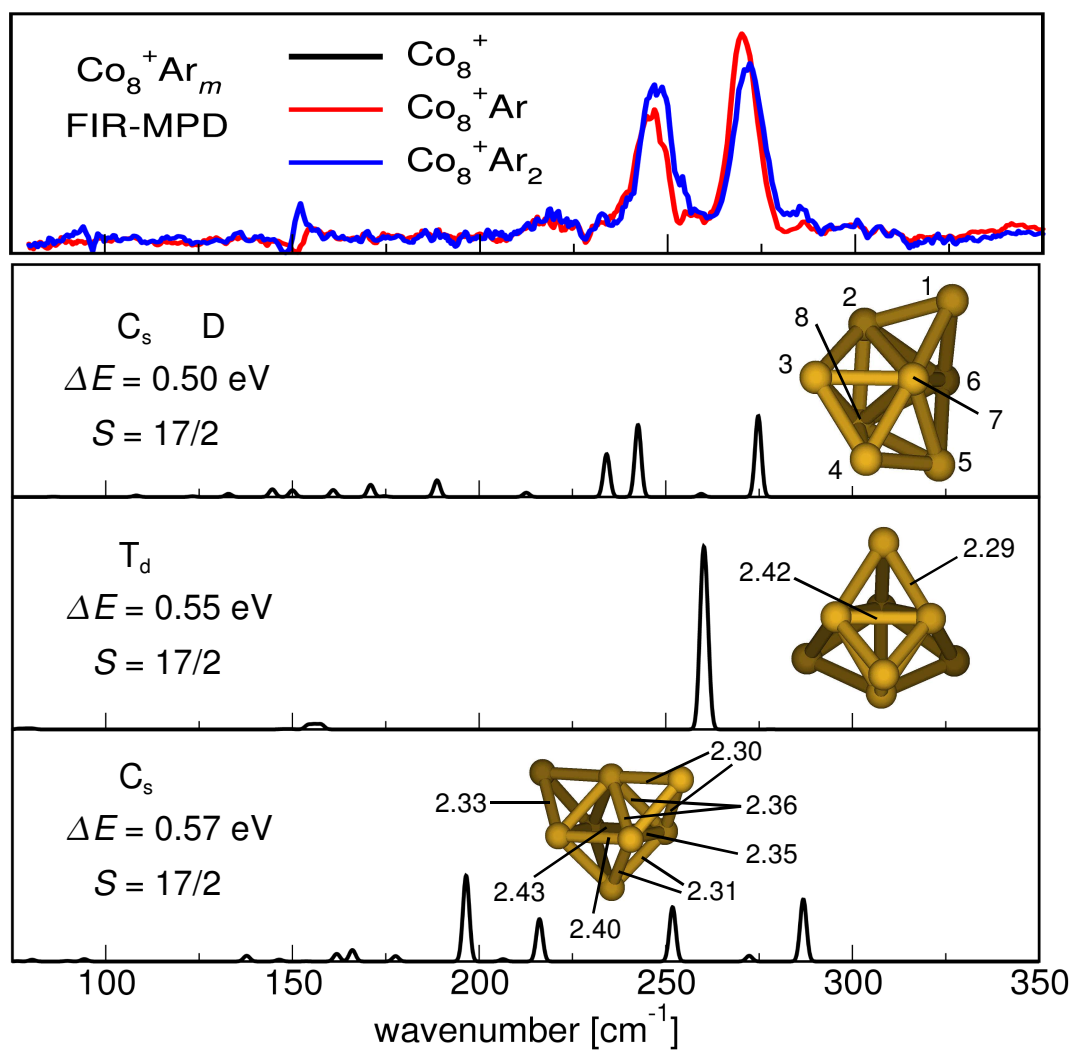


Figure E.18.: Co_8^+ IR spectra with PBE

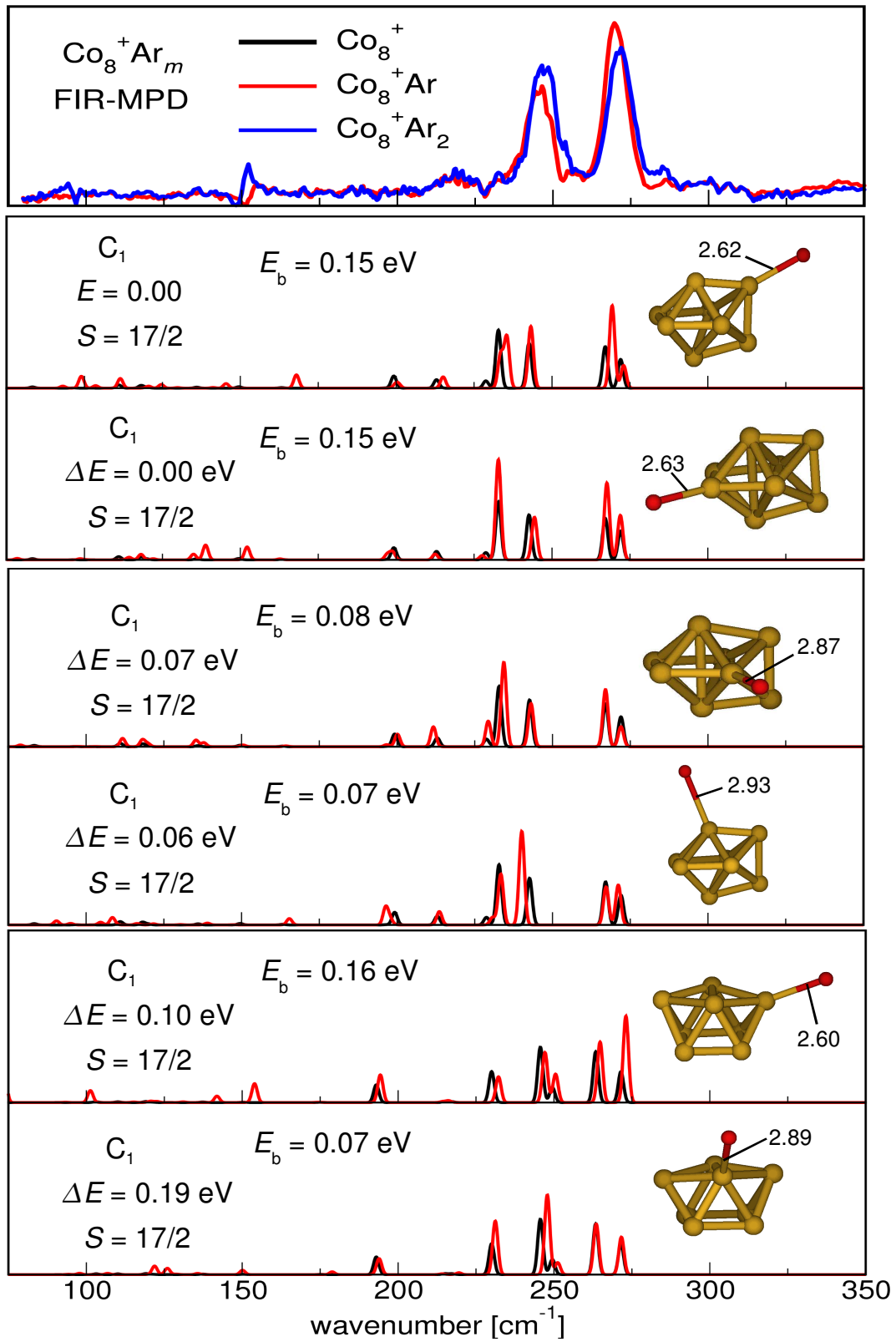


Figure E.19.: Co_8^+Ar IR spectra with PBE

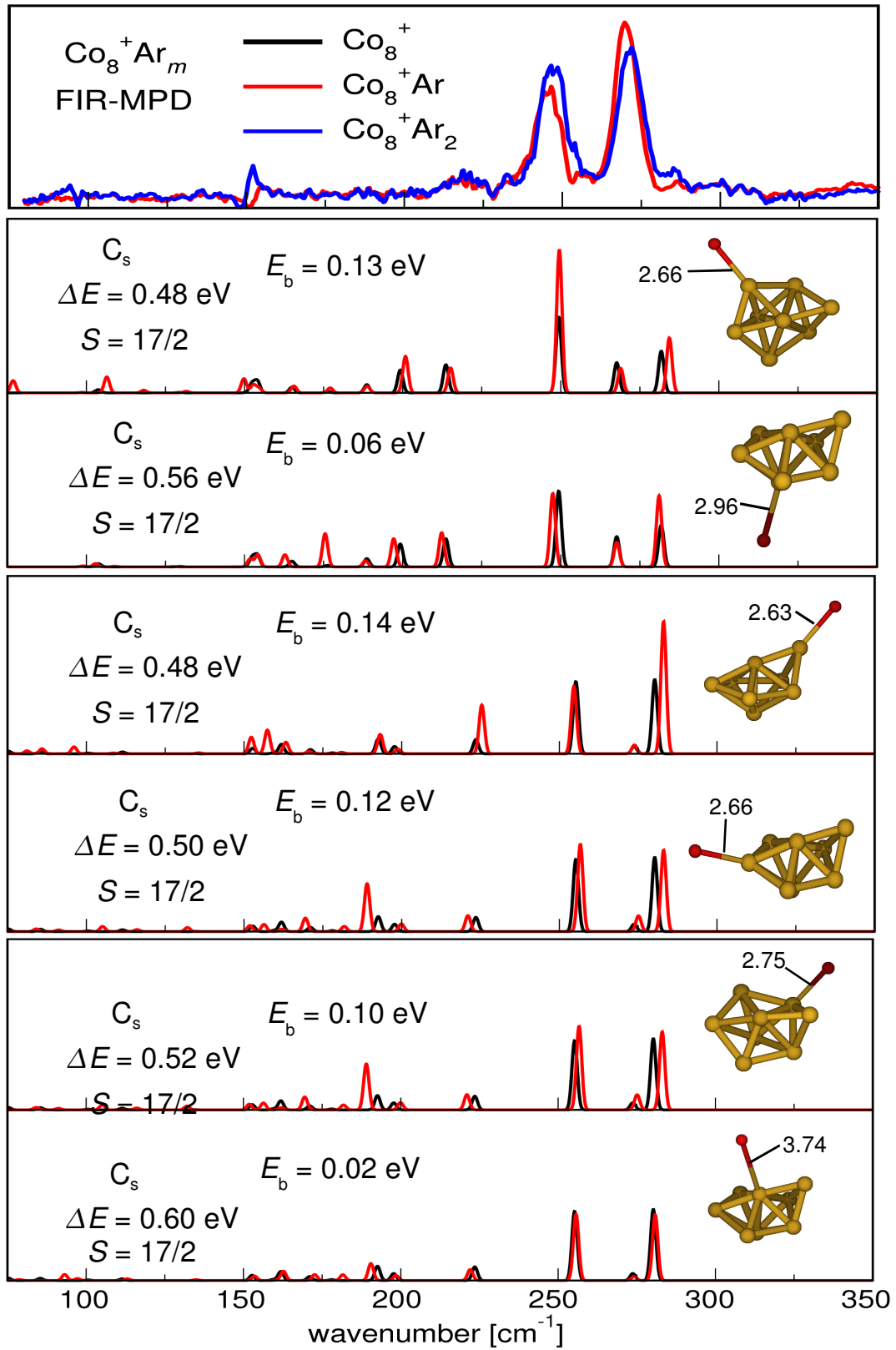


Figure E.20.: $\text{Co}_8^+ \text{Ar}$ IR spectra with PBE

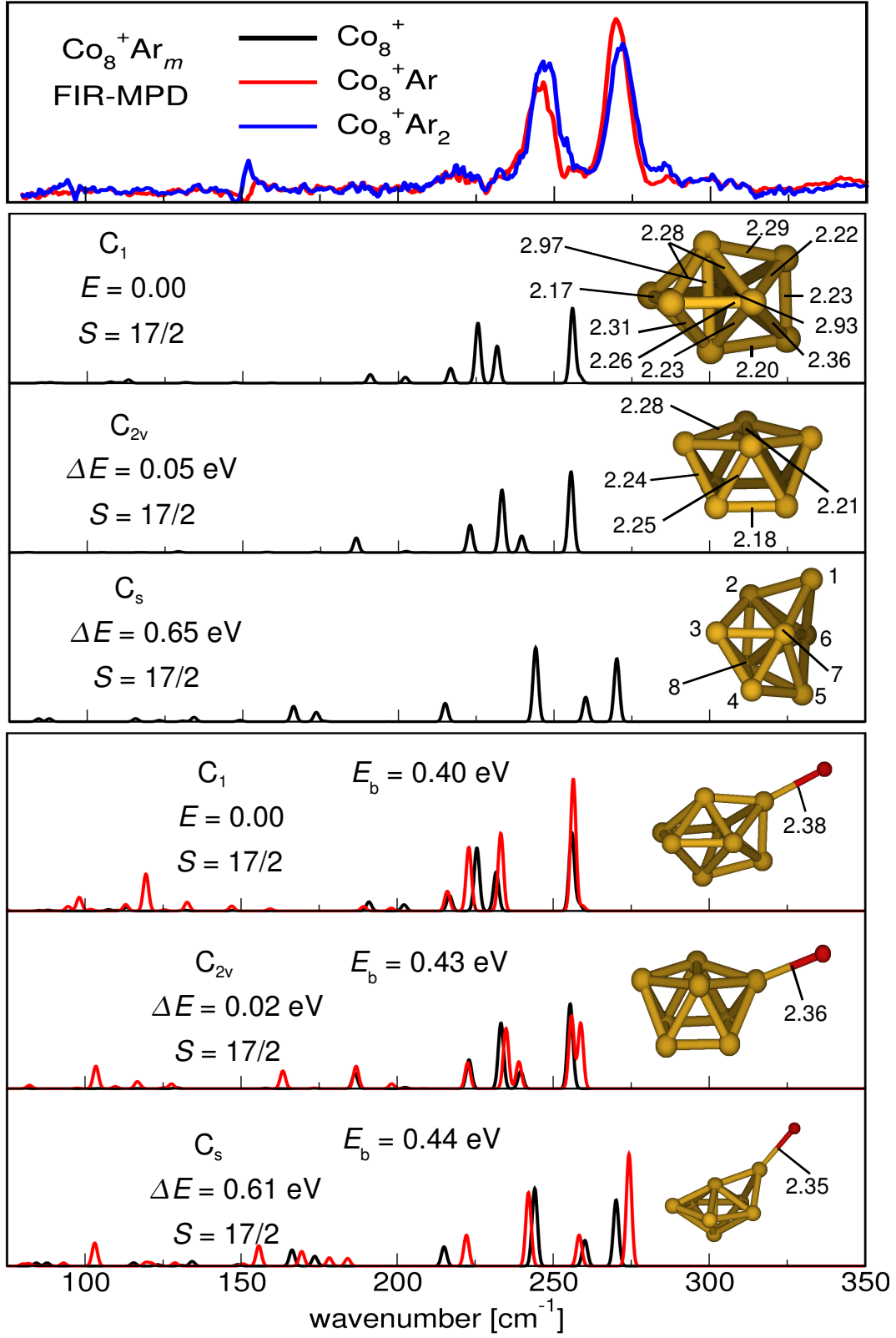


Figure E.21.: $\text{Co}_8^+ \text{Ar}$ IR spectra with PW-LDA. We note that contrary to PBE, the double-capped trigonal prism is not distorted and possesses C_{2v} symmetry.

E. Computed Structures and IR Spectra of $\text{Co}_n^+ \text{Ar}_m$ Complexes

Bond distances for the C_1 isomer of Co_7^+ with PW-LDA [\AA]: $r_{13}=2.37, r_{14}=2.30, r_{15}=2.22, r_{16}=2.59, r_{17}=2.23, r_{34}=2.12, r_{45}=2.30, r_{56}=2.12, r_{67}=2.18, r_{73}=2.18, r_{32}=2.61, r_{42}=2.22, r_{52}=2.29, r_{62}=2.38, r_{72}=2.22$

Bond distances for the C_s A isomer of Co_8^+ with PBE [\AA]: $r_{12}=r_{16}=2.29, r_{72}=r_{76}=2.37, r_{73}=r_{75}=2.36, r_{82}=r_{86}=2.39, r_{83}=r_{85}=2.29, r_{26}=2.42, r_{23}=r_{56}=2.37, r_{34}=r_{45}=2.36, r_{78}=2.41, r_{48}=2.41, r_{47}=2.29, r_{17}=2.31$

Bond distances for the C_s B isomer of Co_8^+ with PBE [\AA]: $r_{12}=r_{16}=2.32, r_{72}=r_{76}=2.34, r_{73}=r_{75}=2.34, r_{82}=r_{86}=2.37, r_{83}=r_{85}=2.29, r_{26}=2.37, r_{23}=r_{56}=2.43, r_{34}=r_{45}=2.32, r_{78}=2.44, r_{48}=2.56, r_{47}=2.32, r_{17}=2.30$

Bond distances for the C_1 C isomer of Co_8^+ with PBE [\AA]: $r_{12}=2.35, r_{16}=2.29, r_{72}=2.36, r_{76}=2.45, r_{73}=2.32, r_{75}=2.31, r_{82}=2.38, r_{86}=2.40, r_{83}=2.28, r_{85}=2.29, r_{26}=2.31, r_{23}=2.36, r_{56}=2.33, r_{34}=2.22, r_{45}=2.24, r_{78}=2.84, r_{48}=2.80, r_{47}=2.45, r_{17}=2.27$

Bond distances for the C_s D isomer of Co_8^+ with PBE [\AA]: $r_{12}=r_{16}=2.34, r_{72}=r_{76}=2.44, r_{73}=r_{75}=2.46, r_{82}=r_{86}=2.35, r_{83}=r_{85}=2.51, r_{26}=2.35, r_{23}=r_{56}=2.24, r_{34}=r_{45}=2.27, r_{78}=2.89, r_{48}=2.28, r_{47}=2.31, r_{17}=2.21$

Bond distances for the C_s isomer of Co_8^+ with PW-LDA [\AA]: $r_{12}=r_{16}=2.19, r_{72}=r_{76}=2.26, r_{73}=r_{75}=2.25, r_{82}=r_{86}=2.32, r_{83}=r_{85}=2.21, r_{26}=2.34, r_{23}=r_{56}=2.35, r_{34}=r_{45}=2.21, r_{78}=2.44, r_{48}=2.55, r_{47}=2.31, r_{17}=2.28$

Bibliography

- [1] A. Fielicke, A. Kirilyuk, C. Ratsch, J. Behler, M. Scheffler, G. von Helden, and G. Meijer, Phys. Rev. Lett. **93**, 023401 (2004).
- [2] C. Ratsch, A. Fielicke, A. Kirilyuk, J. Behler, G. von Helden, G. Meijer, and M. Scheffler, J. Chem. Phys. **122**, 124302 (2005).
- [3] A. Fielicke, C. Ratsch, G. von Helden, and G. Meijer, J. Chem. Phys. **122**, 091105 (2005).
- [4] A. Fielicke, C. Ratsch, G. von Helden, and G. Meijer, J. Chem. Phys. **127**, 234306 (2007).
- [5] P. Gruene, A. Fielicke, and G. Meijer, J. Chem. Phys. **127**, 234307 (2007).
- [6] D. J. Wales, *Energy Landscapes* (Cambridge University Press, Cambridge, 2003).
- [7] D. J. Wales, M. A. Miller, and T. R. Walsh, Nature **394**, 758 (1998).
- [8] J. P. K. Doye and D. J. Wales, J. Chem. Phys. **105**, 8428 (1996).
- [9] C. Møller and M. S. Plesset, Phys. Rev. **46**, 618 (1934).
- [10] D. J. Wales and H. A. Scheraga, Science **285**, 1368 (1999).
- [11] V. Blum, R. Gehrke, F. Hanke, P. Havu, V. Havu, X. Ren, K. Reuter, and M. Scheffler, Comp. Phys. Commun., (*accepted*); <http://www.fhi-berlin.mpg.de/aims>.
- [12] M. Born and R. Oppenheimer, Ann. Phys. **389**, 457 (1927).
- [13] E. B. Wilson, Jr., J. C. Decius, and P. C. Cross, *Molecular vibrations* (Dover Publications Inc., New York, 1980).
- [14] J. N. Murrell and K. J. Laidler, Trans. Faraday Soc. **64**, 371 (1968).
- [15] D. J. Wales, J. Chem. Phys. **113**, 3926 (2000).
- [16] R. G. A. Bone, T. W. Rowlands, N. C. Handy, and A. J. Stone, Mol. Phys. **72**, 33 (1991).
- [17] F. H. Stillinger and T. A. Weber, Phys. Rev. A **25**, 978 (1982).
- [18] F. H. Stillinger, Phys. Rev. E **59**, 48 (1999).

Bibliography

- [19] F. H. Stillinger and T. A. Weber, *Science* **225**, 983 (1984).
- [20] R. E. Kunz and R. S. Berry, *J. Chem. Phys.* **103**, 1904 (1995).
- [21] R. S. Berry and R. Breitengraser-Kunz, *Phys. Rev. Lett.* **74**, 3951 (1995).
- [22] F. Jensen, *Introduction to Computational Chemistry* (Wiley, Chichester, 1999).
- [23] D. F. Shanno, *Math. Oper. Res.* **3**, 244 (1978).
- [24] M. J. D. Powell, Nonconvex minimization calculations and the conjugate gradient method, in *Lecture Notes in Mathematics*, Vol. 1066, pp. 122–141, Springer, Berlin, 1984.
- [25] R. Fletcher and C. M. Reeves, *Comp. J.* **7**, 149 (1964).
- [26] M. R. Hestenes and E. L. Stiefel, *J. Res. Nat. Bur. Stand.* **49**, 409 (1952).
- [27] W. K. Press, S. A. Teukolsky, W. T. Vetterlin, and B. T. Flannery, *Numerical Recipes*, 3rd edition ed. (Cambridge University Press, Cambridge, 2007).
- [28] L. T. Wille and J. Vennik, *J. Phys. A* **18**, L419 (1985).
- [29] S. Kirkpatrick, C. D. Gelatt, Jr., and M. P. Vecchi, *Science* **220**, 671 (1983).
- [30] N. Metropolis, A. W. Rosenbluth, M. N. Rosenbluth, A. H. Teller, and E. Teller, *J. Chem. Phys.* **21**, 1087 (1953).
- [31] Y. Xiang, D. Y. Sun, W. Fan, and X. G. Gong, *Phys. Lett. A* **233**, 216 (1997).
- [32] H. Szu and R. Hartley, *Phys. Lett. A* **122**, 157 (1987).
- [33] Y. Xiang, D. Y. Sun, and X. G. Gong, *J. Phys. Chem. A* **104**, 2746 (2000).
- [34] Z. Li and H. A. Scheraga, *Proc. Natl. Acad. Sci. U.S.A.* **84**, 6611 (1987).
- [35] D. J. Wales, J. P. K. Doye, M. A. Miller, P. N. Mortenson, and T. R. Walsh, *Adv. Chem. Phys.* **115**, 1 (2000).
- [36] J. Pillardy and L. Piela, *J. Phys. Chem.* **99**, 11805 (1995).
- [37] J. P. K. Doye, M. A. Miller, and D. J. Wales, *J. Chem. Phys.* **110**, 6896 (1999).
- [38] J. P. K. Doye and D. J. Wales, *Phys. Rev. Lett.* **80**, 1357 (1998).
- [39] D. M. Deaven and K. M. Ho, *Phys. Rev. Lett.* **75**, 288 (1995).
- [40] D. M. Deaven, N. Tit, J. R. Morris, and K. M. Ho, *Chem. Phys. Lett.* **256**, 195 (1996).
- [41] S. Goedecker, *J. Chem. Phys.* **120**, 9911 (2004).

Bibliography

- [42] S. Goedecker, W. V. Hellmann, and T. Lenosky, Phys. Rev. Lett. **95**, 055501 (2005).
- [43] R. P. Bell, Proc. R. Soc. London, Ser.A **154**, 414 (1936).
- [44] M. G. Evans and M. Polanyi, Trans. Faraday Soc. **32**, 1333 (1936).
- [45] D. J. Wales and J. P. K. Doye, J. Phys. Chem. A **101**, 5111 (1997).
- [46] U. H. E. Hansmann and L. T. Wille, Phys. Rev. Lett. **88**, 068105 (2002).
- [47] L. Zhan, J. Z. Y. Chen, and W.-K. Liu, Phys. Rev. E **73**, 015701 (2006).
- [48] W. Pauli, Z. Phys. **31**, 765 (1925).
- [49] R. P. Feynman, R. B. Leighton, and M. Sands, *The Feynman Lectures on Physics*, Vol. III (Addison-Wesley, London, 1965).
- [50] W. Ritz, J. Reine Angew. Math. **135**, 1 (1908).
- [51] A. R. Leach, *Molecular Modelling: Principles and Applications*, 2nd ed. (Prentice-Hall, Pearson, 2001).
- [52] B. O. Roos, P. R. Taylor, and P. E. Siegbahn, Chem. Phys. **48**, 157 (1980).
- [53] R. J. Bartlett, J. Phys. Chem. **93**, 1697 (1989).
- [54] D. M. Ceperley and B. J. Alder, Science **231**, 555 (1986).
- [55] R. G. Parr and W. Yang, *Density-Functional Theory of Atoms and Molecules* (Oxford University Press, New York, 1989).
- [56] P. Hohenberg and W. Kohn, Phys. Rev. **136**, B 864 (1964).
- [57] R. M. Dreizler and E. K. U. Gross, *Density Functional Theory* (Springer-Verlag, Berlin Heidelberg, 1990).
- [58] W. Kohn and L. J. Sham, Phys. Rev. **140**, A 1133 (1965).
- [59] V. L. Lignères and E. A. Carter, An introduction to orbital-free density functional theory, in *Handbook on Materials Modeling*, edited by S. Yip, pp. 137–148, Springer, Dordrecht, 2005.
- [60] Y. A. Wang, N. Govind, and E. A. Carter, Phys. Rev. B **60**, 16 350 (1999).
- [61] B. Zhou and E. A. Carter, J. Chem. Phys. **122**, 184108 (2005).
- [62] E. Wigner and F. Seitz, Phys. Rev. **46**, 509 (1934).
- [63] M. Gell-Mann and K. A. Brueckner, Phys. Rev. **106**, 364 (1957).

Bibliography

- [64] W. J. Carr, Jr. and A. A. Maradudin, Phys. Rev. **133**, A371 (1964).
- [65] W. J. Carr, Jr., Phys. Rev. **122**, 1437 (1961).
- [66] P. Nozières and D. Pines, Phys. Rev. **111**, 442 (1958).
- [67] D. M. Ceperley and B. J. Alder, Phys. Rev. Lett. **45**, 566 (1980).
- [68] S. H. Vosko, L. Wilk, and M. Nusair, Can. J. Phys. **58**, 1200 (1980).
- [69] J. P. Perdew and Y. Wang, Phys. Rev. B **45**, 13 244 (1992).
- [70] J. P. Perdew, K. Burke, and M. Ernzerhof, Phys. Rev. Lett. **77**, 3865 (1996).
- [71] J. P. Perdew, J. A. Chevary, S. H. Vosko, K. A. Jackson, M. R. Pederson, D. J. Singh, and C. Fiolhais, Phys. Rev. B **46**, 6671 (1992).
- [72] O. Gunnarsson and B. I. Lundqvist, Phys. Rev. B **13**, 4274 (1976).
- [73] U. von Barth and L. Hedin, J. Phys. C **5**, 1629 (1972).
- [74] P. Pulay, Chem. Phys. Lett. **73**, 393 (1980).
- [75] G. Kresse and J. Furthmüller, Comp. Mat. Sci. **6**, 15 (1996).
- [76] N. D. Mermin, Phys. Rev. **137**, A1441 (1965).
- [77] M. Methfessel and A. T. Paxton, Phys. Rev. B **40**, 3616 (1989).
- [78] C.-L. Fu and K.-M. Ho, Phys. Rev. B **28**, 5480 (1983).
- [79] B. Delley, J. Chem. Phys. **92**, 508 (1990).
- [80] G. B. Arfken and H. J. Weber, *Mathematical Methods for Physicists*, 5th ed. (Academic Press, San Diego, 2001).
- [81] A. Zunger and A. J. Freeman, Phys. Rev. B **15**, 4716 (1977).
- [82] T. Ozaki and H. Kino, Phys. Rev. B **69**, 195113 (2004).
- [83] A. D. Becke, J. Chem. Phys. **88**, 2547 (1988).
- [84] F. Hirshfeld, Theor. Chim. Acta (Berl.) **44**, 129 (1977).
- [85] J. Baker, J. Andzelm, A. Scheiner, and B. Delley, J. Chem. Phys. **101**, 8894 (1994).
- [86] V. Lebedev, Zh. Vychisl. Mat. mat. Fiz. **15**, 48 (1975).
- [87] V. Lebedev, Zh. Vychisl. Mat. mat. Fiz. **16**, 293 (1976).
- [88] V. Lebedev and D. Laikov, Doklady Mathematics **59**, 477 (1999).

Bibliography

- [89] B. Delley, J. Comp. Chem. **17**, 1152 (1995).
- [90] A. D. McLaren, Math. Comput. **17**, 361 (1963).
- [91] A. H. Stroud, *Approximate Calculation of Multiple Integrals* (Prentice-Hall, Englewood Cliffs, 1971).
- [92] B. I. Dunlap, J. W. D. Connolly, and J. R. Sabin, J. Chem. Phys. **71**, 3396 (1979).
- [93] B. Delley, J. Chem. Phys. **94**, 7245 (1991).
- [94] H. Hellmann, Z. Phys. **85**, 180 (1933).
- [95] R. P. Feynman, Phys. Rev. **56**, 340 (1939).
- [96] P. Pulay, Mol. Phys. **17**, 197 (1969).
- [97] E. K. Parks, L. Zhu, J. Ho, and S. J. Riley, J. Chem. Phys. **100**, 7206 (1994).
- [98] J. Li, X. Li, H.-J. Zhai, and L.-S. Wang, Science **299**, 864 (2003).
- [99] G. von Helden, M. T. Hsu, N. Gotts, and M. T. Bowers, J. Phys. Chem. **97**, 8182 (1993).
- [100] K.-M. Ho, A. A. Shvartsburg, B. Pan, Z.-Y. Lu, C.-Z. Wang, J. G. Wacker, J. L. Fye, and M. F. Jarrold, Nature **392**, 582 (1998).
- [101] P. Weis, Int. J. Mass Spectrom. **245**, 1 (2005).
- [102] D. Schooss, M. N. Blom, J. H. Parks, B. v. Issendorff, H. Haberland, and M. M. Kappes, Nano Lett. **5**, 1972 (2005).
- [103] M. N. Blom, D. Schooss, J. Stairs, and M. M. Kappes, J. Chem. Phys. **124**, 244308 (2006).
- [104] X. Xing, B. Yoon, U. Landman, and J. H. Parks, Phys. Rev. B **74**, 165423 (2006).
- [105] A. Fielicke, G. von Helden, and G. Meijer, Eur. Phys. J. D **34**, 83 (2005).
- [106] D. Oepts, A. F. G. van der Meer, and P. W. van Amersfoort, Infrared Phys. Technol. **36**, 297 (1995).
- [107] S. Minemoto, A. Terasaki, and T. Kondow, J. Chem. Phys. **104**, 5770 (1996).
- [108] J. Oomens, A. G. G. M. Tielens, B. G. Sartakov, G. von Helden, and G. Meijer, Astrophys. J. **591**, 968 (2003).
- [109] D. Porezag and M. R. Pederson, Phys. Rev. B **54**, 7830 (1996).
- [110] H. B. Jansen and P. Ros, Chem. Phys. Lett. **3**, 140 (1969).

- [111] S. F. Boys and F. Bernardi, *Mol. Phys.* **19**, 553 (1970).
- [112] H. Wang, Y. G. Khait, and M. R. Hoffmann, *Mol. Phys.* **103**, 263 (2005).
- [113] C. Jamorski, A. Martinez, M. Castro, and D. R. Salahub, *Phys. Rev. B* **55**, 10905 (1997).
- [114] S. Datta, M. Kabir, S. Ganguly, B. Sanyal, T. Saha-Dasgupta, and A. Mookerjee, *Phys. Rev. B* **76**, 014429 (2007).
- [115] D. A. Hales, C.-X. Su, L. Lian, and P. B. Armentrout, *J. Chem. Phys.* **100**, 1049 (1994).
- [116] D. Frenkel and B. Smit, *Understanding Molecular Simulation*, Computational Science Series Vol. 1 (Academic Press, San Diego, 1996).
- [117] K. Raghavachari and C. M. Rohlfing, *J. Chem. Phys.* **89**, 2219 (1988).
- [118] X. Zhu and X. C. Zeng, *J. Chem. Phys.* **118**, 3558 (2003).
- [119] S. Yoo and X. C. Zeng, *Angew. Chem. Int. Ed.* **44**, 1491 (2005).
- [120] W. V. Hellmann, R. G. Hennig, S. Goedecker, C. J. Umrigar, B. Delley, and T. Lenosky, *Phys. Rev. B* **75**, 085411 (2007).
- [121] W. V. Hellman, *Exploring the Born-Oppenheimer surface of small and medium-sized Si clusters using the dual minima hopping method*, PhD thesis, Universität Basel, 2007.
- [122] C. Massobrio, A. Pasquarello, and A. Dal Corso, *J. Chem. Phys.* **109**, 6626 (1998).
- [123] P. Calaminici, A. M. Köster, A. Vela, and K. Jug, *J. Chem. Phys.* **113**, 2199 (2000).
- [124] K. Jug, B. Zimmermann, P. Calaminici, and A. M. Köster, *J. Chem. Phys.* **116**, 4497 (2002).
- [125] M. Yang and K. A. Jackson, *J. Chem. Phys.* **122**, 184317 (2005).
- [126] M. Yang, K. A. Jackson, C. Koehler, T. Frauenheim, and J. Jellinek, *J. Chem. Phys.* **124**, 024308 (2006).
- [127] J. Behler and M. Parrinello, *Phys. Rev. Lett.* **98**, 146401 (2007).

Publications

- *Ab Initio Molecular Simulations with Numeric Atom-Centered Orbitals: FHI-aims*, Volker Blum, **Ralf Gehrke**, Felix Hanke, Paula Havu, Ville Havu, Xinguo Ren, Karsten Reuter and Matthias Scheffler, Comp. Phys. Commun. (*accepted*); <http://www.fhi-berlin.mpg.de/aims>.
- *Nature of Ar bonding to small Co_n^+ clusters and its effect on the structure determination by far-infrared absorption spectroscopy*, **Ralf Gehrke**, Philipp Gruene, André Fielicke, Gerard Meijer and Karsten Reuter, J. Chem. Phys. **130**, 034306 (2009)
- *Assessing the efficiency of first-principles basin-hopping sampling*, **Ralf Gehrke** and Karsten Reuter, Phys. Rev. B **79**, 085412 (2009)

Kurzfassung

Die Motivation dieser Arbeit war die Entwicklung und Analyse eines Dichtefunktional-Theorie (DFT) basierten Basin-Hopping Algorithmus zur Strukturbestimmung atomarer Cluster. Diese methodische Arbeit wurde zur Interpretation von Multiphotonenabsorptionsspektren im nahen Infrarotbereich kleiner $\text{Co}_n^+ \text{Ar}_m$ ($n=4-8$) Cluster angewendet, die in der Gruppe von Prof. Gerard Meijer in der Abteilung für Molekülphysik des FHI gemessen wurden. Hierbei wurde zunächst durch gleichförmiges Abtasten des Konfigurationsraumes ein Datensatz von Isomeren generiert, der unter anderem verschiedene Jahn-Teller verzerrte Versionen desselben strukturellen Motivs besaß, die demnach im Falle des üblichen Ansatzes, Motive aufgrund chemischer Intuition zu wählen, nicht gefunden worden wären. Für die identifizierten Isomere wurden dann die Infrarotspektren berechnet und mit den gemessenen Daten verglichen. Diese Methode des Abgleichs schwingungsspektroskopischer Fingerabdrücke basiert dabei auf der Annahme, dass unterschiedliche Isomere charakteristische Spektren besitzen, die eindeutig zuzuordnen sind. In dieser Arbeit besaßen jedoch viele Isomere, insbesondere die verschiedenen Jahn-Teller Verzerrungen, qualitativ ähnliche Fingerabdrücke, was somit diese Methode limitierte. Nur in einigen Fällen war hier eine eindeutige Strukturzuordnung möglich. Zur eindeutigeren Eingrenzung ist es daher ratsam, zusätzliche, unabhängige spektroskopische Daten in Betracht zu ziehen, wie beispielsweise Photoelektronenspektren.

Ein weiterer Aspekt dieser Studie betraf die Rolle des involvierten Ar Sondenatoms. Nach der bisherigen Vermutung, die sich auf frühere Arbeiten zu kationischen Vanadium, Niob und Tantal Clustern stützt, ist der Einfluss des Edelgasatoms auf das Infrarotspektrum vernachlässigbar, sodass das gemessene Absorptionsspektrum als das des reinen Übergangsmetallclusters betrachtet werden kann. Im Falle der Cobalt Cluster konnte jedoch erstmals eine starke Abhängigkeit der Spektren von der Zahl der gebundenen Ar Atome beobachtet werden, die insbesondere für die kleineren Cluster stärker ausgeprägt war. Dies veranlasste uns, näher auf die Natur der Co-Ar Bindung einzugehen. Die Annahme, dass das Ar Atom rein elektrostatisch an den geladenen Cobalt Cluster gebunden ist, konnte hierbei durch ein elektrostatisches Modell bestätigt werden. Vereinfacht ausgedrückt ist demnach die positive Ladung des Clusters auf dessen Oberfläche verschmiert und erzeugt dadurch lokale Dipolmomente, die auf den Atomen lokalisiert und radial bzgl. des Clusterzentrums orientiert sind. Das Ar Atom bindet durch induzierte Dipol-Dipol Wechselwirkung auf einem Top-Platz, wobei das Dipolfeld des direkt koordinierten Co Atoms bindet, während die Dipolfelder aller anderen Co Atome repulsiv wirken. Im Rahmen dieses Modells konnte damit die Variation der Bindungsenergien und -abstände für unterschiedliche Clustergrößen und Isomere ebenfalls auf diese rein elektrostatischen Effekte zurückgeführt werden und somit Rückschlüsse auf das unterschiedliche Verhalten des Ar Atoms in den früheren Studien gezogen werden.

Im zweiten Teil dieser Arbeit wurde der methodische Aspekt des Abtastens des Konfigurationsraumes näher untersucht. Aufgrund des exponentiellen Wachstums der Anzahl der lokalen Minima mit der Systemgröße sind die Grenzen heutiger Rechenkapazitäten schnell erreicht, insbesondere im Zusammenhang mit einer rechenintensiven *ab initio* Energetik wie DFT. Anhand kleiner Silizium und Kupfer Cluster als Benchmarksysteme wurde daher der Einfluss der unterschiedlichen technischen Parameter auf die Effizienz des Abtastens untersucht, um mögliche Strategien für Optimierungen herauszuarbeiten. Hierbei stellte das Messen von Effizienz bereits in sich eine Herausforderung dar, da zum einen eine Maßzahl für Effizienz eingeführt werden musste und zum anderen statistisch signifikante Mittelwerte eine hohe Zahl an Abtastzyklen erforderlich machte. Dieses wurde durch das eingeführte Konzept einer "Hopping Matrix" vereinfacht, die die Übergangswahrscheinlichkeiten verschiedener Isomere zusammenfasst und statistisch signifikante Mittelwerte dann ohne weitere *ab initio* Rechnungen liefert. Die Analyse fokussierte sich auf den wesentlichen technischen Aspekt für diese Systemgröße, die Generierung neuer Zufallsstrukturen. Das Basin-Hopping Verfahren erwies sich hierbei als relativ robust bzgl. der technischen Parameter, wobei ungünstige Einstellungen zudem über ein einfaches adaptives Verfahren vermieden werden können. Die Bandbreite, über die die Effizienz bei den untersuchten kleinen Clustergrößen variiert, lässt jedoch nicht auf signifikante Effizienzsteigerungen hoffen, ohne den Anspruch aufzugeben, gleichförmig und ohne jegliche chemische Intuition abzutasten. Stattdessen empfiehlt es sich, den Fokus nicht auf das Abtasten des Konfigurationsraumes selbst, sondern auf die Auswertung der Energieoberfläche zu richten, um Alternativen für die numerisch intensiven *ab initio* Rechnungen zu finden.

Curriculum vitae

| | |
|---------------------|------------------|
| Name | Ralf Gehrke |
| Geburtsdatum | 16. Februar 1979 |
| Geburtsort | Bocholt |
| Staatsangehörigkeit | Deutsch |

Ausbildungsweg

| | |
|----------------------------------|--|
| Dezember 2004 - Januar 2009 | Promotion in der Theorieabteilung des Fritz-Haber-Institutes in der Nachwuchsgruppe von PD Dr. Karsten Reuter |
| Oktober 2003 - September 2004 | Diplomarbeit in der Arbeitsgruppe von Prof. Entel, Theoretische Tieftemperaturphysik, Universität Duisburg-Essen, Campus Duisburg Titel: "Entwicklung einer Dichtefunktionalmethode unter Verwendung von Ortsraumverfahren zur Untersuchung von Clustern" |
| Oktober 1999 - September 2003 | Studium der Physik Universität Duisburg-Essen, Campus Duisburg |
| Juli 1985 - Juni 1998 | Schul Ausbildung Abitur am St. Georg-Gymnasium, Bocholt |

Beschäftigungen

| | |
|------------------------------------|--|
| seit Dezember 2004 | wissenschaftlicher Angestellter in der Nachwuchsgruppe von PD Dr. Reuter |
| September 2002 - September 2004 | Studentische Hilfskraft in der Arbeitsgruppe von Prof. Entel |
| August 2001 - September 2002 | Studentische Hilfskraft in der Arbeitsgruppe von Prof. Rumpf, Numerische Mathematik und Wissenschaftliches Rechnen, Universität Duisburg-Essen, Campus Duisburg |

Acknowledgements

Finally, I would like to appreciate all the help I obtained from many people along my way. First of all, I would like to thank my supervisor Karsten Reuter for giving me the chance to work on such a challenging project in a friendly and stimulating environment, for his support at any time and for the many opportunities to get in contact with different people at many conferences. A special thanks goes to Volker Blum for the exciting work on FHI-aims, from which I gained precious insights into the heart of a DFT code, and for valuable discussions about literally everything. In that sense, I am indebted to the whole FHI-aims team, in particular to Ville Havu, Paula Havu and Felix Hanke.

A special thanks goes to my present office mate Michael Rieger for the support in case of any kind of little problem as well as to Jörg Meyer for permanently being helpful in case of any kind of computer accident.

I further appreciate the discussions with all present and past members of the Theory Department, in particular Jörg Behler, John Kitchin and Patrick Rinke, and all other people that are too many to mention here.

Computational physics becomes much more lively when things that are calculated really happen. In that sense, special thanks goes to Philipp Gruene, André Fielicke and Gerard Meijer for the stimulating and fruitful cooperation, and not least for their patience.

For not being alone in the huge configurational space, I would like to thank Vladimir Froltsov. Special thanks goes also to Matthias Gramzow for all open-minded discussions along my tedious way towards self-consistency.

For the friendly welcome and kind introduction, I would like to thank my former office mate Jutta Rogal.

Additionally, I would like to thank my second supervisor Eberhard Gross for his time to read my thesis and his kind invitations to his seminars.

For the nice time, also outside the institute, I thank Sami Amira, Laura Cano-Cortes, Erik McNellis, Hakim Meskine and all other present and past members of the Junior Research Group.

Finally, my biggest thanks goes to my family and friends for their permanent support and showing me what it is worth working for.